Three-dimensional organoid cell culture models for the study of liver injury

Author:
Collins, Scott

Publication Date:
2021

DOI:
https://doi.org/10.26190/unsworks/2054

License:
https://creativecommons.org/licenses/by/4.0/
Link to license to see what you are allowed to do with this resource.

THREE-DIMENSIONAL ORGANOID CELL CULTURE MODELS FOR THE STUDY OF LIVER INJURY

SCOTT DAVID COLLINS

A THESIS SUBMITTED IN FULFILMENT OF THE REQUIRMENTS FOR THE DEGREE OF

DOCTOR OF PHILOSOPHY

DISCIPLINE OF MEDICINE RESEARCH

SOUTH WESTERN SYDNEY CLINICAL SCHOOL

FACULTY OF MEDICINE

UNSW SYDNEY

2021

Thesis/Dissertation Sheet

Surname/Family Name	:	Collins
Given Name/s	:	Scott David
Abbreviation for degree as give in the University calendar	:	PhD
Faculty	:	Medicine
School	:	South Western Sydney Clinical School
Thesis Title	:	Three-Dimensional Organoid Cell Culture Models for the Study of Liver Injury

Abstract 350 words maximum: (PLEASE TYPE)

The focus of this thesis is the application of 3D liver organoids to model and analyse the molecular and cellular effects of liver injury. We established a 3D liver organoid cell culture model from primary mouse tissue and characterised the capacity of these organoids to model liver characteristics in vitro and used this model to define the interactions between organoid hepatocytes and hepatic stellate cells in a co-culture trans-well system. The impact of inflammatory cytokines tumour necrosis factor-α and transformation growth factor-β on this model, as well as other variables such as hypoxia and the anti-fibrosis drug Halofuginone were assessed. Hepatic stellate cell dependent decreases in organoid viability and organoid dependent increases in hepatic stellate cell viability were observed, as well as Halofuginone dependent decreases in hepatic stellate cell viability were also observed. Markers characteristic of liver injury and fibrosis, such as Actn1 and Lamb3 were upregulated in hepatic stellate cells, although collagen expression was downregulated in these cells.

Transcriptional profiling revealed a tumour necrosis factor-α mediated apoptotic response in organoids and an inflammatory response in both the organoids and hepatic stellate cells. We concluded that while liver organoids and hepatic stellate cells responded to experimental variables, there were limitations when it came to the cross talk between the cultures in the trans-well system. While apoptotic bodies from the organoids may have stimulated proliferation of hepatic stellate cells, many key genes responsible for liver injury were either not upregulated or were downregulated in co-culture.

Electron microscopy analysis of liver organoids showed important ultrastructural changes compared to a whole liver section. We also demonstrated how the use of high-resolution field emission scanning electron microscopy with automated scan resolution can generate a high-resolution ultrastructure map of the whole organoid. This method can also be combined with correlative light electron microscopy for immunofluorescent labelling of proteins of interest using quantum dot nanoparticles. Overall, our 3D organoid model of liver injury had encouraging results and furthering our understanding of pathogenesis of liver fibrogenesis in vitro and the study of novel anti-fibrotic therapeutic agents.

ORIGINALITY STATEMENT

'I hereby declare that this submission is my own work and to the best of my knowledge it contains no materials previously published or written by another person, or substantial proportions of material which have been accepted for the award of any other degree or diploma at UNSW or any other educational institution, except where due acknowledgement is made in the thesis. Any contribution made to the research by others, with whom I have worked at UNSW or elsewhere, is explicitly acknowledged in the thesis. I also declare that the intellectual content of this thesis is the product of my own work, except to the extent that assistance from others in the project's design and conception or in style, presentation and linguistic expression is acknowledged.'

Signed   …………………………………………….................

Date   …………………………….............
03/03/2022

INCLUSION OF PUBLICATIONS STATEMENT

UNSW is supportive of candidates publishing their research results during their candidature as detailed in the UNSW Thesis Examination Procedure.

Publications can be used in their thesis in lieu of a Chapter if:

- The candidate contributed greater than 50% of the content in the publication and is the "primary author", ie. the candidate was responsible primarily for the planning, execution and preparation of the work for publication
- The candidate has approval to include the publication in their thesis in lieu of a Chapter from their supervisor and Postgraduate Coordinator.
- The publication is not subject to any obligations or contractual agreements with a third party that would constrain its inclusion in the thesis

Please indicate whether this thesis contains published material or not:

☒ This thesis contains no publications, either published or submitted for publication
(if this box is checked, you may delete all the material on page 2)

☐ Some of the work described in this thesis has been published and it has been documented in the relevant Chapters with acknowledgement
(if this box is checked, you may delete all the material on page 2)

☐ This thesis has publications (either published or submitted for publication) incorporated into it in lieu of a chapter and the details are presented below

---

CANDIDATE'S DECLARATION

I declare that:

- I have complied with the UNSW Thesis Examination Procedure

- where I have used a publication in lieu of a Chapter, the listed publication(s) below meet(s) the requirements to be included in the thesis.

Candidate's Name Scott David Collins	Signature	Date (dd/mm/yy) 03/03/2022

THREE-DIMENSIONAL ORGANOID CELL CULTURE MODELS FOR THE STUDY OF LIVER INJURY

SCOTT DAVID COLLINS

A thesis submitted in fulfilment of the requirements for the degree of

Doctor of Philosophy

Discipline of Medicine Research

South Western Sydney Clinical School and the Faculty of Medicine

UNSW Sydney

2021

DECLARATION

Unless otherwise acknowledged, the work described in this thesis was carried out personally by the author between February 2017 and March 2021 in the Gastroenterology and Liver Laboratory at the Ingham Institute for Applied Medical Research, as a part of the South Western Sydney Clinical School, UNSW Sydney.

None of this work has been submitted previously for the purpose of obtaining any other degree.

Scott David Collins

25th March 2021

ACKNOWLEDGEMENTS

I am excited to be at the end of a challenging but rewarding PhD. The challenges being the difficulty and inherent risk of establishing and applying a relatively new experimental 3D cell culture technique, with no prior experience with 3D cell culture or an available mentor. While this can be a blessing, because as a researcher you have no options, but to become comprehensively versed in your field, this is a very long, expensive, and risky process of developing competency.

I would first like to acknowledge my primary supervisors Dr. Chandana Herath and Prof. Nicholas Shackel for their guidance during this project. As well as my secondary and co-supervisors, A/Prof. Kevin Spring, Dr. Katherine Bryant and Dr. Scott Read.

I would like to acknowledge A/Prof. Miriam Levy of the Liver Cancer and Disease Centre Academic Unit, Liverpool Hospital for funding my PhD research scholarship. The UNSW Graduate Research School of Medicine for funding my Higher Degree Research Completion Scholarship. The South Western Sydney Local Health District for the SWSLHD Academic Grant and the Triple I Research Grant for providing funding for my research.

I would also like to acknowledge my colleagues at the Gastroenterology and Liver research group, Vincent Chiu, Christine Yee, Dr. Aimei Lee, Lisa Tran, Igor Strevanoski, Nathan Main, Okelewey Dabere, Rida Hanna, Dr. Magdalena Budzinska, Dr. Thomas Tu and Dr. Gloria Yuen.

ACKNOWLEDGEMENTS

PUBLICATIONS

Collins SD, Yuen G, Tu T, Budzinska MA, Spring K, Bryant K, Shackel NA (2019). Chapter 3: In Vitro Models of the Liver: Disease Modelling, Drug Discovery and Clinical Applications. Janina E.E. Tirnitz-Parker, MSc, PhD (ed), *Hepatocellular Carcinoma*. (pp. 47-67) Brisbane Australia: Condon Publications. PubMed: NBK549195

AWARDS

Liver Cancer Scholarship   **2017-2020**

Ph.D. Research Scholarship, Liver Disease and Cancer Centre, Liverpool Hospital, Australia

Gastroenterology Society of Australia Travel Grant   **2018**

Boehringer Ingelheim Fonds Travel Grant   **2019**

1st Prize Microphotography Competition   **2019**

NSW Cell & Developmental Biology Meeting, Australia

HDR Completion Scholarship   **2021**

Ph.D. Research Scholarship, Graduate Research School of Medicine, UNSW Sydney

PRESENTATIONS

Research Oral Presentations

Gastroenterology Society of Australia Research Workshop	2018 (Gold Coast, Australia)
CONCERT 2nd All Members Day	2019 (Sydney, Australia)
Virology Research Seminar Series, NSW Pathology	2020 (Sydney, Australia)

Research Poster Presentations

ComBio	2018 (Sydney, Australia)
EMCR Symposium	2018 (Sydney, Australia)
Health Beyond Research & Innovation Showcase	2018 (Sydney, Australia)
3rd Australian Biology of Ageing conference	2018 (Brisbane, Australia)
Health Beyond Research & Innovation Showcase	2019 (Sydney, Australia)
NSW Cell & Developmental Biology Meeting	2019 (Sydney, Australia)
EMBO Practical Course: Current Methods in Cell Biology	2019 (Heidelberg, Germany)
ASCB	EMBO Cell Bio Meeting	2020 (Virtual Conference)
GESA AGW 2020 Symposia	2020 (Virtual Conference)

EMBO | EMBL Symposium: Organoids: Modelling Organ Development and Disease in 3D Culture   2020 (Virtual Symposium)

ABBREVIATIONS

2D	Two-dimensional
3D	Three-dimensional
5-FU	5-fluorouracil
5-HT	5-hydroxytryptamine receptors
5-HTBR2	5-hydroxytrypamine receptor 2B
A1AT	Alpha-1 antitrypsin
ADMET	Absorption, Distribution, Metabolism, Excretion and Toxicity
aFGF	acidic fibroblast growth factor
ALB	Albumin
ANOVA	Analysis of Varience
APC	Allophycocyanin
aSC	Adult Stem Cells
AT1R	Type 1 Angiotensin II Receptor
BSA	Bovine Serum Albumin
BMP	Bone Morphogenetic Protein
CB	Cannabinoid Receptor
CC	Cholangiocarcinoma
CCL	C–C Motif Chemokine
CCl_4	Carbon Tetrachloride
CCRs	C–C Chemokine Receptors
CD133	Prominin 1
CFTR	Cystic Fibrosis Transmembrane Conductance Regulator
CHC	Hepatocellular-Cholangiocarcinoma
CK	Cytokeratin
CK19	Cytokeratin 19
CLEM	Correlative Light Electron Microscopy
Col	Collagen
CPA	Collagen Proportionate Area
CRISPR	Clustered Regularly Interspaced Short Palindromic Repeats
CTGF	Connective Tissue Growth Factor
CTGF	Connective Tissue Growth Factor
CXCL	C–X–C Motif Chemokine
CYP450	Cytochrome P450
DALYs	Disability-Adjusted Life-Years
DAMPs	Damage-Associated Molecular Patterns
DAPI	4′,6-diamidino-2-phenylindole
DDRs	Discoidin Domain-containing Receptors
Diff	Differentiated

ABBREVIATIONS

DMEM	Dulbecco's Modified Eagle Medium
DNA	Deoxyribonucleic Acid
ECM	Extracellular Matrix
EGF	Epidermal Growth Factor
EpCAM	Epithelial Cell Adhesion Molecule
ER	Endoplasmic Reticulum
ERK	Extracellular Signal-Regulated Kinases
ES	Embryonic Stem Cells
ET	Endothelin
FACS	Fluorescence-Activated Cell Sorting
FasL	Fas Ligand
FBS	Fetal Bovine Serum
FDA	U.S. Food and Drug Administration
FDR	False Discovery Rate
FESEM	Field Emission Scanning Electron Microscopy
FGF	Fibroblast Growth Factor
FITC	Fluorescein Isothiocyanate
FXR	Farnesoid X Receptor
GPCRs	G Protein-Coupled Receptors
GPR91	Succinate Receptor 1
GSEA	Gene Set Enrichment Analysis
Halo	Halofuginone
HBV	Hepatitis B Virus
HCC	Hepatocellular Carcinoma
HCV	Hepatitis C Virus
HDV	Hepatitis D Virus
Hep	Hepatocytes
HBsAg	Hepatitis B Surface Antigen
HGF	Hepatocyte Growth Factor
Hh	Hedgehog Signalling
HIFs	Hypoxia-Inducible Factors
hiPSCs	Human Induced Pluripotent Stem Cells
HNF4α	Hepatocyte Nuclear Factor 4 Alpha
HRSEM	High Resolution Field Emission Scanning Electron Microscopy
HSCs	Hepatic Stellate Cells
IF	Immunofluorescence
IFN-γ	Interferon-γ
IGF1	Insulin-like Growth Factor 1
IGFBP5	Insulin-like Growth Factor Binding Protein 5
IgG	Immunoglobulin G
IL	Interleukin
iPSC	Induced Pluripotent Stem Cells
IVC	Inferior Vena Cava
JS1	Mouse Hepatic Stellate Cell Line

ABBREVIATIONS

KGF	Keratinocyte Growth Factor
LAMP2	Lysosome-associated Membrane Protein 2
Lgr5	Leucine Rich Repeat Containing G Protein-Coupled Receptor 5
LPCs	Liver Stem/Progenitor Cells
LPS	Lipopolysaccharide
LPV	left Portal Vein
LSECs	Liver Sinusoidal Endothelial Cells
LSM	Laser Scanning Microscope
LXR	Liver X Receptor
MCP1	Monocyte Chemoattractant Protein 1
MDS	Multidimensional Scaling
MIP-1α	Macrophage Inflammatory Protein-1 Alpha
miRNAs	microRNAs
MMP	Matrix Metalloproteinase
MTT	(4,5-Dimethylthiazol-2-yl)-2,5-Diphenyltetrazolium Bromide
MYC	Myelocytomatosis Gene Family
NAFLD	Non-Alcoholic Fatty Liver Disease
NASH	Non-Alcoholic Steatohepatitis
Neg Con	Negative Control
NES	Normalised Enrichment Score
NK	Natural Killer Lymphocytes
NKT	Natural Killer T
NOS	Nitric Oxide Synthetase
NOX	NADPH Oxidase
NR4A1	Nuclear Receptor Subfamily 4 Group A Member 1
O_2	Oxygen
Org	Mouse Liver Organoids
PAI	Plasminogen Activator Inhibitor
PAR2	Proteinase-Activated Receptor 2
PBS	Phosphate Buffered Saline
PCTS	Precision-Cut Tissue Slices
PDGF	Platelet-Derived Growth Factor
PDO	Patient-Derived Organoids
PFA	Paraformaldehyde
PPARs	Peroxisome Proliferator-Activated Receptors
PV	Portal Vein
QDs	Quantum Dot Nanocrystals
RNA	Ribonucleic Acid
ROIs	Regions of Interest
ROS	Reactive Oxygen Species
RPV	Right Portal Vein
Rspo	R-spondin
RT	Reverse Transcriptase

ABBREVIATIONS

RT qPCR	Reverse Transcriptase quantitaive Polymerase Chain Reaction
SARS-CoV-2	Severe Acute Respiratory Syndrome Coronavirus 2
SEM	Scanning Electron Microscopy
SMA	α-Smooth Muscle Actin
SMO	Smoothened Homolog
Sox9	SRY-Box Transcription Factor 9
SOX9	SRY (sex determining region Y)-box 9
TEM	Transmission Electron Microscopy
TERT	Telomerase Reverse Transcriptase
TGF-α	Transforming Growth Factor-Alpha
TGF-β	Transforming Growth Factor-Beta
TIMP	Tissue Inhibitor of MMP
TLR	Toll-like Receptor
TNF	Tumour Necrosis Factor-Alpha
TNFR1	TNF receptor 1
TRAIL	TNF-related Apoptosis-Inducing Ligand
TUMOROID	The Tumour Organoids: Feasibility to Predict Sensitivity to Treatment in Cancer Patients Study
Undiff	Undifferentiated
VDR	Vitamin D3 Receptor
VEGF	Vascular Endothelial Growth Factor
WES	Whole-Exome Sequencing
Wnt	Wingless-related Integration Site
ZO-1	Zonula Occludens-1

TABLE OF CONTENTS

TABLE OF CONTENTS

TABLE OF CONTENTS

TABLE OF CONTENTS

FIGURES AND TABLES

FIGURES AND TABLES

CHAPTER 2 MATERIALS AND METHODS

CHAPTER 3 CHARACTERISATION OF MOUSE LIVER ORGANOIDS

CHAPTER 5 TRANSCRIPTIONAL PROFILING ANALYSIS OF THE IN VITRO MODELLING OF LIVER INJURY AND FIBROSIS

FIGURES AND TABLES

CHAPTER 6 ULTRSTRUCTURE MAPPING AND CHARACTERISATION OF LIVER ORGANOIDS USING SCALABLE HIGH RESOLUTION FIELD EMISSION SCANNING ELECTRON MICROSCOPY

ABSTRACT

Chronic liver diseases including cirrhosis and primary liver cancer are a significant health burden worldwide. Liver cirrhosis is end stage liver injury resulting in a progressive fibrosis phenotype, in which the hepatic architecture is distorted. The most common cause of cirrhosis is chronic liver injury caused by hepatitis B, alcohol related liver disease, hepatitis C or non-alcoholic steatohepatitis. Primary liver cancer is a leading cause of cancer mortality globally and is commonly observed as a progression of liver cirrhosis.

Liver injury usually occurs because of immune-mediated or direct injury to the hepatocytes and involves multiple cellular subsets; including hepatic stellate cells, liver adipocytes, liver resident macrophages kupffer cells, endothelial cells and infiltrating immune cells. Injury to these cells result in the release of reactive oxygen species, proinflammatory signals, proliferation-associated cytokines, and the activation of repair pathways. A chronic activation of these signals can result in dysregulation of the normal repair response and generation of a pathogenic fibrotic response. A broadly canonical response, chronic inflammation drives fibrosis and cirrhosis irrespective of liver injury aetiology.

The burden of liver disease provides the impetus to pursue the use of representative *in vitro* models of liver function and responses to injury. Improved 2D and 3D *in vitro* disease models would enhance our understanding of the causes of liver injury and the development of cirrhosis and primary liver cancer while increasing the efficacy of preclinical drug discovery. Current 2D *in vitro* assays based on cell lines such as HepG2 that have reduced metabolic capacities compared to primary hepatocytes *ex vivo*, and the use of primary human hepatocytes suffers from high donor-to-donor variation and only retain *in vivo* characteristics for a short time *ex*

ABSTRACT

vivo. The shortcomings of 2D cell culture models have driven the development of 3D cell culture techniques. The advantages of 3D models include replicating the complex attributes of the liver beyond liver specific metabolism, such as increased cell density, organisation, and cell-cell signalling, O_2 zonation, as well as the anatomy of the liver lobule and the circulatory system. After a comprehensive review of all the current *in vitro* models of the liver we hypothesised that a liver organoid cell culture model co-cultured with myofibroblast like hepatic stellate cells can model liver injury. An organoid cell culture is defined as a collection of cells culturing several cell types that develop from stem cells or organ progenitors and self-organise through cell sorting and spatially restricted lineage commitment, similar to organogenesis *in vivo*. Liver organoids have demonstrated many advantages over conventional *in vitro* models such as long-term genetic stability, 2D *in vivo*-like organisation, and maintaining the necessary cellular cross talk and behavioural characteristics of their primary corresponding cells.

The focus of this thesis is the application of 3D liver organoids to model and analyse the molecular and cellular effects of liver injury. We established a 3D liver organoid cell culture model from primary mouse tissue and characterised the capacity of these organoids to model liver characteristics *in vitro* and used this model to define the interactions between organoid hepatocytes and hepatic stellate cells in a co-culture trans-well system. The impact of inflammatory cytokines tumour necrosis factor-α and transformation growth factor-β on this model, as well as other variables such as hypoxia and the anti-fibrosis drug Halofuginone were assessed. Hepatic stellate cell dependent decreases in organoid viability and organoid dependent increases in hepatic stellate cell viability were observed, as well as Halofuginone dependent decreases in hepatic stellate cell viability were also observed. Markers characteristic of liver injury and fibrosis, such as *Actn1* and *Lamb3* were upregulated in hepatic stellate cells, although collagen expression was downregulated in these cells.

ABSTRACT

Transcriptional profiling revealed a tumour necrosis factor-α mediated apoptotic response in organoids and an inflammatory response in both the organoids and hepatic stellate cells. We concluded that while liver organoids and hepatic stellate cells responded to experimental variables, there were limitations when it came to the cross talk between the cultures in the trans-well system. While apoptotic bodies from the organoids may have stimulated proliferation of hepatic stellate cells, many key genes responsible for liver injury were either not upregulated or were downregulated in co-culture.

Electron microscopy analysis of liver organoids showed important ultrastructural changes compared to a whole liver section. Our findings of secreted exosomes, microvilli within the lumen of the organoids, and many ultrastructural features found within liver cells *in vivo* confirm that our 3D liver organoids closely resemble the liver. We also demonstrated how the use of high-resolution field emission scanning electron microscopy with automated scan resolution can generate a high-resolution ultrastructure map of the whole organoid. This method can also be combined with correlative light electron microscopy for immunofluorescent labelling of proteins of interest using quantum dot nanoparticles. Overall, our 3D organoid model of liver injury had encouraging results and furthering our understanding of pathogenesis of liver fibrogenesis *in vitro* and the study of novel anti-fibrotic therapeutic agents.

CHAPTER 1

INTRODUCTION

CHAPTER 1

INTRODUCTION

Liver injury and fibrosis are the mostly clinically undiscovered precursors to chronic liver diseases such as cirrhosis and primary liver cancer, which are significant causes of morbidity and mortality worldwide. Due to the canonical nature of liver disease and the mostly irreversible nature of chronic liver diseases a good strategy for reducing morbidity and mortality would be to inhibit the progression of liver injury and fibrosis to cirrhosis and cancer using a prophylactic drug given to at risk populations. While preventing, treating and/or eliminating the risk factors of liver disease is an effective strategy for reducing the harm caused by chronic liver diseases the dysregulation of normal repair responses, called the pathogenic fibrotic response, can still cause chronic liver disease even if the cause of the initial injury has been eliminated.

To develop a drug intervention that inhibits the pathogenic fibrotic response, an *in vitro* model of liver injury will need to be developed for preclinical anti-fibrosis drug discovery. In this chapter I will describe the anatomy and cell biology of the liver, the epidemiology of chronic liver disease, the cell biology of liver injury, fibrosis, and cirrhosis. I will also review all relevant *in vitro* models of the liver for the best candidate for modelling liver injury.

CHAPTER 1 INTRODUCTION

1.1 The Human Liver

In the human body the liver is a critical internal organ which governs blood volume, energy metabolism, endocrine control of growth signalling, immune system support as well as the breakdown of xenobiotic compounds (Trefts *et al* 2017; Rui 2014), weighing between 1.2 – 1.5 kg in adults and located in the in the right upper quadrant of the abdomen (Figure 1.1) (Bioulac-Sage *et al* 2007; Sherlock and Dooley 2002).

1.1.1 Liver Functions

Food digested by the gastrointestinal tract releases carbohydrates, fatty acids and amino acids into the blood steam which are then transported to the liver via the portal vein. In this 'fed' state glucose and fructose are removed from the gut by liver hepatocytes for the purposes of providing readily accessible energy. Glucose undergoes glycolysis or is converted into either glycogen or triglycerides to build energy stores to be released during times of fasting (Figure 1.2). Ingested fatty acids are also converted into triglycerides or are catabolised into acetyl-CoA by β-Oxidation for energy production. Amino acids may also be oxidized for energy production or utilized as anaplerotic substrates for the tricarboxylic acid cycle (Treft *et al* 2017; Rui 2014; Burt and Day 2002). During a 'fasted' state the liver becomes an essential source of energy for other tissues as hepatocytes produce glucose by glycogenolysis and gluconeogenesis. The liver also performs endogenous fatty acid synthesis and oxidation to produce ketones for energy needs.

Other crucial functions performed by the liver include lipoprotein formation for lipid transport, plasma protein synthesis, cholesterol synthesis, the synthesis and modification of non-essential amino acids, the re-amination of essential amino acids, and the breakdown of amino acids producing ammonia and urea (Treft *et al* 2017; Rui 2014; Burt and Day 2002). Hepatocytes also uniquely metabolize bilirubin for clearing old or damaged red blood cells and converts

cholesterol to bile acid for emulsifying and absorbing dietary lipids in the intestine (Burt and Day, 2002). The liver is also the principal site for the biotransformation of drugs and xenobiotics. Performed in two phases, the *Phase I reactions* which convert compounds to more polar metabolites by oxidation, reduction or hydrolysis (which is often sufficient for excretion), and the *Phase II reactions* that conjugate compounds with an endogenous molecule such as glucuronic acid (Burt and Day 2002). A significant system involved in oxidising of endogenous substances, drugs and carcinogens is the Cytochrome P450 (CYP450) superfamily of enzymes located in the smooth endoplasmic reticulum of hepatocytes (Burt and Day 2002). Bile formation is another unique function of the liver which is vital for digestion and absorption of fats and fat-soluble vitamins in the small intestine, as well as waste products like bilirubin which are eliminated from the body by secretion into bile before excretion for the body as faeces. Bile is a complex aqueous secretion that originates from hepatocytes and is modified distally by absorptive and secretory transport systems in the bile duct epithelium. Bile then enters the gallbladder where it is concentrated or is delivered directly to the intestinal lumen (Boyer 2013). The liver is also an immunologically complex organ, responsible for producing acute phase proteins, complement components, cytokines and chemokines, and contains large, diverse populations of resident immune cells (Robinson *et al* 2016).
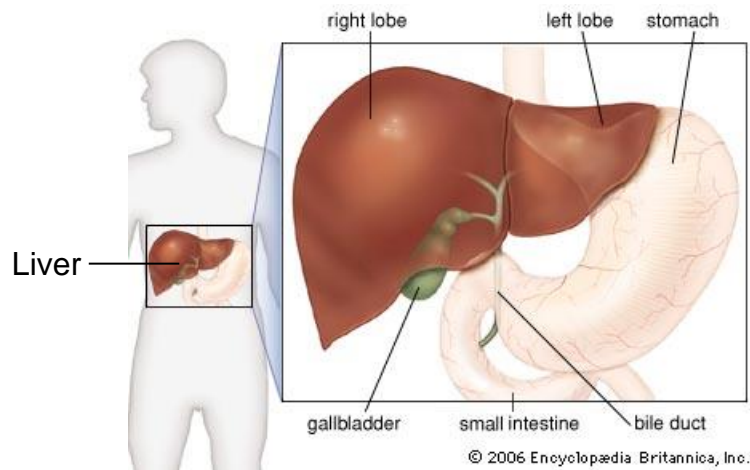
Figure 1.1 The Human Liver's Position in Relation to Other Organs. (source: britannica.com)
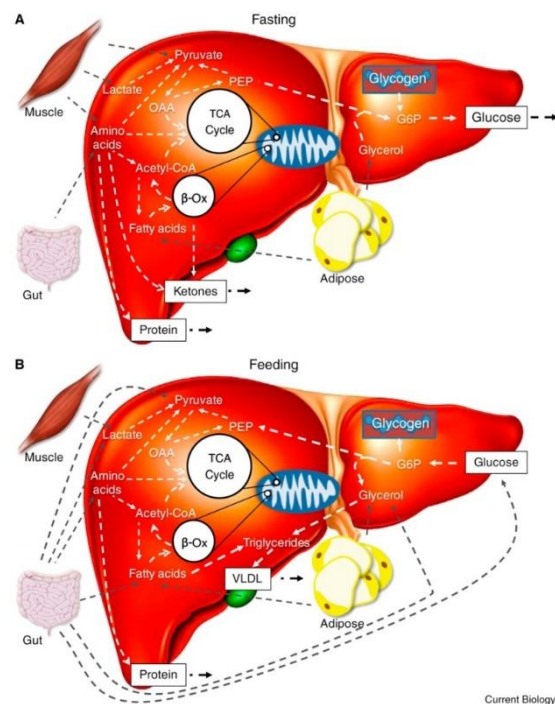
Figure 1.2 The Liver in the Fasted and Fed State. A and B. This figure summarises the central molecular pathways of glucose metabolism by the liver in the fasting and feeding states in relation to the muscles, gut and adipose tissues. PEP = phosphoenolpyruvate, OAA = oxaloacetic acid, TCA Cycle = Tricarboxylic acid cycle, G6P = Glucose 6 Posphate, β-Ox = Beta-oxidation, VLDL = Very Low Density Lipids (Treft *et al*, 2017)

1.1.2 Liver Anatomy

The traditional anatomical lobes of the liver are the larger right lobe (anterior view) which is attached by the falciform ligament to the smaller left lobe, the caudate lobe and the quadrate lobe (Figure 1.3) each of which is demarcated from the other by peritoneal folds, hepatic fissures, extrahepatic blood vessels and extrahepatic bile ducts (Fasel *et al* 2007). The liver has a double blood supply consisting of the portal vein which brings venous blood from the intestine and spleen, and the hepatic artery coming from the coeliac axis, which supplies the liver with arterial blood. The portal vein and hepatic artery divide into branches into the right and left lobes, and the right and left hepatic ducts emerge from the liver and unite in the porta hepatis to form the common hepatic duct. Venous drainage from the liver is through the right and left hepatic veins which emerge from the back of the liver and at once enter the inferior vena cava very near its point of entry into the right atrium of the heart. The inferior vena cava makes a deep groove to the right of the caudate lobe about 2 cm from the mid-line, and the gallbladder lies in a fossa extending from the inferior border of the liver to the right end of the porta hepatis (Sherlock and Dooley 2002). The liver is chiefly attached to the diaphragm by the right and left coronary ligaments which extent laterally to form the triangular ligaments, it is also attached to the stomach and duodenal bulb by the lesser omentum (Fasel *et al* 2007). An idealised subdivision of the liver into 8 portal venous segments has been adopted worldwide by radiologist, hepatologists, and surgeons. As described by Couinaud in 1957 (Figure 1.4) the liver is subdivided into 8 different territories by means of vertical and transverse scissures. The vertical planes contain the inferior vena cava and the right, middle and left hepatic veins. The transverse plane passes through the right and left branches of the portal vein. The liver tissue behind the portal bifurcation is considered as a separate segment, from which the numbering starts in a clockwise pattern (Fasel *et al* 2007). While this schema is widely accepted to describe the localization of focal hepatic lesions and the most common types of liver resections,

conceptual reappraisal has been proposed due to recent studies into the branching patterns in the livers of cadavers (example in Figure 1.5) have found portal venous territories ranging from 9 to 44 per person with an average of 20 (Fasel *et al* 2007; Fasel 2008; Fasel *et al* 2010).
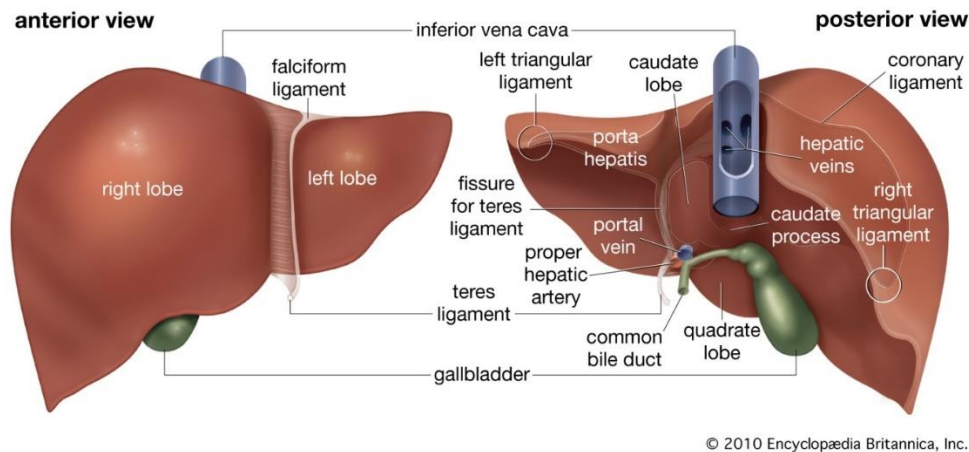
Figure 1.3 Anterior and posterior views of the liver. Macro anatomy of the liver including the lobes and ligaments, as well as the position of the gallbalder, common bile duct, proper hepatic artery, portal vein, inferior vena cava, and hepatic veins. (source: britannica.com)
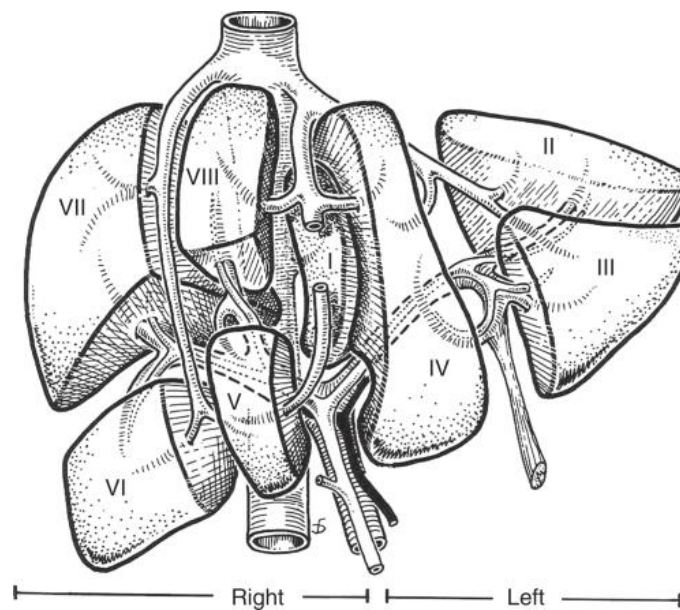
Figure 1.4 The Segments of the Liver as First Described. The liver is subdivided into 8 different territories by means of vertical and transverse scissures. The vertical planes contain the inferior vena cava and the right, middle and left hepatic veins. (Couinaud *et al* 1957)
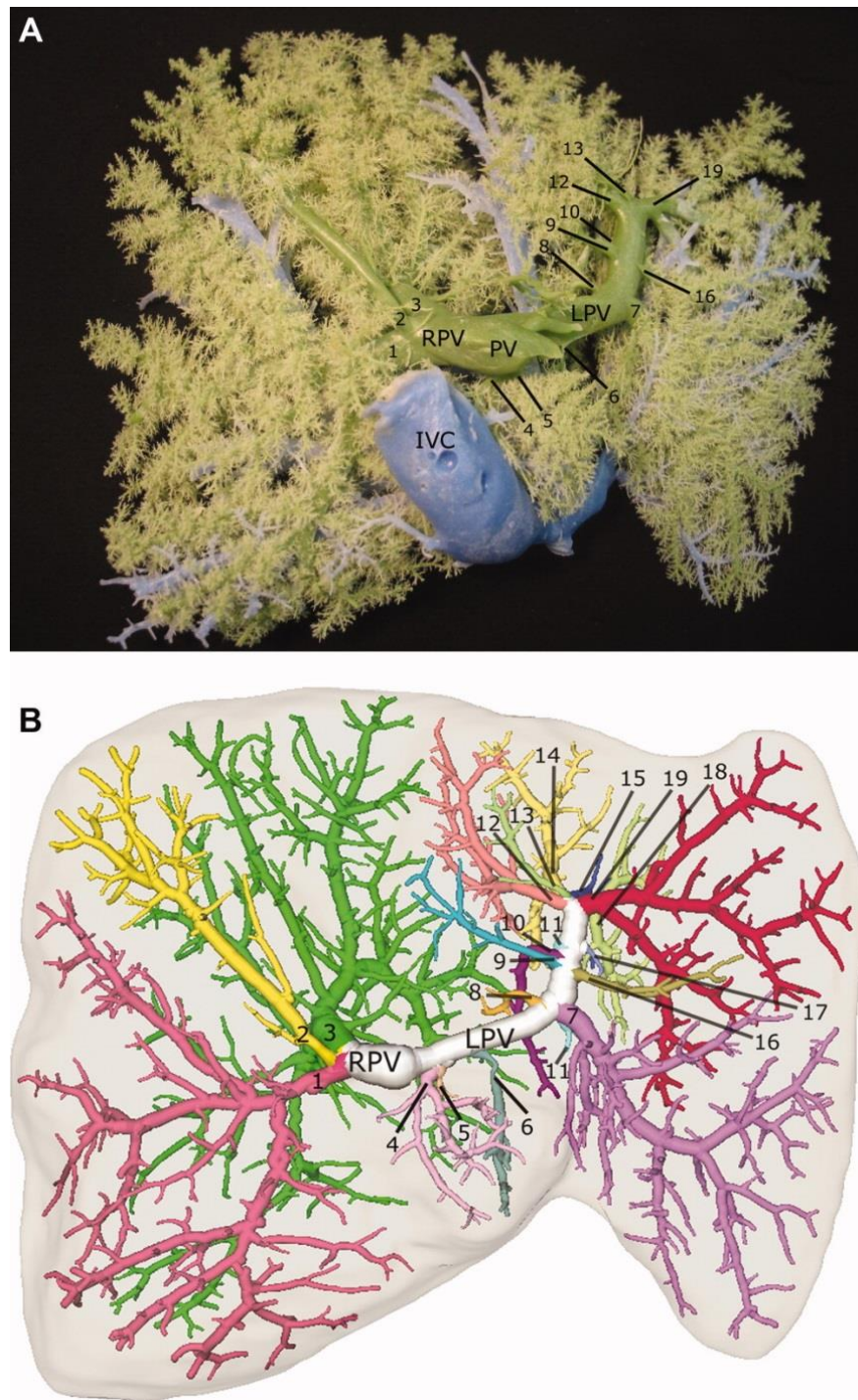
Figure 1.5 Inferior View of the Portal Venous Branching Pattern in a Human Liver. A.
Anatomical specimen (corrosion cast). The portal vein (PV) are labelled in green, the inferior
vena cava (IVC) and hepatic veins have been labelled blue. **B**. A Digital reconstruction of the
portal venous tree after CT imaging of the anatomical specimen. The different branches have
been numbered 1 to 19 as well as labelled by different colors. RPV = Right Portal Vein, LPV
= Left Portal Vein. (Fasel 2008).

1.1.3 Histological Morphology

The apparent structural unit of the liver is the lobule, a polyhedral prism (approximately 0.7 X 2 mm), the boundaries of which are limited by four to five portal triads prolonged by connective tissue septa (Figure 1.6). The portal triad consist of the terminal portal vein, terminal hepatic arteriole and bile duct. Using histological sections, the portal tracts, central veins and lobular parenchyma can be identified. The portal tracts contain branches of the hepatic artery and portal vein, one or two bile ducts, lymphatics, nerves, a few lymphocytes and fibroblasts in loose connective tissue. The hepatic sinusoids allow exchange between blood and the unicellular sheets of hepatocytes between the incoming vessels of the portal tracts and the central veins (Figure 1.7) (Bioulac-Sage *et al*, 2007). Adjacent to the sinusoid is the canal of Hering (Figure 1.8) of the ductal system, specialized channels lined by both hepatocytes and cholangiocytes (Tabibian *et al*, 2013).

There are significant metabolic differences within hepatocytes between the perivenous zone where the central vein is located, the periportal zone where portal triad is located and the intermediary zone in between (Figure 1.7) (Kietzmann, 2017). The intercellular oxygen concentration of the lobule can vary between 15-20 mm Hg in the perivenous zone to 45-50 mm Hg in the periportal zone (Jungermann & Kietzmann, 2000). Metabolic processes like glucose uptake, glycolysis, glutamine synthesis, bile acid synthesis and glucuronidation are also all higher in perivenous cells, which is where the highest concentration of CYP450 enzymes exist. In contrast oxygen uptake, glucose delivery, gluconeogenesis, urea synthesis, fatty acid oxidation, cholesterol synthesis and sulfation are all higher in periportal cells. Non-parenchymal cells such as bile duct cells and hepatic stellate cells are also more abundant in the oxygen rich periportal zone. This zonation is regulated by several factors including β-catenin and hedgehog signalling which are controlled by the oxygen gradient (Jungermann & Kietzmann, 2000).
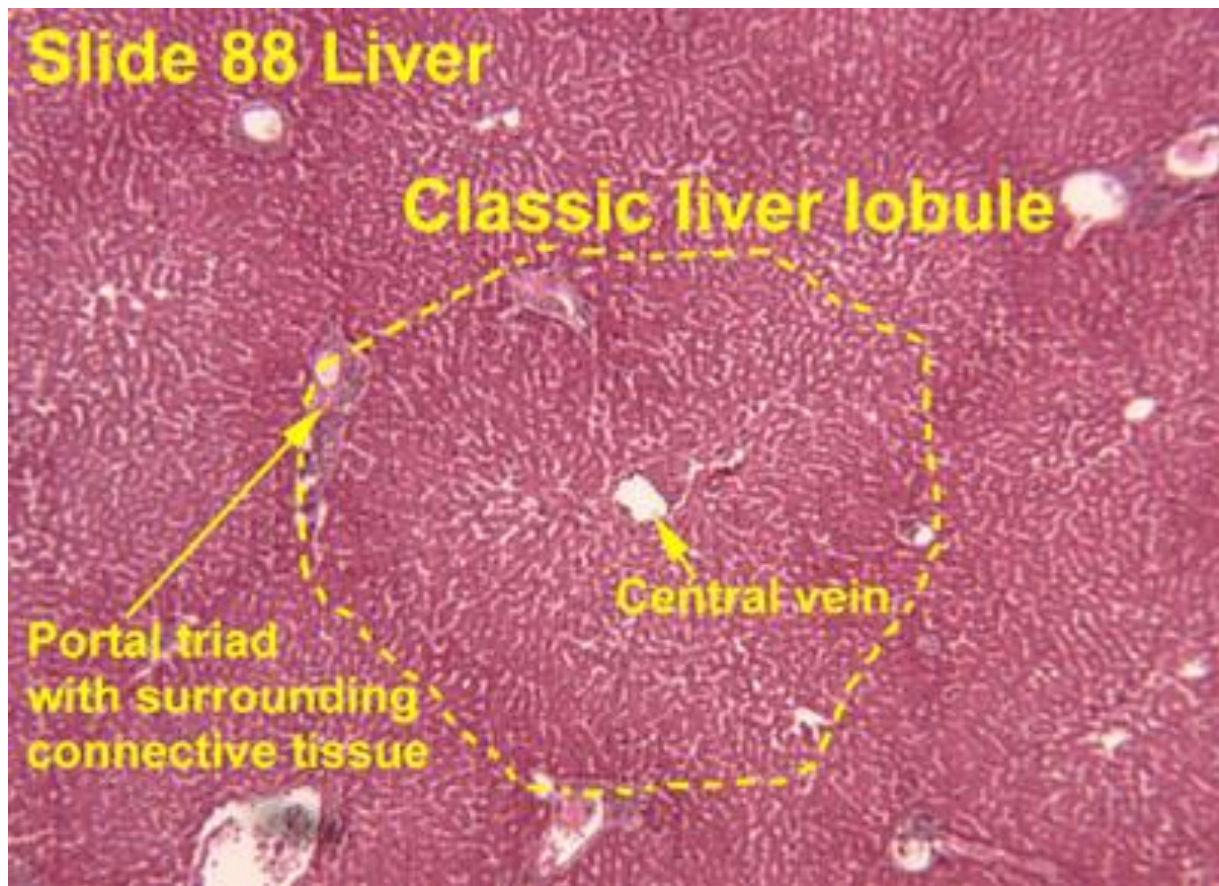
Figure 1.6 Classic Human Liver Lobule. Histological image of a human liver lobule with the classic polyhedral prism shape, a central vein in and portal triads with surrounding connective tissue. (Source: University of Oklahoma, Health Science Center, Interactive histology Atlas)
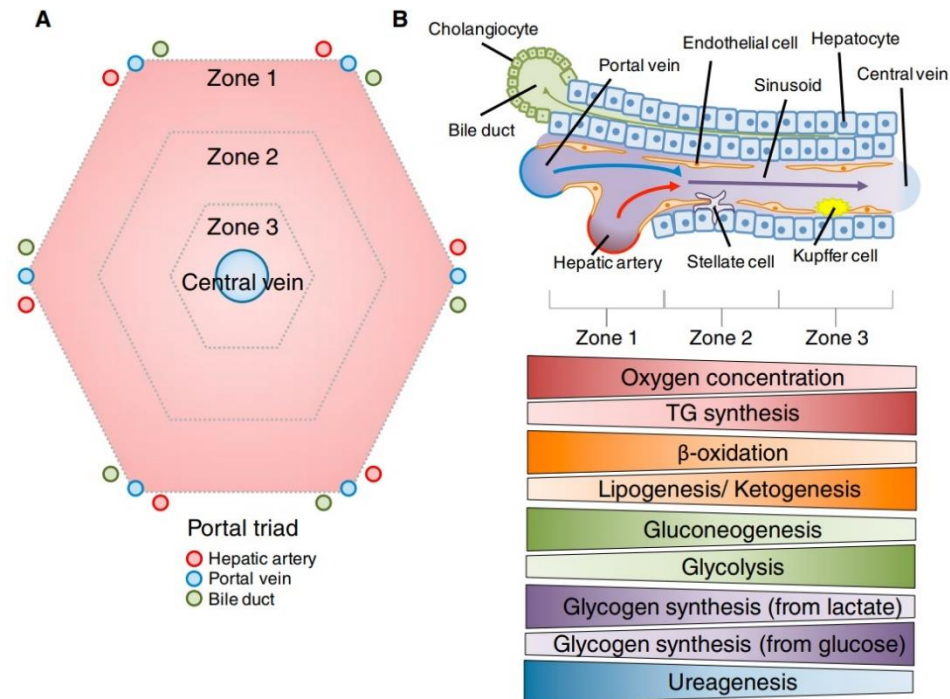
Figure 1.7 Organisation of the Liver Lobule and Hepatic Sinusoids. A and B. Diagram illustrating the location, cellular organisation and zonal molecular characterisitics of the hepatic sinusoids. (Trefts *et al*, 2017).
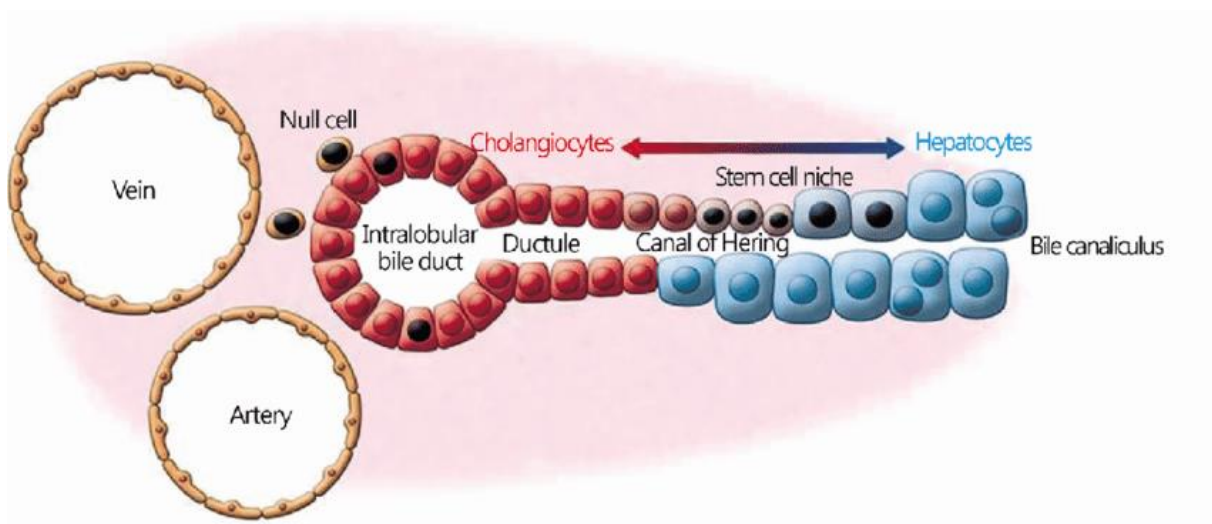
Figure 1.8 Hepatic Stem Cell Niche in the Canals of Hering. Anatomy of the hepatic stem stell niche in the Canal of Hering, proximal to the portal triad of the liver lobule. (Kordes, Häussinger, 2013).

1.2 Hepatic Cell Populations

The hepatic sinusoid is populated primarily by hepatocytes and lined by liver sinusoidal endothelial cells (LSECs). Associated with the sinusoids are the phagocytic Kupffer cells of the reticulo-endothelial system and hepatic stellate cells (Figure 1.7) (Sherlock & Dooley, 2002, Chapter 1). The canal of Hering populated by hepatocytes and cholangiocytes is believed to be the location of the hepatic stem cell niche where liver stem/progenitor cells continuously generated new hepatocytes in the portal field (Figure 1.8) which mature on their way to the central vein (Kordes and Häussinger, 2013).

1.2.1 Hepatic Parenchymal Cells

Hepatocytes comprise approximately 60% of the liver's cells. They are 30 µm in diameter and polygonal. The hepatocyte has three membrane surfaces, one facing the sinusoidal, the second facing the canalicular and the third lateral membrane facing the neighbouring hepatocytes (Sherlock & Dooley, 2002). The sinusoidal membrane makes up 70% of the total cell surface area and is covered in 0.5 µm long microvilli, which increases the surface area sixfold. Material exchange between the blood and hepatocytes through the Disse space is a function solely of the sinusoidal plasma membrane. The canalicular membrane is the biliary pole of the hepatocyte and make up 15% of the cell surface. The surface is covered in microvilli and isolated from the Disse space by tight junctions. The lateral membrane makes up the final 15% of the cell surface, is almost entirely straight and is separated from adjacent lateral membranes by an interspace of 15 µm and tight junctions, gap junctions, intermediate junctions (zonula adherens) and desmosomes (Bioulac-Sage *et al*, 2007). Hepatocytes have to sustain two countercurrent flow systems—the synthesis and secretion of bile, and the uptake, processing, and secretion of sinusoidal blood components, including ones of the bile itself returning through the portal venous blood. Their capacity to do so is provided by the highly polarized

state of healthy adult hepatocytes. The polarity of a hepatocyte is multifaceted. It is manifested primarily by polarized plasma membrane domain structure, identity, and distribution, but is rooted in intracellular pathways that control polarized trafficking of proteins and cytoskeletal dynamics (Treyer and Müsch, 2013).

Cholangiocytes are heterogeneous epithelial cells that line a three-dimensional network of bile ducts known as the biliary tree. Their major physiologic function lies in the modification of hepatic canalicular bile as it is transported along the biliary tree. Cholangiocytes possess an apical (luminal) and a basolateral plasma membrane. Adjacent cholangiocytes are joined by tight junctions (zonula occludens) located near the apical membrane. These junctions play a central role in establishing and maintaining epithelial cell polarity. Cholangiocytes also possess gap junctions, channels that permit direct cytoplasmic communication between adjacent cells. Extending from the apical membrane of cholangiocytes are numerous microvilli, which provide a fivefold increase in cell surface area. Each cholangiocyte also contains a single primary cilium a long, tubular organelle which extends from the apical plasma membrane and protrudes into the bile duct lumen (Tabibian *et al*, 2013).

1.2.2 Hepatic Nonparenchymal Cells

LSECs are highly specialized endothelial cells representing approximately 15 to 20% of liver cells but only 3% of the total liver volume. LSECs have a discontinuous architecture meaning that fusion of the luminal and abluminal plasma membrane occurs at sites other than cell junctions, in areas called fenestrae. These fenestrae allow these endothelial cells to act as a sieve between the sinusoid blood and the Disse space plasma, and they are more abundant yet smaller in the perivenous zone than the periportal zone. Fenestrae are not static structures. Their number and size varies in physiological conditions like fasting that decreases the number but increases the size of the fenestrae. (Poisson *et al*, 2017; Sherlock & Dooley, 2002).

CHAPTER 1 INTRODUCTION

Kupffer cells are highly mobile macrophages attached to the endothelial lining of the sinusoid. More numerous in the peri-portal area (Zone 1, Figure 1.7) of the lobule they have microvilli, intra-cytoplasmic-coated vesicles and dense bodies which make up the lysosomal apparatus (Sherlock & Dooley, 2002). Kupffer cells remove damaged and old blood cells, cellular debris, bacteria, viruses, parasites and tumour cells, through the process of endocytosis (phagocytosis, pinocytosis). Activation is caused by agents such as endotoxin, sepsis, shock, interferon- γ, arachidonic acid and tumour necrosis factor (TNF), producing products like hydrogen peroxide, cytokines, nitric oxide, TNF, interleukin (IL) 1, IL6 and IL10, interferon-α and β, transforming growth factor (TGF-β) and various prostanoids (Sherlock & Dooley, 2002).

Hepatic stellate Cells (HSCs) also known as perisinusoidal cells, Ito cells and lipocytes, lie within the sub-endothelial space of Disse. They have long cytoplasmic extensions, some giving close contact with parenchymal cells, and others reaching several sinusoids, where they may regulate blood flow (Sherlock & Dooley, 2002). HSCs contain approximately 80% of the body's vitamin A with a gradual distribution in the liver lobules that depends on the total amount and is genetically determined (Weiskirchen and Tacke, 2014). In a healthy liver they are the major storage site of retinoids, giving the morphological characteristic of cytoplasmic lipid droplets. When empty of these droplets, they resemble fibroblasts (Sherlock & Dooley, 2002).

Pit cells are highly mobile liver-specific natural killer (NK) lymphocytes attached to the sinusoidal surface of the endothelium. Pit cells remain in the liver for 2 weeks and work synergistically with Kupffer cells. They have characteristic granules and rod-cored vesicles and show spontaneous cytotoxicity against tumour cell and virus infected hepatocytes (Wisse *et al*, 1997; Sherlock & Dooley, 2002).

1.2.3 Liver Stem/Progenitor Cells

In both humans and animals, the liver has a remarkable capacity to regenerate itself. This is best demonstrated by the total restoration which occurs following partial hepatectomy to an appropriate ratio between liver mass, and body size (MacSween *et al*, 2002). The signals that regulate the initiation and termination of this process are likely to be related to hepatic function rather than anatomical formation, due to growth of the liver remnant occurring without morphological restoration of the lobes removed at operation, but the enlargement of the remaining tissue, a process that can be induced multiple times over.

The regeneration potential of the liver is driven by inflammatory mediators like IL-1α, TNF and IL-6, key growth factors like epidermal growth factor (EGF), hepatocyte growth factor (HGF), transforming growth factor-alpha (TGF-α), acidic fibroblast growth factor (aFGF) and TGF-β, and liver-resident immune cell populations (MacSween *et al*, 2002; Robinson *et al* 2016). In the partial hepatectomy model of regeneration, all differentiated liver cell compartments are capable of proliferation to meet the demands of cell loss; however it is believed that when hepatic injury is extensive or replication is inhibited, differentiated hepatocytes are unable to undertake regeneration, under such conditions so-called 'reserve' cells proliferate new hepatocytes for regeneration (Figure 1.9). First proposed by Leduc and Wilson in 1958, new hepatocytes can form from the bile ductules (cholangioles) of the liver during recovery from severe hepatic injury, but not after partial hepatectomy (Leduc & Wilson, 1958). In this model a small population of small primitive epithelial cells with oval nucleus and scant cytoplasm proliferates in association with or before hepatocyte multiplication. Believed to be located in the canal of Hering these oval cells constitute a heterogeneous population of non-parenchymal epithelial cells and cells expressing phenotypic markers of both immature hepatocytes (like α-fetoprotein) and bile duct cells, and a subset of these oval cells

are pluripotent with the capacity to differentiate toward hepatocytes, bile ductular cells and intestinal epithelium (MacSween *et al*, 2002).

In recent years these liver 'reserve' cells which are now described as "Liver Stem/Progenitor Cells" (LPCs) have undergone purification by cell sorting and subsequent culturing *in vitro* (Smith, 2006). In the context of liver biology, the terms "Stem" and "Progenitor" cells are often used interchangeably due to the ongoing challenges of demarcating these cell types. Stem cells are cells that can continuously produce unaltered daughters and have the ability to produce daughter cells with different, more restricted properties, while progenitor cells are any dividing cell with the capacity to differentiate, including putative stem cells in which self-renewal has not yet been demonstrated (Smith, 2006).
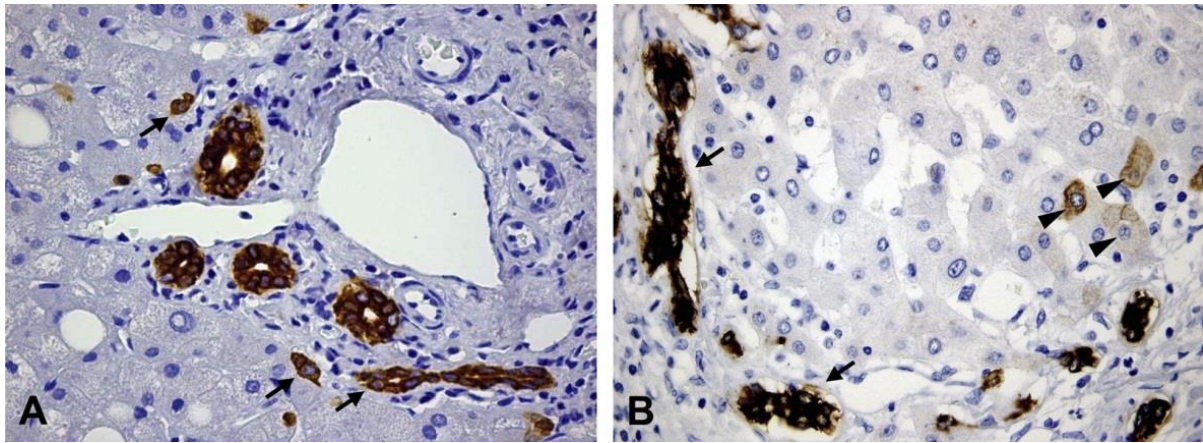
Figure 1.9 Immunohistochemistry for Cytokeratin 7 A. Normal human liver. Liver Stem/Progenitor Cells are stained for progenitor cell marker Cytokeratin 7. Stem/Progenitor Cells are located at the interface of the portal space and the canals of Hering (arrows) as well as the ductular–canalicular junction. **B.** Primary biliary cirrhosis. In this pathological condition Liver Stem/Progenitor Cells highly proliferate with the formation of reactive ductules (arrows) and intermediate hepatocytes (arrowheads) (original magnification 40×) (Gaudio *et al*, 2009).

CHAPTER 1 INTRODUCTION

1.2.4 Liver Stem/Progenitor Cell Molecular Markers

The most reliable markers for identifying LPCs have been Cytokeratin 7 (Figure 1.9) and Cytokeratin 19, which are also typically expressed by cholangiocytes and interlobular bile ducts. They express mature hepatocyte proteins like albumin and Cytokeratin 8, immature foetal hepatoblasts marker α-fetoprotein, haematopoietic stem cell markers Prominin 1 (CD133) and c-Kik (Gaudio *et al*, 2009). It has been demonstrated that the cholangiocytes/LPC marker-positive subset of cells from an injured liver contain facultative liver stem cell populations, which have been defined *in vitro* by clonogenicity and bilineage differentiation potential (Figure 1.10) (Miyajima *et al*, 2014). Potential liver stem cell populations are identified as positive for cholangiocytes markers EpCAM , CD133 and MIC1-1C3 antigen (Okabe *et al*, 2009; Kamiya *et al*, 2009; Dorrell *et al*, 2011), while common markers of LPCs are CK19, EpCAM, CD133, SOX9, osteopontin and MIC1-1C3 antigen (Okabe *et al*, 2009; Rountree *et al*, 2007; Suzuki *et al*, 2008; Yovchev *et al*, 2007; Carpentier *et al*, 2011; Dorrell et al, 2008; Dorrell *et al*, 2011; Matsuo *et al*, 2011; Miyajima *et al*, 2014; Tanimizu and Mitaka, 2014).
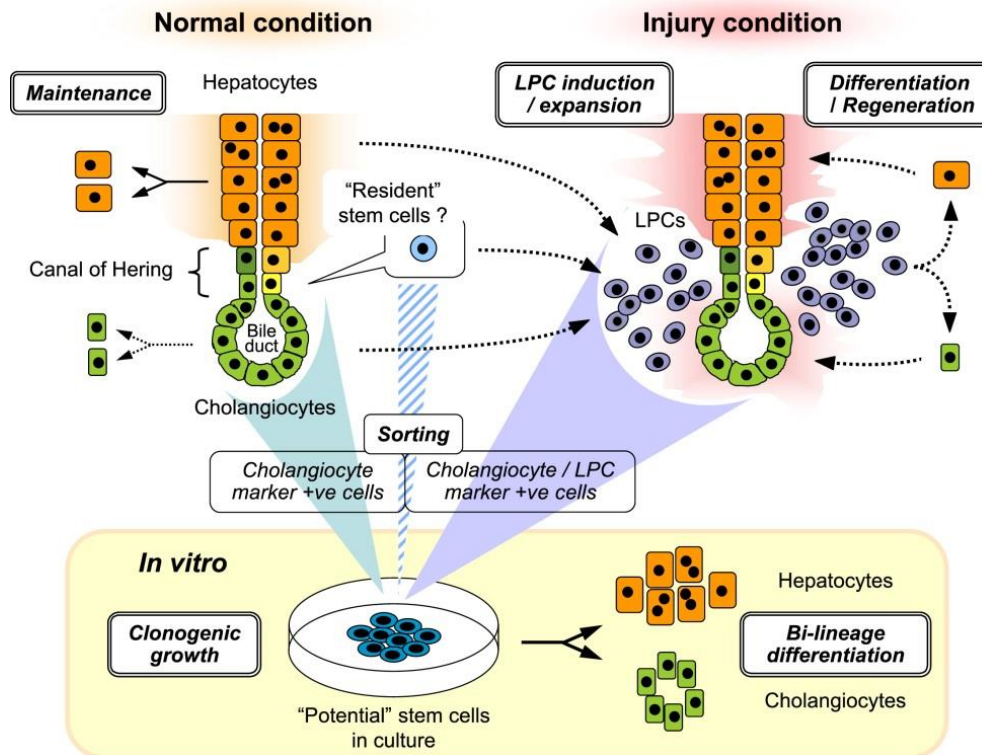
Figure 1.10 Stem/Progenitor Cells in Adult Liver under Normal and Injured Conditions.
Under normal physiological conditions, homeostatic maintenance of hepatocytes is achieved predominantly by proliferation of mature hepatocytes. Upon certain types of injury condition, unique epithelial cell populations with an immature phenotype emerge and expand, and are thought to contribute to the regeneration process due to their bilineage differentiation potential to both hepatocytes and cholangiocytes. Although the origin of LPCs is still not clear, the dominant theory is that they are derived from the canal of Hering, which may harbor putative "resident" stem cells as the exact cell of origin. Purification by cell sorting and subsequent culture experiments have demonstrated that the cholangiocyte marker-positive population from normal liver, as well as the cholangiocyte/LPC marker-positive subset from injured liver, contains a "potential" liver stem cell population defined in vitro by clonogenicity and bilineage differentiation potential (Miyajima *et al* 2014).

CHAPTER 1 INTRODUCTION

Similar to extrahepatic tissue stem/progenitor cells, developmental signals including Wnt (Apte *et al*, 2008; Boulter *et al*, 2012; Hu *et al*, 2007; Itoh *et al*, 2009; Yang *et al*, 2008), Notch (Boulter *et al*, 2012, Fiorotto *et al*, 2013, Kitade *et al*, 2013) and Fibroblast growth factor (FGF) (Takase *et al*, 2013) have been demonstrated to play an important role in the regulation of LPCs, while growth factors such as HGF and EGF have been implicated in regulating the proliferation and/or differentiation of LPCs (Ishikawa *et al*, 2012; Kitade *et al*, 2013; Miyajima *et al*, 2014). Animal experiments which aimed to characterise the facultative liver stem cells within the LPC population found that Trop2$^+$, Foxl1$^+$ and Lgr5$^+$ cells are not present in the normal liver, but are induced by injury (Okabe *et al*, 2009; Shin *et al*, 2011, Huch *et al*, 2013). Among these, Foxl1$^+$ and Lgr5$^+$ cells differentiate into mature hepatocytes and cholangiocytes (Tanimizu and Mitaka, 2014).

Wnt, Notch and Hedgehog signalling pathways are essential to regulating stem cell quiescence, proliferation and cell fate within the stem cell niche of organs like the intestine, bone marrow and brain (Crosnier *et al*, 2006; Gaudio *et al*, 2009). Huch and colleagues in 2013 observed that under normal conditions the Wnt signalling pathway is exclusively active in perivenous hepatocytes, while in the bile ducts Wnt signalling only becomes active following liver injury. These injured ductal cells would increase expression of many Wnt and R-spondin (a positive regulator of Wnt signalling) target genes previously characterised in intestinal crypt cells, including the Leucine Rich Repeat Containing G Protein-Coupled Receptor 5 (Lgr5). These Lgr5$^+$ cells also expressed Sox9 (a broad ductal progenitor marker) and did not express mature hepatocyte or stellate cell markers and occurred in groups of small cells near the bile ducts clearly distinguishable from neighbouring hepatocytes. Lineage tracing also demonstrated that these Lgr5$^+$ cells generated hepatocytes and bile ducts *in vivo* which led the researchers to embed these cells into Matrigel and culture them with EGF, Rspo1, Fgf10, HGF and nicotinamide, which caused most of them to expand *in vitro* into 3D liver tissue buds called

organoids that expressed biliary cell markers and could be further induced to produce mature

hepatocyte markers and functions (Huch *et al* 2013).

CHAPTER 1 INTRODUCTION

1.3 Chronic Liver Diseases Epidemiology

According to the 2017 Global Burden of Diseases, Injuries, and Risk Factors study chronic liver diseases including cirrhosis caused an estimated 1.32 million deaths worldwide which constituted 2.4% of all deaths that year, and while the age-standardised death and disability-adjusted life-years (DALYs) rates have decreased from 1990 to 2017, the numbers of deaths and DALYs for chronic liver diseases proportional to all global deaths have increased (Sepanlou *et al* 2020).

1.3.1 Cirrhotic Liver Disease Epidemiology

Cirrhosis is the leading cause of liver-related death globally (Roth *et al* 2018), with the highest recorded rates occurring in Egypt, Mongolia, Cambodia, Turkmenistan, and Moldova (Figure 1.11) (Sepanlou *et al* 2020). It is the end stage of liver injury with progressive liver fibrosis, in which the hepatic architecture is distorted. In the initial stages, cirrhosis is compensated, hence most patients are asymptomatic at this stage, and cirrhosis is usually discovered incidentally during medical encounters for other reasons. Thus, reports on the prevalence of compensated cirrhosis are almost always underestimated (Anthony *et al* 1977). Cirrhosis is generally considered to be irreversible at later stages, although reversal has been documented in many individuals with compensated cirrhosis after treating the underlying cause. The most common causes of cirrhosis related death in descending order are chronic hepatitis B, alcohol related liver disease, chronic hepatitis C and non-alcoholic steatohepatitis (NASH) (Figure 1.12). Patients with decompensated cirrhosis are susceptible to complications and a reduction in life expectancy (Sepanlou *et al* 2020).
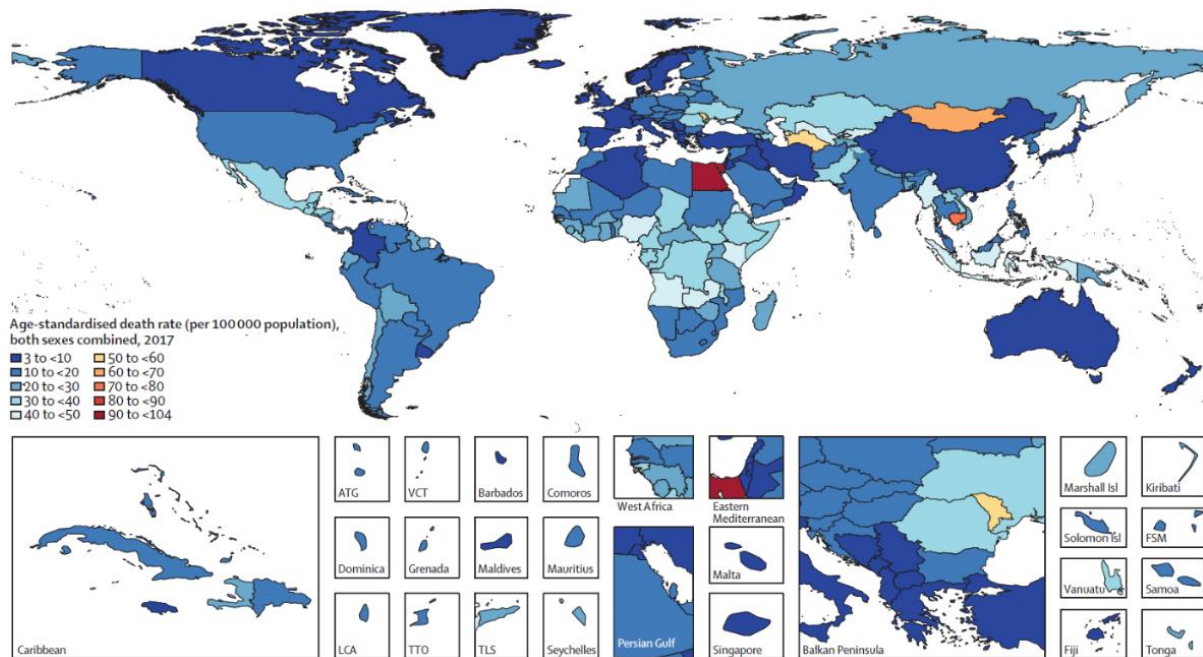
Figure 1.11 Age-Standardised Death Rate for Liver Cirrhosis in 2017. World map illustrating the age-standardised death rate for liver cirrhosis per 100,000 people for both sexes combined in 2017. Penels in the lower third used to illustrate more detail of smaller nations. (Sepanlou *et al* 2020).
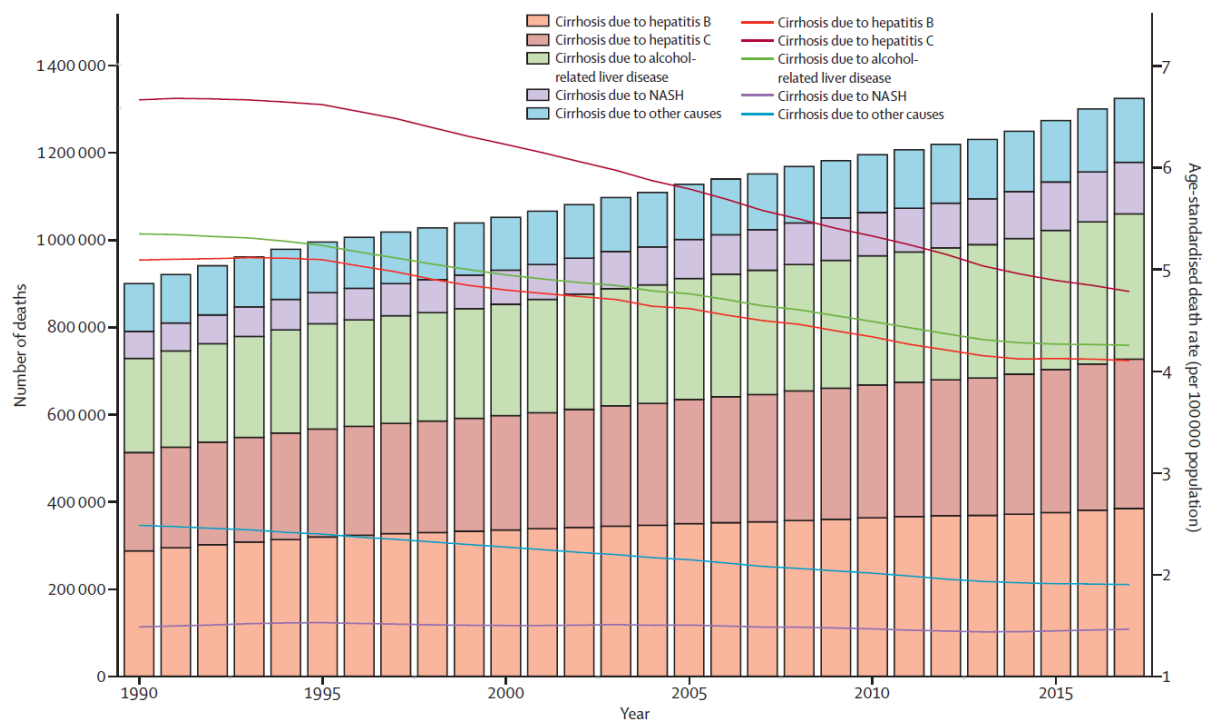
Figure 1.12 Number of deaths and age-standardised death rates at the global level by caused by cirrhosis, 1990–2017. Bars refer to number of deaths in each year. Lines refer to age-standardised death rate in each year per 100,000. NASH, non-alcoholic steatohepatitis (Sepanlou *et al* 2020).

1.3.2 Liver Cancer Epidemiology

In 2015 an estimated 810,000 people died from liver cancer (Wang *et al* 2016). Liver cancer is the fifth most common cause of cancer in men and the tenth most common in women and due to poor prognosis rates is the fourth most common cause of cancer related death (Bray *et al* 2018). The dominant form of liver cancer: Hepatocellular carcinoma (HCC) accounts for 85-90% of primary liver cancers worldwide (El-Serag and Rudolph 2007). Developing HCC is more likely in males and patients over the age of 65 and is commonly observed as a progression of liver cirrhosis with 80-90% of patients having a history of cirrhosis (Bartolomeo *et al* 2011; Fattovich *et al* 2004). Other risk factors for HCC include high HBV viral load, duration of HBV infection, alcohol consumption, Type 2 diabetes, obesity, hereditary conditions (such as hemochromatosis), the consumption of aflatoxin B1-contaminated foods, tobacco use and a range of metabolic disorders (Chen *et al* 2006; Chen *et al* 1997; Marrero *et al* 2005). Incidence rates of HCC worldwide are based on the prevalence of risk factors (Figure 1.13) for example, 80% of HCC occurs in sub-Saharan Africa and eastern Asia where the main risk factors are HBV and aflatoxin B1 exposure, while in Europe, Japan and USA the main risk factors are HCV and alcohol abuse (El-Serage 2012; Morgan *et al* 2004).
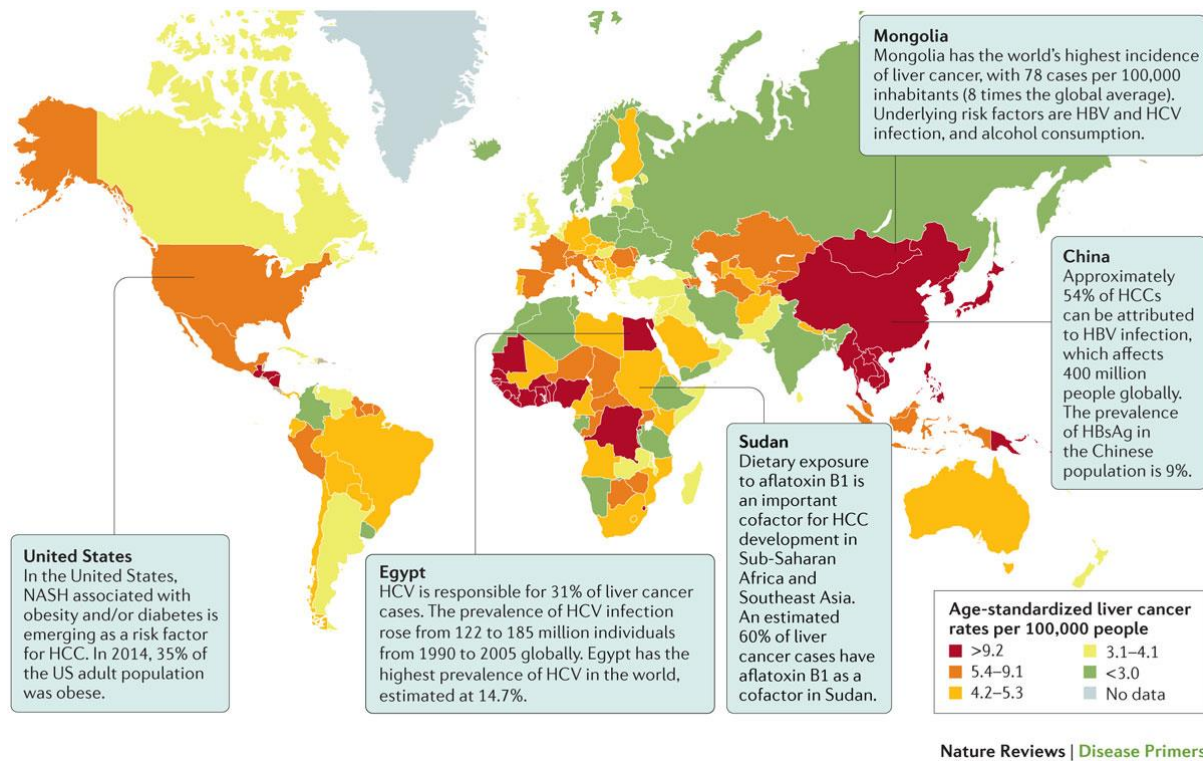
Figure 1.13 Global Burden of HCC. The incidence of hepatocellular carcinoma (HCC) is shown. The main risk factors for HCC development are hepatitis C virus (HCV) infection (for example, Egypt), hepatitis B virus (HBV) infection (China), alcohol intake, non-alcoholic steatohepatitis (NASH; Unites States) and aflatoxin B1 ingestion (Sudan). Mongolia has the highest incidence of HCC globally. HBsAg: hepatitis B surface antigen (Llovet *et al* 2016).

1.3.3 Hepatocellular Carcinoma Epidemiology

HCC development is a multistep process involving inflammatory damage, with hepatic necrosis and regeneration (Forner *et al* 2018). The risk of HCC usually emerges with the establishment of cirrhosis, impaired liver function and accumulation of somatic genomic alterations in passenger and driver genes displaying epigenetic modifications (Forner *et al* 2018). Inflammation is typically present in all disease stages, associated with the development of advanced fibrosis and cirrhosis (Seki and Schwabe 2015). Inflammation also contributes to several hallmarks of HCC, such as promoting proliferative, survival signalling, inducing angiogenesis, evading immune surveillance, supporting cancer stem cells, inducing genome instability, while activating invasion and metastasis (Yu *et al* 2018). The sequence of events begins with successive development of pre-cancerous cirrhotic nodules with low-grade dysplasia that develops into high-grade and can transform into more advanced HCC. HCC can originate from mature hepatocytes and LPCs (Llovet *et al* 2016).

Genetic heterogeneity is probably caused by clonal branching because early dysplastic nodules present relatively uniform genomes, whereas advanced tumours have extensive molecular heterogeneity or genomic instability. Two oncogenic events of note are MYC activation which may be important for transformation of hepatocytes to HCC, and TERT activation which is required for unlimited growth (Marquardt *et al* 2015). While the risk of HCC emerges with the accumulation of somatic genomic alterations in passage and driver genes and epigenetic modifications, no molecular classifications of HCC so far proposed have been able to predict disease progression or recurrences (Schulze *et al* 2016; Piñol *et al* 2017; Forner *et al* 2018).

HCC can be prevented by avoiding direct causes and associated risk factors, for example once chronic infection of HBV is acquired, antiviral agents that eliminate viral replication reduced, but did not eliminate the risk of HCC developing (Papatheodoridis *et al* 2015). HCV infection rates can be reduced by preventing transmission through contaminated blood. Patients that

acquire HCV that undergo effective antiviral therapy should prevent progression to cirrhosis and the development of HCC, however if cirrhosis has been established the risk of HCC remains (Singal *et al* 2010; Morgan *et al* 2013).

1.4 Liver Injury

Liver injury is caused by cell-indiscriminate injuries including mechanical trauma, ischemia, and liver resection. Cholestatic insults which are typified by bile duct injuries and generally caused by mechanical injury or by presumed-autoimmune conditions that cause a chronic loss and/or narrowing of bile ducts and subsequent build-up of bile in the liver (cholestasis), which damages the cholangiocytes that line the ducts. However, liver injury usually occurs as a result of immune-mediated or direct injury to the hepatocytes (Tu *et al* 2015). Hepatocytes are the first cells to process dietary contents after absorption and can be exposed to injuries from ingested toxins (such as aflatoxin-B1), alcohol, or drugs (such as acetaminophen/ paracetamol). In diseases causing dysregulation of the liver's storage capabilities, hepatocytes can be overloaded with copper (Wilson's disease), iron (hemochromatosis), and fat (non-alcoholic fatty liver disease). Importantly, hepatotropic infectious pathogens, particularly hepatitis B virus (HBV) and hepatitis C virus (HCV), cause the majority of chronic liver disease. These non-cytolytic viruses selectively infect hepatocytes causing chronic immune-mediated cell death (Tu *et al* 2015). During injury, hepatocytes engage in crosstalk with multiple cellular subsets (including liver adipocytes, endothelial cells, HSCs, and infiltrating immune cells), resulting in the release of reactive oxygen species (ROS), proinflammatory signals, proliferation-associated cytokines, and the activation of repair pathways (Figure 1.14). A chronic activation of these signals can result in dysregulation of the normal repair response and generation of a pathogenic fibrotic response (Tu *et al* 2015).

A broadly canonical response with chronic inflammation leads to fibrosis, and then cirrhosis occurs irrespective of liver injury etiology. The course of progressive liver injury can be summarized and broadly split into three phases: initiation, regeneration, and resolution, all in which the hepatocyte plays significant roles (Figure 1.15). During injury initiation ROS released by stressed and dying hepatocytes are major stimuli for ongoing injury via the

activation of HSCs and immune cells (Tu *et al* 2015). NADPH oxidase (NOX) is a transmembrane enzyme complex that generates ROS in response to a range of stimuli, and loss of NOX1 or NOX4 attenuates liver injury, inflammation and fibrosis in mice (Lan *et al* 2015; Tsuchida and Friedman 2017).

Hepatocyte apoptosis is a prominent sign in all forms of liver injury. A major cause of hepatocyte apoptosis is mitochondrial dysfunction, because the inner and outer mitochondrial membranes isolate a number of proapoptotic proteins within the intermembrane space. Hence mitochondrial outer membrane permeabilization leads to the release of these apoptosis mediators resulting in apoptosis (Malhi and Gores, 2008). Mitochondrial outer membrane permeabilization can occur downstream of death receptor–triggered signalling cascades (extrinsic pathway), lysosomal permeabilization, endoplasmic reticulum (ER) stress pathways, or activation of intracellular stress kinases (Malhi and Gores, 2008).

Dying cells release endogenous compounds such as damage-associated molecular patterns (DAMPs) that can activate these cells. The subsequent innate immune system activation signals through a complex of proteins called the inflammasome and causes HSCs and immune cells, which take up apoptotic bodies and DAMPs, to develop a pro-fibrotic phenotype. These activated cell populations are key mediators of the regeneration response (Tu *et al* 2015).

During liver injury initiation activated Kupffer cells can become potent producers of pro-inflammatory cytokines such as IL-1, IL-6 and TNF as well chemokines such as MIP-1α and RANTES. This Kupffer cell pro-inflammatory response is induced following signalling via MyD88-independent Toll-like receptors. In this inflammatory microenvironment, liver-primed T-cells can develop into functional T effector cell populations and mediate pathogen clearance. Acute liver inflammation leads to the recruitment and activation of leukocyte populations, and the induction of fibrotic responses at the site of inflammation (Robinson *et al* 2016). Mounting

evidence suggests that hepatocytes can directly alter the extracellular matrix (ECM), as well as display an injury phenotype, which synergistically interacts with fibrogenesis mediators in surrounding cells particularly HSCs (Tu *et al* 2015).

The regeneration phase of liver injury is characterised by hepatocyte repopulation (Tu *et al* 2015). In response to lost liver mass, hepatocytes undergo a complex and heavily regulated regeneration process and the activation of HSCs. Resolution of liver injury occurs in cases where the cause of chronic inflammation is removed and there is a reversal of liver fibrosis. Further, apoptosis of activated HSCs is known to be an important factor in the resolution of fibrosis (Tu *et al* 2015).

The resolving fibrosis observed during acute injury acts to protect surviving hepatocytes by reducing pro-apoptotic signalling and increasing resistance to a range of toxins. This fibrotic process is regulated by inflammatory cytokines and growth factors, released by leukocytes that traffic to the damaged tissue. These cytokines include TNF, IL-6, platelet derived growth factor and TGF-β. These cytokines lead to activation and proliferation of HSCs, which are potent producers of extra-cellular matrix components, including α-smooth muscle actin and type I collagen (Figure 1.16). Fibrosis only becomes clinically relevant when it alters tissue structure and function due to dysregulated or excessive inflammation (Robinson *et al* 2016).
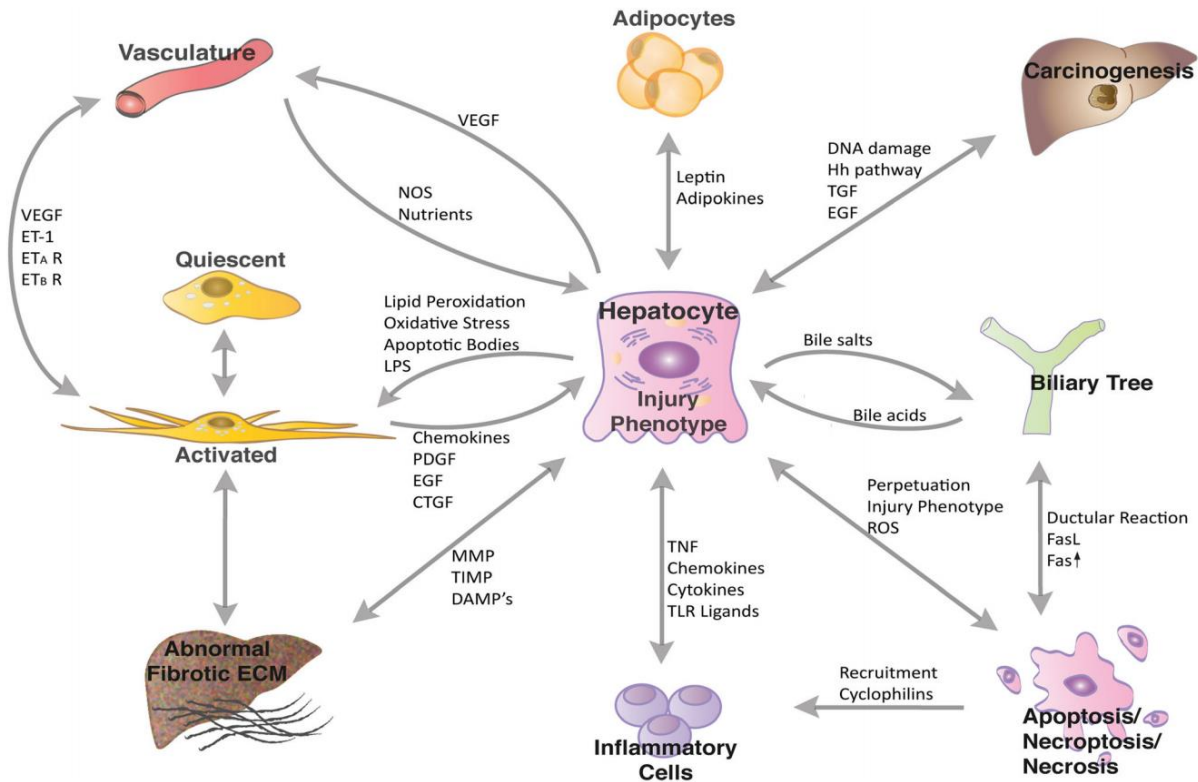
Figure 1.14 The Network of Hepatocytes Interactions that Occur During Liver Injury.
The hepatocytes are involved in a wide variety of interactions during liver injury. This figure highlights the complex network of molecular interactions that occur during liver injury and how central hepatocytes are this process. DAMP, damage-associated molecular pattern; ECM, extracellular matrix; Hh, hedgehog signalling; MMP, matrix metalloproteinase; TIMP, tissue inhibitor of MMP; TLR, toll-like receptor; ROS, reactive oxygen species; VEGF, vascular endothelial growth factor; ET, endothelin; NOS, Nitric oxide synthetase; LPS, lipopolysacchiride; PDGF, platelet-derived growth factor; EGF, epidermal growth factor; CTGF, connective tissue growth factor; TNF, tumour necrosis factor (Tu *et al* 2015).
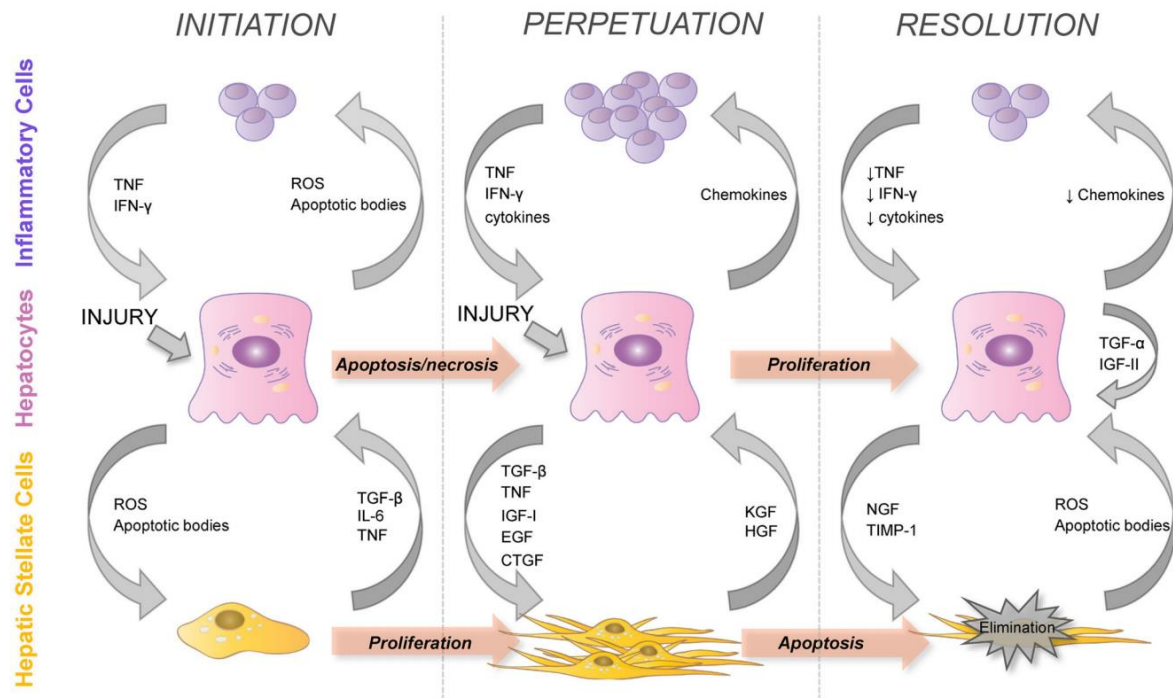
Figure 1.15 Hepatocyte Intercellular Interactions During the Progression of Liver Injury.
Timeline of the stages of liver injury, the behaviour of hepatocytes, inflammatory cells and hepatic stellate cells during each stage, and the interactions which occur between these cells during each stage. IFN-γ, interferon-γ; IL, interleukin; ROS, reactive oxygen species; TGF, transforming growth factor; TIMP, tissue inhibitor of matrix metalloproteinase; KGF, Keratinocyte Growth Factor; HGF, hepatocyte growth factor (Tu *et al* 2015).
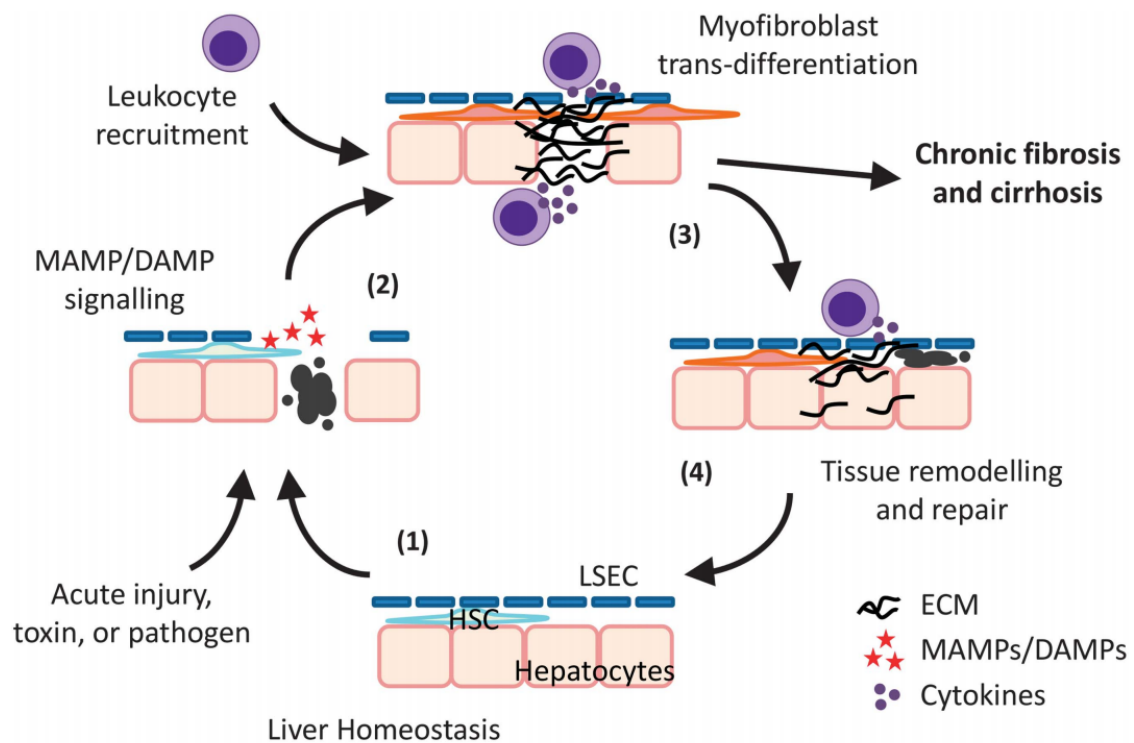
Figure 1.16 Maintenance of local Homeostasis in the Liver in Response to Liver Injury.
Inflammatory processes are vital to maintain liver homeostasis following cell death or infection. Upon acute injury, cell death or infection, apoptotic hepatocytes release a variety of DAMPs and/or MAMPs (1) that are recognized by and activate neighbouring hepatocytes, HSCs, and liver-resident immune cell populations. Activated cells secrete inflammatory mediators leading to leukocyte recruitment and HSC trans-differentiation into myofibroblasts, which initiate fibrosis through the synthesis of extra-cellular matrix components (2). The initiation of inflammation leads to the expression of pro-resolving factors from recruited leukocytes and myofibroblast apoptosis (3), enabling tissue regeneration and a return to homeostasis (4). If this resolution phase does not occur persistent inflammation results in the progressive development of liver fibrosis and eventual cirrhosis. Abbreviations: DAMPs, damage-associated molecular patterns; ECM, extra-cellular matrix components; HSCs, hepatic stellate cells; MAMPs, microbial associated molecular patterns (Robinson *et al* 2016).

1.5 Liver Fibrosis

Liver fibrosis often goes unrecognised unless the patient manifests symptoms from complications of cirrhosis (Shipley *et al* 2019). Risk factors for developing liver fibrosis include metabolic syndrome, heavy alcohol consumption, exposure to hepatotoxic substances, and the use of hepatotoxic medications. Physical exam findings that assist with diagnosis include jaundice, spider angioma, a nodular liver on palpation, splenomegaly, ascites, caput medusae, palmar erythema, gynecomastia, asterixis, and Type 2 diabetes. However, many patients are without physical findings and advanced fibrosis is diagnosed by abnormalities on haematological, biochemical, endoscopic, or radiologic evaluation (Shipley *et al* 2019). A full review of the recent advances in the clinical diagnosis, management, and treatment of liver fibrosis has been covered elsewhere by Shipley *et al* 2019.

Matrix components present in hepatic fibrosis include collagens, proteoglycans and matrix glycoproteins. The progression from a matrix rich in laminins and collagen type IV, to and matrix rich in collagen I and III is associated with inflammation and fibrosis, and likely to critically alter cell-matrix interactions, resulting in activation and perpetuation of activation of HSCs (Iredale and Guha 2007; Tsuchida and Friedman 2017). In the normal liver, interstitial collagens (types I and III) are concentrated in portal tracts and around central veins, with occasional bundles in the space of Disse. Delicate strands of type IV collagen (reticulin) course alongside hepatocytes in the space of Disse.

The major source of excess collagen in cirrhosis appears to be perisinusoidal stellate cells (Friedman 1993). In the normal liver, hepatic stellate cells, hepatocytes and sinusoidal endothelial cells are capable of synthesizing type I and IV collagen. Type III collagen and fibronectin can also be elaborated by these cells (Geerts *et al* 1984). When abnormal disposition of extracellular matrix occurs, the up regulation of matrix genes is almost exclusively confined to non-hepatocytes cells, particularly stellate cells. There is a marked increase in the expression

of messenger RNAs for collagens I, III, IV and laminin, and no increase of collagen formation by hepatocytes (Nakatsukasa *et al* 1990: Milani *et al* 1989).

1.5.1 Hepatic Stellate Cell Activation

With the absences of liver injury, HSCs maintain a non-proliferative, quiescent phenotype, that following injury becomes activated, transdifferentiating from vitamin-A-storing cells to myofibroblasts. These activated cells migrate and accumulate at the sites of tissue repair where they proliferate, contract, causing inflammation and are characterized by large amounts of ECM production (Tsuchida and Friedman 2017; Arriazu *et al* 2014). Key signals that drive HSC activation are summarized in Figure 1.17 and include TGF-β, platelet-derived growth factor (PDGF), vascular endothelial growth factor (VEGF) and connective tissue growth factor (CTGF) (Tsuchida and Friedman 2017).

HSCs express two types of collagen receptors, Integrins which can control the release and activation of TGF-β and Discoidin Domain-containing Receptors (DDRs) which are receptor tyrosine kinases that signal in response to triple helical collagen rather than soluble peptide growth factors.

DDR2 which signals in response to type I collagen, promotes matrix metalloproteinase 2 (MMP-2) mediated proliferation and invasion. Moreover, type I collagen-dependent upregulation of DDR2 expression establishes a positive feedback loop in activated stellate cells, leading to further proliferation and enhanced invasive activity (Olaso *et al* 2001). DDR1 is activated primarily by collagen types I, II, III, V, and XI, whereas DDR2 is activated mainly by collagen types I and III (Vogel *et al* 1997; Schlessinger 1997).

There are many different mediators of HSC activation from hepatocyte injury, include the afore mentioned ROS, hedgehog ligands, nucleotides, Damage-associated Molecular Patterns (DAMPs), and Cytokines IGF1 and VEGF (which is released under hypoxia) (Tsuchida and Friedman 2017; Novo and Parola 2008). Cell-cell signalling that activates HSCs are summarized in Figure 1.18.
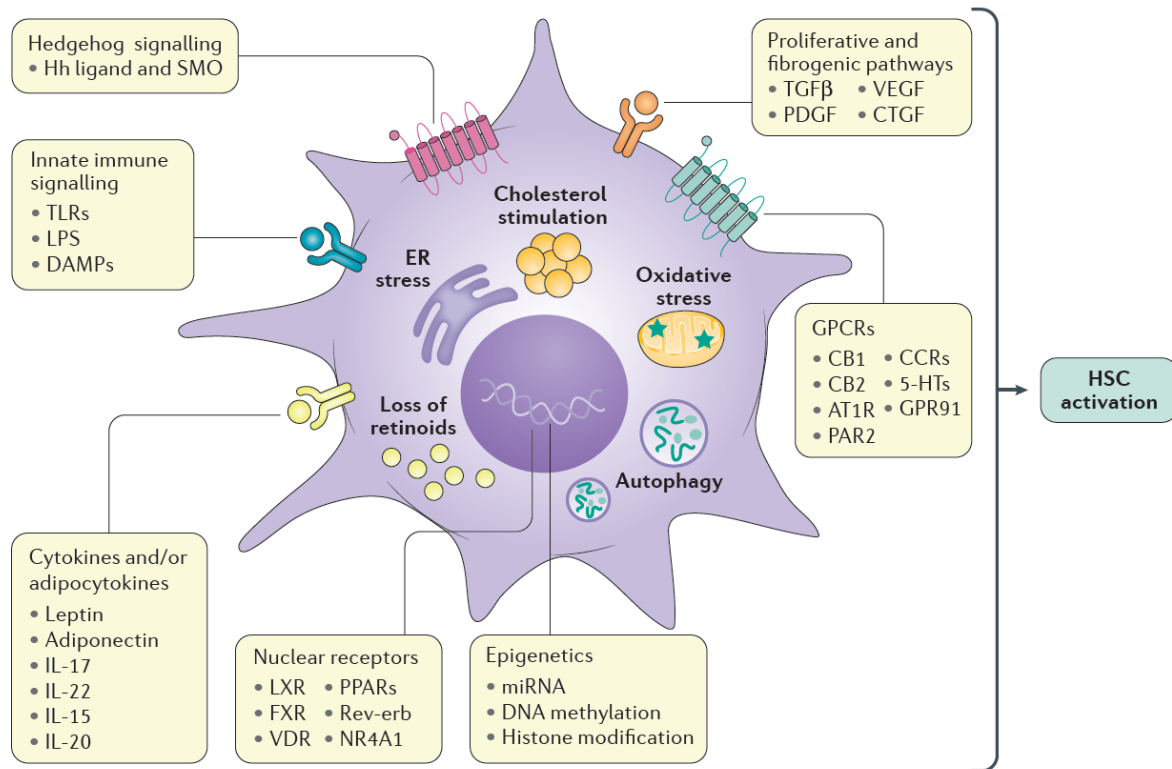
Figure 1.17 Signalling Molecules and Pathways Involved in HSC ctivation. A plethora of signals drive hepatic stellate cell activation. This figure illustartes the known contributors to hepatic stallate cell activation as described by Tsuchida and Friedman (2017) including: key fibrogenic and proliferative pathways contributing to fibrosis, include transforming growth factor-β, platelet-derived growth factor (PDGF), vascular endothelial growth factor (VEGF) and connective tissue growth factor (CTGF). Hedgehog (Hh) ligand and its receptor smoothened homolog (SMO) promote HSC activation. G protein-coupled receptors (GPCRs) expressed by HSCs can either negatively or positively affect HSC activation. Innate immune signalling, especially that mediated by Toll-like receptors (TLRs) and cytokines, has been implicated in HSC activation. Adipokines mediate crosstalk between liver, adipose and other tissues. Autophagy drives HSC activation by providing energy substrates and is linked to increased endoplasmic reticulum (ER) stress. Oxidative stress is a feature of chronic liver disease that activates HSCs. Loss of retinoid is a defining characteristic of HSC activation. Free cholesterol stimulates HSCs by rendering them susceptible to TGFβ. Nuclear receptors

negatively modulate HSC activation. Epigenetic signals including microRNAs (miRNAs), DNA methylation and histone modification control both activation and inactivation of HSCs. 5-HT, 5-hydroxytryptamine receptors; AT1R, type 1 angiotensin II receptor; CB, cannabinoid receptor; CCRs, C–C chemokine receptors; DAMPs, damage-associated molecular patterns; FXR, farnesoid X receptor; GPR91, succinate receptor 1; LPS, lipopolysaccharide; LXR, liver X receptor; NR4A1, nuclear receptor subfamily 4 group A member 1; PAR2, proteinase-activated receptor 2; PPARs, peroxisome proliferator-activated receptors; VDR, vitamin D3 receptor (Tsuchida and Friedman, 2017).
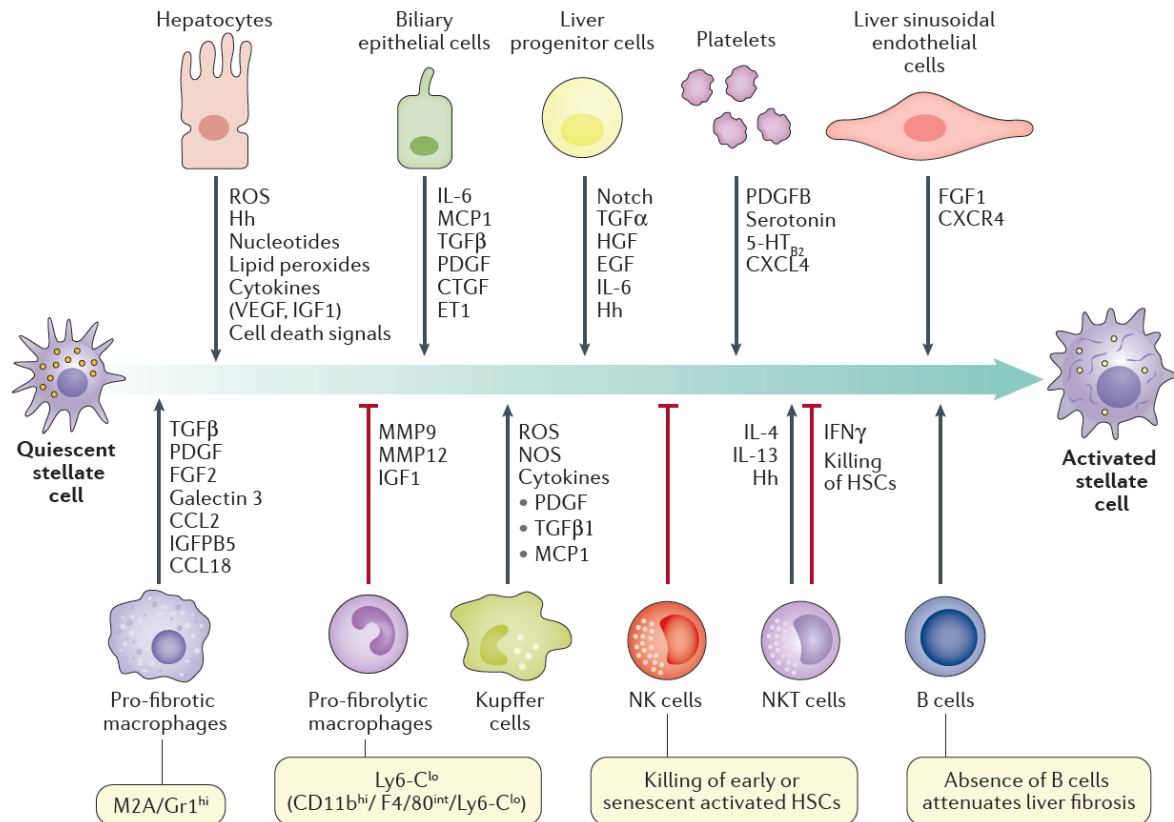
Figure 1.18 Extracellular Stimuli to HSC Activation. This figure describes that various interactions between other liver cells and the hepatic stellate cells which lead to activation. These include hepatocytes, macrophages, biliary epithelial cells, liver stem/progenitor cells, liver sinusoidal endothelial cells, natural killer cells, natural killer T cells, platelets and B cells promote (green arrows) or inhibit (red lines) the activation of hepatic stellate cells through production of hormones, cytokines and other signalling molecules. 5-HTBR2, 5-hydroxytrypamine receptor 2B; CCL, C–C motif chemokine; CTGF, connective tissue growth factor; CXCL, C–X–C motif chemokine; EGF, epidermal growth factor; ET1, endothelin 1; FGF, fibroblast growth factor; HGF, hepatocyte growth factor; Hh, hedgehog; IGF1, insulin-like growth factor 1; IGFBP5, insulin-like growth factor binding protein 5; MCP1, monocyte chemoattractant protein 1 (also known as CCL2); MMP, matrix metalloproteinase; NK, natural killer; NKT, natural killer T; NOS, nitric oxide synthase; PDGF, platelet-derived growth factor; ROS, reactive oxygen species; TGF, transforming growth factor; VEGF, vascular endothelial growth factor (Tsuchida and Friedman 2017).

1.5.2 TNF and Liver Fibrosis

Hepatocyte death is an initial event that drives liver inflammation and fibrosis, which leads to the engulfing of apoptotic bodies by HSCs and Kupffer cells and induces the upregulation of profibrogenic factors TGF-β and the death ligand TNF (Figure 1.19) (Yang and Seki 2015). TNF triggers the extrinsic cell death pathway via the caspase cascade, but it also affects the survival pathway via NFκB activation (Luedde *et al* 2014).

TNF is a pleiotropic cytokine produced by a variety of immune cells including macrophages/monocytes (Yang and Seki 2015). TNF can trigger multiple signalling pathways involved in inflammation, proliferation, and apoptosis. The initiation phase is perpetuated by TNF production, which results in the activation of resident HSCs into fibrogenic myofibroblasts (Yang and Seki 2015). The TNF receptor 1 (TNFR1) knockout mice showed reduced carbon tetrachloride (CCl_4)-induced liver fibrosis (Sudo *et al* 2005). It is no doubt that TNF can promote fibrosis, although *in vitro* TNF treatment suppresses collagen α1 gene expression, apoptosis, and proliferation in activated HSCs (Saile *et al* 1999; Yang and Seki 2015). Although TNF has been implicated in the pathogenesis of chronic liver inflammation that leads to liver fibrosis, the role of TNF in liver fibrosis has not been fully characterized (Yang and Seki 2015). TNF treatment is known to induce the production of periostin, a secretory profibrogenic protein, in HepG2 cells, while fibroblasts treated with a supernatant collected from TNF-treated HepG2 cells have increased type 1 collagen expression, which may be through the production of periostin (Amara *et al* 2015).
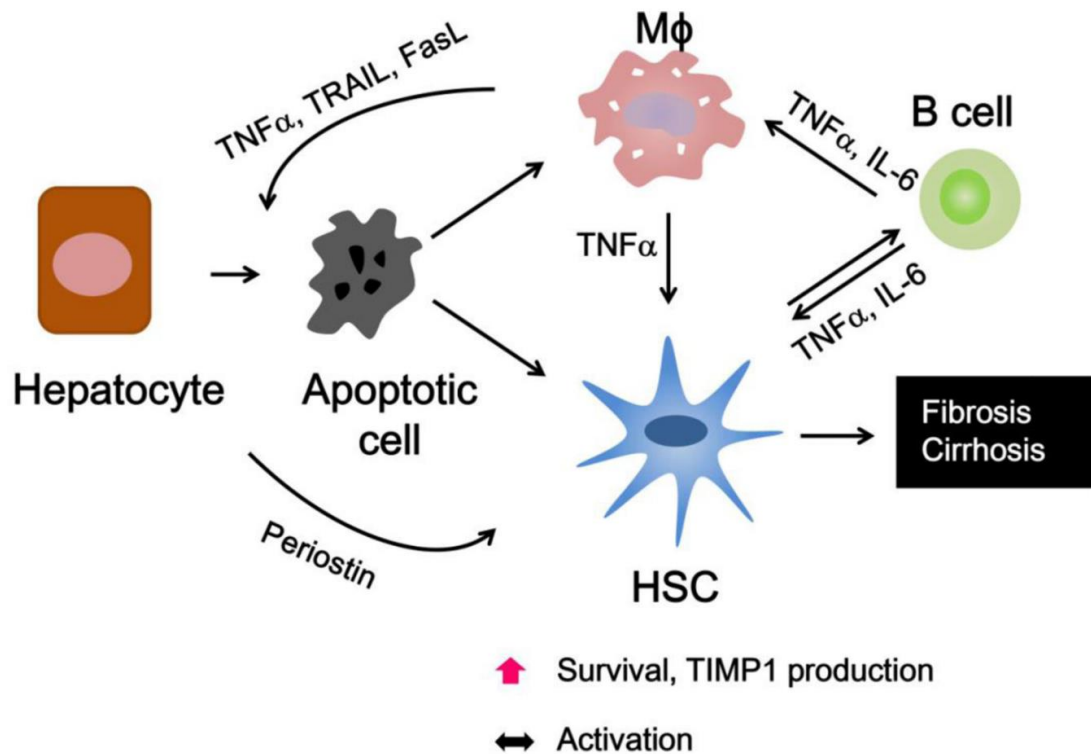
Figure 1.19 Overview of TNFα-mediated Liver Fibrosis TNFα Augments HSC Survival, But Not Activation. Hepatocyte apoptosis results in the engulfment of apoptotic bodies by macrophages and HSCs. It enhances the production of death ligands (e.g., TNF, TNF-related apoptosis-inducing ligand (TRAIL) and FasL) by macrophages, which further stimulates hepatocyte death. Engulfment of apoptotic bodies by HSCs increases the profibrogenic responses. TNF-treated hepatocytes produce periostin, which can mediate collagen production in HSCs. HSCs also promote B cell survival. In fibrotic liver, B cells produce proinflammatory cytokines and chemoattractants (e.g., TNFα, IL-6, MCP-1, and MIP-1α), which can accelerate liver fibrosis (Yang and Seki 2015).

1.5.3 TGF-β and Liver Fibrosis

Migration and proliferation of activated HSC are at least partially induced by TGF-β through various mechanisms (Fabregat *et al* 2016). After acute liver injury, TGF-β and PDGF synergistically enhance collagen synthesis by activated HSC via the Phosphorylated Small Mothers Against Decepentaplegic 2 Dually and 3 Dually (pSmad2L/C and pSmad3L/C) pathways. In the resolution stage of acute liver injury, Smad7 induced by TGF-β negatively regulates the fibrogenic TGF-β signalling. In contrast, PDGF-mediated pSmad3L cannot induce Smad7 in myofibroblasts even if high concentration of TGF-β is observed in chronic liver diseases. Under a low level of Smad7, myofibroblasts can constitutively exhibit the mitogenic pSmad3L and fibrogenic pSmad2L/C signalling, thereby accelerating liver fibrosis (Yoshida and Matsuzaki 2012).

1.5.4 Hypoxia and Liver Fibrosis

Several studies have demonstrated that regions of hypoxia develop in the liver after acute liver injury, the mechanism by which this occurs is not certain, but it most likely results from a disruption of the hepatic architecture, which impedes blood flow through damaged regions (Roth and Copple 2015).

Hypoxia-inducible factors (HIFs) are heterodimeric transcription factors apart of the innate oxygen-sensing system. During hypoxia various genes involved in cellular functions aimed at maintaining homeostasis, such as metabolism, proliferation, and migration are upregulated by HIFs, while under normoxic conditions, the HIF α subunit is immediately targeted for degradation by the 26S proteasome (Roth and Copple 2015; Huang *et al* 1998).

HIF-1α has been found to be activated in macrophages and hepatocytes within and at the periphery of regions of necrosis, both areas where hypoxia is present. HIF-1α is also detected

in SMA-α expressing myofibroblasts within regions of bridging fibrosis (Copple *et al* 2012). HIF-1α regulates a number of genes that have been implicated in fibrosis development, including PDGF, FGF-2, VEGF, and plasminogen activator inhibitor-1 (PAI-1) (Roth and Copple 2015). Depletion of HIF-1α in animal models prevented up-regulation of several key profibrotic mediators including PDGF-A, PDGF-B, PAI-1, and FGF-2 (Moon *et al* 2009). Hypoxic hepatocytes also activate latent TGF-β1 in a HIF-dependent manner (Copple 2010). Although the mechanism by which this occurs is not fully understood, it is possible that hypoxia increases expression of several matrix metalloproteinases and thrombospondin-1 in hepatocytes, all of which can activate latent TGF-β1 (Roth and Copple 2015).

Hypoxia has also been found to stimulate HSCs to produce collagen which may lead to chronic injury, due to continuous stimulus leading to fibrosis (Roth and Copple 2015). Exposure of culture-activated, primary mouse HSCs to hypoxia activated both HIF-1α and HIF-2α (Copple *et al* 2011). Hypoxia also increases the expression of several genes that could contribute to fibrosis development. For instance, hypoxia increased expression of two genes involved in collagen metabolism, prolyl-4-hypdroxylase α1 and prolyl-4-hydroxylase α2, which are key enzymes that contribute to the formation of stable collagen triple helices (Copple *et al* 2011). As expected, hypoxia also increased expression of several genes involved in angiogenesis, including VEGF, angiopoietin-like-4, placental growth factor, and macrophage-migration inhibitory factor (Copple *et al* 2011).

1.6 Liver Cirrhosis

Cirrhosis which is defined by morphology not mechanism of injury is a diffuse process characterised by fibrosis and the conversion of normal liver architecture into structurally abnormal nodules, secondary to chronic injury, which leads to alterations of the normal lobular organization of the liver (Anthony *et al* 1977; Sherlock and Dooley 2002; Iedale and Guha 2007; Sharma and John 2019).

Cirrhosis is histologically characterised by diffuse nodular regeneration surrounded by dense fibrotic septa with subsequent parenchymal extinction and collapse of liver structures, together causing pronounced distortion of hepatic architecture. This distortion results in increased resistance to portal blood flow and hence in portal hypertension and in hepatic synthetic dysfunction (Figure 1.20) (Tsochatzis *et al* 2014). Fibrosis is present in the form of delicate bands (portal-central, portal-portal and central-central), or broad scars replacing multiple adjacent lobules. Parenchymal nodules are created by fibrotic isolation of islands of hepatic parenchyma. These may vary from micronodules (less than 3 mm in diameter) to macronodules (3 mm to several centimetres in diameter), as a consequence, the parenchymal architecture of the entire liver is disrupted. Several features should be understood: paraenchymal injury and fibrosis are diffuse, extending throughout the liver. Focal injury with scarring does not constitute cirrhosis, nor does diffuse nodular transformation without fibrosis. Nodularity is requisite for the diagnosis; regeneration is not. The parenchymal distance from portal tract to terminal hepatic vein is of the order 0.8 – 1.5 mm and scarring at the lobular level may produce nodularity on a mm scale. However, the hepatic capacity for regeneration is enormous, and it may produce nodules exceeding 3.0 cm in diameter (Anthony *et al* 1977; Crawford 2002).

In cirrhosis, excess of types I and III collagen are laid own not only on portal tracts, but also in the lobule, creating delicate or broad septal tracts. Concomitantly, the sinusoids are converted into capillaries with a basement membrane so that blood-hepatocytes solute exchange is
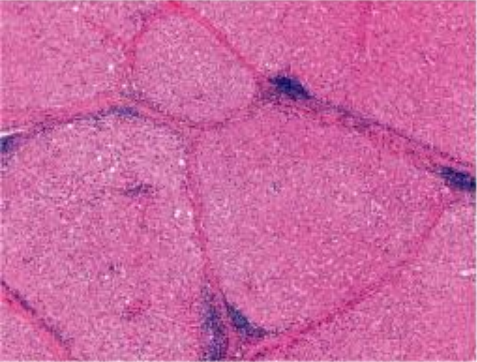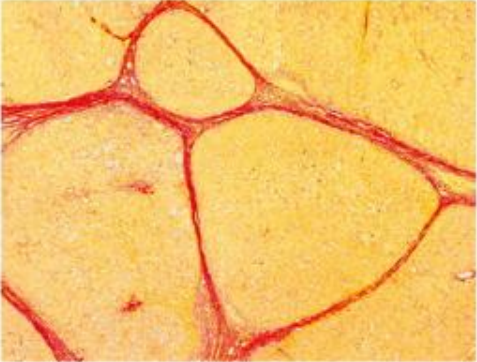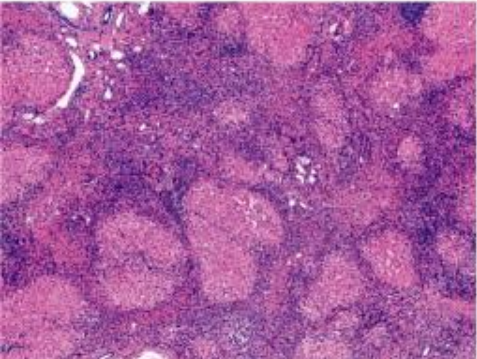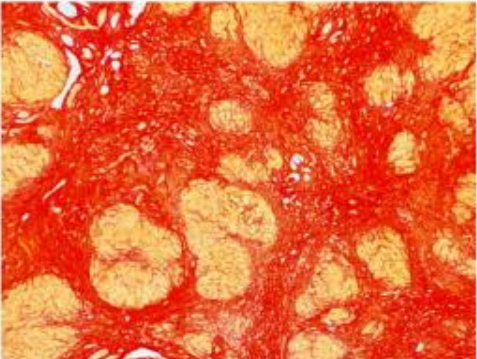
impaired despite maintenance of absolute hepatocyte volume (Figures 1.21 and 1.22) (Ohara *et al* 1993; Crawford 2002).

While the functional reserves of the liver masks to some extent the clinical impact, progressive injury carries the risk, not just of liver cancer, but diffuse parenchymal disease and impaired hepatic function which become life-threatening. Not strictly the end stage of hepatic scarring, rather a dynamic biphasic process dominated by progressive parenchymal fibrosis and severe distortion of normal lobular architecture by the separation of parenchymal into residual islands, i.e., nodules (Crawford 2002). The pathological process eventuating in cirrhosis is a complex interplay of the damage to, and response of cells endogenous to the liver. The latter includes fibrogenic mediators, and the deposition of aberrant extracellular matrix by perisinusoidal stellate cells in the parenchyma, without or with a contribution from portal tract-based fibroblasts (Gressner 1992; Crawford 2002). Loss of liver function is the main determinant of survival (Ohara *et al* 1993).

The three major pathological mechanisms that combine to create cirrhosis are cell death, fibrosis and regeneration. The process is usually initiated by cell death but only after this has occurred consistently and persistently over a long period of time (Crawford 2002).

Figure 1.20 Histological Methods of Subclassifying Cirrhosis. Histological methods of subclassifying cirrhosis Laennec system (haematoxylin and eosin stain) and quantitative assessment of liver collagen with collagen proportionate area (CPA, picro-sirius red stain, collagen tissue stained red). Patient 1 is a 53-year-old man with chronic hepatitis C; the sample shows early cirrhosis. With haematoxylin and eosin stain, the cirrhotic nodules are large with thin internodular septum; the CPA is 9%. Patient 2 is a 53-year-old man with alcoholic liver disease; the sample shows advanced cirrhosis. Small cirrhotic nodules, thick internodular septum, and large quantity of fibrotic tissue with a CPA of 62% are seen. CPA=collagen proportionate area (Tsochatzis *et al* 2014).
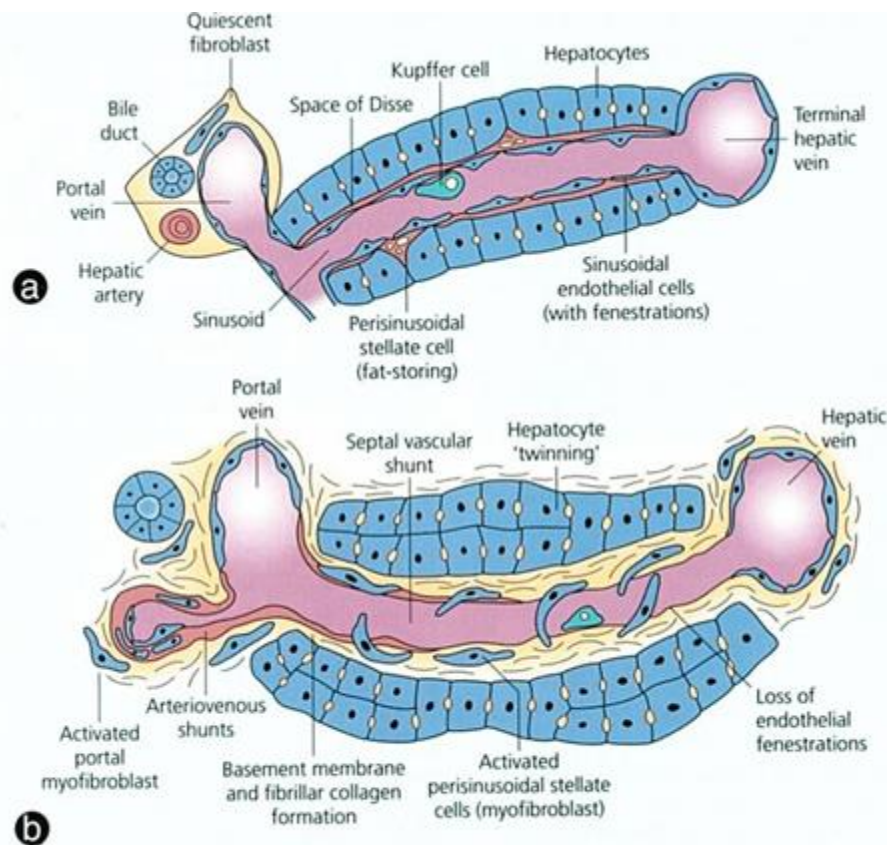
Figure 1.21 Key Events in the Evolution of Cirrhosis. a. The normal microanatomy of the liver is depicted, showing especially the channels for flow of portal venous blood through the sinusoids of the parenchyma, and normal sinusoidal architecture. **b.** With evolution to cirrhosis, the following key events occur. Abnormal arteriovenous shunts and vascular shunts from portal to hepatic veins develop. Portal tract fibroblasts proliferate and become myofibroblasts. Perisinusoidal stellate cells lose their fat stores, proliferate and develop a myofibroblast phenotype. Both populations of cells deposit extracellular matrix, expanding portal tracts and the space Disse, respectively. Hepatocyte regeneration, leading to 'twinning' of hepatocyte plates, also is shown (Crawford 2002).
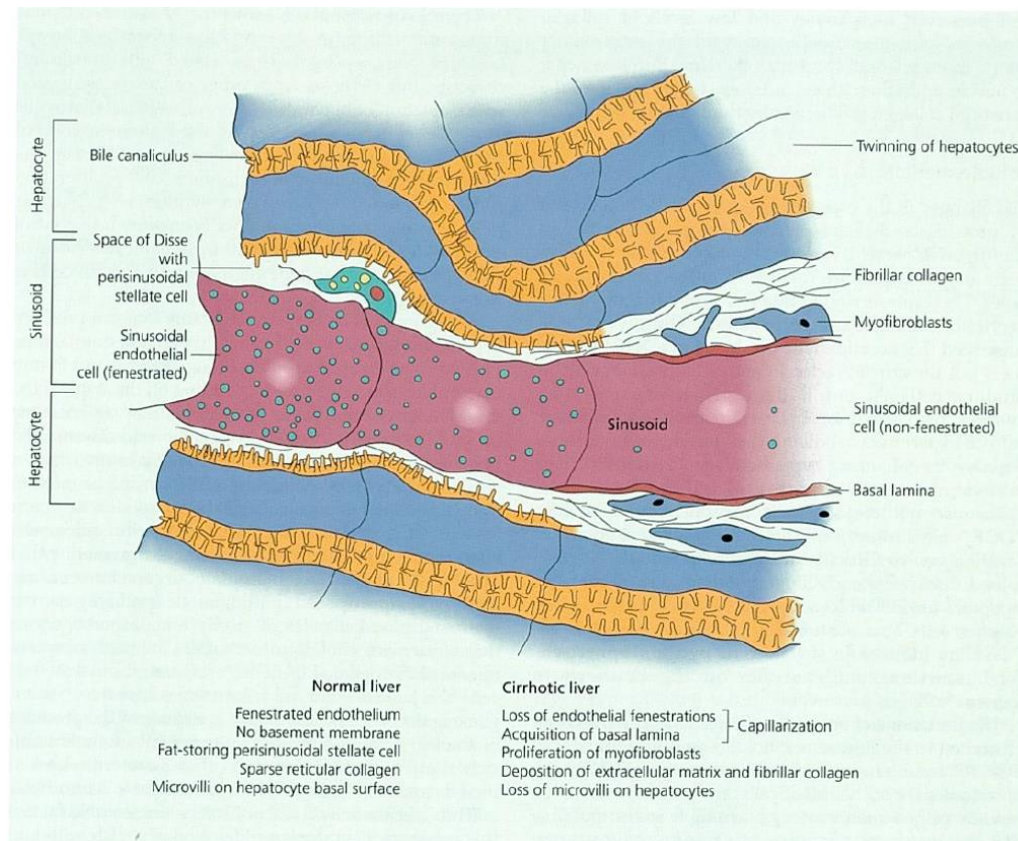
Figure 1.22 'Capillarization' of Sinusoids. In this scanning electron microscope perspective, the normal sinusoidal microanatomy is depicted on the left and cirrhotic liver on the right. The sinusoidal channel is bounded by sinusoidal endothelial cells, which normally are fenestrated but lose their fenestrations in the cirrhotic liver. The space of Disse normally contains scattered fat-storing perisinusoidal stellate cells; these proliferate and become muofibroblasts in the cirrhotic liver. These are normally only delicate reticular collagen fibrils in the space of Disse. Activated myofibroblastic stellate cells are the primary source of fibrillar collagen and other extracellular matrix proteins which are deposited in the space of Disse. Notably, a basal lamina is deposited under the non-fenestrated endothelial cells, completing the process of 'capillarization'. Lastly, hepatocytes lose their abundant basal microvilli (faceing the space of Disse); regeneration of hepatocytes leads to thickened hepatocellular plates ('twinning') (Crawford 2002).

50

1.7 *In Vitro* Models of Liver Disease

The large burden of liver disease and primary liver cancer along with the management difficulties encountered have provided the impetus to pursue the use of representative *in vitro* models of liver function, response to injury and development of malignancy. Improved 2D and 3D *in vitro* disease models would enhance our understanding of the cause of liver injury and cancer, increase the efficacy of preclinical drug discovery, and be a useful clinical tool for precision medicine. The increasing popularity of organ on a chip technology and improvements in 3D cell cultures has enabled unique insights into liver disease (Astashkina *et al* 2012; Zeilinger *et al* 2016). The chief purpose of *in vitro* models in research and medicine is to minimalize experimental variables to effectively isolate different organ components or structures for study under well-controlled, reproducible and easily assessed conditions. *In vitro* liver models can be assessed on their organotypic characteristics including cell type, liver function, zonation and likely application in basic research, drug discovery and clinical practice (Figure 1.23).
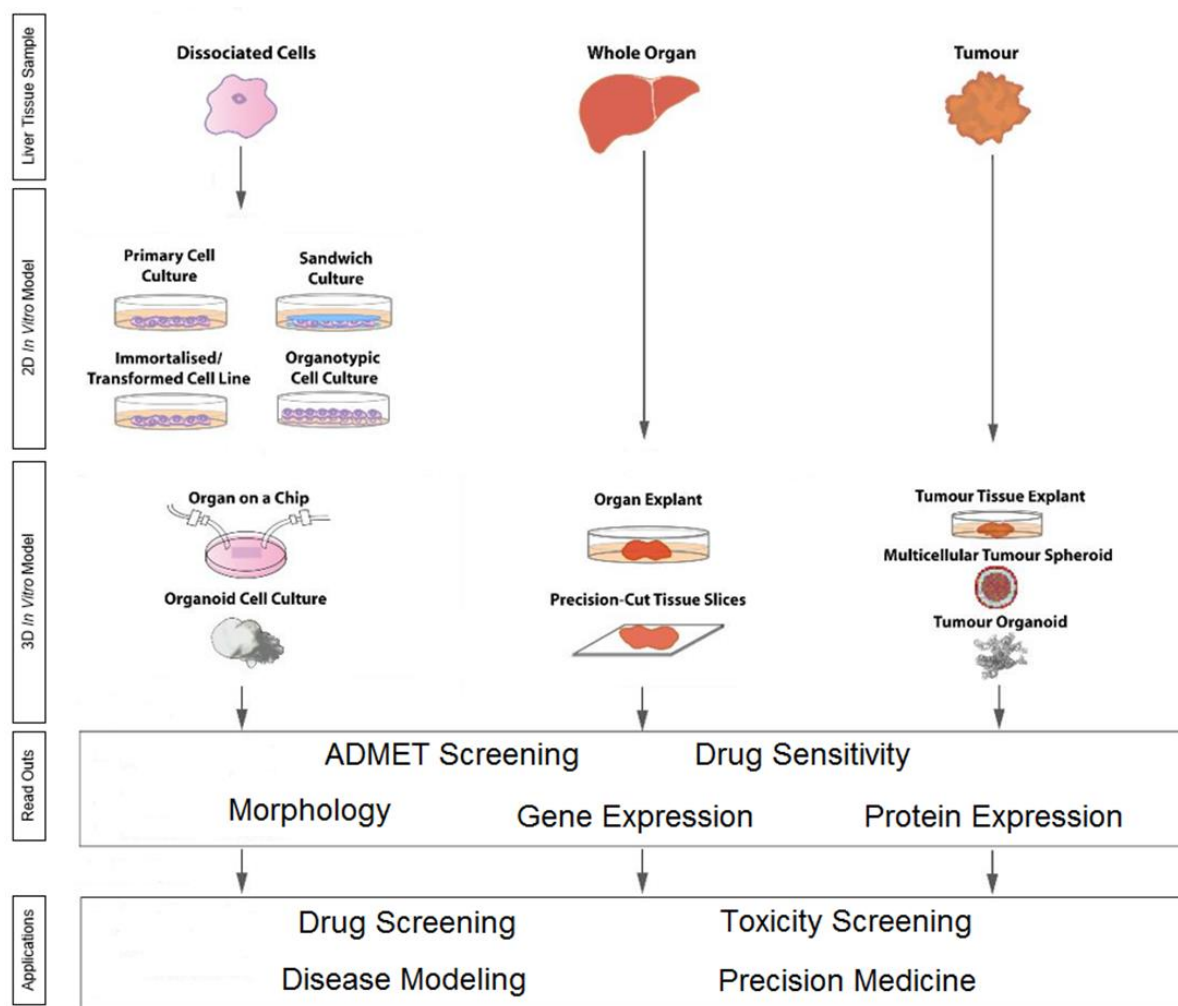
Figure 1.23 Overview of 2D and 3D *in vitro* **Models of the Liver**. Flow diagram indicates the *in vitro* models of the liver, their readouts, and applications. Each model was categorized by the type of sample it is derived from and whether it is 2D or 3D model.

CHAPTER 1 INTRODUCTION

Increasing the efficacy of drug development and toxicity texting by improving *in vitro* models is of monetary interest to the pharmaceutical industry (Moffat *et al* 2017). In 2015 the cost of bringing a new drug to market was estimated at 2.6 billion USD (Avorn 2015), with the major contributor to this cost being the very low clinical success rate of new compounds (approx. 11.8 %) (Di Masi *et al* 2015). This high burden of cost necessitates the exploration of new approaches including advances in preclinical methods which select new drug interventions for clinical trials.

In the discovery and preclinical development stages of drug development candidates are identified by correlating drug-responses in cell cultures and preclinical animal models; usually one rodent and one non-rodent species (Zhang *et al* 2012). Screening for Absorption, Distribution, Metabolism, Excretion and Toxicity (ADMET screening, also commonly referred to as ADME or the study of Drug Metabolism and Pharmacokinetics), optimises preclinical testing by enabling better understanding of the pharmacokinetic/pharmacodynamics properties of drug candidates (Tsaioun and Jacewicz 2009). Desirable drug-like properties identified by ADMET screening include adequate absorption and distribution, low metabolism, complete elimination from the body and a minimal toxicological risk (Zhang *et al* 2012).

A significant challenge in this field is predicting human specific liver toxicity (Xu *et al* 2004). Animal models do not always reflect human toxicity due to differences in physiology, interspecies metabolic capacities, and disease adaptations. Similarly, *in vitro* models often do not accurately predict toxicity due to non-linear dose–toxicity relationships, unclear mechanisms, non-organ specific toxicity, as well as adverse downstream effects (Astashkina *et al* 2012; Xu *et al* 2004). Drug-induced hepatic injury is the most frequently cited reason for approved drugs being removed from the market (Lee 2003). Current 2D *in vitro* assays based on cell lines such as HepG2 that have reduced metabolic capacities compared to primary hepatocytes, while the use of primary human hepatocytes suffers from high donor-to-donor

variation and only retain *in vivo* characteristics for a short time *ex vivo* (Tsaioun and Jacewicz 2009). The effect of improving these *in vitro* assays may potentially lead to more effective and rapid pre-clinical drug development.

After completing of the human genome project in the early 2000s there was significant optimism for the potential of genomic medicine to revolutionise the diagnosis and treatment of many illnesses. That is the clinical application of genetic predictors to better understand patient risks of disease, potential drug responsiveness and potential designer drugs based on targeting specific molecular pathways (Collins and Mac Kusick 2001). In 2011 the US National Research Council coined the term 'Precision Medicine' to inspire a new taxonomy for disease via a knowledge network. They define precision medicine as, "The tailoring of medical treatment to the individual characteristics of each patient…to classify individuals into subpopulations that differ in their susceptibility to a particular disease or their response to a specific treatment. Preventative or therapeutic interventions can then be concentrated on those who will benefit, sparing expense and side effects for those who will not". This is different to Personalized Medicine which refers to "an approach to patients that considers their genetic make-up but with attention to their preferences, beliefs, attitudes, knowledge and social context" (Ginburg and Phillips, 2018). The disease treatment strategies that have benefited the most so far from precision medicine are for cystic fibrosis and cancer management using genome sequencing to enhance patient care by improved diagnostic sensitivity allowing for more precise genetic therapeutic targeting (Ashley 2016). Since the early success of the ABL1 kinase inhibitor Imatinib for targeted therapy for chronic myeloid leukaemia, oncology has moved towards molecular classification (Ashley 2016), but currently there are only 11 genomic alterations known to drive tumour progression in different tissues matched directly with approved targeted therapies (Remon and Dienstmann 2018).

1.7.1 Conventional 2D *In Vitro* Liver Cell Cultures

Essentially, cell biology relies on 2D models generated from dissociated cell cultures that are expanded on plastic surfaces often treated with extracellular matrix scaffolding. These are primary cell cultures derived directly from harvested tissue or immortalised cell lines (primary cells genetically transformed to produce rapidly proliferating, uniform, easily cultured, artificial phenotypes). A major reason for the popularity of dissociated cell cultures is that the majority of mammalian cells can be expanded into adherent colonies on culture plates and these have proven to be relatively low cost and easy to manipulate and maintain. A high throughput cultured monolayer of cells receives a consistently homogenous amount of nutrients, growth factors and exposure to oxygen. Commercialized cell lines are available across a diverse range of tissue types and there is extensive commercial support for these cultures such as the availability of different culture media and consumables. Furthermore, there are various options for genetic manipulation; such as CRISPR, gene transfer, insertion, deletion, silencing, and cell fusion (Astashkina *et al* 2012).

1.7.2 Primary Cell Cultures

Human hepatocyte primary cell cultures are a physiologically relevant model for studying drug biotransformation and toxicity (Ponsoda *et al* 2001; Gómez-Lechón *et al* 2003). Although, cells grown in this way have a number of issues; due to only maintaining their wildtype characteristics for a limited time when cultured on 2D surfaces because of de-differentiation, also *in vitro* manipulation often results in a loss of wild-type characteristics, slow proliferation, changes in metabolism and early senescence after a limited number of passages (Ponsoda *et al* 2001; Gómez-Lechón *et al* 2003). Therefore, cell cultures require successive tissue harvests which incur higher associated costs. Moreover, the harvesting of tissue is susceptible to

contamination from non-applicable cell types thereby compromising the model's integrity (Astashkina *et al* 2012).

The ECM has a profound effect on primary cell function, differentiation, signalling and morphology (Caron 1990; Lee and Streuli, 1999). For example, culturing primary hepatocytes with the scaffold matrix Matrigel®, induces gene expression which more closely resembles liver tissue *in vivo*, as well as improving cellular morphology by enhancing cuboidal shape, have cells with clearly defined cell borders and allowing the formation of highly organised cellular networks (Page *et al* 2007).

Primary hepatocyte cell cultures have been useful for understanding the mechanisms in liver regeneration (Michalopoulos *et al* 1982) and discerning the relationship between the liver cytoskeleton and liver-specific protein expression (Ben-Ze'ev *et al* 1988). Similarly, primary cultures of hepatic stellate cells have been instrumental in understanding the causes of liver fibrosis and identification of key fibrogenic mediators (Bataller and Brenner 2005; Wasser and Tan 1999). In drug testing, primary human hepatocyte cell cultures are considered the "gold standard" because they display many phenotypic functions of the liver when compared to other *in vitro* models (Kegel *et al* 2016; Gómez-Lechón *et al* 2007). However, this approach has been heavily criticised as reductionist with "hits" requiring very specific molecular targets or phenotypic requirements (Ranga *et al* 2014). Other fundamental issues include cells being cultured at densities of only approximately 1% of physiologically normal tissue densities thereby impairing intercellular signalling. Furthermore, these cultures are non-homeostatic as conditions are optimised for rapid growth and thereby prevent correct cell differentiation (Hartung and Daston 2009). Primary hepatocytes experience a decline in CYP450 expression when grown *in vitro* (Wright and Paine 1992), while the transcription of common genes is unaffected leading to a decrease in CYP450 proteins and activity, significantly limiting the translatability of this model (Rodríguez-Antona *et al* 2002).

1.7.3 Sandwich-Cultured Hepatocytes

Culturing primary hepatocytes between two layers of collagen, termed sandwich-cultured hepatocytes (SCH), results in retained cellular polarity with correct localization of basolateral and canalicular transporters as well as formation of functional bile networks (Le Cluyse *et al* 1994; Liu *et al* 1998). Discovered by Dunn and colleagues, SCH maintains mRNA expression, as well as cell functions such as the secretion of albumin, transferrin, fibrinogen, bile acids and urea for 6 weeks (Dunn *et al* 1991; Dunn *et al* 1992), and CYP450 isozymes for 2 weeks (Kern *et al* 1997). SCH have proven to be a useful tool to study hepatobiliary drug disposition and mechanisms of drug-induced liver injury, for example elucidating transport mechanisms responsible for elimination of the antifungal agent, micafungin (Yanni), and the mechanisms of bile acid mediated drug induced liver injury (Yang *et al* 2016).

1.7.4 Immortalised or Transformed Cell Lines

Immortalised/transformed cell lines are dissociated cell cultures which have been genetically modified or selected for an oncogenic phenotype. Typically, these cultures show rapid proliferation, resistance to de-differentiation, improved passaging, and greater resilience to senescence, making these cells convenient to maintain, expand and retain phenotypic consistency between experiments (Astashkina *et al* 2012). These cell cultures have been successfully used to study HBV and hepatitis D virus (HDV) infections. Mechanisms of HBV viral entry were discovered in HepRG cell lines (Gripon *et al* 2002), the expression/replication of HBV in HepG2 (Verrier *et al* 2016) and the complete HDV replication cell cycle in HepG2 and Huh7 (Lampp *et al* 2018; Verrier *et al* 2016). The shortcomings of these cell lines include significant changes in differentiation potential, altered genomic content (Yamasaki *et al* 2009), abnormal proteome expression and the loss of features such as cellular polarity (Prozialeck *et*

al 2006), contact inhibition (Milyavsky *et al* 2003; Holt *et al* 2010), metabolic CYP450 potential (Cummings *et al* 2000; Donato *et al* 2008), the induction of inflammatory mediators (Chamberlain *et al* 2009) as well as paracellular transport (Pan *et al* 2009).

Due to most immortalised human hepatic cell lines having reduced liver specific functionality (Ramboer *et al* 2015), different strategies have been used to counteract this issue including co-culture systems with primary human hepatocytes and overexpressing liver-enriched transcription factors, CYP450 enzymes or proliferation inhibitors to increase hepatic functions (Ramboer *et al* 2015). Immortalised human hepatic cell lines have been successfully used to investigate the life cycle of Hepatitis C and B viruses (Kato *et al* 1996; Ikeda *et al* 1997; Brown *et al* 2000; Yu *et al* 2010), as well as acting as cellular models of hepatocarcinogenesis (Heim *et al* 2015) and steatosis (De Gottardi *et al* 2007). Furthermore, immortalised hepatic cell lines have also been found suitable as *in vitro* tools for drug screening and safety testing; Hc3716-hTERT, immortalised foetal hepatocytes and telomerase immortalized hepatic stellate cells NPC-hTERT, have been used as models for predicting side-effects of telomere-targeting drugs (Waki *et al* 2010), and Fa2N4 cells for screening for pregnane X receptor-mediated CYP3A4 induction (Ramboer *et al* 2015).

1.7.5 Organotypic Cultures

A major limitation of dissociated cell cultures is their homogeneity as they fail to represent liver tissue heterogeneity. While hepatocytes comprise the majority of cells within the liver, liver function is dependent on a number of different cell types. 2D organotypic culture uses multiple different cell types to recapitulate *in vivo*-like cell heterogeneity. Co-cultures of hepatocytes and macrophages have been successfully used to model their intercellular cross-talk, their roles in the regulation of liver regeneration, hepatocyte function and the acute phase

response to septic liver injury (Godoy *et al* 2013). Long-term co-cultures of hepatocytes and LSECs either on top of or sandwiched between a collagen gel retained the LSEC phenotype and enhanced hepatocyte functions such as increased CYP450 activity (Bale *et al* 2015). In contrast, co-cultures of primary hepatocytes and endothelial cells maintained under high oxygen conditions preserved cell morphology, high CYP450 levels and native gene expression (Kidambi *et al* 2009). A recent example by Ware and colleagues was a triculture of primary human hepatocytes with 3T3-J2 fibroblasts and liver sinusoidal endothelial cells overlayed with Matrigel®, which was shown to display a stable phenotype with increased albumin and urea secretion for 3 weeks (Ware *et al* 2018).

1.7.6 Shortcomings of Conventional 2D Liver Cell Cultures

While these models have many uses, a significant issue with 2D liver models is their lack of most hepatic sinusoid heterogeneity, *in vivo*-like cell density, oxygen induced zonation and the liver circulatory system. The clinical applications of 2D cell cultures are limited due to significant issues of cell contamination, non-reflective cell differentiation, genetic drift, variable drug responsiveness and a limited capacity to predict toxicity creating a confluence of uncertainty when using 2D culture as a model for potential treatments, with a possible exception of patients derived tumour cell lines for precision medicine (Mitra *et al* 2013).

1.7.7 3D *In Vitro* Liver Models

The shortcomings of 2D cell culture models have driven the development of 3D cell culture techniques. The advantages of 3D models include replicating the complex attributes of the liver beyond liver specific metabolism, such as increased cell density, organisation, and cell-cell

signalling, O_2 zonation, as well as the anatomy of the liver lobule and the circulatory system (Figure 1.24). Some of these models are limited by their low applicability for high-throughput screening as well as their laborious preparation, lack of reliable protocols and short-term survival of these models in culture. However, 3D models have proven useful in developmental and toxicological studies and represent an exciting opportunity for more functionally relevant clinical modelling.

1.7.8 Whole Organ Explants

Whole mouse liver organ explants have been used to study the effects of oxidation on the progression of hepatocarcinoma. Torricelli and colleagues in 2016 reported inoculating the murine hepatocarcinoma cell line Hep1A1s into the livers of live mice, which proliferated *in vivo* for 20 days before the livers were removed and used as a whole organ explant model to study the effects of the antioxidant, Citozym, on tumour size in culture over a 4-week period (Torricelli *et al* 2016).
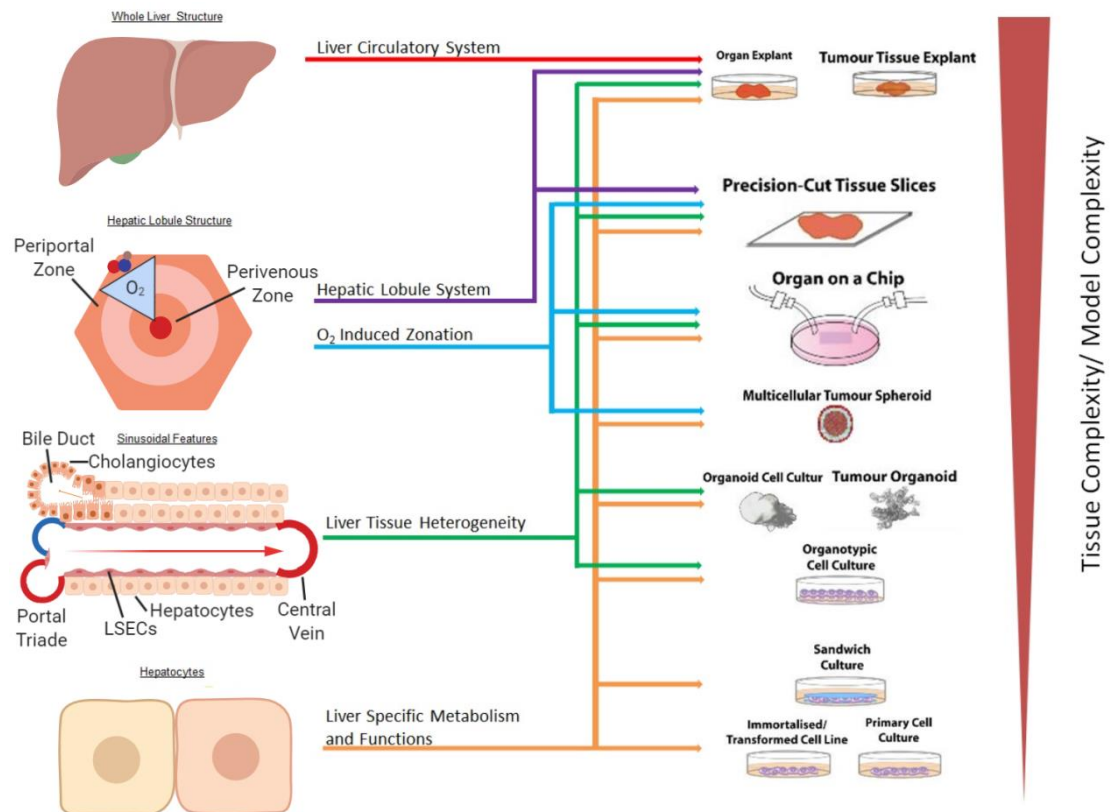
Figure 1.24 Different Levels of Structural Complexity in the Liver and their Attributes Represented in *in vitro* Models. The different structures of the liver and their corresponding liver models on a gradient, based on their tissue complexity. Structures of the liver are then linked by attributes represented in the *in vitro* models discussed. Levels of complexity include containing hepatocytes for liver specific metabolism and functions. Having multiple liver cell types, representing liver tissue heterogeneity. An oxygen gradient to induce liver zonation. The anatomy of the hepatic lobule and the whole anatomy of the liver.

1.7.9 Precision-Cut Tissue Slices

Liver 'Precision-Cut Tissue Slices' (PCTS) have mostly been undertaken using rat livers, but the technique has also been used in other species including humans (de Graaf *et al* 2010). Slicing allows sufficient oxygen and nutrient supply to the inner cell layers and hepatocytes retain their membrane and intracellular polarisation (Groothuis *et al* 1981). Rat liver slices from Vickers and colleagues have been fully capable of metabolising compounds and maintain fibrogenic pathways such as activation of stellate cells, the proliferation of myofibroblast-like cells, and an increased collagen deposition for 4 days under appropriate conditions (Vickers *et al* 2004). As with 2D cultures CYP450 expression decreases during prolonged culturing, but this has been shown to slow when the medium is supplemented with insulin, dexamethasome and foetal calf serum (de Graaf *et al* 2007; de Graaf *et al* 2010).

1.7.10 Tumour Tissue Explants

A 'Tumour Tissue Explant' is a 3D model of cancer whereby excised human tumour tissue is embedded in collagen and feed tissue culture media (Freeman and Hoffman 1986). Mainly used as an *in vitro* model of drug efficacy, this method has been demonstrated by Vaira and colleagues to preserve pathway activation, pharmacological inhibition, internal 3D architecture, cell viability and global gene expression profiles up to 5 days *ex vivo* (Vaira *et al* 2010). Unfortunately, this model is can not be reproduced due to tissue heterogeneity, techniques like imaging and flowcytometry are limited and the culture is only viable for a short period of time making it impractical for any form of high-throughput, long-term or clinical investigations (Nath and Devi 2016).

1.7.11 Multicellular Tumour Spheroid

The best characterised 3D organotypic models of cancer are 'Multicellular Tumour Spheroids' which are constructed from homogeneous tumour cells or co-cultures on nonadherent surfaces where the cell suspension undergoes aggregation and compaction (Weiwald *et al* 2015; Nath and Devi 2016). Spheroids re-establish morphological, functional and mass transport properties of their corresponding tissue, and resemble the avascular tumour nodules/micrometastases or intervascular regions of large solid tumours (Friedrich *et al* 2009). These have been used to gain insights into therapeutic challenges associated with drug resistance, metabolic and proliferation gradients, and the importance of cell-cell/cell-matrix interactions (Friedrich *et al* 2009). Liver multicellular tumour spheroids have been used for understanding microenvironmental chemoresistance of HCC associated with the crosstalk between HCC cells, hepatic stellate cells and other stromal cells (Song *et al* 2016; Seo 2015). For instance, liver cancer spheroids of Huh7 cells co-cultured with human umbilical vein endothelial cells promoted HCC gene expression and oncogenic properties such as cell proliferation, increased expression of cancer stem cell markers and extracellular cytokines-mediated signalling (Jung *et al* 2017). Furthermore, this multicellular tumour spheroid model survived higher anti-cancer drug concentrations than the monolayer control, which may be due to the hypoxic conditions within the spheroid activating extracellular signal-regulated kinases (ERK), critical in tumour cell proliferation (Jung *et al* 2017).

1.7.12 Organ-on-a-Chip

An 'Organ-on-a-Chip' utilises microfluidic technology to replicate the *in vivo* microenvironment and homeostasis of living human organs (Esch *et al* 2015). Often consisting of transparent 3D polymeric microchannels lined by human tissue cultures, these devices are

designed to mimic the 3D microarchitecture, organ-specific mechanical/biochemical microenvironment and the functional tissue-tissue interfaces in organs. Many use micro-channels of matrix-coated porous membranes with a layer of endothelial cells populated by the desired co-culture, connected by wells containing the preferred perfusion medium (Esch *et al* 2015). These devices have also been designed with compartmentalised channels allowing for independent fluidic/aerosol access to individual tissue types enabling selective treatment conditions and analysis (Weiwald *et al* 2015). 'Liver-on-a-Chip' systems have been shown to predict clearances, toxicity and the mechanism of action of certain drugs (Usta *et al* 2015).

Commercially available Liver-on-a-Chip microfluidic systems such as the 3D perfused cell culture platform from Zyoxel and the Microliver chip from HµRel® corporation have been used for toxicity testing, but none of these systems have been fully validated. Most current models use primary human hepatocytes to populate the system and a few include a co-culture with non-parenchymal cells, which has improved their capacity to predict liver toxicity (Starokozhko and Groothuis 2017). For example, the anticancer prodrug Flutamide was tested for hepatotoxicity using human HepG2/C3a cells in a microfluidic biochip and showed metabolic results consistent with reports in the literature, demonstrating perturbation of the tricarboxylic acid cycle and impaired urea cycle with reduced uptake of essential amino acids (Snouber *et al* 2013). Bhise and colleagues in 2016 have also had success in drug toxicity analysis with a Liver-on-a-Chip platform using human HepG2/C3a spheroids encased in hydrogel within a bioreactor for long-term culturing (Bhise *et al* 2016). Furthermore, biochips using primary hepatocytes have been used to measure the pharmacokinetics of several drugs, with results that resembles data in relevant clinical trials (Baudoin *et al* 2013). The use of human induced pluripotent stem cells (hiPSCs) to generate hepatocyte-like cells has been assessed for populating Liver-on-a-Chip systems, but differentiated cells were found to have reduced functionality and immature gene/protein expression (Yu *et al* 2012). Focused efforts

at recapitulating lobule zonation have had mixed success using Liver-on-a-Chip systems (Allen and Bhatia, 2003; Allen *et al* 2005). A controlled oxygen gradient has been maintained in primary rat hepatocytes which induced *in vivo*-like heterogeneous CYP450 localization and toxicity. This is significant because most studies only model one lobule zone (usually the perivenous zone), hence the expression of intermediate metabolites may be exaggerated, while detoxification is underestimated (Usta *et al* 2015).

1.7.13 Organoids

An 'Organoid Cell Culture' is defined as a collection of cells culturing several cell types that develop from stem cells or organ progenitors and self-organise through cell sorting and spatially restricted lineage commitment, similar to organogenesis *in vivo* (Lancaster and Knoblich 2014). To be an organoid they must contain more than one cell type of the organ they model, exhibit functions specific to that organ, and mimic its structural organisation. Organoids are usually formed by exploiting the expansion potential of three cell types; pluripotent embryonic stem cells (ES), induced pluripotent stem cells (iPSC) or organ-specific adult stem cells (aSC), forming new primary tissue buds made of self-organising daughter cells, that are induced to differentiate in culture. These daughter cells display the capacity to self-organise into structures that reflect crucial aspects of the tissue for which they are fated (Clevers 2016). What makes 3D liver organoid cell cultures different from other *in vitro* models in that they bridge the gap between the microenvironmental integrity of organ explants and PCTS yet have the high throughput accessibility of immortal cell lines.

Liver organoids have demonstrated advantages over conventional *in vitro* models such as long-term genetic stability, *in vivo*-like organisation, and maintaining the necessary cellular cross talk and behavioural characteristics of their primary corresponding cells (Huch *et al* 2015). For

example, adult stem cells from Alpha-1 antitrypsin (A1AT) deficient patients cultured into liver organoids mimic the *in vivo* situation with A1AT protein aggregates and signs of ER stress (Huch *et al* 2015). Liver organoids were first created by Huch and colleagues by exploiting the expansion potential of LGR5$^+$ progenitor/stem cells in damaged mouse adult liver tissue, by Wnt-driven regeneration. They then induced hepatocyte maturation by inhibiting Notch and TGF-β signalling, which led to the expression for genes involved in cholesterol and lipid metabolism, as well as from the CYP450 superfamily. Immunofluorescent analysis revealed Hnf4α and Albumin expression, hepatocyte binuclation, as well as a patch of ductal marker Cytokeratin 19. 90% of these cells were also competent for low-density lipoprotein uptake and accumulated glycogen (Huch *et al* 2013).

Huch and colleagues established the first organoid culture system for human liver from primary bile duct stem cells (Huch *et al* 2015). These organoids displayed high stability both chromosomally and structurally with low rates of genetic alterations over a 3-month culture. Using the established methods developed for mouse liver organoids they induced hepatocyte differentiation in the human liver organoids that began to display hepatocyte gene expression, Albumin secretion, CYP450 metabolism, bile acid production, ammonia elimination, low-density lipoprotein uptake, and glycogen storage (Huch *et al* 2015). Further, organoids could be readily up-taken *in vivo* upon transplantation in mice (Huch *et al* 2015).

It has been proposed that liver organoids may be a useful model for studying the transition of NAFLD to non-alcoholic steatohepatitis if these organoids were cocultured with hepatic stellate cells, Kupffer cells, and other inflammatory cells (Nantasanti *et al* 2016). Retroviral transduction and liposomal transfection with green florescent protein expressing vectors, have been successful methods of genetic manipulation in liver organoids (Broutier *et al* 2016), another exciting avenue to explore is CRISPR gene editing, with success already achieved in

intestinal organoids of cystic fibrosis patients, where the *CFTR* locus was corrected *in vitro* by homologous recombination (Schwank *et al* 2013).

Although 3D liver organoid cell cultures are becoming a research focus, challenges for the technology include the recapitulation of the ECM *in vivo*. It has been suggested that the use of decellularised liver ECM populated with liver organoids may improve hepatocyte functions (Huch *et al* 2015), which has had success in promoting survival and maturation compared to Collagen type I (Lee *et al* 2014). Limitations of liver organoids include the lack of a native microenvironment thus inhibiting the study of the interactions between stem cells and their niches, a lack of all necessary *in vivo* growth factors/signalling gradients and an inability to accurately model immune responses. A possible solution to this is organotypical co-culturing and the application of microfluidic technologies. Further heterogeneity between organoid cultures can cause inconsistency in reproducing phenotypic traits such as size, shape, cellular composition and 3D architecture (Fatehullah *et al* 2016; Huch *et al* 2017).

In drug development an *in vitro* organoid system comprised of human cells complex enough to demonstrate organotypic composition, morphology and functionality (Table 1.) would be ideal in closing the gap in phenotypic drug discovery (Wasser and Tan 1999). Increasing the chain of translatability for target-agnostic investigations remains a significant challenge (Lu 1996) and human organoids may build a rational and sustainable discovery pipeline reducing false-positives and cost. The reason for this is that organoids may present a more phenotypical disease-associated functional response to treatment than 2D cell lines as well as a more accurate disease-free associated phenotype. Phenotypic drug discovery with generic readouts like viability or apoptosis in cancer cell lines often provide little insight into disease-pathways or mechanisms of action, while *in vitro* 3D organoid models exhibit potential to become highly predictive cell-based tools for preclinical drug toxicity assessments (Astashkina and Grainger 2014).

To date there have only been a few successful clinical uses of *in vitro* organoid models. One example was a robust functional drug assay for cystic fibrosis developed using human intestinal organoids, which demonstrated the clinical potential organoids have for being applied to precision medicine (Dekkers *et al* 2013). Using automated fluorescent image analysis, the function of the cystic fibrosis transmembrane conductance regulator (CFTR) (which is defective in cystic fibrosis) was able to be assessed allowing the authors to efficiently test drug responses of patients and treat rare forms of this disease (Chakradhar 2017). This assay has advantages over established *in vitro* models such rectal biopsies and primary airway tissue culture models because organoids can be passaged into large screening arrays for high throughput precision medicine (Dekkers *et al* 2013).

1.7.14 Tumour Organoids

Despite the precision medicine approach only a minority of patients with cancer, derive clear benefit from matching genetic targets with treatment. Currently precision oncology based on emerging biomarkers remains an investigational strategy and the current approach of matching single agents to patients is currently suboptimal (Remon and Dienstmann 2018).

To address such as issue Pauli and colleagues piloted a study that combined whole-exome sequencing (WES) of patient metastatic and primary tumours, with tumour organoid drug sensitivity assays facilitating the integration of genomic data with drug screening in an iterative platform to identify effective therapeutic regimens for individual patients (Pauli *et al* 2017). Sequencing of 769 specimens identified somatic cancer gene alterations that were actionable by FDA-approved drugs in 3 specimens (0.4% of the total) but found somatic alterations with potential clinically actionable by off-label use in 71 of the remaining specimens (9.6% of the total). Fifty-six organoid tumour lines and 19 patient-derived organoid xenografts were successfully established and characterised using cytology and histology, leading to patient

derived tumour organoids from 4 candidates being selected and subjected to 2D high throughput drug screening. The tumours screened were from uterine carcinoma, endometrial carcinoma, and two lines of stage IV colorectal cancer. Single and combination compounds selected by this process were then validated in 3D cell culture. Drug combinations were further validated in patient-derived xenografts for two patients. In both cases the drugs selected by the screening were found to be more effective at reducing tumour growth than the patient's current regimen. These results demonstrate that the optimal drug combinations can be identified using sequential drug-sensitivity screens followed by validation in personalized patient-derived tumour organoid xenograft models in a clinically relevant time frame of 7 and 12 weeks (Pauli *et al* 2017).

TABLE 1 Assessment of in vitro liver models based on their organotypic morphology/functions/interactions, technical ease of use, ease of maintenance, and throughput, with comment on their benefits and disadvantages. Each category is graded either as good (green), moderate (yellow) or poor (red)

	Primary Cell Culture	Sandwich Culture	Immortalised/ Transformed Cell Line	Organotypic Cell Culture	Organ Explant	Precision-Cut Tissue Slices	Tumour Tissue Explant	Multicellular Tumour Spheroid	Organ on a Chip	Organoid Cell Culture	Tumour Organoid
Organotypic Morphology/ Function/ Interactions	Poor	Poor	Poor	Poor	Good	Good	Good	Moderate	Moderate	Good	Good
Technical Ease of Use	Good	Good	Good	Good	Poor	Poor	Poor	Moderate	Good	Good	Moderate
Ease of Maintenance	Good	Good	Good	Good	Poor	Poor	Poor	Moderate	Moderate	Good	Good
Throughput	Good	Poor	Good	Good	Poor	Poor	Poor	Moderate	Moderate	Good	Moderate
Comments	Hepatocytes Preserve Many Phenotypic Functions Low Cost (Tissue Dependent) Extensive Commercial Support De-Differentiate within a Short Time No ECM Unnatural Gene Expression/ Morphology Impaired Cell Signalling Decline in CYP450 Expression Susceptible to Contamination No Zonation	Hepatocytes Preserve Many Phenotypic Functions for 6 Weeks Retain Cellular Polarity Low Cost Present ECM No Zonation	Rapid Proliferation Low Cost Extensive Commercial Support Resistant to De-Differentiation Phenotypically Consistent Wide Variety of Commercially Available Genetic Variants Easy to Genetically Manipulate No ECM Impaired Cell Signalling Changed Differentiation Potential Altered Genomic Content Abnormal Proteome Loss of Cellular Polarity Decline in CYP450 Expression (Line Depended) No Zonation	Preserves Hepatocyte and Non-Parenchymal Cell Signalling, Preserving Some Functions Low Cost (Tissue Dependent) May Contain ECM No Zonation	Preserves Hepatocyte and Non-Parenchymal Cell Signalling, Preserving Some Functions Low Cost (Tissue Dependent) May Contain ECM No Zonation	Preserves All In Vivo Structures and Functions Sufficient Oxygen and Nutrient Supply Laborious Preparation and Maintenance Decline in CYP450 Expression	Preserves All In Vivo Structures and Functions Short-term Survival Laborious Preparation and maintenance Unreproducible	Re-establishes Morphological, Functional and Mass Transport Properties Preserves Cellular Cross-Talk, Proliferation and Drug-Resistance Present ECM Zonation Present	Preserves Hepatocyte and Non-Parenchymal Cell Signalling, Preserving Some Functions Preserves Homeostasis Sufficient Oxygen and Nutrient Supply Large Range of Different Designs May Contain ECM (Design Depended) Present (Design Depended) Zonation	Re-established In Vivo Cell Organisation, Morphology, Microenvironment and Function Preserves Cellular Cross-Talk, Proliferation and Drug-Resistance Long-term Genetic Stability Present ECM High Heterogeneity No Zonation	Re-established In Vivo Cell Organisation, Morphology, Microenvironment and Function Preserves Cellular Cross-Talk, Proliferation and Drug-Resistance Long-term Genetic Stability Present ECM High Heterogeneity No Zonation

Legend: Good (green) — Moderate (yellow) — Poor (red)

CHAPTER 1 INTRODUCTION

The utility of tumour organoids to be passaged into large data sets while retaining an individual patient's disease phenotype cannot be under-appreciated, as the power to rationally delineate the optimal therapy for every individual patient removes ambiguity and could exponentially speed the rate of patient recovery. Pauli and colleagues demonstrated that 3D patient-derived tumour organoids can be a powerful tool for individual drug sensitivity assays, the results of which can be verified in xenograph models (Pauli *et al* 2017).

In 2018, Tiriac and colleagues assembled a library of pancreatic ductal adenocarcinoma patient-derived organoids (PDO) from both surgical resection specimens and fine-needle biopsies, for the purposes of establishing a drug testing pipeline that could determine drug-sensitivity profiles of each PDO within a clinically meaningful timeframe. Using retrospective analysis this pipeline they termed "Pharmacotyping" was able to reflect patient responses to therapy (Tiriac *et al* 2018). The generated pancreatic cancer PDO from this library also encompassed a broad spectrum of disease stages, uncommon genetic events as well as the previously established subtypes of pancreatic cancer.

A prospective clinical study by Ooft and colleagues in 2019 found that patient derived tumour organoids from the metastatic lesions of colorectal cancer patients can be used to predict the outcome of irinotecan-based chemotherapy. The Tumour Organoids: feasibility to predict sensitivity to treatment in cancer patients (TUMOROID) study was a multicentre study focused on regimens commonly used for colorectal cancer. Patients received standard-of-care chemotherapy, including infusional 5-fluorouracil (5-FU) or capecitabine (oral prodrug of 5-FU), in combination with either oxaliplatin or irinotecan, or irinotecan alone. Bevacizumab was allowed in all treatments, but patients who received additional cetuximab or panitumumab after the biopsy was taken were excluded (Ooft *et al* 2019). The primary objective was the development of an assay to accurately identify non-responders to chemotherapy which was defined as patients with progressive disease after three cycles of chemotherapy. Interestingly

there was a discrepancy between the predictive value of PDOs from irinotecan and oxaliplatin based treatments, suggesting that the sensitivity and necessary conditions of testing might differ across types of chemotherapy.

In late 2017 the clinical potential of tumour organoids derived from human primary liver cancer was demonstrated by Broutier and colleagues (Broutier *et al* 2017). Tumour organoids from HCC, cholangiocarcinoma (CC) and combined hepatocellular-cholangiocarcinoma (CHC) retained features from their tissue of origin, such as the vast majority of cancer-related genetic variants, gene expression profile and tissue histology. Immunohistochemistry and immunofluorescence showed that even after long-term expansion in culture disease specific protein expression was conserved, including the HCC markers HepPar1 and Alpha-fetoprotein in HCC/CHC, and the Ductal/CC marker EpCAM in CC/CHC. Once established the liver tumour organoid cultures were used to develop drug assays to identify patient-specific drug sensitivity. This was achieved by using a simple cell viability assay and observing the rate of organoid viability in the presence of range treatments such as Sorafenib, gemcitabine and SCH772984. Of these drugs the sensitivity of the ERK inhibitor SCH772984 was then able to be validated in a patient-derived xenograft model transplanted with a CC tumour organoid (Broutier *et al* 2017).

Another precision medicine study by Nuciforo and colleagues using human liver tumour organoids found that HCC tumour derived organoids maintained the growth pattern and differentiation grade of the originating primary tumour, also Alpha-fetoprotein, Glypican 3, glutamine synthetase, and heat shock protein 70 protein expression was preserved. Whole exome sequencing found that of the total somatic and non-synonymous somatic mutations in the HCC biopsies were observed at a rate of 88% and 90% respectively in the corresponding HCC organoids at early passages. The tumour organoid cultures also displayed variable sensitivity to Sorafenib exposure demonstrating that organoids derived from biopsies can be

used to test tumour-specific sensitivities to growth-inhibitory substances. Although a direct comparison of *in vitro* Sorafenib activity with the clinical response was not feasible, because none of the patients for whom organoid cultures were generated were treated with Sorafenib (Nuciforo *et al* 2018).

These studies demonstrated the value-added tumour organoids may have in the pursuit of precision medicine in treating primary liver cancer. While precision medicine has focused mainly on matching genetic targets with treatments, tumour organoids may be used to validate these matches in *in vitro* models or discovery potential treatment options in the patient, which can be further validated *in vivo*, using tumour organoid xenografts models.

1.7.15 Future Directions of *In Vitro* Models of the Liver

Future *in vitro* models of the liver need to be standardised to satisfy requirements of 1) high throughput with ease of use and cell maintenance, and 2) replicating aspects of the anatomy and metabolic zonation of the liver lobule. Future *in vitro* models of the liver will combine material advancements made in Organ-on-a-Chip biotechnologies, bioprinting and the cell biology advancements in organoid research. This could be achievable using permeable microfluidic tubes lined with LSECs to simulate blood flow and bile excretion or within a modified liver on a chip system populated by liver organoids and co-cultured with non-parenchymal cells, similar to the early intestinal organoid populated organ-on-a-chip devices recently developed, which have recapitulated important structural features and functions of the native duodenum (Workman *et al* 2017; Kasendra *et al* 2018). Zonal inter-hepatic heterogeneity of the model may be controlled by applying an oxygen gradient across the hepatic cell population. Other considerations include assembly on a matrix that accurately models composition of the *in vivo* ECM for increased *in vivo*-like cell-ECM interactions. This

would be similar to the bioprinted liver lobules created by Grix and colleagues, whereby populated HepaRG cells and human stellate cells had microchannel structures, which demonstrated flushing, higher levels of albumin and CYP450 gene expression, while maintaining overall metabolism (Grix *et al* 2018). Or the liver organoid-on-a-chip system by Wang and colleagues who combine a perfusable organ on a chip system with hiPSC derived liver organoids which demonstrated improved cell viability and higher expression of mature hepatic genes and endodermal genes (Wang *et al* 2018).

1.7.16 *In Vitro* Models of the Liver Conclusion

In vitro models of liver disease represent an exciting opportunity to better understanding liver homeostasis, response to injury and cancer development. Conventional methods that use 2D primary human hepatocytes and immortalised cell lines or 3D Organ Explant/PCTS have progressed to using 3D Organ-on-a-chip and Organoid models with microfluidics and appropriate co-cultures in which the complex cellular heterogeneity of the originating organ is recapitulated *ex vivo*. Although well characterised immortalised cell lines will remain relevant for studying highly conserved cellular processes and interactions, but they cannot be regarded as completely accurate models of liver biology *in vivo*. It is also possible that in the future as methods become established and validated *in vitro* models of the liver will increase the efficacy of pre-clinical drug development leading to more therapies to treat liver disease, as well Tumour derived organoids may also play an essential role in fulfilling the promises of precision medicine, as a method of validating prospective drugs for individual patients.

CHAPTER 1 INTRODUCTION

1.8 Discussion and Conclusion

Chronic liver diseases are a significant cause of morbidity and mortality worldwide. Due to the canonical nature of chronic liver diseases a good strategy for reducing morbidity and mortality could be to inhibit the progression of liver injury to fibrosis and cirrhosis using a prophylactic drug (Figure 1.25). While preventing, treating and/or eliminating the risk factors of liver disease is an effective strategy for reducing morbidity and mortality, as discussed earlier a pathogenic fibrotic response can still lead to the progression of liver injury, hence treating at risk populations with an intervention that inhibits the development of fibrosis, would also prevent the development of cirrhosis and cancer. To develop this intervention, representative *in vitro* models of liver injury will need to be created to increase the efficacy of preclinical drug discovery.

Such a model would aim to represent the hepatic phenotype observed during liver injury, the intercellular interactions between liver inflammatory cells, hepatocytes, and HSCs, as well as HSC activation, and the TNF and TGF-β signalling pathways. Such a model would also need to satisfy the criteria of being able to minimalize experimental variables to effectively isolate different organ components or structures for study under well-controlled, reproducible, and easily assessed conditions. After assessing the different forms of *in vitro* liver models (Table 1.1) 3D liver organoids should satisfy most these criteria, while organoids are not populated with inflammatory cells or HSCs, they may be treated with inflammatory cytokines like TNF and TGF-β, while being co-cultured with an immortalised HSC cell line. This design should create a more representative *in vitro* models of liver injury, hence can be used to assess preclinical anti-fibrosis drugs.

This thesis aims to establish and describe a 3D Organoid cell culture model from mouse liver tissue, characterise the capacity these organoids to model liver characteristics *in vitro*, and use

this model for preclinical drug discovery of an anti-fibrosis drug. Novel methods for analysing

organoid ultrastructure using high resolution field emission electron microscopy has also been

described.
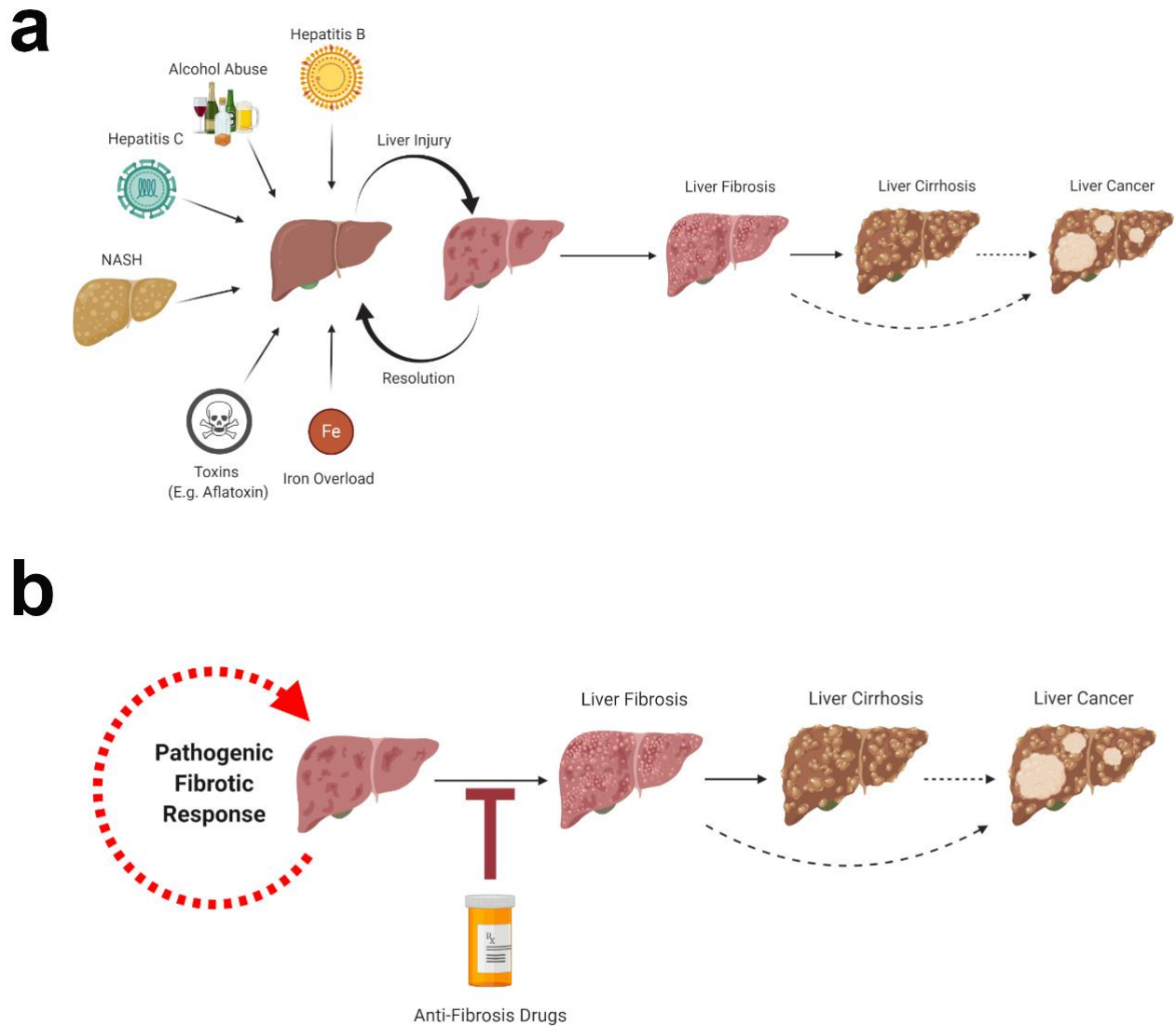
Figure 1.25 The Etiology of Liver Injury, Fibrosis, Cirrhosis and Cancer. a. Flow diagram illustrating the canonical process of chronic liver disease (timeline goes from left ot right), and the most important disease etiologies which contribute to liver disease. When liver injury and resolution is chronic it can progress to liver diseases like fibrosis, cirrhosis and liver cancer over time. **b.** Flow diagram illustrating that the pathogenic fibrotic response generated by the dysregulation of normal repair responses can still cause chronic liver disease even if the cause of the initial injury has been eliminated, hence the impetus to develop drugs that inhibit the pathogenic fibrotic response.

CHAPTER 1 INTRODUCTION

1.9 Hypotheses and Aims

1.9.1 Hypothesis

The hypothesis being tested in this thesis is that 3D mouse liver organoids cell cultures can accurately model mouse liver tissue *in vitro* and that these cultures can accurately model liver injury, fibrosis, and recovery response *in vitro*.

1.10 Aims

1. To test the first part of the stated hypothesis, the first aim is to establish a 3D Organoid cell culture model from mouse liver tissue (Chapter 3).

2. To test the first part of the stated hypothesis, the second aim is to characterise the capacity of organoids to model liver characteristics *in vitro*, assessing genetic, protein, functional and morphological markers (Chapter 3).

3. To test the second part of the states hypothesis the third aim is to model liver injury, fibrosis and recovery from liver injury and fibrosis using anti-fibrotic drugs *in vitro*, using a novel 3D organoid/HSC Co-culture (Chapter 4).

4. To test the second part of the states hypothesis the forth aim is to use transcriptional profiling to assess the gene expression of our organoid model as a model of liver injury *in vitro* (Chapter 5).

5. To test the whole of the stated hypothesis the fifth aim is to test the limitations of High Resolution field emission Scanning Electron Microscopy to characterise organoid Ultrastructure (Chapter 6).

CHAPTER 2

MATERIALS AND METHODS

CHAPTER 2 MATERIALS AND METHODS

2.1 Mouse Liver Tissue

Mouse liver tissues were collected from male C57Bl/6 mice, fed *ad libitum* on a chow diet between the ages of 3-12 months. Mice were euthanized using CO_2 asphyxiation in accordance with the UNSW Animal Care and Ethics Committee's guidelines (Ethics approval: 17/19A and 18/23A). The tissue was removed under sterile conditions and placed in ice cold Advanced Dulbecco's Modified Eagle Medium/Ham's F-12 (Gibco™ 12634010) with 1% 10,000 U/mL Penicillin-Streptomycin (Pen/Strep) (Gibco™ 15140122), 1% GlutaMAX™ Supplement (Gibco™ 35050061) and 10 mM 4-(2-Hydroxyethyl)piperazine-1-ethanesulfonic acid, N-(2-Hydroxyethyl)piperazine-N′-(2-ethanesulfonic acid) (HEPES) (SIGMA-ALDRICH H4034) (Basal Medium) for less than 1 hour before digestion.

2.2 Mouse Liver Tissue Digestion

Liver Tissue was finely cut into a pulpy mass using metal surgical scissors and straight metal tweezers in ice cold basal medium. The tissue was then washed 2 times with Dulbecco's Modified Eagle Medium (DMEM) (LONZA 12-604F), 1% Fetal Bovine Serum (FBS) (Cellsera Australia 10111112), and 1% Pen/Strep (Wash Medium) with 300 g of applied centrifugal force at 4 ^{O}C for 10 minutes to separate fluids and fat from the tissue.

Tissue was then digested using wash medium with 0.125 mg/mL Collagenase (SIGMA-ALDRICH C9407), 0.125 mg/mL Dispase II (Thermofisher 17105041) and 0.1 mg/mL DNase I (SIGMA-ALDRICH DN25) (Digestion Medium) at 37 ^{O}C for 1 hour with vigorous agitation. The tissue was then washed 2 times using ice cold wash medium and 300 g of applied centrifugal force at 4 ^{O}C for 10 minutes to remove the digestion medium. Tissue was then digested using TrypLE™ solution (Thermofisher 12605028) at 37 ^{O}C for 5 mins. The tissue

was then washed 2 times using ice cold wash medium and 300 g of applied centrifugal force at 4 ^{O}C for 10 minutes to remove the TrypLE™ solution. The tissue was then filtered through a 40 µm strainer and resuspended in ice cold wash medium with 10 µM of ROCK inhibitor Y-27632 dihydrochloride (Abcam 120129). The tissue had become a primary single cell culture ready for seeding.

2.3 Mouse Liver Primary Cell Culture Seeding with Isolation Medium for Organoid Generation

Wash medium with 10 µM Y-27632 dihydrochloride was removed using 300 g of applied centrifugal force at 4 ^{O}C for 10 minutes, and the primary cell culture was then resuspended at 5 x10^7 cells per mL in ice cold Cultrex® PathClear Reduced Growth Factor BME Type 2 (Cultrex®) (TREVIGEN® 3533-005-02). The primary cell culture was then carefully dropped 50 µL at a time into the centre of the wells of a 24 well cell culture plate (Greiner bio-one 662160), avoiding the sides of the wells. The primary cell culture was then incubated in a cell culture incubator for 10 mins at 37 ^{O}C with 5% CO_2.

After incubation the primary cell culture was treated with 500 µL per well of basal medium with 1:50 B27 MACS® NeuroBrew-21 w/o Vitamin A (Miltenyi Biotec 130-097-263), 1 mM N-acetylcysteine (SIGMA-ALDRICH A0737), 5% (vol/vol) Rspo1-conditioned medium (Custom: methods described in section 2.7, page 83), 10 mM nicotinamide (SIGMA-ALDRICH N0636), 10 nM recombinant human [Leu15]-gastrin I (SIGMA-ADRICH G9145), 50 ng/ml recombinant mouse EGF (PeproTech 315-09), 100 ng/ml recombinant human FGF10 (Peportech 100-26) and 50 ng/ml recombinant human HGF (PeproTech 100-39) (Expansion Medium), with the addition of 30% vol/vol Wnt-3a conditioned medium (Custom: methods described in section 2.8, page 84), 25 ng/mL Recombinant Human Noggin (PeproTech 120-

10C) and 10 µM Y-27632 dihydrochloride (Isolation Medium). The primary cell culture was then incubated for 3-4 days at 37 ^{O}C with 5% CO_2 until mouse liver organoids were visible using phase-contrast light microscopy.

2.4 Mouse Liver Organoid Expansion Cell Culture

After organoid isolation medium was replaced by expansion medium, the organoid cell cultures were incubated at 37 ^{O}C with 5% CO_2 with the expansion medium being changed every 2-3 days for 12 days. At this point the organoid cell cultures were passaged to increase organoid numbers. After the first passage organoids were treated with expansion medium every 2-3 days and passaged every 5-7 days (confluents dependent).

2.5 Passaging a Mouse Liver Organoid Cell Culture

To passage the organoid cell culture expansion medium was removed and replaced with ice cold basal medium. The Cultrex® was then disrupted using a pipette tip and the organoids were resuspended with ice cold basal medium and pooled together. Organoids were vortexed and subjected to 300 g of applied centrifugal force at 0 ^{O}C for 10 minutes to remove the Cultrex®, and the supernatant and the organoids were resuspended in ice cold basal medium. This step was repeated. After the Cultrex® was completely removed the organoids were broken apart be mechanical force using vigorous pipetting, Organoids were the vortexed and subjected to 300 g of applied centrifugal force at 4 ^{O}C for 10 minutes. The Supernatant was removed and the organoids were resuspended in ice cold Cultrex® and then carefully dropped 50 µL at a time into the centre of the wells of a 24 well cell culture plate avoiding the sides of the wells. The organoid cell culture was then incubated in a cell culture incubator for 10 mins at 37 ^{O}C with

5% CO_2. After incubation for 10 mins the organoid cell culture was treated with 500 µL per well of expansion medium and incubated at 37 ^{O}C with 5% CO_2.

2.6 Mouse Liver Organoid Differentiation Cell Culture

After passaging, the organoid cell cultures were incubated with expansion medium for 3 days which was then replaced with basal medium with 1:50 B27 MACS® NeuroBrew-21 w/o Vitamin A, 1 mM N-acetylcysteine, 5% (vol/vol) Rspo1-conditioned medium, 10 nM recombinant human [Leu15]-gastrin I, 50 ng/ml recombinant mouse EGF, 100 ng/ml recombinant human FGF10, 500 nM A83-01 (SIGMA-ALDRICH SML0788) and 10 µM DAPT (Abcam ab120633) (Differentiation Medium). The organoid cell culture was incubated at 37 ^{O}C at 5% CO_2 with the differentiation medium for 9 days, with the medium being changed every 24-48 hours. After 9 days the medium was replaced by Differentiation medium with 3 µM dexamethasone (SIGMA-ALDRICH D4902) with the medium being changed every 24 hours. At this point the mouse liver organoid cell culture was ready for analysis.

2.7 R-spondin-1 Conditioned Medium

R-pondin-1 conditioned medium was harvested from a 293T-HA-Rspo1-Fc cell line (Trevigen 3710-001-K) subcultured at 70% confluent in basal medium for 7 days at 37 ^{O}C with 5% CO_2, before being filter sterilised and stored at -20 ^{O}C until used.

CHAPTER 2 MATERIALS AND METHODS

2.8 Wnt3a Conditioned Medium

Wnt3a conditioned medium was harvested from a L Wnt-3A producing cell line (ATCC® CRL2647™) subcultured at 70% confluent in DMEM with 10% FBS and 1% Pen/Strep for 7 days at 37 ^{O}C with 5% CO_2, before being filter sterilised and stored at 4 ^{O}C until used.

2.9 Organoid/HSC Co-culture in Trans-well System for Modelling Liver Injury

Differentiated liver organoids were passaged and seeded into the polycarbonate membrane cell culture inserts of a Corning® Transwell® (SIGMA-ALDRICH CLS3421) and treated with 500 µL differentiation medium and incubated overnight at 37 ^{O}C with 5% CO_2. The C57Bl/6 male mouse HSC cell line JS1 (TLR4-/- Mouse Hepatic Stellate Cells Expressing WT TLR4) (Kerafast EMS404) (Guo *et al* 2009) was seeded at 50000 cells per well in the bottom of the transwell plate and treated separately with 500 µL differentiation medium and incubated overnight at 37 ^{O}C with 5% CO_2. The next day the differentiation medium was removed and transwell inserts were combined with seeded wells dependent on the experiment group and treated with 600 µL of differentiated medium for 48 hours at 37 ^{O}C with 5% CO_2. Depending on the experimental group the differentiated medium may have 50 ng/µL of TNF (Preprotech 300-01A), 10 ng/µL TGF-β (Preprotech 100-21) or 100 ng/µL Halofuginone hydrobromide (Tocris 1993). For the hypoxia experimental groups, the co-cultures were incubated for 48 hours at 1% O_2 at 37 ^{O}C with 5% CO_2, using a Heracell™ VIOS 160i CO_2 Incubator (Thermofisher 51030285).

CHAPTER 2 MATERIALS AND METHODS

2.10 Contrast Phase Microscopy

Contrast phase microscopy images were taken using an Inverted ECLIPSE TS100 Microscope (Nikon®), a DS-Fi2 5.24 megapixel camera (Nikon®) and a DS-L3 Camera Control Unit (Nikon®).

2.11 Live Cell Analysis

Live cell analysis was performed using an IncuCyte® ZOOM live-cell analysis system (Essen Bioscience 8000-0338-B00) mounted inside of a Forma™ Series II Water-Jacketed CO_2 Incubator (ThermoFisher 3111).

2.12 Hypoxia Treatment

Cell cultures were treated with 1% O_2 using a Heracell™ VIOS 160i CO_2 Incubator with variable oxygen control (tri-gas) (ThermoFisher 51030406), the rest of the time cell cultures were incubated in Heracell™ VIOS 160i CO_2 Incubators at 21% O_2 (ThermoFisher 51030285).

2.13 Mouse Primary Hepatocyte Extraction by Liver Pump Perfusion

A perfusion machine (GILSON®, MINIPULS 3) was loaded with Hank's Balanced Salt Solution (Sigma-Aldrich, 55021C) with a 26-gauge needle attached. Mouse euthanized and dissected inside a sterile biological hood with the liver still attached. The needle was inserted into the inferior vena cava toward the liver and Hank's Balanced Salt Solution perfused into the liver slowly. The portal vein was cut to release the pressure caused by the solution. 25 mL of Hank's Balanced Salt Solution was perfused through the liver. The perfusion solution was

then changed to Hank's Balanced Salt Solution with 0.5 mM EDTA (Vetec, V800170) for 25 mL, and then back to Hank's Balanced Salt Solution for 25 mL. The perfusion solution was then changed to Hank's Balanced Salt Solution with 0.5 mg/mL collagenase (Sigma-Aldrich C9407) and 5 mM $CaCl_2$ (Biochemicals, BIOCD0050) for 25 mL. The perfusion solution was then changed back to Hank's Balanced Salt Solution for 25 mL. At this point the liver was removed from the mouse body and placed in a petri dish with ice cold Advanced Dulbecco's Modified Eagle Medium/Ham's F-12 (Gibco™ 12634010), primary liver cells were scrapped off using a scalpel blade avoiding the ductal structure. Cell culture was filtered through a 70 µm strainer and spun at 500 g for 5 mins at 8 ^{O}C. Supernatant was removed and replaced with media for culturing or freezing down.

2.14 Cyto-spinning Cells

Ten mL cell suspensions were spun onto a 15 mm poly lysine coverslip using a custom plastic cell spin cartridge inside a 50 mL falcon tube. Tubes were spun at 400 g for 10 minutes at 4 ^{O}C.

2.15 RNA Phase Extraction

To extract RNA from the organoid cell culture using phase extraction; the culture medium was removed and replaced with ice cold basal medium. The Cultrex® was then disrupted using a pipette tip and the organoids were resuspended with ice cold basal medium and pooled together. Organoids were vortexed and subjected to 300 g of applied centrifugal force at 0 ^{O}C for 10 minutes to remove the Cultrex® and, the supernatant and the organoids were resuspended in ice cold basal medium. This step was repeated once. The samples were then subjected to 300 g of applied centrifugal force at 0 ^{O}C for 10 minutes, the basal medium was removed from the pellet.

The samples were then treated with 1 mL of RNAzol® RT (Sigma-Aldrich, R4533) and repeatedly pipetted until homogeneous. The samples were then topped up with 400 μL of MilliQ water, shaken vigorously for 15 seconds and left at room temperature for 10 minutes. The samples were subjected to 12000 g of applied centrifugal force at room temperature for 10 minutes, and the top clear aqueous phase of the samples was transferred to a fresh Eppendorf tube. These samples were treated with 1 mL of 100 % isopropanol (Sigma-Aldrich, I9516) and left at room temperature for 10 minutes. The samples were then subjected to 12000 g of applied centrifugal force at room temperature for 10 minutes. The supernatant was removed, samples were washed by adding 75 % ethanol (Sigma-Aldrich, E7023) to the samples, vortexing, and being subjected to 6000 g of applied centrifugal force at room temperature for 5 minutes. This RNA pellet washing step was repeated. The supernatant was removed and the pellet was allowed to air dry for 5 minutes before being resuspended in nuclease-free water (Sigma-Aldrich, W4502).

CHAPTER 2 MATERIALS AND METHODS

2.16 RNA Column Extraction

To extract RNA from cell culture including organoids using column extraction a RNeasy®
Mini Extraction kit (Qiagen, 74106) was used. The cell culture medium was removed, cells
were washed twice with ice cold PBS and lysed using 350 µL of Buffer RLT with 10 µL per
mL β-mercaptoethanol (Sigma- Aldrich M3148) and pipetting. Samples were transferred to a
1.5 mL Eppendorf tube, 350 µL of 70% ethanol (Sigma-Aldrich, E7023) was added to each
sample and mixed well by pipetting. Samples were then transferred to a RNeasy spin column
inside a 2 mL collection tube and subjected to 8000 g of applied centrifugal force at room
temperature for 15 seconds. The flow-through was then discarded. The samples within the
columns were washed with 700 µL of Buffer RW1 and subjected to 8000 g of applied
centrifugal force at room temperature for 15 seconds. The flow-through was then discarded.
The samples within the columns were then washed with 500 µL of Buffer RPE and subjected
to 8000 g of applied centrifugal force at room temperature for 2 minutes. The flow-through was
then discarded. The RNeasy column was then transferred to a new 1.5 mL collection tube. The
samples within the columns were then treated with 30 µL of RNase-free water and subjected
to 8000 g of applied centrifugal force at room temperature for 1 minute to elute the purified
RNA sample into the water.

2.17 RNA purity, Quantity, and Integrity Analysis

RNA purity and concentration were determined using a NanoDrop™ 2000 Spectrophotometer
(Thermo Scientific, ND-2000). RNA integrity was determined using a Qubit RNA IQ Assay
(Thermo Scientific, Q32856) and Qubit 4 Fluorometer (Thermo Scientific, Q33238).

CHAPTER 2 MATERIALS AND METHODS

2.18 cDNA Synthesis

Ten μL of 200 ng/ μL of RNA of each sample was treated with 1 μL of Random Hexamer (Life Tech, N8080127), 1 μL of 10 mM dNTP mix (Life Tech, 10297018) and incubated for 5 minutes at 65 ^{O}C followed by an incubation for 10 mins at 4 ^{O}C. Each sample was then treated with a 2 μl of MiliQ water, 4 μL of First-Strand buffer, 1 μL of 0.1 M DTT, and 1 μL of SuperScript™ III Reverse Transcriptase (RT) (Life Tech, 18080093). Each mixture was then incubated for 10 minutes at 4 ^{O}C, 5 minutes at 25 ^{O}C, 60 minutes at 50 ^{O}C, followed by inactivation of RT enzyme at 70 ^{O}C for 15 mins. The cDNA samples were then stored at 4 ^{O}C until used in downstream assays.

2.19 Real Time Quantitative Polymerase Chain Reaction Analysis using SYBR Green

Real time quantitative polymerase chain reaction (RT qPCR) to assess target gene expression in organoid samples were performed using a SensiFAST SYBR Lo-Rox kit (Bioline, 94005) and QuantStudio™ 12K Flex system (Applied Biosystems™, 4471087). Reaction set up was per supplier instructions, using 2 μL DNA template, 10 μL 2x SensiFAST, 6 μL MiliQ water and 2 μL of 10 μM target gene forward and reverse mixed primers per reaction. All reactions were performed in quadruplicates. One-step RT qPCR was performed with initial denaturation at 95 ^{O}C for 2 minutes, followed by 45 cycles of 95 ^{O}C for 5 seconds and 60 ^{O}C for 30 seconds. Thermo Fisher Connect^{TM} software was used for data analysis. The comparative C_T method was used, that is Ct values obtained from two different experimental RNA samples were directly normalized to a housekeeping gene and then compared. Then, the difference in the ΔCt values between the experimental and control samples $\Delta\Delta$Ct was calculated to assess the relative quantity of the genes of interest.

Gene Symbol	Function	Primers
Alb	Albumin Expression	Forward 5'- CTAGTTCGCTACACCCACAAAG- 3' Reverse 5' - GACAGATAGTCTTCCACACAAGG- 3'
Cyp3All	Cytochrome P450 3A11 Expression	Forward 5'-TGGTCAAACGCCTCTCCTTGCTG- 3' Reverse 5' -ACTGGGCCAAAATCCCGCCG- 3'
G6pc	Glucose-6-Phosphatase Expression	Forward 5'-GAATTACCAAGACTCCAGG- 3' Reverse 5' -TGAGACAATACTTCCGGAGG- 3'
ZO-1(Tjp1)	Zonula occludens-1 Expression	Forward 5'-ACGATCTCCTGACCAACGTT- 3' Reverse 5' -GCTTTGGGTGGATGATCGTC- 3'
Hnf4a	Hepatocyte Nuclear Factor 4 Alpha Expression	Forward 5'-TCTGTAAGCACTGACCTGGG- 3' Reverse 5' -CCACCCACTCTCCACATTCT- 3'
Tbx3	T-Box 3 Transcription Factor Expression	Forward 5'-ATGGAACCCGAAGAAGACGT- 3' Reverse 5' -CATTCGCCTTCCTGACTTCG- 3'
Fah	Fumarylacetoacetate Hydrolase Expression	Forward 5'-GGTGCCTGCAGACTCTTAGA- 3' Reverse 5' -TGGAAATGGGGATTGGCTCT- 3'
Mrp4 (Abbcc4)	Multidrug resistance-associated protein 4 Expression	Forward 5'-TCTTCTTCCCGTCAGCCATT- 3' Reverse 5' -TGTCTAGTGCCTTGTCCCAG- 3'
Lgr5	LGR5 expression	Forward 5'-GGAAATGCTTTGACACACATT- 3' Reverse 5' -GGAAGTCATCAAGGTTATAAT- 3'
Ck19	Cytokeratin 19 Expression	Forward 5'-GTCCTACAGATTGACAATGC- 3' Reverse 5' -CACGCTCTGGATCTGTGACA- 3'
Prom1	Prominin 1 Expression	Forward 5'-TCCTGGGACTGCTGTTCATT- 3' Reverse 5' -CCTTTGATCCGAGTCCTGGT- 3'
Sox9	SRY-box 9 Expression	Forward 5'-AGATAAGTTCCCCGTGTGCA- 3' Reverse 5' -TGACGTGTGGCTTGTTG- 3'
Ck7	Cytokeratin 7 Expression	Forward 5'-TTCCCCGAATCTTTGAGGCT- 3' Reverse 5' -TCTTCCACCACATCCTGCAT- 3'
Cd34	CD34 expression	Forward 5'-GCACAGAACTTCCCAGCAAA- 3' Reverse 5' -AGCAGAACTCCAGAGGTGAC- 3'
Hprt	Hypoxanthine Phosphoribosyltransferase 1 Expression	Forward 5'-AGGACCTCTCGAAGTGTTGG- 3' Reverse 5' -TTGCAGATTCAACTTGCGCT- 3'

Table 2.1 Primers for RT-qPCR Analysis.

2.20 RT-qPCR Analysis using Taqman Assay

Primer-probe detection RT qPCR was used to assess target gene expression in samples using Taqman® probes, a TaqMan™ Universal PCR Master Mix (Applied Biosystems™, 4305719) and QuantStudio™ 12K Flex system (Applied Biosystems™, 4471087). Reaction set up was per supplier instructions, using 2 µL cDNA template, 0.625 µL 20X TaqMan® Probe/primer, 3.625 µL Nuclease-free water and 6.25 µL TaqMan® Universal Master Mix. All reactions were performed in quadruplicates. RT qPCR was performed with initial hold at 50 ^{O}C for 2 mins, denaturation at 95 ^{O}C for 10 minutes, followed by 40 cycles of 95 ^{O}C for 15 seconds and 60 ^{O}C for 60 seconds. Thermo Fisher Connect^{TM} software was used for data analysis. The comparative C_T method was used, that is Ct values obtained from two different experimental RNA samples were directly normalized to a housekeeping gene and then compared. Then, the difference in the ΔCt values between the experimental and control samples $\Delta\Delta$Ct was calculated to assess the relative quantity of the genes of interest.

CHAPTER 2 MATERIALS AND METHODS

2.21 Openarray PCR analysis

cDNA samples for openarray analysis were diluted with Openarray PCR Master Mix (Thermofisher 4462159) in a 96-well plate. The 96-well plate was spun at 1000 rpm for 1 min at room temperature. These samples were then transferred to a 384-well plate, spun this time at 1000 rpm for 10 mins at room temperature. The 384-well plate was then place in the Accufill Robot machine (Thermofisher 4457243) for the samples to be loaded to an openarray chip. Samples were loaded and sealed inside openarray chip with immersion fluid, screwed tight to close and compressed as per manufacturer's instructions. qPCR reaction was initiation by a QuantStudio™ 12K Flex system (Applied Biosystems™, 4471087). RT qPCR was performed with initial hold at 50 ^{O}C for 2 mins, denaturation at 95 ^{O}C for 10 minutes, followed by 40 cycles of 95 ^{O}C for 15 seconds and 60 ^{O}C for 60 seconds. Results were exported into excel for analysis. The comparative C_T method was used, that is Ct values obtained from two different experimental RNA samples were directly normalized to a housekeeping gene and then compared. Then, the difference in the ΔCt values between the experimental and control samples $\Delta\Delta$Ct was calculated to assess the relative quantity of the genes of interest.

Gene Symbol	Gene Name	Assay ID
Col1a1	collagen, type I, alpha 1	Mm00801666_g1
Col4a1	collagen, type IV, alpha 1	Mm01210125_m1
Fn1	fibronectin, type I	Mm0125744_m1
Ctgf	connective tissue growth factor	Mm01192932_g1
Bsg	Basigin (CD147)	Mm01144228_g1
Hif1a	hypoxia inducible factor 1, alpha subunit	Mm00468869_m1
Mmp14	matrix metallopeptidase 14 (membrane-inserted)	Mm00485054_m1
Timp2	tissue inhibitor of metalloproteinase 2	Mm00441825_m1
Hprt	hypoxanthine guanine phosphoribosyl transferase	Mm01545399_m1

Table 2.2 Taqman® Gene Expression Assays for Openarray qPCR Analysis.

CHAPTER 2 MATERIALS AND METHODS

2.22 RNA Sequencing Analysis

Samples were sequenced using custom Multiplex bulk RNA sequencing developed by Dr. Trevor Wilson at the medical genomics facility of the Hudson Institute of Medical Research at Monash University, Melbourne, Australia.

RNA quality was assessed using the Agilent Bioanalyser and quantitated by Qubit (ThermoFisher Q32856) and high-quality samples selected for analysis. RNA-Seq libraries were prepared using a multiplex 3' capture method. Briefly, 20ng of total RNA from each sample was tagged with an 8 base sample index and a 10 base unique molecular identifier (UMI) during initial poly(A) priming and reverse transcription. Samples were then pooled and amplified using a template switching oligonucleotide. The Illumina P5 (5' AAT GAT ACG GCG ACC ACC GA 3') and P7 (5' CAA GCA GAA GAC GGC ATA CGA GAT 3') sequences were added by PCR and Nextera transposase, respectively. The library was designed so that the forward read (R1) utilizes a custom primer (5' GCC TGT CCG CGG AAG CAG TGG TAT CAA CGC AGA GTA C 3') to sequence directly into the index and then the 10 base UMI. The reverse read (R2) uses the standard Illumina R2 primer to sequence the cDNA in the sense direction for transcript identification. Sequencing was performed on the NextSeq550 (Illumina), using the V2.5 High output kit generating 2 paired reads per cluster (19 bp R1; 72 bp R2).

Bioinformatic analysis of the raw data was initially accomplished in R by A/Prof. David Powell using the custom pipeline developed at Monash Bioinformatics Platform of Monash University, Melbourne, Australia, and visualised using Degust. (degust.erc.monash.edu)

2.23 MTT Assay

Cell culture medium was removed, and organoids were washed with 500 µL of Phosphate-buffered saline (PBS). Each well was treated with 500 µl of 0.5 mg/mL MTT (4,5-Dimethylthiazol-2-yl)-2,5-Diphenyltetrazolium Bromide (Life Technologies Australia, M6494) in Basal medium for 1-4 hours, incubated at 37 ^{O}C with 5% CO_2. After incubation, the MTT medium was collected and the cells were treated with 500 µL of 40 mM HCl in 100% isopropanol (Fisher scientific, AC423830025) for 5 mins with gentle agitation at room temperature. One hundred µL of acid-isopropanol per sample was transferred to a 96 well plate and absorbance was measured at 562 nm wavelength using an optical SpectraMax M2e Microplate Reader (Molecular Devices, 12762).

2.24 CellTiter-Glo® 3D Cell Viability Assay

Organoid cell culture plates were removed from incubation and allowed to equilibrate at room temperature for 30 minutes. Cell culture medium was removed and organoids were washed with 500 µL of PBS. An equal volume of CellTiter-Glo® 3D Reagent (Promega, G7570) was added to all cell culture wells and mixed vigorously for 5 minutes to induce cell lysis. The plate was incubated at room temperate for 25 minutes and then the reagent was transferred to an opaque-walled 96 well plate for measuring luminescence using a SpectraMax M2e Microplate Reader (Molecular Devices, 12762).

2.25 Fixing Organoids for Immunolabelling

Organoids where fixed in 4% paraformaldehyde (PFA) (ELECTRON MICROSCOPY SCIENCES 15710) (pH 7.4) with ice cold PBS (SIGMA-ALDRICH P4417) for 30 mins on ice. Fixative was then removed, and the organoids were resuspended in ice cold PBS and kept at 4 ^{O}C until they were used for clearing.

2.26 Tissue Clearing

For clearing organoids PBS was removed and the organoids were resuspended in Modifed ScaleCUBIC-1 Reagent-1A (Custom) made from PBS with 10% Triton X-100 (SIGMA-ALDRICH T8787), 5% NNNN-tetrakis(2- hydroxypropyl)ethylenediamine (SIGMA-ALDRICH 87640), 10% Urea (SIGMA-ALDRICH U5378), and 25 mM NaCl (SIGMA-ALDRICH S6546) for 24 hours at 4 ^{O}C. Then the Modifed ScaleCUBIC-1 Reagent-1A was removed and the organoids were resuspended in ice cold PBS and kept at 4 ^{O}C until they were used for immunofluorescent staining.

Alternatively, for clearing organoids the PBS was removing and the organoids were resuspended in Fructose–glycerol clearing solution (Custom) made from 60% Glycerol (SIGMA G5516) and 2.5 M D-(-)-Fructose (SIGMA F0127), for 20 mins at room temperature before being resuspended in PBS.

CHAPTER 2 MATERIALS AND METHODS

2.27 Immunolabelling of Organoids

For primary antibody staining organoids where incubated for blocking in PBS with 1% Bovine serum albumin (BSA) (SIGMA-ALDRICH A3059), 1% DMSO (SIGMA-ALDRICH D8418), 1% Triton X-100 (SIGMA-ALDRICH T8787) and 1% secondary antibody animal serum (when a secondary antibody is required) (PBSDT) for 3 hours at room temperature with gentle agitation. PBSDT was removed and the samples were resuspended with primary antibodies solution diluted with PBSDT as described (Table. 2.3). Incubation with primary antibodies was performed for 48 hours at 4 ^{O}C with light protection and gentle agitation. Primary antibody solution was removed and the organoids were resuspended in PBS with 0.1% BSA and 1% Triton X-100 (Wash solution). Organoids were gently inverted 10 times and allowed to settle under gravity on ice for 10 mins, the wash solution was then removed. This step was then repeated another 7 times. Organoids were then resuspended in ice cold PBS and ready for secondary staining or immunofluorescent analysis.

For Organoids that required secondary staining, they were incubated with a secondary antibody solution diluted 1:250 in PBS with 0.1% BSA (PBSB) for at least 2 hours at room temperature with gentle agitation and light protection. Secondary antibody solution was removed and the organoids were resuspended in wash solution. Organoids were gently inverted 10 times and allowed to settle under gravity on ice for 10 mins, wash solution was then removed. This step was then repeated another 7 times. Organoids were then resuspended in ice cold PBS and were ready for DNA staining or immunofluorescent analysis.

CHAPTER 2 MATERIALS AND METHODS

2.28 DNA Staining of Organoids

For Organoids that required DNA staining, samples were incubated with 10 mg/ mL Hoechst dye 33342 (ThermoFisher H3570) diluted 1:2000 in PBS for 15 minutes at room temperature with gentle agitation and light protection. The supernatant was then removed and the Organoids were resuspended in PBS and were ready for immunofluorescent analysis.

2.29 Whole Mounting Organoids for Analysis

For 2D immunofluorescent analysis organoids require whole mounting. Whole mounting was achieved by very thinly and evenly coating grease (Eppendorf 5810 350.050-01) using rubber gloves and Kimwipes (Kimberly Clark Professional 34120) on to Superfrost Plus™ Adhesion microscope slides (ThermoFisher J1800AMNT), and dropping the organoids in suspension into the slide with a PBSB coated transfer pipette. Organoids were allowed to settle for 10 minutes and then the PBS was carefully removed. A Menzel™ microscope coverslip (ThermoFisher 11911998) was then placed on top of the slides and the organoids were ready for confocal laser scanning microscope.

For 3D Z-stack immunofluorescent analysis the samples were transferred to the wells of a glass bottom CELLVIEW Cell Culture Slide (Greiner bio-one, 543079) using a PBSB coasted transfer pipette and suspended in PBS with the slide's lid removed, ready for confocal laser scanning microscope.

CHAPTER 2 MATERIALS AND METHODS

2.30 Immunolabelling of Adherent Cells

Adherent Cells were prepared for immunolabelling by removing all cell culture medium from the dish and washed gently with PBS before fixing with 4 % PFA (pH 7.4) for 10 mins at 37 ^{O}C. The PFA solution was then removed and the adherent cells were gently washed 3 times with PBS. Adherent cells were permeabilized with 0.1 % Triton X-100 in PBS (PBS-T) for 15 minutes at room temperature. The PBS-T was removed and the adherent cells were gently washed with PBS 3 times. Blocking was achieved by incubating the adherent cells with 2% BSA in PBS for 60 minutes. Blocking solution was removed and the adherent cells were stained with the primary antibody solution, at the correct dilution in PBSB with gentle agitation, for 3 hours at room temperature, or overnight at 4 ^{O}C.

Primary staining solution was removed and adherent cells were washed gently 3 times with PBS. Adherent cells were then stained if necessary with secondary fluorescent antibodies at the desired concentration and Hoechst dye 33342 in PBSB for 45 minutes at room temperature with light protection. These cells were then washed 3 times with PBS-T before being treated with PBS and stored for imaging at 4 ^{O}C.

CHAPTER 2 MATERIALS AND METHODS

2.31 Confocal Laser Scanning Microscope

An LSM 800 with Airyscan system (ZEISS) confocal microscope was used for confocal images with the ZEN Imaging Software version 2.3. The laser excitations lines used were 350, 546, 594 and 647 nm. The objective lens of 10x (Numerical Aperture 0.3) and 20x (Numerical Aperture 0.5) and 40X (Numerical Aperture 0.8) (with oil immersion). Images were acquired using sequential scanning, between laser excitations lines to avoid cross-talk or bleed-trough between fluorophores. Z-stack images were obtained at optimal intervals recommended by the ZEN Imaging Software and reconstructed to form three-dimensional projections before being processed by Airyscanning. The Samples were then analysed using the ZEN Black software version 2.3.

2.32 Light-Sheet Microscopy

A Lightsheet Z.1 system (ZEISS) microscope was used for light-sheet imaging. Organoids were suspended in 1% Agarose heated to 60^OC, before being placed within a glass capillary and air cooled to room temperature. The organoids were held in place within the observation chamber of the Lightsheet Z.1 system and immersed in PBS. The Samples were then imaged and analysed using the ZEN Black software version 2.3.

Marker	Structures	Antibody	Application	Dilution
ALB	Functioning Hepatocytes	Rabbit polyclonal to Anti-mouse serum Albumin (Abcam, ab19196)	IF	1:400
SOX9	Progenitor liver nucleus	Rabbit Polyclonal Anti-mouse Transcription Factor Sox-9 (Sigma-Aldrich AB5535)	IF	1:250
CYP450 1A2	Functioning Hepatocytes	Mouse Monoclonal Anti-Mouse Cytochrome P450 1A2 (Abcam ab22717)	IF	1:1000
ZO-1	Hepatocyte tight junctions	Rabbit polyclonal Anti-Mouse ZO1 tight junction protein (Abcam ab216880)	IF	1:1000
CK19	Hepatic Progenitor cell	Rabbit polyclonal to Anti-mouse CK19 (Abcam ab7755)	IF	1:1000
EpCAM	Ductal cells	Goat polyclonal Anti-mouse EpCAM (Santa Cruz sc-23788)	IF	1:50
LGR5	Progenitor cells, Wnt signalling protein	Conjugated VioBright FITC Anti-mouse LGR5 (Miltenyi Biotec 130-111-393)	IF	1:500
		Conjugated APC Anti-mouse LGR5 (Miltenyi Biotec 130-111-390)	FACS	1:500
HNF4α	Functioning Hepatocytes nucleus	Mouse monoclonal Anti-mouse HNF4α (Abcam ab41898)	IF	1:1000
αSMA	Actin in Smooth Muscle	Rabbit monoclonal Anti-mouse αSMA (Abcam 32575)	IF	1:1000
Col I	Collagen I	Rabbit polyclonal to Collagen I (Abcam 21286)	IF	1:1000

Table 2.3 Primary Antibodies for Staining. ALB=albumin, IF=immunofluorescence, SOX9=SRY (sex determining region Y)-box 9, CYP450= cytochrome P450, ZO-1= zonula occludens-1, CK=cytokeratin, EpCAM= epithelial cell adhesion molecule, LGR5= leucine-rich repeat-containing G-protein coupled receptor 5, Wnt=wingless/integrated, FITC=fluorescein isothiocyanate, APC= allophycocyanin, FACS=fluorescence-activated cell sorting, HNF4α= hepatocyte nuclear factor 4 alpha, αSMA=alpha smooth muscle actin.

Antibody	Dilution
Alexa Fluor® 546 Goat anti-mouse IgG (Invitrogen A-11003)	1:250
Alexa Fluor® 594 Goat anti-rabbit IgG (Invitrogen A-11037)	1:250
Alexa Fluor® 647 Rabbit anti-goat IgG (Invitrogen A-21446)	1:250

Table 2.4 Secondary Antibodies for Staining. IgG=immunoglobulin G

CHAPTER 2 MATERIALS AND METHODS

2.33 Organoid Topographical High Resolution Field Emission Scanning Electron Microscopy Imaging

Organoids were removed from Cultrex using ice cold wash medium. Organoids were washed multiple times to remove all remaining Cultrex that had adhered to the samples. Organoids were then washed once with ice cold PBS and kept on ice. In the fume hood organoids were treated with Karnovsky's fixative, which is made up of 2.5% Glutaraldehyde (Sigma-Aldrich, 340855), 2% paraformaldehyde (Sigma-Aldrich 158127), 0.1 M Sodium Cacodylate (Sigma-Aldrich C0250) and distilled water (pH 7.4), and fixed overnight at 4 ^{O}C.

In the fume hood the fixative was removed and the samples were washed 4 times with molecular grade water. After the samples are sufficiently clean, each sample was dehydrated with 50% ethanol (Sigma-Aldrich, E7023) for 10 mins, 70% ethanol for 10 mins, 95% ethanol for 10 mins, 100% ethanol for 10 mins and 100% ethanol for 15 mins. Ethanol was then removed from the samples and each sample was washed with 100% acetone (Sigma-Aldrich, 179973) for 10 minutes, then again for 15 minutes and again for 20 mins. Samples were then mounted on glass microscopy slides and allowed to air dry for at least 1 hour.

Organoids were then carbon coated using an Automatic SEM Carbon Coater (Agar Scientific, UK) and the entire surface of the organoids was imaged using a GeminiSEM 300 (Zeiss) Field Emission Scanning Electron Microscope at 2 kV at a working distance of 2 mm using the Inlens detector. Pre-checked imaging conditions were optimised in order to maximise brightness and contrast and avoid astigmatism for each section.

CHAPTER 2 MATERIALS AND METHODS

2.34 Organoid Ultrastructure Sub-Nanometre Field Emission Scanning Electron Microscopy Imaging

Organoids were removed from Cultrex using ice cold wash medium. Organoids were washed multiple times to remove all remaining Cultrex that had adhered to the samples. Organoids were then washed once with ice cold PBS and kept on ice. In the fume hood organoids were treated with Karnovsky's fixative overnight at 4 ^{O}C.

After fixation the samples are rinsed with Sodium Cacodylate buffer, which is made of 0.1 M Sodium cacodylate (Sigma-Aldrich C0250), 0.1 % calcium chloride, 3 % HCl (pH 7.4) in distilled water, for 1 hour and again for 20 mins. Samples are then treated with 2% osmium tetroxide for 4 hours, 2% uranyl acetate for 1 hour, Sodium Acetate for 1 hour, and then dehydrated with 50% ethanol for 10 mins, 70% ethanol for 10 mins, 95% ethanol for 10 mins, 100% ethanol for 10 mins, 100% ethanol for 20 mins and two treatments of 100% Acetone for 15 mins.

Samples were then treated with Spurr low viscosity epoxy resin 1:1 (Sigma-Aldrich EM0300) with Acetone for 30 mins. Samples were then treated with Spurr low viscosity epoxy resin 6:1 with Acetone for 22 hours. Samples were finally treated with 100% Spurr low viscosity epoxy resin for 60 mins before being cured at 70°C for 15 hours.

For sub-nanometer field emission scanning electron microscopy, 120-250 nm thick sections were cut with an Ultramicrotome (RMC Boeckeler) fitted with an Ultra 45° diamond knife (Diatome) and mounted on silicon wafer substrate. The samples were carbon coated using an Automatic SEM Carbon Coater (Agar Scientific, AGB7367A). Acquisition of 2D large area electron microscope images of the resin sections were performed using Atlas 5.2 in tile scan mode attached to the GeminiSEM 300 (Zeiss) equipped with field emission gun. The Atlas system was used to control automated and pre-defined image acquisition, tiling, image-

stitching and shade correction. Images were obtained using the angular selective backscattered detector (AsB) at 10 kV at a working distance of 3.5 mm. All images have been inverted to give a TEM-like appearance. Pre-checked imaging conditions were optimised in order to maximise brightness and contrast and avoid astigmatism for each image.

CHAPTER 3

CHARACRTERISATION OF MOUSE LIVER ORGANOIDS

CHAPTER 3

CHARACTERISATION OF MOUSE LIVER ORGANOIDS

KEY FINDINGS

1. Ductal structures and single cells expanded into organoids in cell culture over the expected timeframe.

2. These organoids displayed self-folding, budding and expansion.

3. Gene expression analysis showed a shift in expression characteristic from a liver stem-like phenotype to a differentiated hepatocyte phenotype.

4. Analysis of protein expression relieved a general change in cell phenotypes characteristic of transitioning from a stem-like phenotype to a hepatic phenotype.

5. Using immunolabeling we were able to observe the variation in cell type within the organoids.

6. The organoids that were crated appeared to accurately model the morphological, gene expression and protein characteristics of mouse liver tissue *in vitro*.

CHAPTER 3 CHARACTERISATION OF MOUSE LIVER ORGANOIDS

3.1 BACKGROUND

The widespread implementation of organoid-based technologies across academia and industry is a testament to their importance as near-physiological models for use in both basic and translational research. Organoids have been successfully generated from many regions of the mouse gastrointestinal tract, ranging from the tongue to the colon, achieved through the understanding of stem cell fate initiation and cellular differentiation (Fatehullah *et al* 2016). In the laboratory, initiating stem cells to generate organoids requires a wide array of different niche and differentiation factors, while the cells are seeded in a rich ECM scaffold (Summarised in Figure 3.1).

Adult hepatocytes and cholangiocytes are the two endodermal-derived cell types in the adult liver, yet the organ is composed of mesoderm-derived hepatic mesenchymal cells (Lancaster and Huch 2019). The liver develops from a population of endodermal progenitors and the genes and molecular pathways regulating embryonic development of the liver are evolutionarily conserved among all vertebrates studied. These include the FGF, HGF, Wnt, bone morphogenetic protein (BMP), Retinoic Acid and TGFβ pathways that promote progenitor proliferation, migration, and survival (Broutier *et al* 2016).

As described in chapter 1 single Lgr5$^+$ cells from damaged mouse liver tissues can be clonally expanded into organoids in Rspo1-based culture medium over several months. Huch and colleagues found that following acute injury pathways involved in bile duct and islet formation/regeneration, facultative stem cells were reactivated, facilitating the identification of the adult stem cell pool (Huch *et al* 2013). Liver bile duct fragments plated into Matrigel® and supplemented with EGF, R-spondin, HGF, FGF10 and nicotinamide generated cystic organoids. These organoids contained cells expressing biliary ductal markers, which could be differentiated into a functional hepatocyte lineage by the inhibition of the Notch and TGF-β

signalling pathways (Huch *et al* 2013; Fatehullah *et al* 2016). It was previously shown that primary liver cells could be maintained in culture in the presence of EGF, HGF and the corticoid dexamethasone. However, these conditions did not allow the long-term expansion of liver progenitors (Broutier *et al* 2016). Combining their knowledge from developmental studies, and their own expertise in stem cell cultures from the small intestine and stomach, Huch and colleagues defined, for the first time, culture conditions for the expansion and differentiation of the mouse and human adult primary liver cell (Huch *et al* 2013; Broutier *et al* 2016).

The aim of the studies described in this chapter were to establish a 3D Organoid cell culture model from mouse liver tissue, characterise the capacity these organoids to model liver characteristics *in vitro*, assessing gene expression, protein and morphological markers. In this chapter we hypothesised that the methods developed by Huch and colleagues (Broutier *et al* 2016) would generate differentiated mouse liver organoids and that these organoids accurately model mouse liver tissue *in vitro*.

3.1.1 METHODS

These organoids were characterised using the appropriate methods described in chapter 2, to corroborate the results described by Broutier *et al* 2016, so that we known the results for modelling liver injury, fibrosis, and recovery in later chapters are valid. Characterisation also gives the opportunity to innovate different forms of analysis.
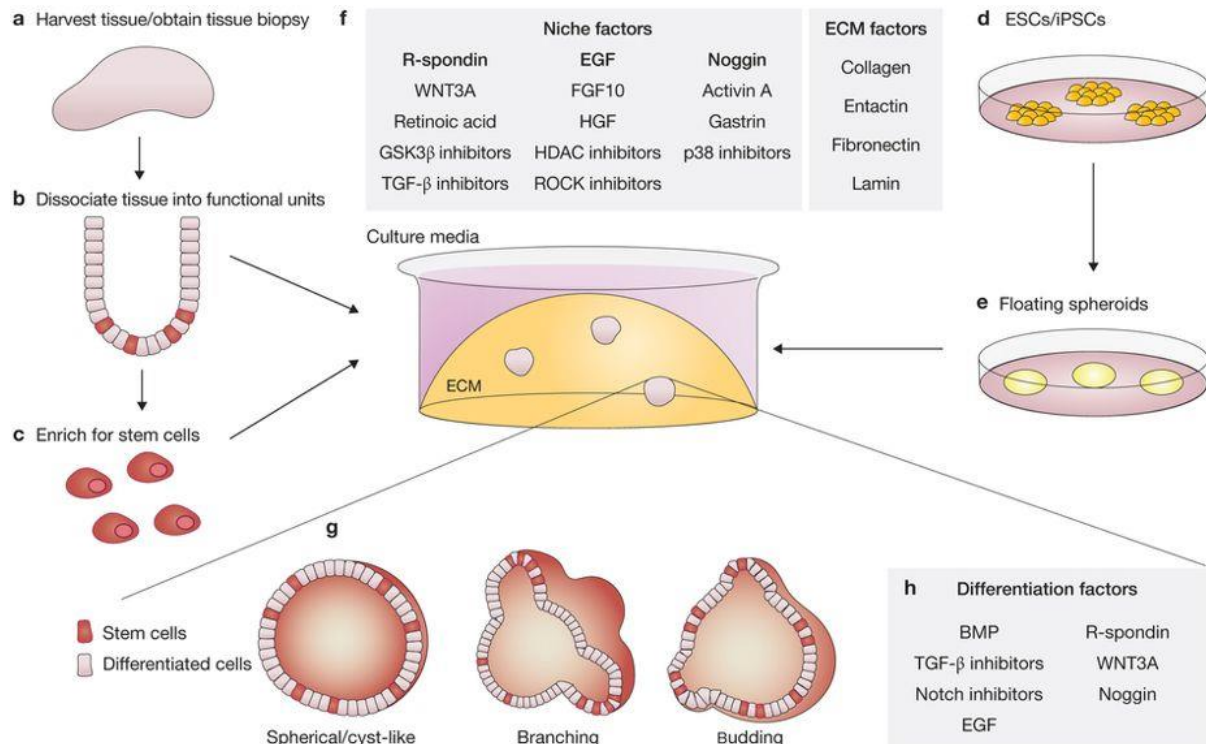
Figure 3.1 Organoid Generation and Culture from Primary Tissue and ESCs/iPSCs. a.
Organoids can be generated from primary tissue that are dissociated into functional sub-tissue
units containing stem cells **b**. These are further digested into single cells and FACS sorted to
enrich for stem cells **c.** Both the functional units and single stem cells can give rise to organoids
under the appropriate culture conditions. **d and e.** Organoids derived from ESCs and iPSCs. **d.**
undergo directed differentiation towards the desired germ lineage, eventually generating
floating spheroids. **e.** that are subsequently embedded in ECM to initiate organoid culture.
Organoids are typically cultured in an ECM surrounded by culture media supplemented with
niche factors specific to the organoid type. **f.** Common niche and ECM factors are listed,
including factors constituting the 'R-spondin method' **g.** Stem cells are maintained and
perpetuated in organoids, continually giving rise to differentiated progeny. Typical
morphologies are classified as spherical, branching or budding. **h.** Organoids can either
differentiate spontaneously or be induced to differentiate towards desired lineages or cell types

by adding suitable differentiation factors (a, b and c) and/or withdrawing factors that promote

stemness (d and e) (Fatehullah *et al* 2016).
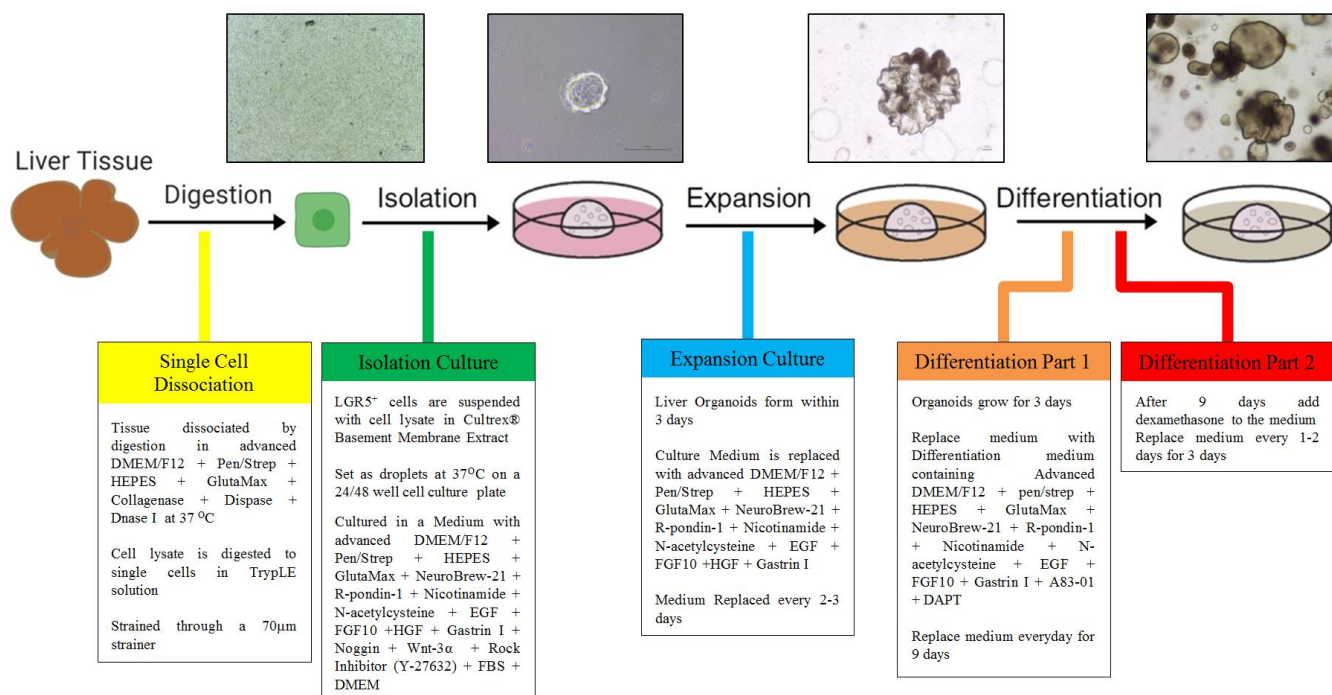
Figure 3.2 Visual Summary of the Steps to Generate Primary Mouse Liver Organoids.

Flow diagram of the methods for mouse liver organoid generation from chapter 2, to be used as a reference when describing the results of this chapter. The steps of mouse liver organoid generation are Digestion, Isolation, Expansion and Differentiation. Each step is labelled with a short description box.

3.2 RESULTS

The methods described in chapter 2 of mouse tissue collection, digestion, cell isolation, organoid expansion, passaging, and differentiation were used to generate mouse liver organoids. These methods were also used to generate undifferentiated organoids as a negative control to measure relative genes and protein expression; that is organoid exposed to expansion medium and then instead of being exposed to the differentiation medium was cultured over the same duration of time in expansion medium. For some forms of analysis primary liver tissue or extracted primary hepatocytes were also used as negative controls.

Morphology was observed using contrast phase microscopy, live-cell analysis, confocal laser scanning microscopy and light-sheet microscopy. Electron microscopy was also using to observe organoid topology and ultrastructure, and this led to the development of novel methods and results which are described in chapter 6.

Gene expression was measured using RT-qPCR analysis using SYBR Green. Protein expression was measured by comparing the relative total fluorescent intensity of immunolabelled organoids using confocal laser scanning microscopy.

3.2.1 Contrast Phase Microscopy Analysis
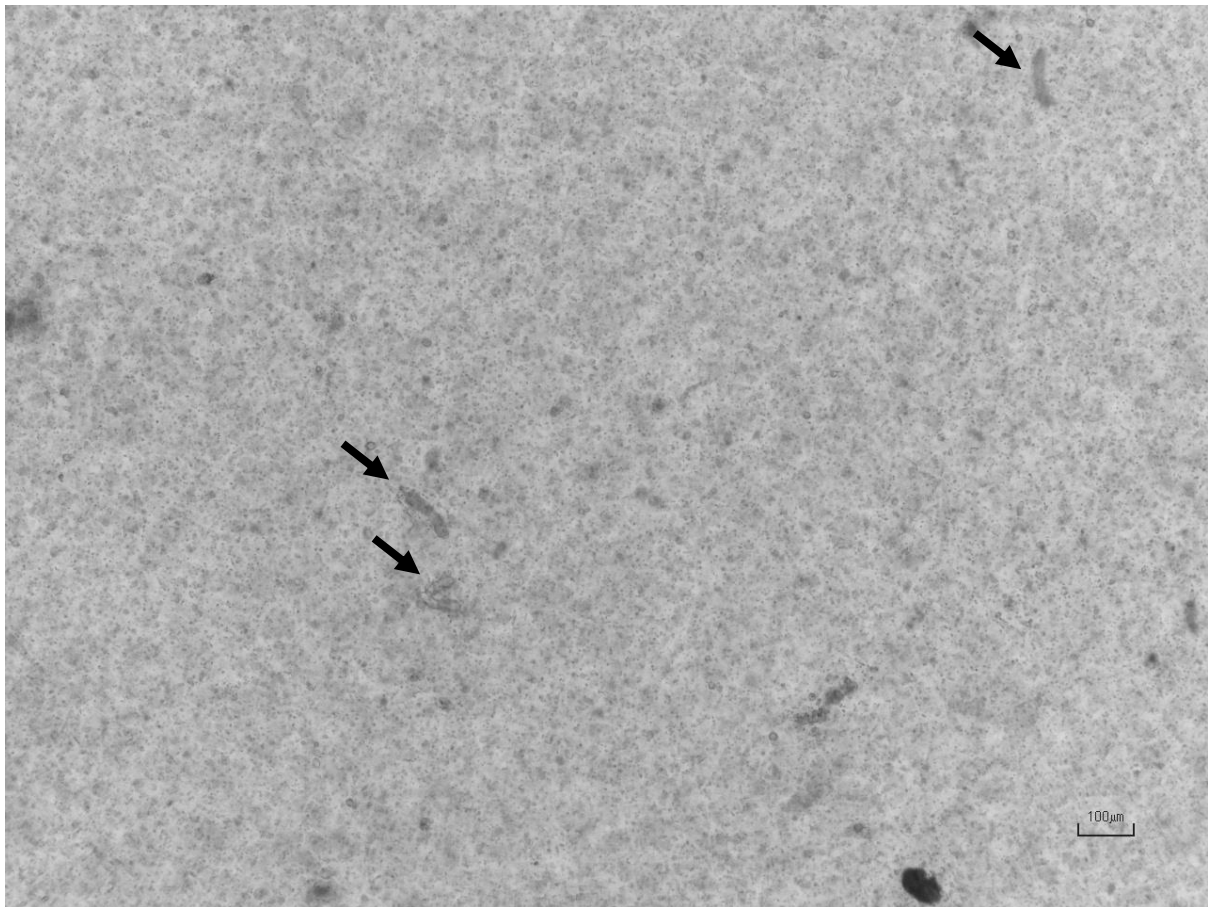
Figure 3.3 Day 0 Mouse Liver Lysate in Cultrex® with Isolation Medium. Ductal Structures

digested from the liver (arrows) in an even lysate of primary liver cells. Imaged with contrast

phase microscopy, recoloured in greyscale (4X objectification) (Scale=100 μm).
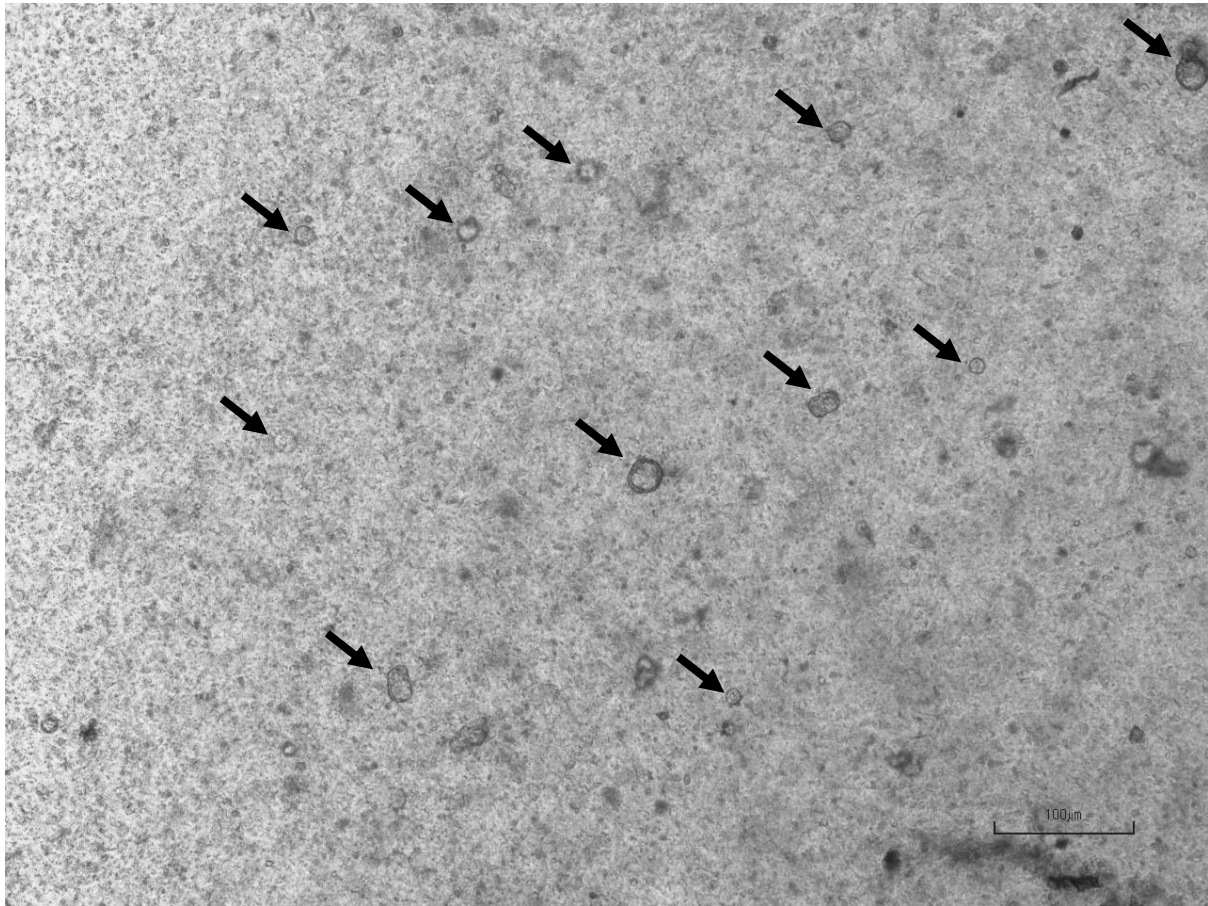
Figure 3.4 Day 4 Mouse Liver Organoid Generation. Ductal structures and single progenitor cells divide into small spherical organoids (arrows) approximately 10-20 µm in diameter after 4 days in Cultrex® with isolation medium. Imaged with contrast phase microscopy, recoloured in greyscale (10X objectification) (Scale=100 μm).
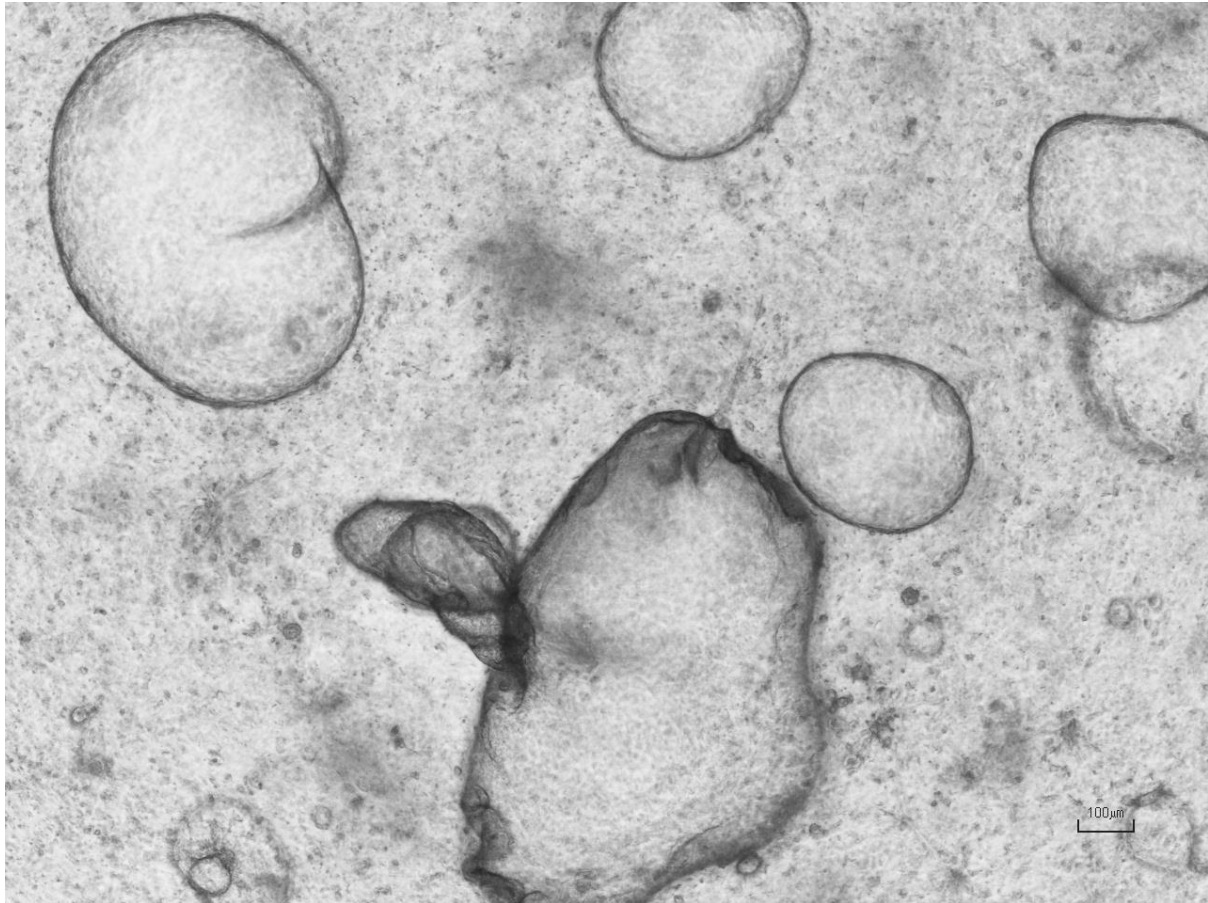
Figure 3.5 Day 8 Mouse Liver Organoid Expansion. Organoids expanded to full size between 100-1000 µm in expansion medium. Organoid size over the same duration appears to vary significantly. Organoids remain spherical/cyst-like especially the smaller organoids under 300 µm. Imaged with contrast phase microscopy, recoloured with greyscale (4X objectification) (Scale=100 µm).
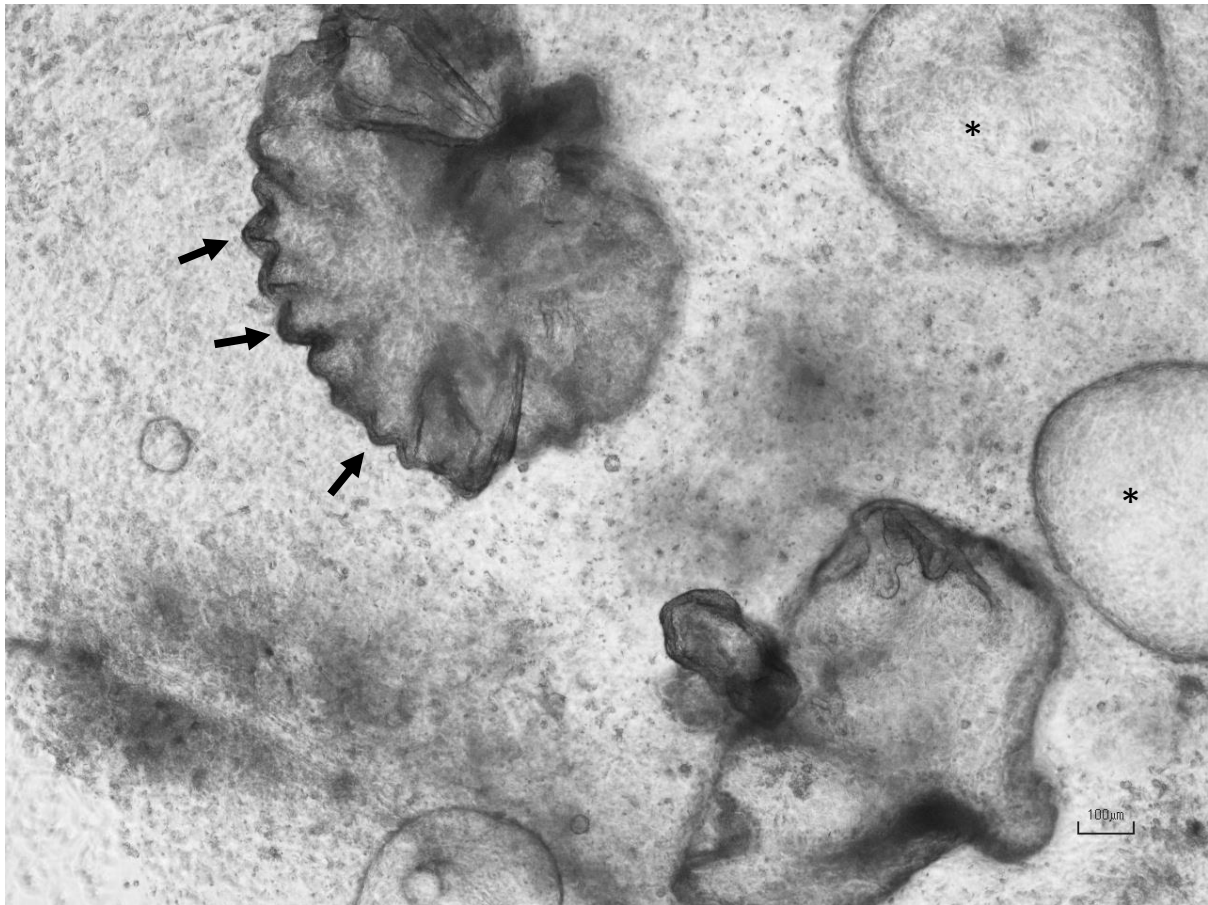
Figure 3.6 Day 11 Mouse Liver Organoid Expansion. Some larger organoids (>300 μm) spontaneously fold in on themselves (Arrow) or retain spherical/cyst-like morphology (Asterisk). Imaged with contrast phase microscopy, recoloured with greyscale (4X objectification) (Scale=100 μm).

Figure 3.7 Day 18, Passage 1 and 3 Days of Mouse Liver Organoid Expansion. Mouse liver organoid reform into within 24 hours of mechanical passaging in expansion medium, significant amount of primary single cells and debris appear to be removed during the passaging process. Some organoids spontaneously branch or bud (arrows). Imaged with contrast phase microscopy, recoloured with greyscale (10X objectification) (Scale=100 μm).
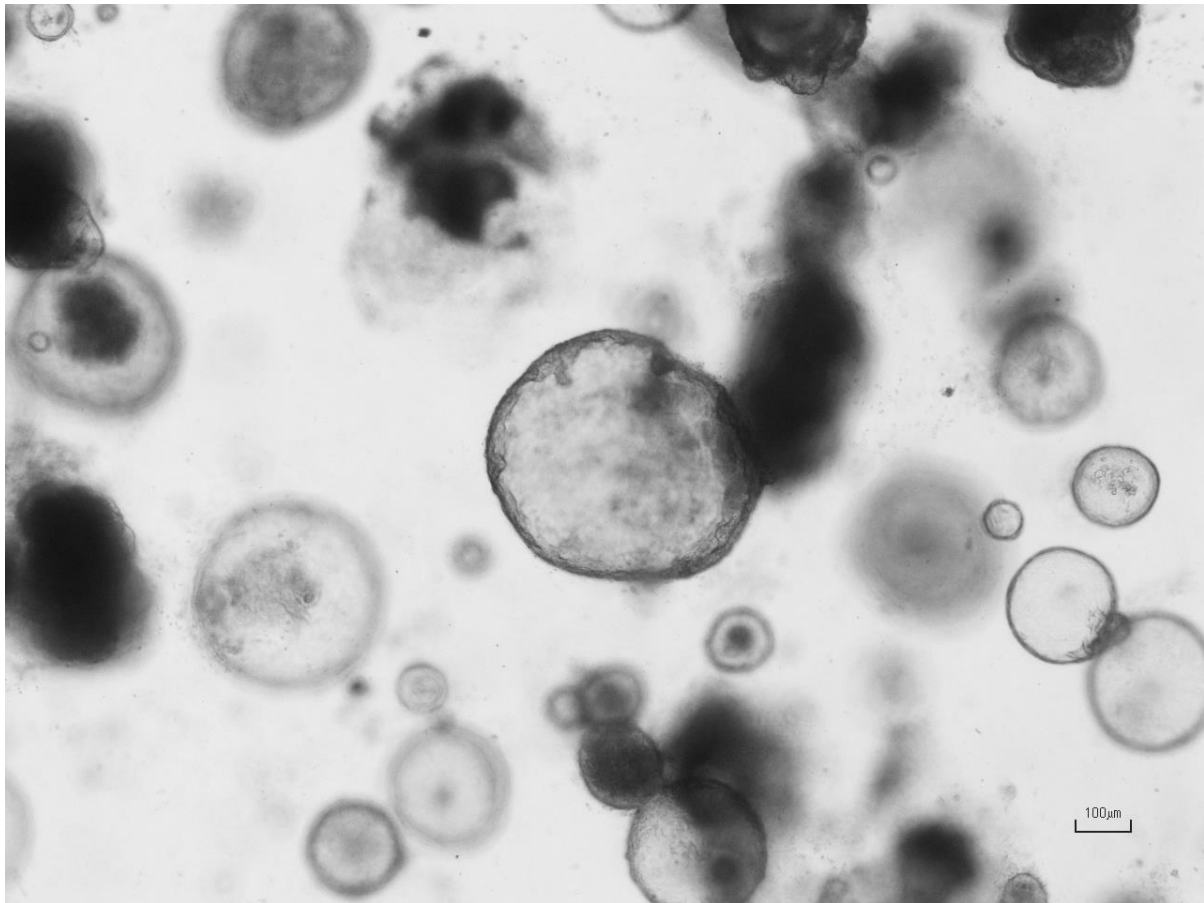
Figure 3.8 Day 30, Passage 1 and 12 Days of Mouse Liver Organoid Differentiation.
Mouse liver organoids display little change in observable morphology by differentiation
medium. Imaged with contrast phase microscopy, recoloured with greyscale (4X
objectification) (Scale=100 μm).
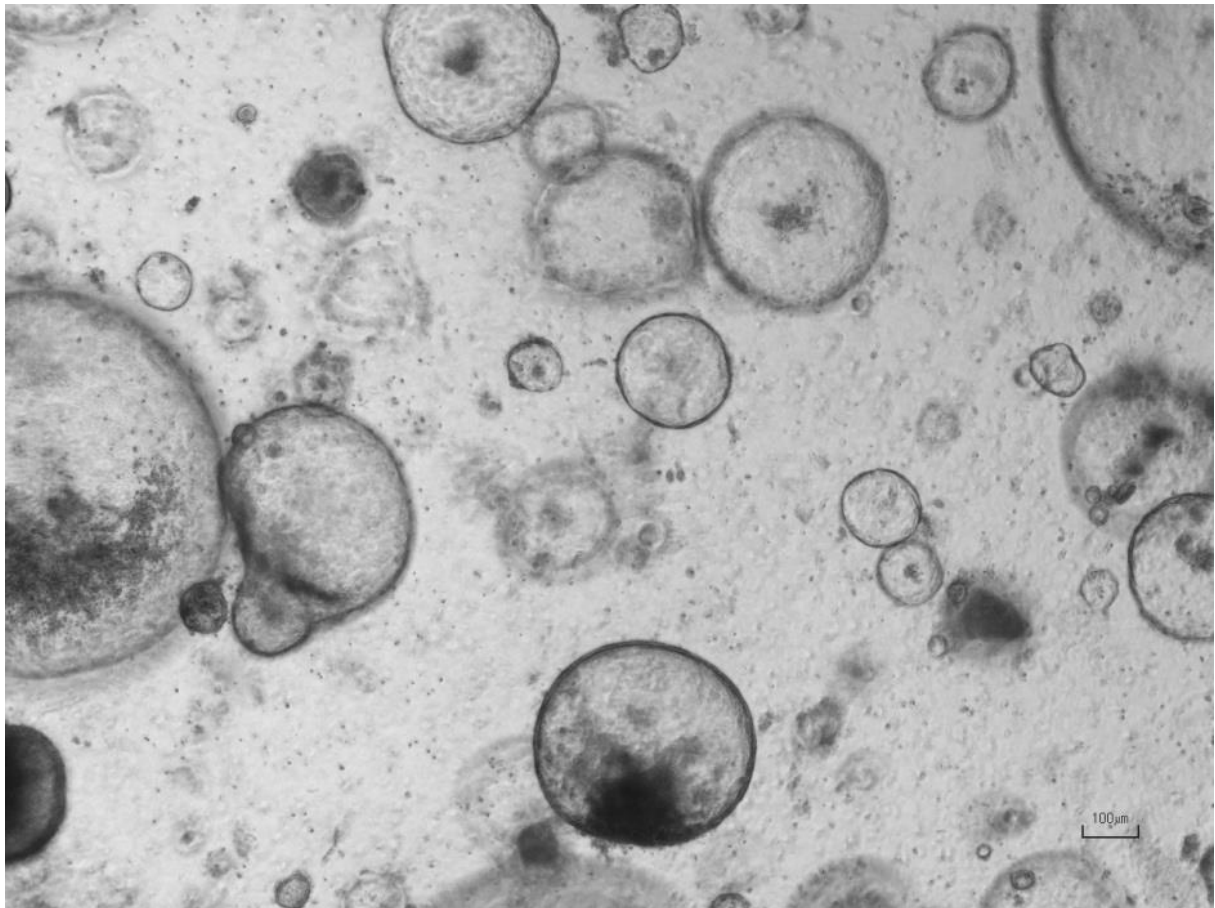
Figure 3.9 Day 69, Passage 7 and 5 Days of Mouse Liver Organoid Expansion Long-term Culture. It was observed that organoids could be cultured in expansion medium over several passages without observable loss of size or decrease in organoid numbers. Imaged with contrast phase microscopy, recoloured with greyscale (4X objectification) (Scale=100 μm).

Contrast phase microscopy images of digested mouse liver tissue in Cultrex® (Figure 3.3) generating organoids from days 0-4. Followed by the expansion of organoids in the same cell culture well at days 4-18 (Figures 3.4-3.7) and the differentiation of organoids in the same well at day 30 (Figure 3.8). As well as a different long-term culture in expansion medium for 69 days (Figure 3.9).

We observed expected expansion of both ductal structures and single cells from the even lysate into round multicellular structures by day 4 (Figure 3.4). At approximately 10-20 µm in diameter a hollow lumen on the interior of the organoids can be observed. The cells that make up the organoids begin to rapidly expand over the next 4-8 days and achieve their full size usually between 100-1000 µm diameter (Figure 3.5). Organoids remain spherical/cyst-like especially the smaller organoids under 300 µm. Some larger organoids (>300 µm) spontaneously fold in on themselves (Figure 3.6) or retain spherical/cyst-like morphology. Organoids can be cultured in expansion medium over several passages without observable loss of size or decrease in organoid numbers. Mouse liver organoids display little change in observable morphology by treatment with differentiation medium (Figure 3.8).

3.2.2 Live-Cell Analysis
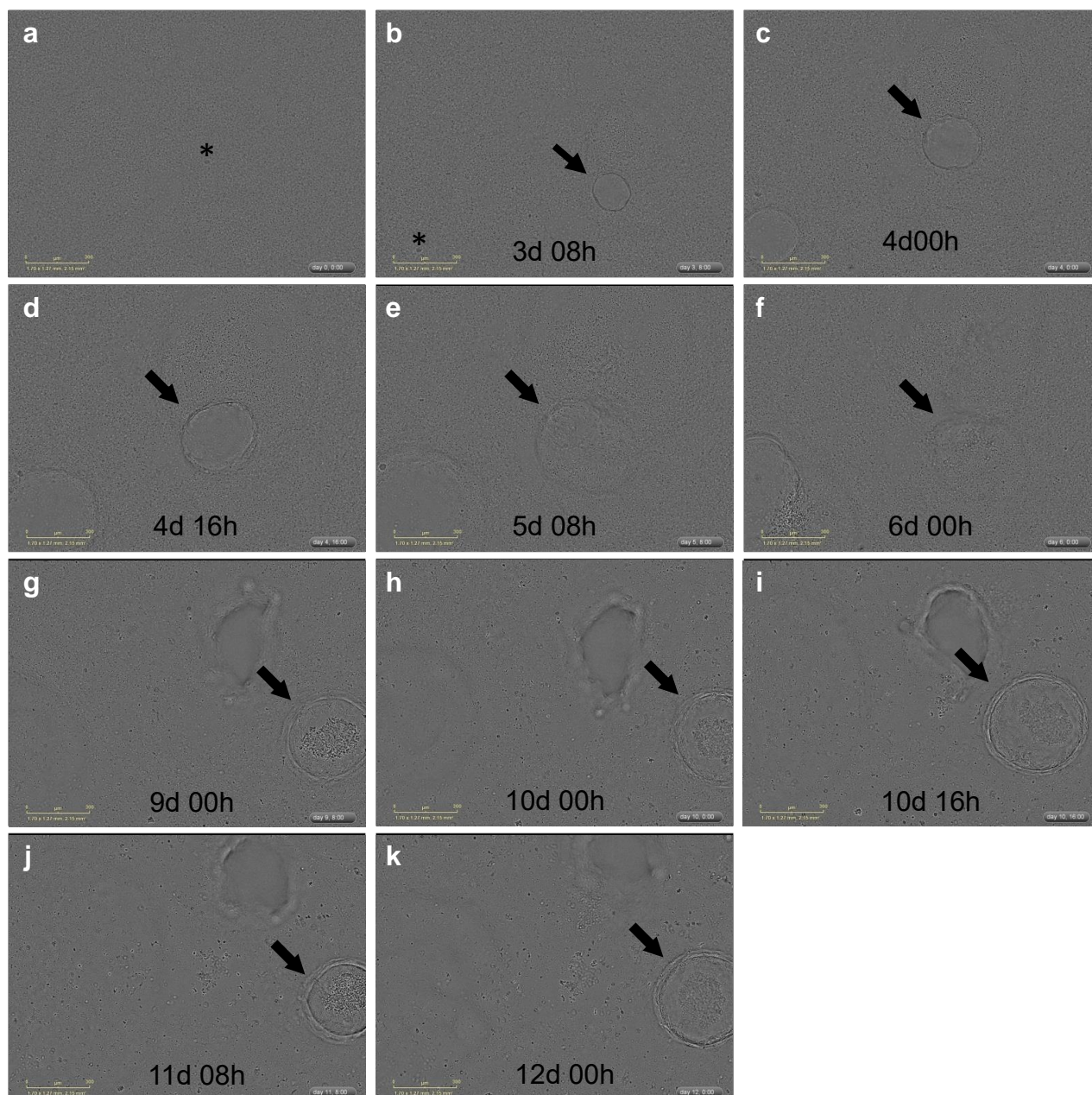
Figure 3.10 Serial Time-lapse Images of Mouse Organoid Generation in Cultrex® taken with an IncuCyte Zoom Live Cell Imager Contrast Phase Microscope. At 3 days organoids were observed growing from the cell lysate (Arrow). These organoids were generated from single cells that appear to divide into a small grouping of cells (Asterisks) until they change their morphology by forming a hollow lumen allowing the cells in the organoid to stretch into a hollow spherical structure (Arrow). 5X Objective Magnification, Cross-sectional image (Scale = 300 μm). d= days, h= hours.
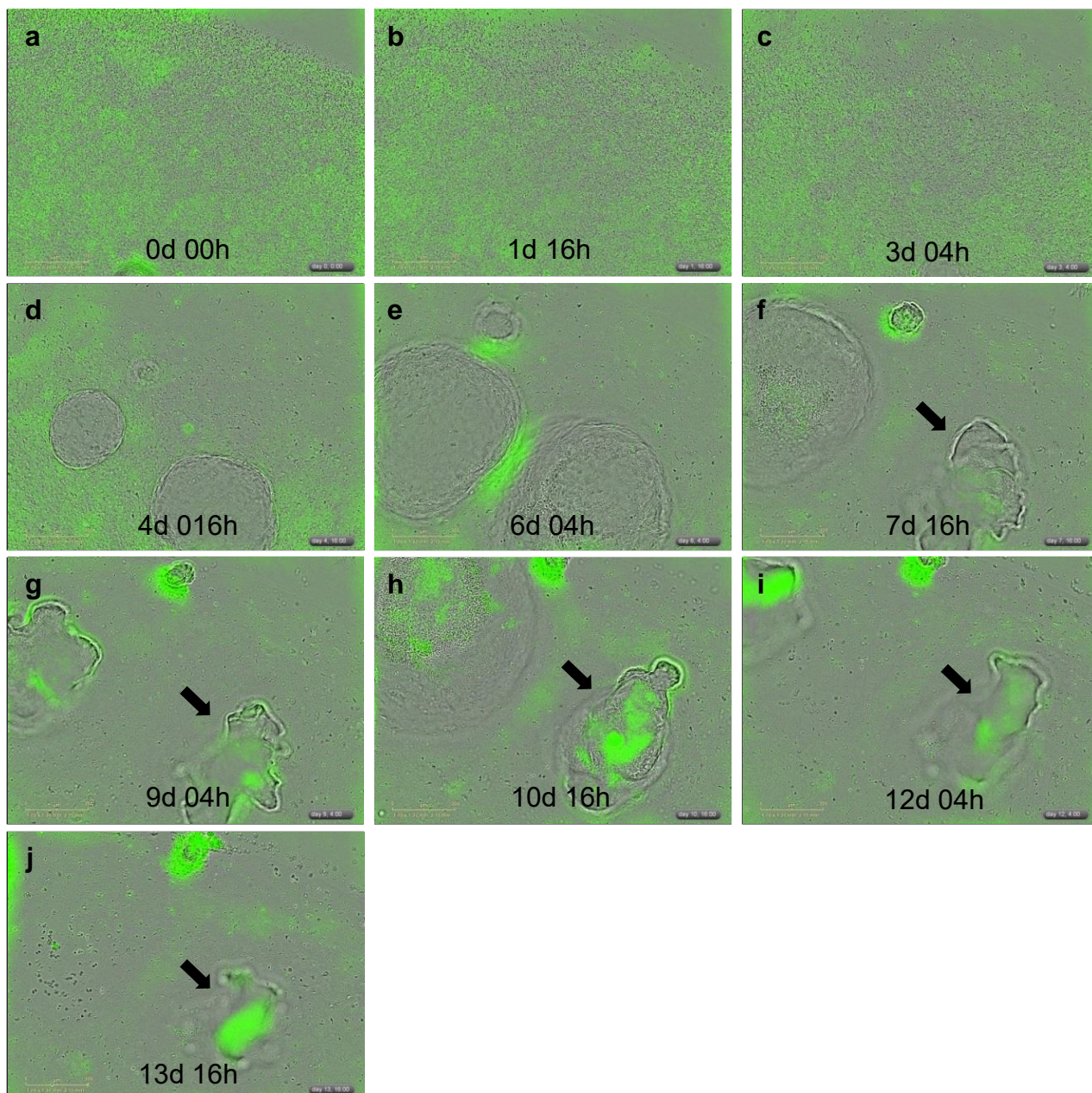
Figure 3.11 Time-lapse images of mouse organoid production in Cultrex taken with an IncuCyte Zoom Live Cell Imager. Cell lysate stained with green fluorescence dye Cytotrack. Organoid are observed growing and spontaneously folding in on themselves (Arrows). Green fluorescence indicates that cells are alive but not dividing. 5X Objective Magnification, Cross-sectional image (Scale = 300 μm). d= days, h= hours.

The IncuCyte® ZOOM Live-cell analysis system is an automated microscope and camera system that can be installed inside a cell culture incubator. This system provides insight into active biological processes in cell cultures in real-time, hence the generation and expansion of organoids was observed using this system to better understand the size, shape, and structure of organoids in these steps. This was achieved by imaging the organoid cell culture every 4 hours from time day 0 to day 14 using previously described methods of organoid generation and expansion (Pages 80-83). Cytotrack dye which emits green fluorescence and dissipates as cells divide was used to observe cell division within the organoids (Figure 3.11).

Live-cell analysis confirmed many of the observation made using light microscopy, such as time frame of expansion and spontaneous folding. We did observe that large organoids (>300 μm in diameter) went through cycles of expanding in a spherical hollow morphology, self-folding, and then expanding again. This can be seen in Figure 3.11 e-h. We were also able to observe that cell division was not ubiquitous between the cells of the organoids and that even by day 13 many of the organoid cells retained Cytotrack dye.

3.2.3 RT-qPCR Analysis
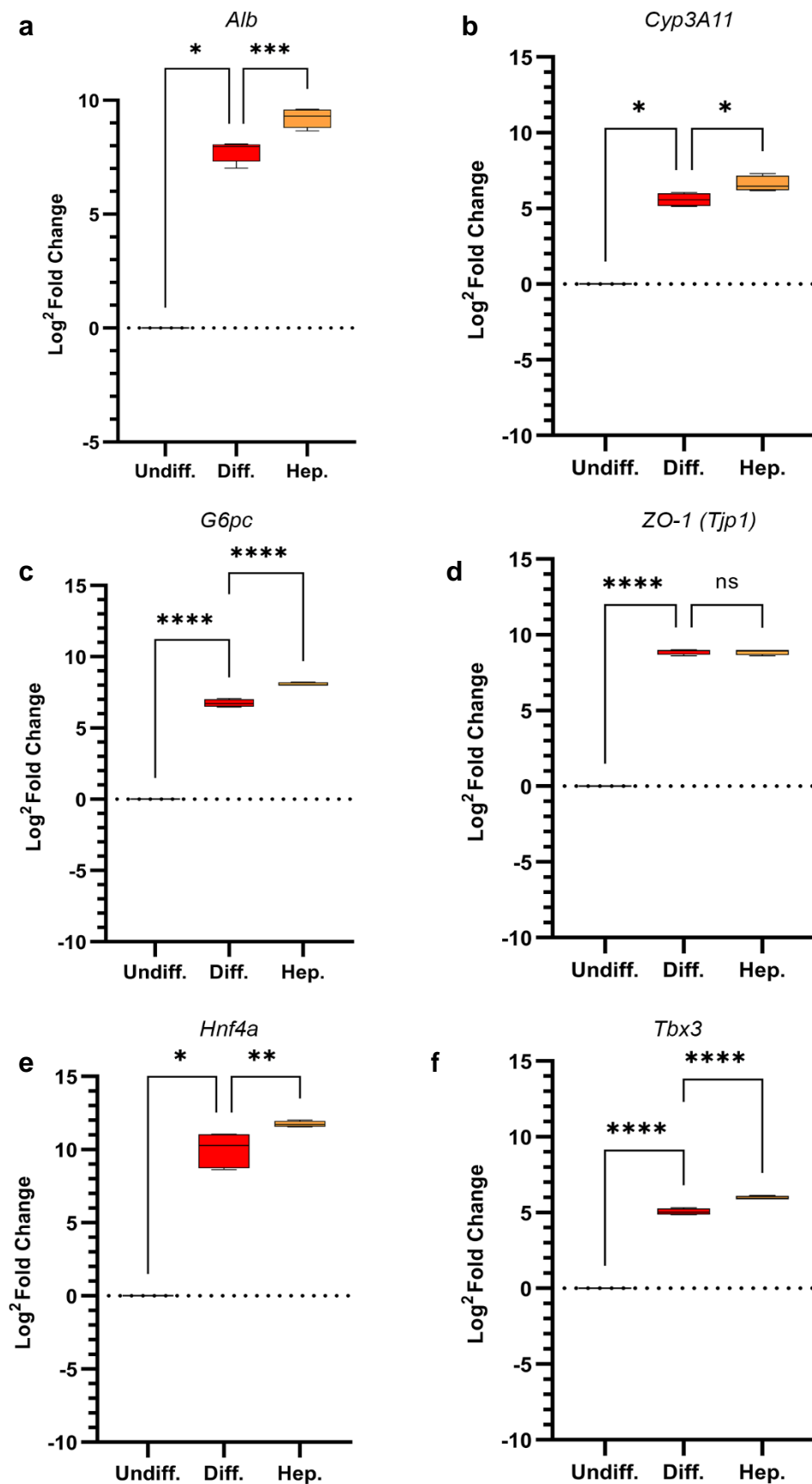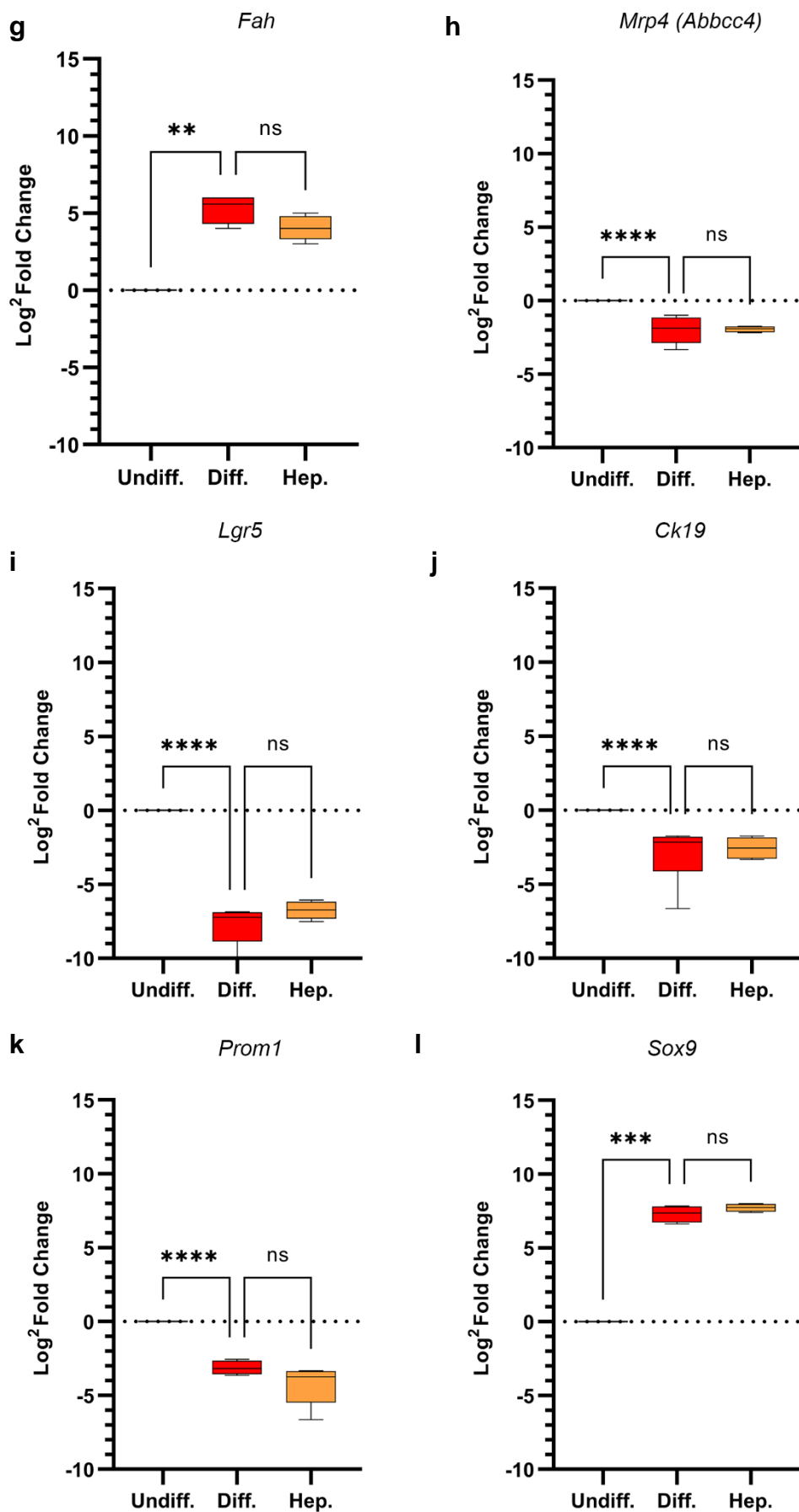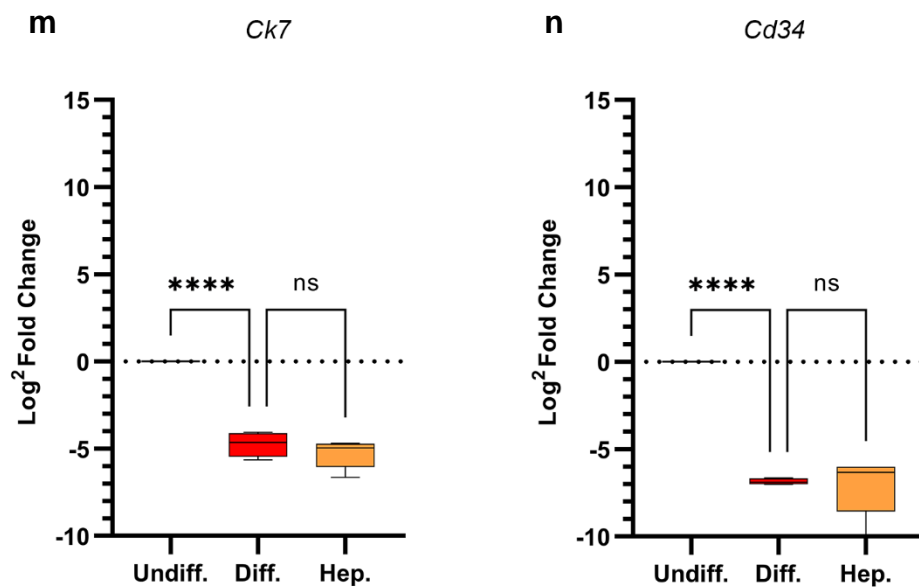
Figure 3.12 Fold Change in Gene Expression Induced by Differentiation. RT-qPCR data was normalised to the relative expression of the undifferentiated mouse liver organoid group (control), housekeeping gene hypoxanthine guanine phosphoribosyltransferase (*Hprt*) was used as a loading control for each sample, (n=4). Data was analysed using a one-way ANOVA to determine if there were significant differences between the means of groups, and a post-hoc Holm-Šídák's multiple comparisons test for the pairwise comparison of the individual groups. * $p \leq 0.05$, ** $p \leq 0.01$, *** $p \leq 0.001$, **** $p \leq 0.0001$, ns $p > 0.05$. Error bars indicate mean ± standard deviation.

Real-Time Quantitative Polymerase Chain Reaction (RT qPCR) analysis is a gold standard method of measuring gene expression in cells or tissues. Using RT-qPCR analysis, the expression of functionally significant hepatic genes like albumin (*Alb*), cytochrome P450 3A11 (*Cyp3A11*), gluscose-6-phophatase (*G6PC*), zonula occludens-1 (*ZO-1*), hepatocyte nuclear factor 4 alpha (*HNF4α*), T-Box 3 transcription factor (*Tbx3*), fumarylacetoacetate hydrolase (*Fah*) and multidrug resistance-associated protein 4 (*MRP4*), and progenitor genes such as leucine-rich repeat-containing G-protein-coupled receptor 5 (*Lgr5*), cytokeratin 19 (*CK19*), prominin1 (*Prom1*), SRY-box 9 (*Sox9*), cytokeratin 7 (*CK7*) and *CD34* were measured between undifferentiated organoids (Undiff.), differentiated organoids (Diff.) and primary mouse hepatocytes (Hep.). Undifferentiated organoids were used as a negative control for functional gene expression (Figure 3.12).

The expression of *Alb*, *Cyp3A11*, *G6pc*, *ZO-1*, *HNF4α*, *Tbx3*, *Fah* and *Sox9* genes in differentiated organoid samples was significantly ($p < 0.05$) increased compared to undifferentiated controls (Fig. 3.12). On the other hand, the expression of *Mrp4*, *Lgr5*, *Ck19*, *Prom1*, *Ck7* and *Cd34* genes in differentiated organoid samples was significantly ($p < 0.001$) decreased compared to undifferentiated controls (Fig. 3.12). Whilst the expression of Alb, *Cyp3A11*, *G6pc*, *HNF4α*, *Tbx3* genes was found to be significantly ($p < 0.05$) lower in differentiated organoid than that of primary hepatocytes, the expression of *ZO-1*, *Fah*, *Mrp4*, *Lgr5*, *Ck19*, *Prom1*, *Sox9*, *Ck7* and *Cd34* genes showed no significant differences between the differentiated organoids and primary hepatocytes (Fig. 3.12).

3.2.4 Confocal Laser Scanning Microscopy Analysis

Hoechst	ALB	Combined
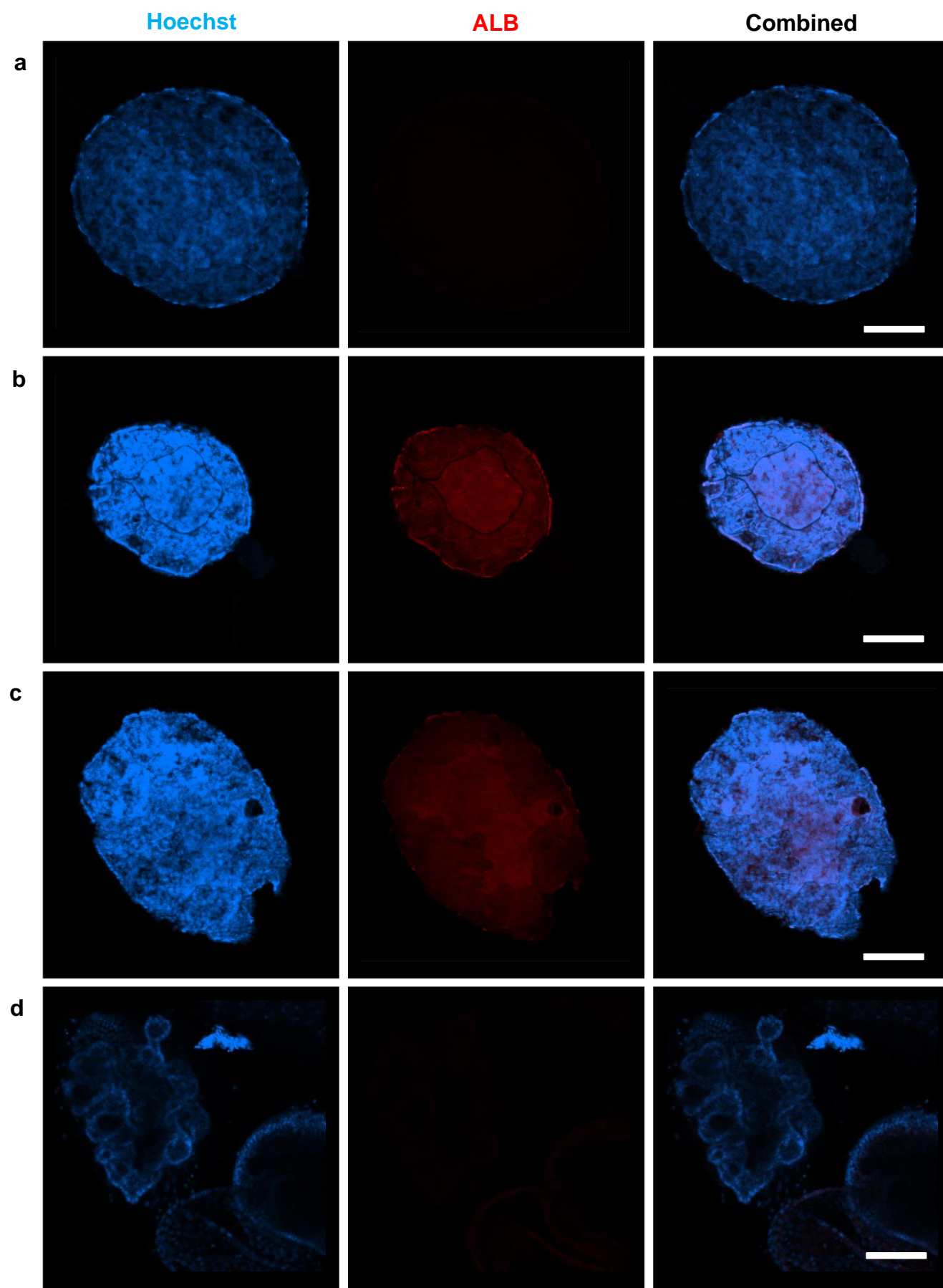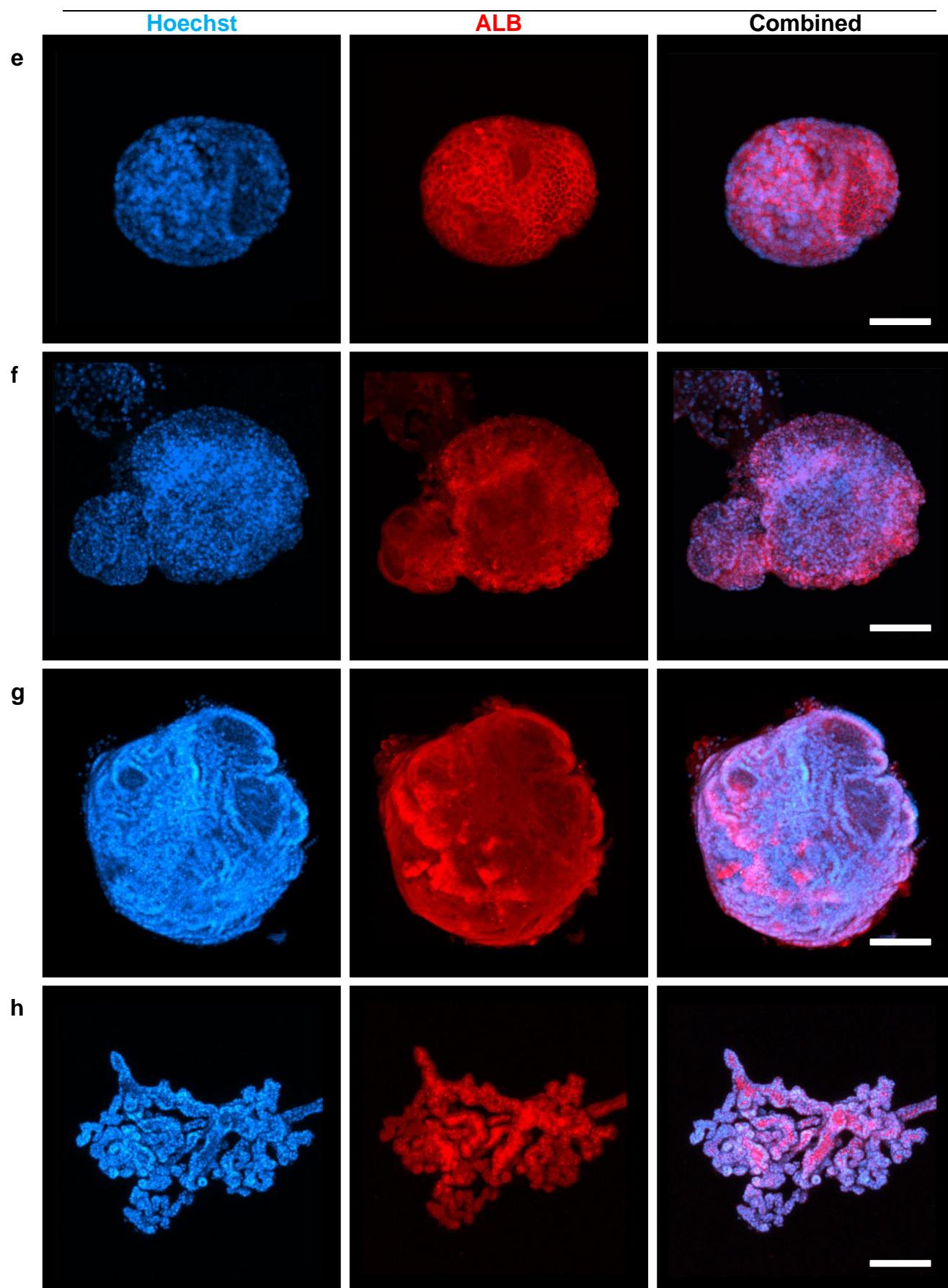
Figure 3.13 Immunofluorescent co-staining of Albumin and DNA in Differentiated and Non-differentiated Mouse Liver Organoids. a-d. Non-differentiated organoids expressed albumin staining signal at very low to undetectable levels. **e-h.** The differentiated organoids expressed albumin staining ubiquitously within the cells of the organoids. Note: Albumin staining signal was also observed in the buffer solution of these samples (not presented here) before being washed for imaging, suggesting albumin secretion by the differentiated liver organoids. (Scale bar = 100 µm).

Hoechst	CYP450	Combined

Hoechst	CYP450	Combined

Hoechst	CYP450	Combined
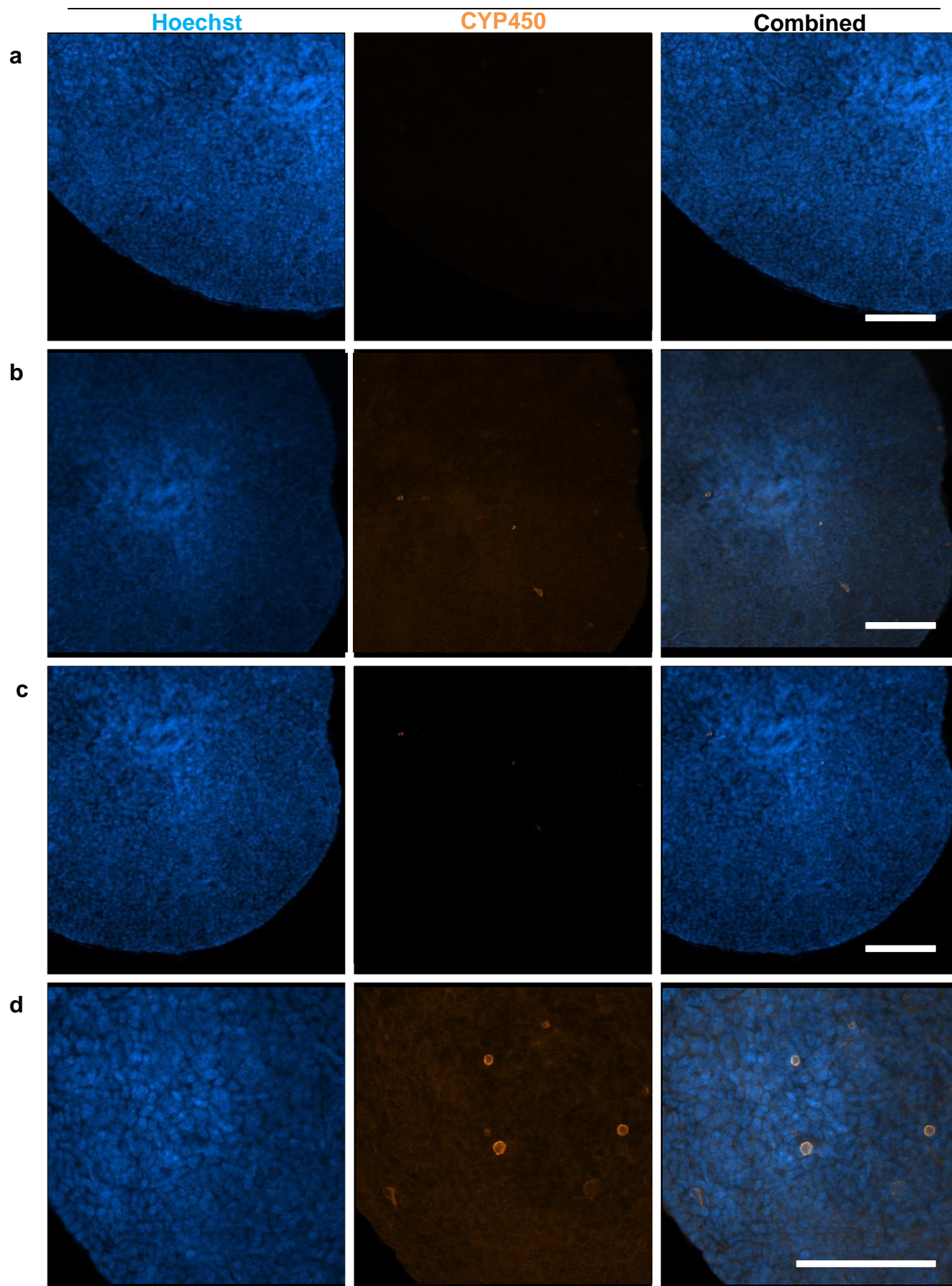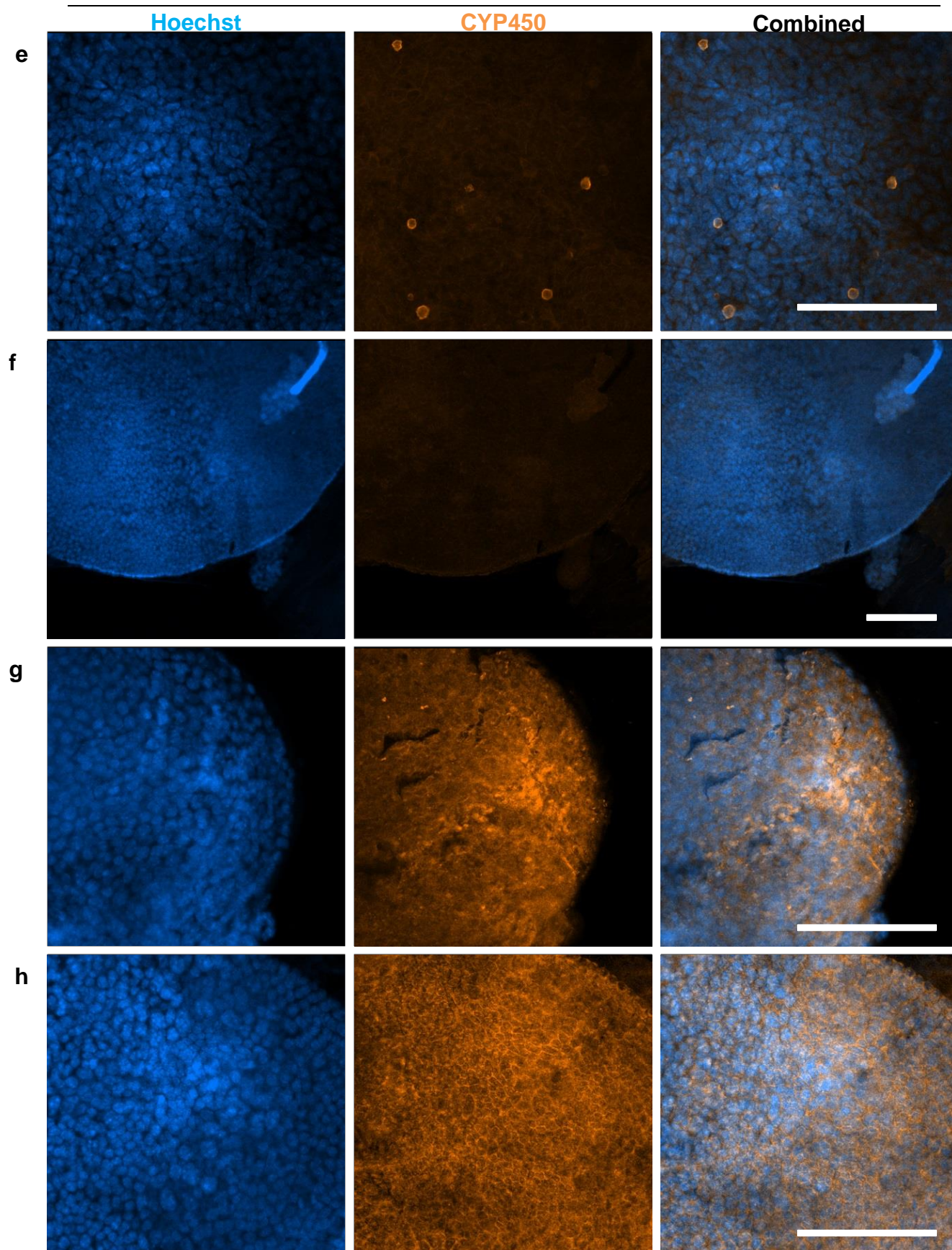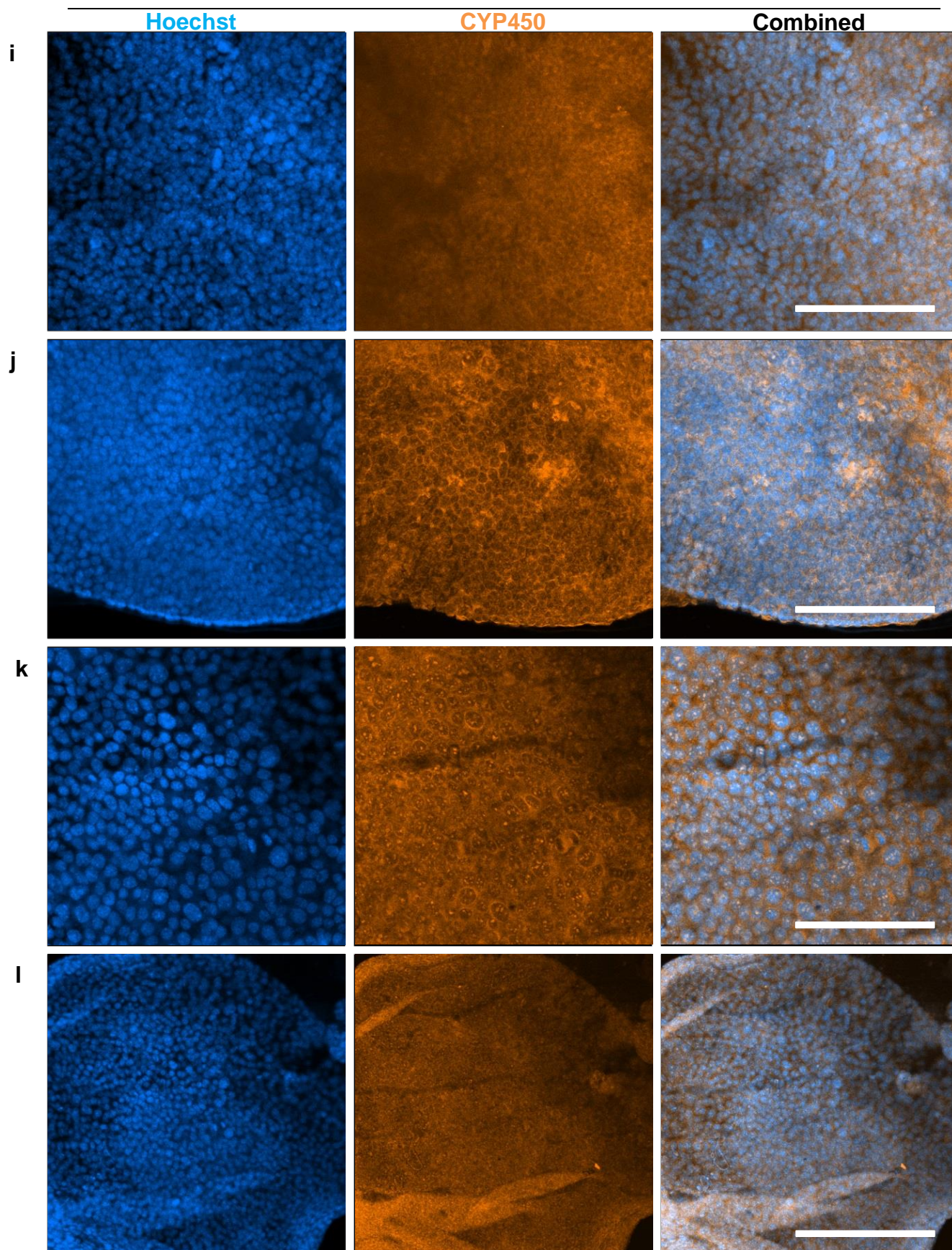
Figure 3.14 Immunofluorescent co-staining of Cytochrome P450 and DNA in Differentiated and Non- differentiated Mouse Liver Organoids. a-f. Non-differentiated organoids expressed cytochrome P450 staining signal at very low levels, with a few individual cells expressing a signal within some organoids (b, d, e). **g-l.** The differentiated organoids expressed cytochrome P450 staining at high levels and ubiquitously within the cells of the organoids. (Scale bar = 100 µm).

Hoechst	ZO-1	Combined

Hoechst	ZO-1	Combined

i
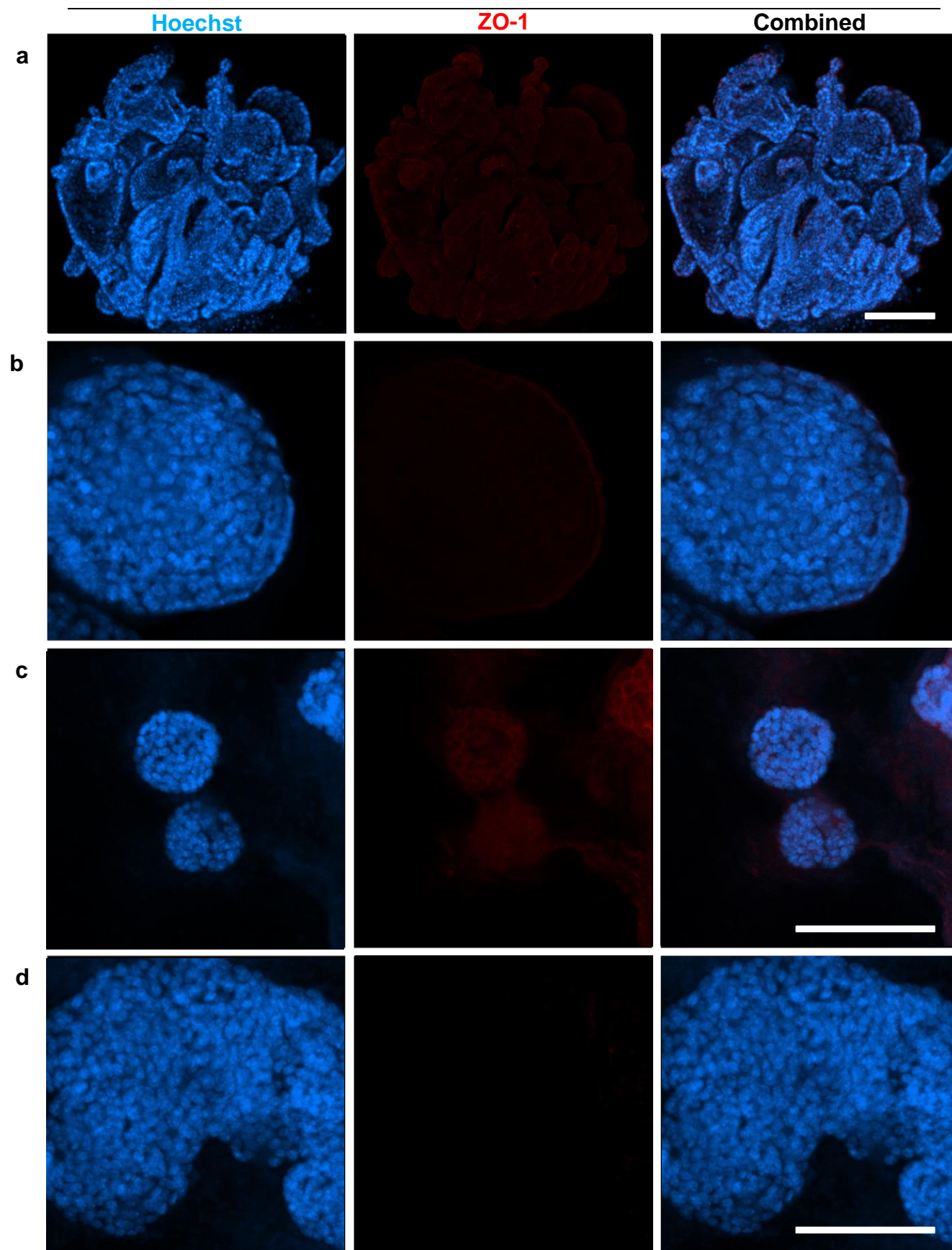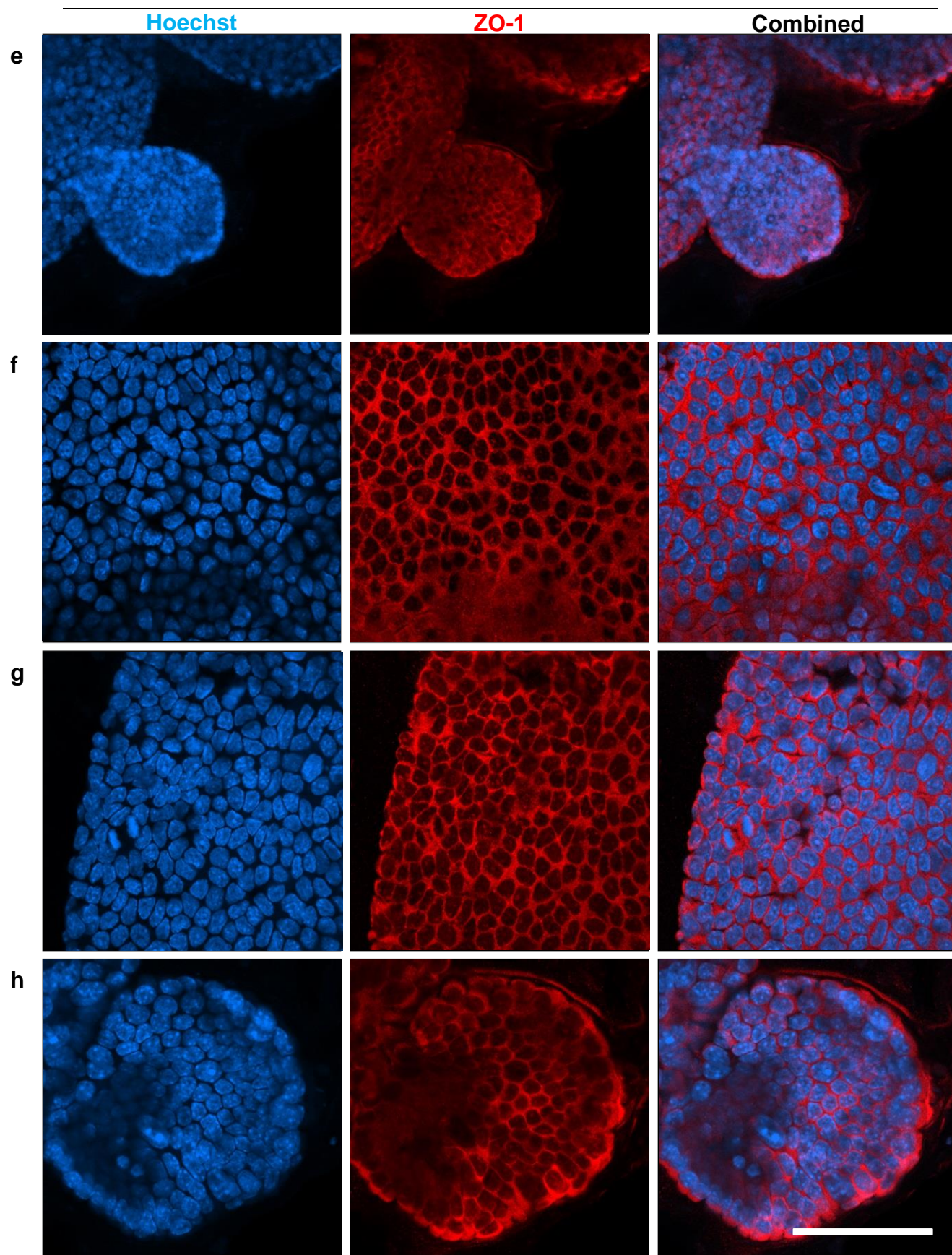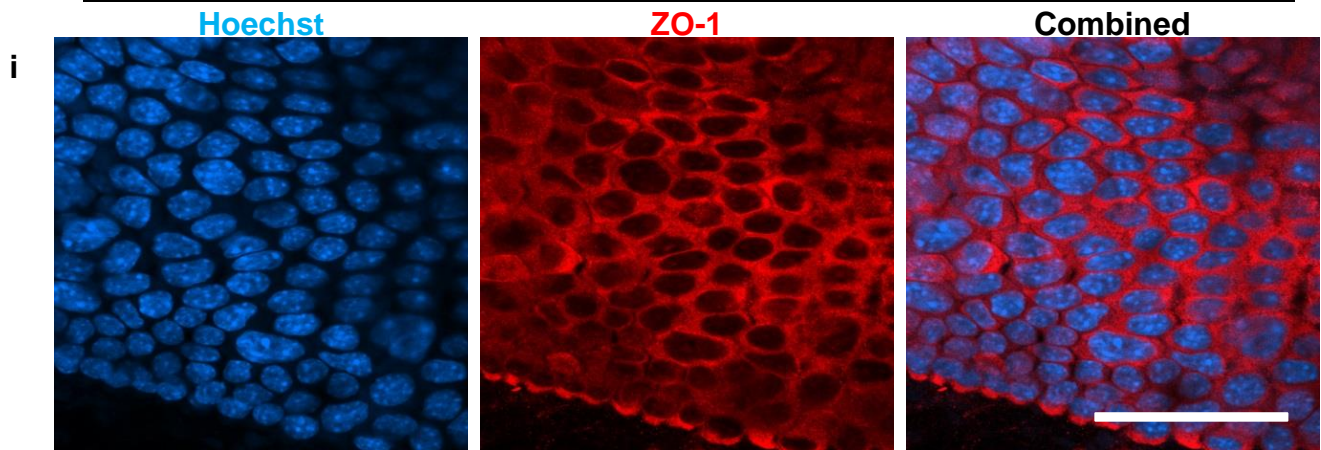
Figure 3.15 Immunofluorescent co-staining of ZO-1 and DNA in Differentiated and Non-differentiated Mouse Liver Organoids. a-d. Non-differentiated organoids expressed the hepatocyte tight junction marker ZO-1 staining signal at very low to undetectable levels. **e-i.** The differentiated organoids expressed ZO-1 staining at high levels located at the junctions where individual cells bind within the organoids. (A-D Scale bar = 100 µm; (E-I) Scale = 50 µm).

Hoechst	HNF4α	Combined

Hoechst	HNF4α	Combined
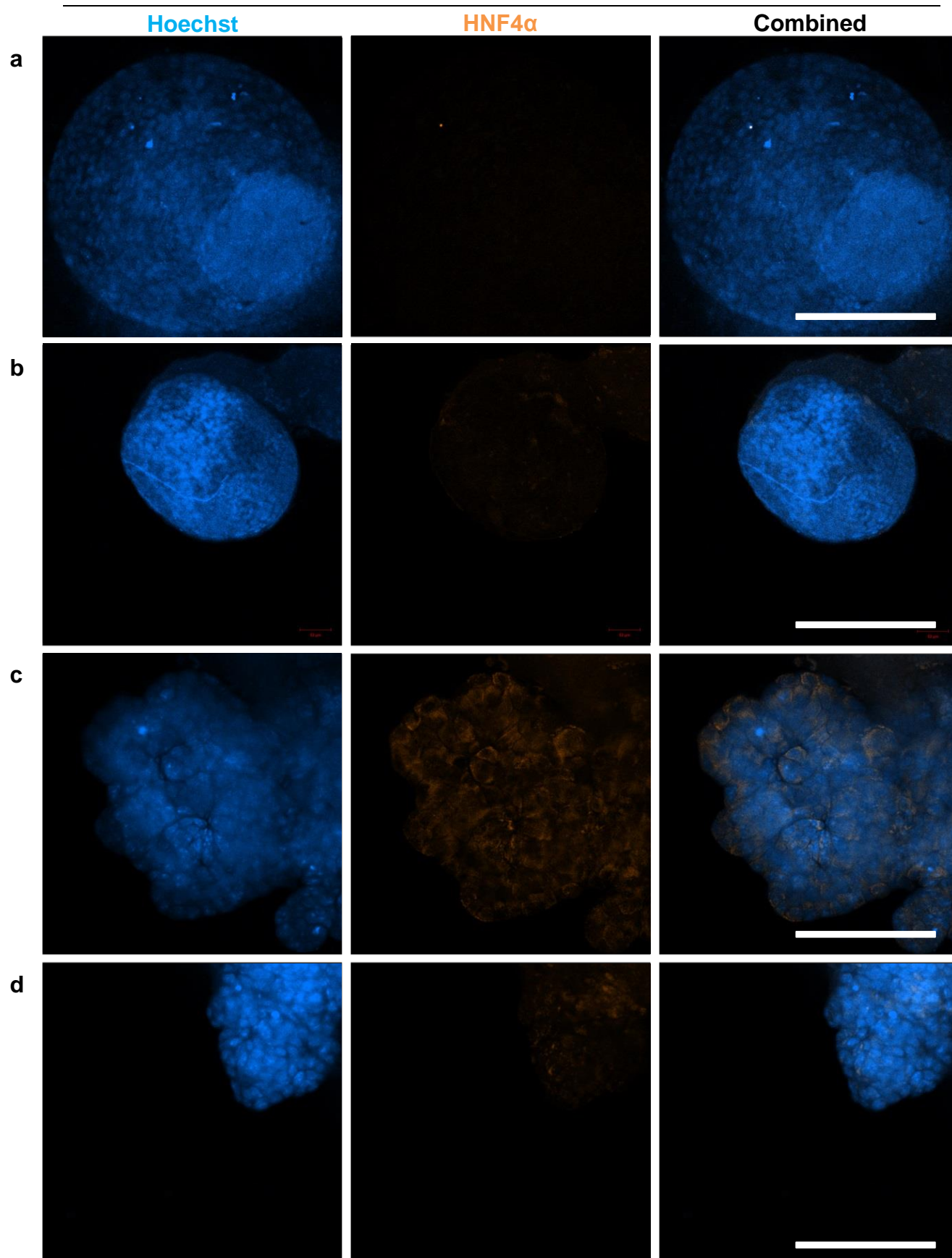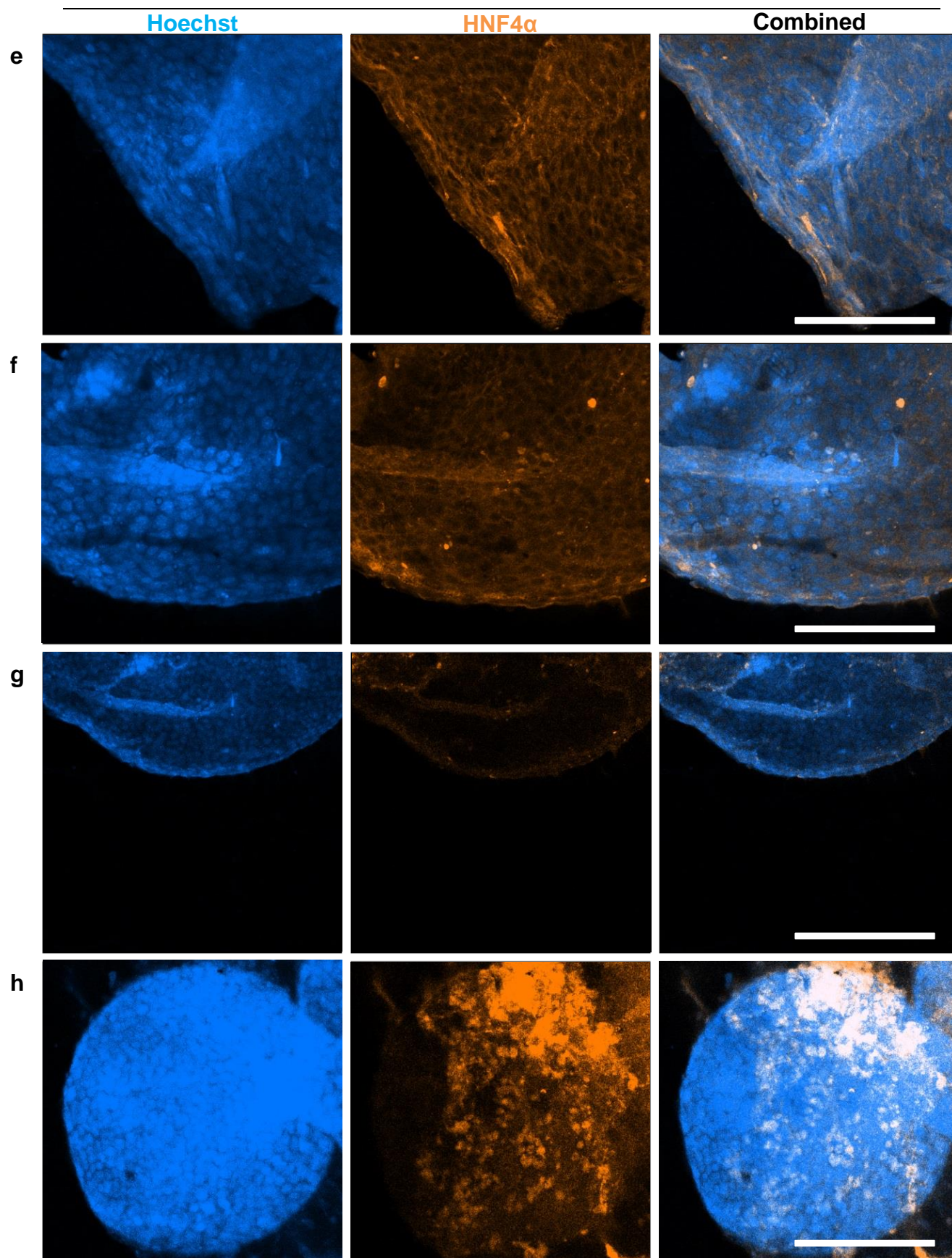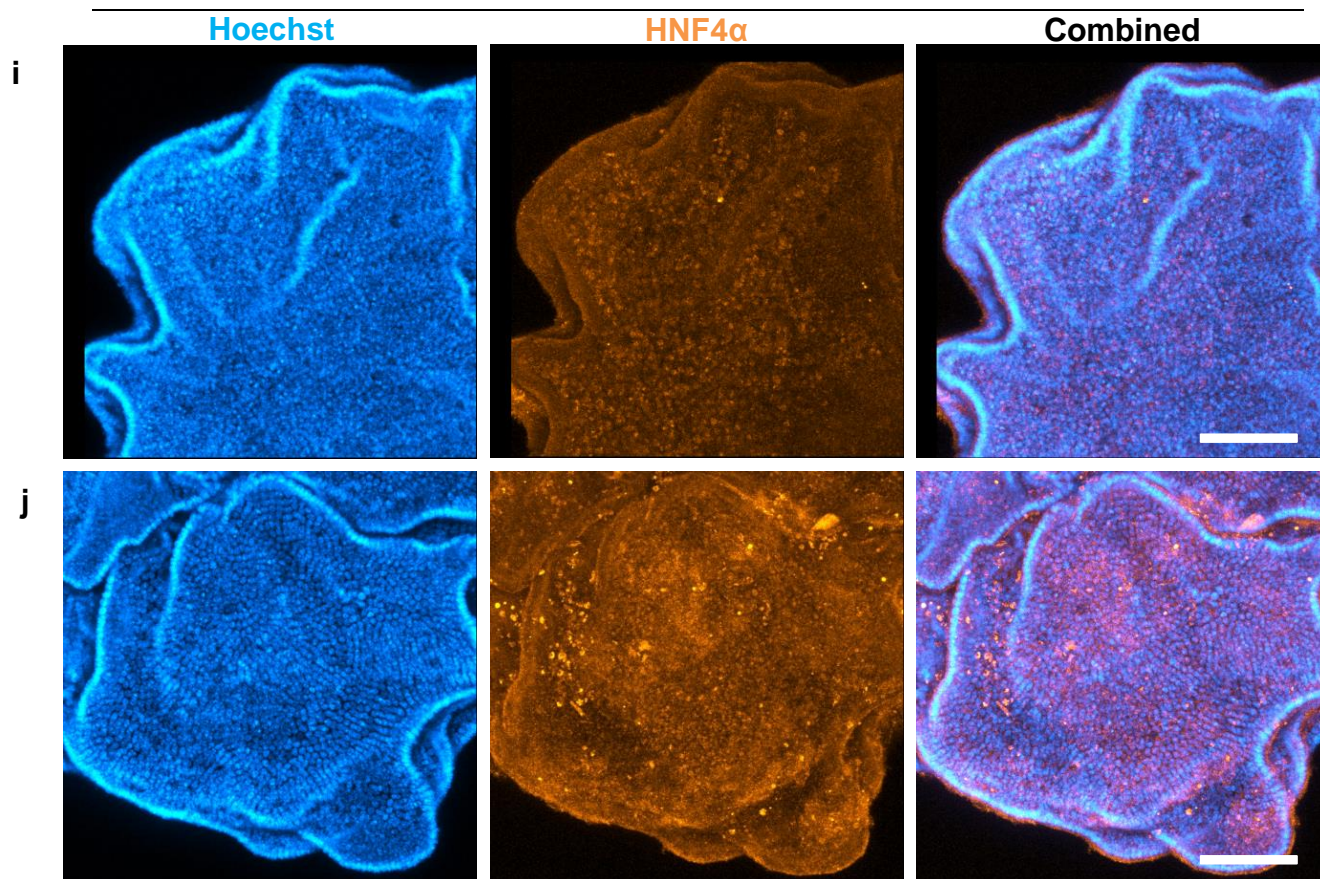
Figure 3.16 Immunofluorescent co-staining of HNF4α and DNA in Differentiated and Non-differentiated Mouse Liver Organoids. a-d. Non-differentiated organoids expressed the Hepatocyte Nuclear Factor 4 alpha staining signal at very low to undetectable levels. **e-j.** The differentiates organoids expressed HNF4α staining at mostly high levels and ubiquitously within the organoids. (Scale bar = 100 µm).

Hoechst	SMA-α	Combined

Hoechst	SMA-α	Combined

e

f

g

h

Hoechst	SMA-α	Combined
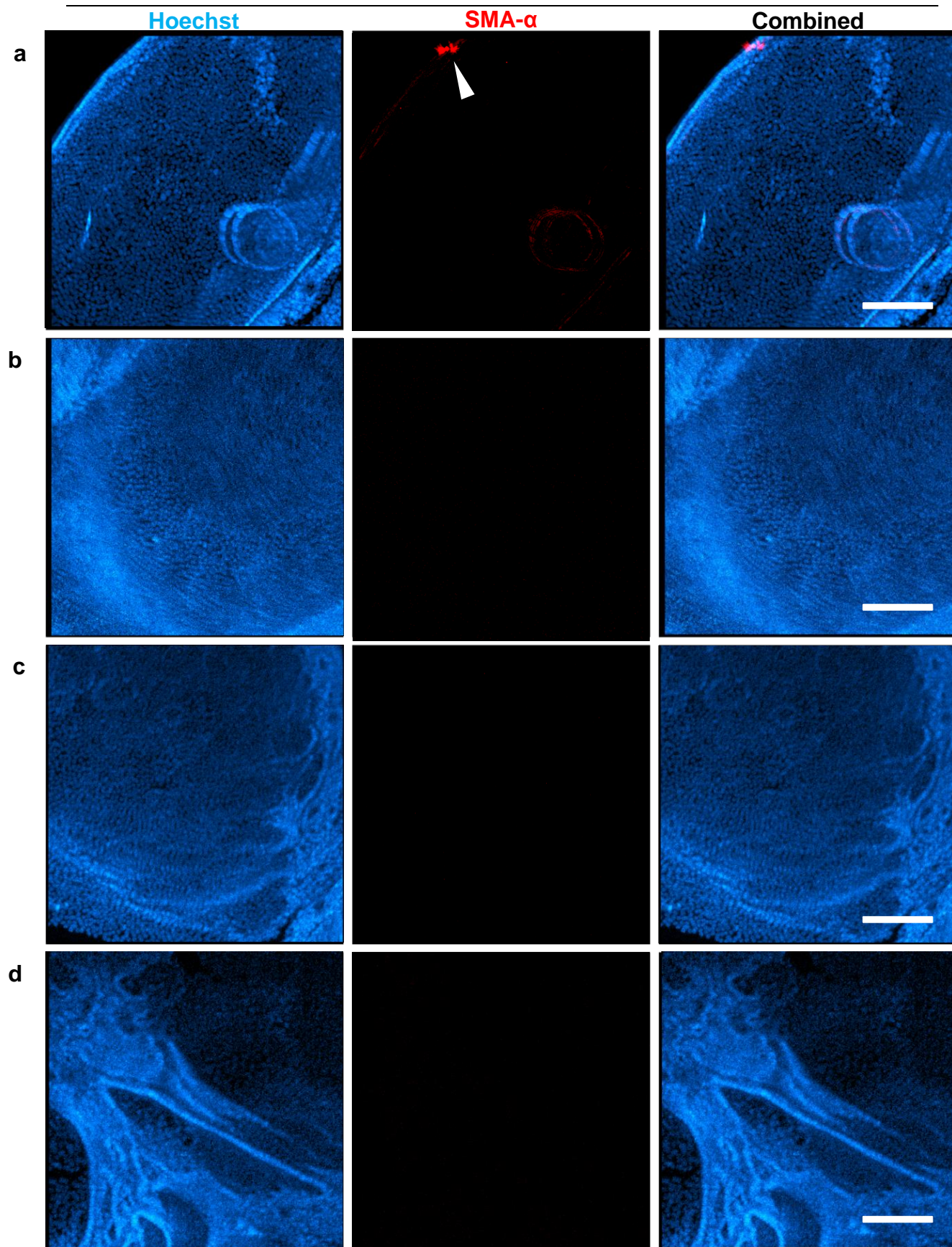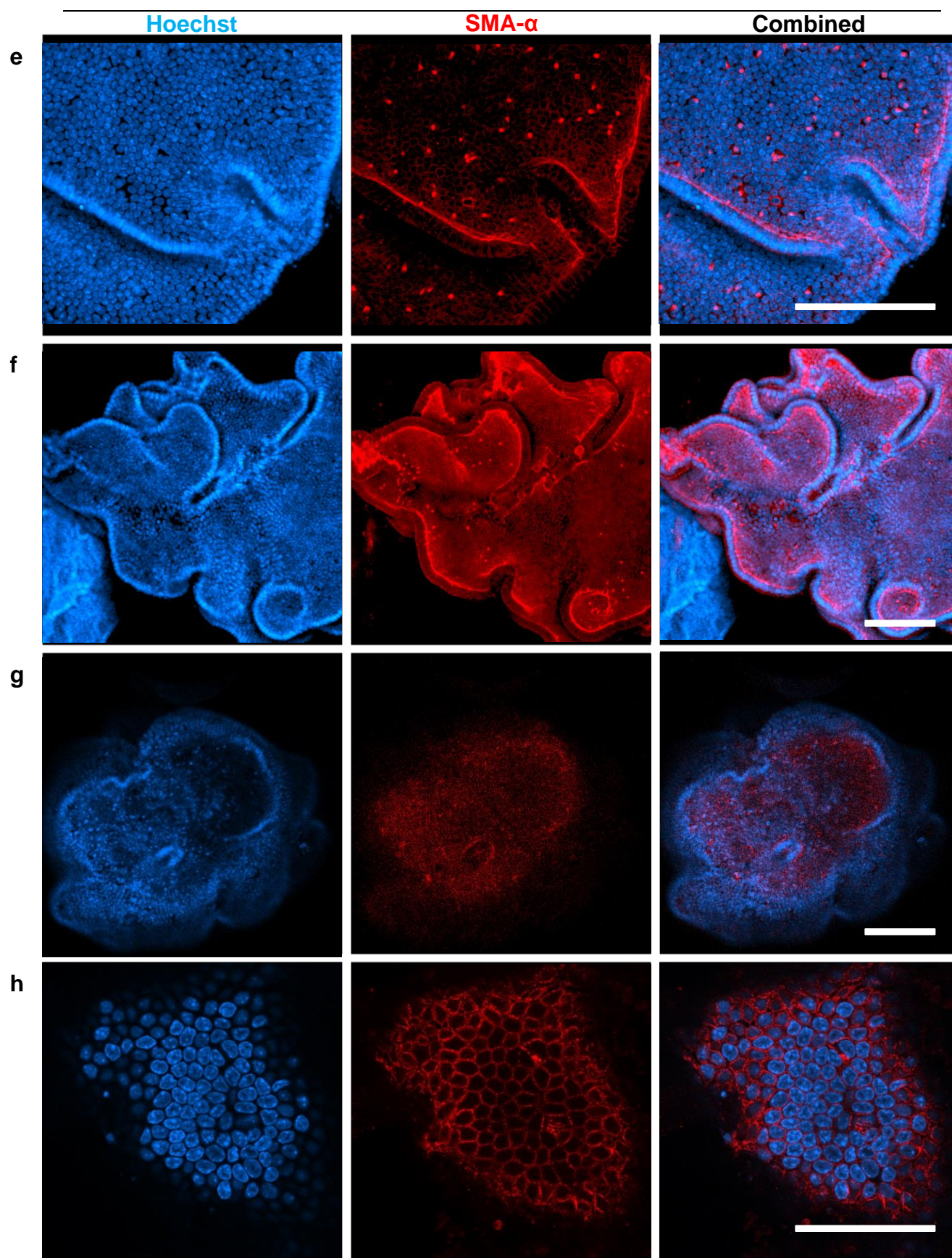
Figure 3.17 Immunofluorescent co-staining of SMA-α and DNA in Differentiated and Non-differentiated Mouse Liver Organoids. a-d. Non-differentiated organoids expressed the smooth muscles actin alpha staining signal at very low to undetectable levels with except a single cell (arrowhead in panel **a**). **e-h.** The differentiated organoids express SMA-α staining at mostly high levels located on the cell membrane on cells in the organoids. (A-G, Scale bar = 100 µm; H Scale bar = 50 µm).

Hoechst	LGR5	Combined

Hoechst	LGR5	Combined
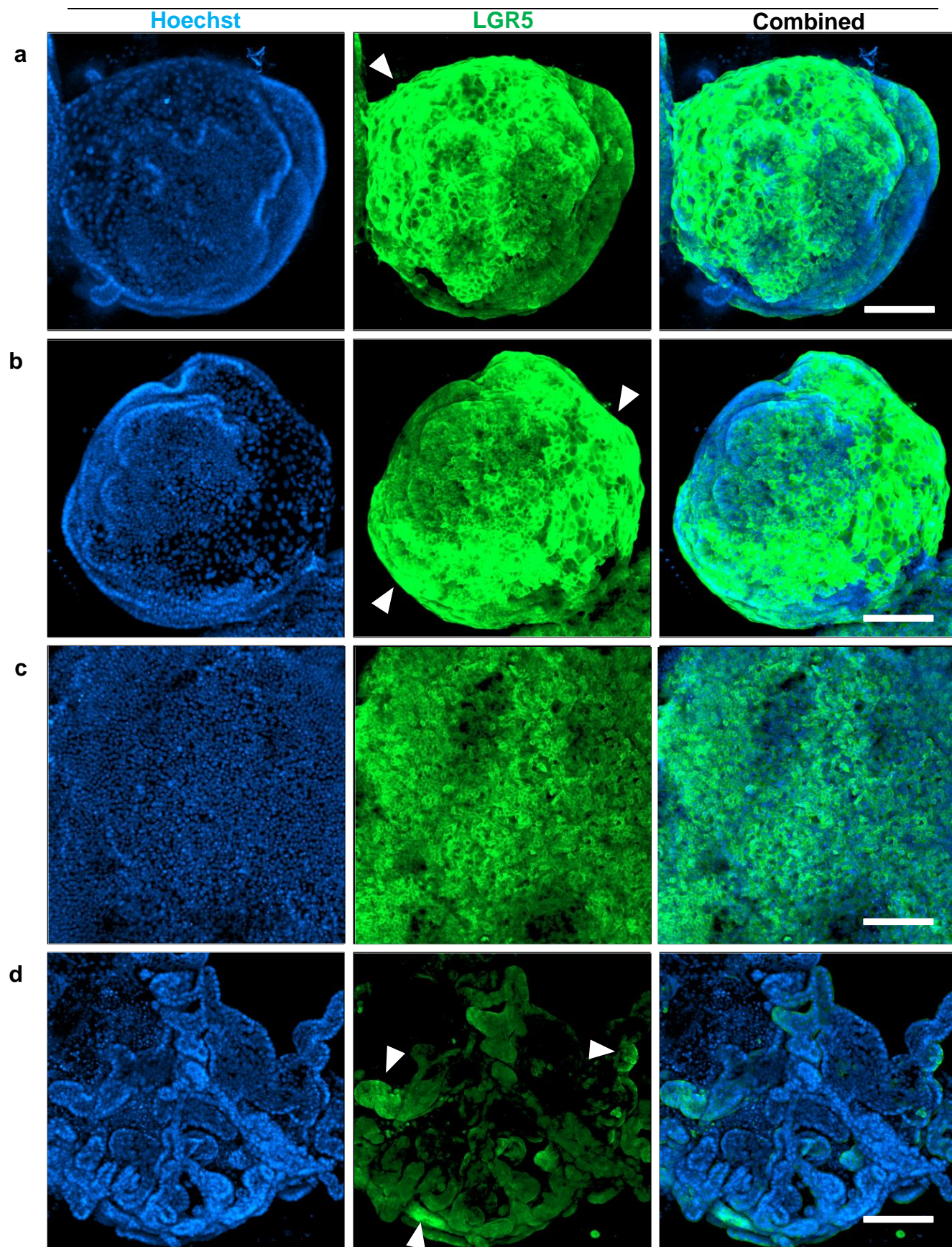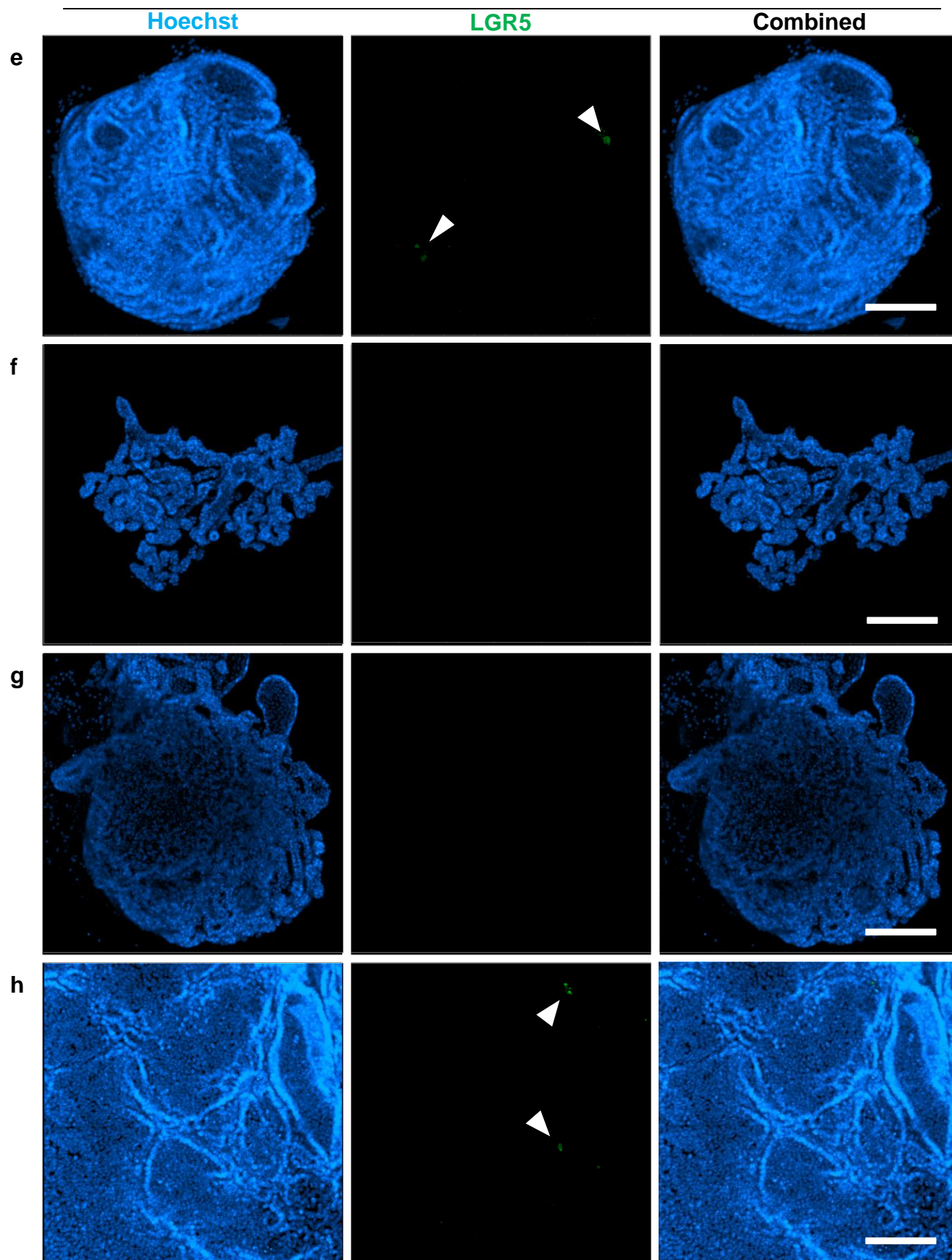
Figure 3.18 Immunofluorescent co-staining of LGR5 and DNA in Differentiated and Non-differentiated Mouse Liver Organoids. a-d. Non-differentiated organoids expressed Leucine containing content repeating G-protein coupled receptor 5 staining signal at very high levels (arrowheads) varying gradually between cells located on the cell membrane on the cells in the organoids. **e-h.** The differentiated organoids expressed LGR5 staining at low levels with the exception of a few cells in the organoids (arrowheads in panel **e** and **h**). (Scale bar = 100 µm).

Hoechst	CK19	Combined

Hoechst	CK19	Combined

Hoechst	CK19	Combined
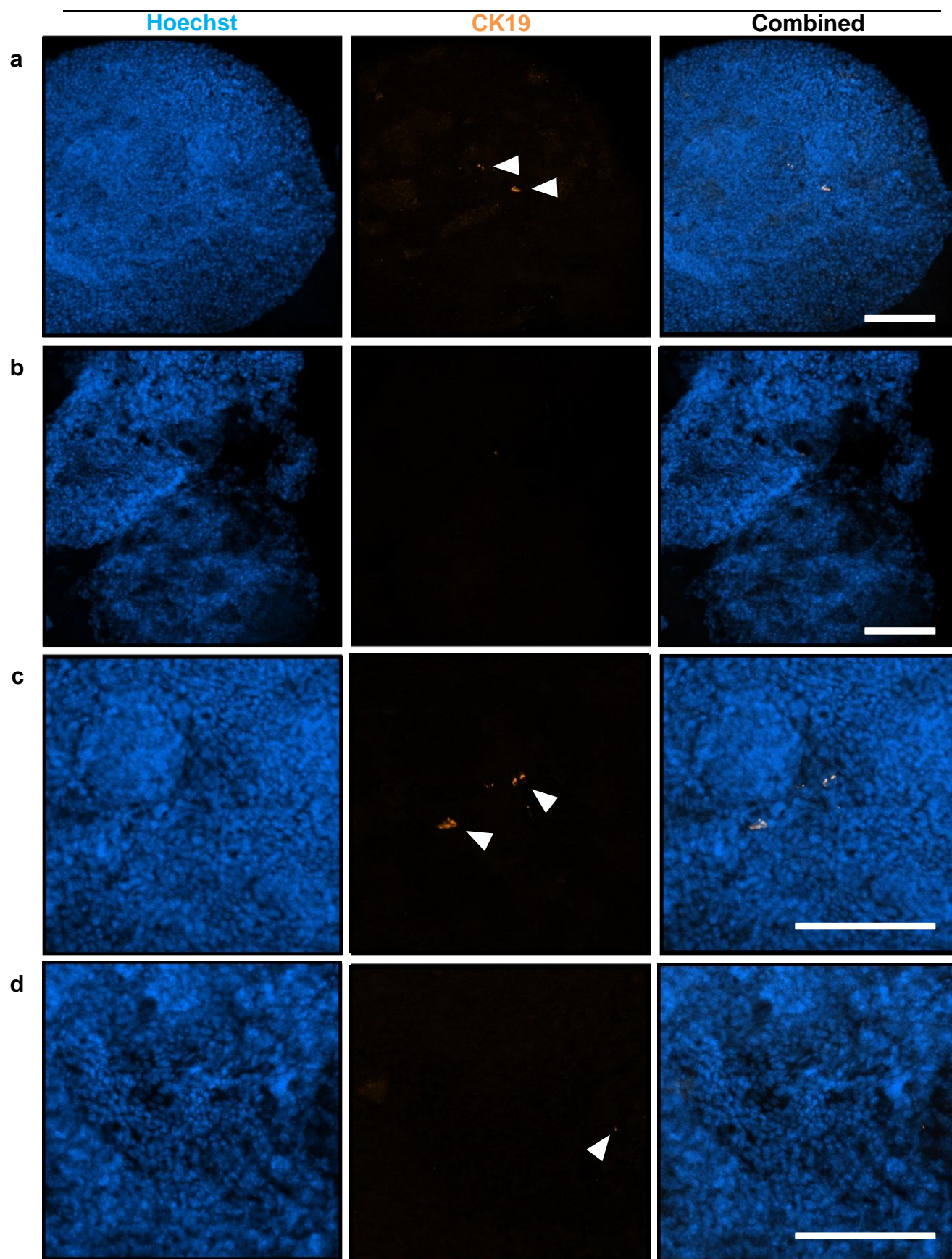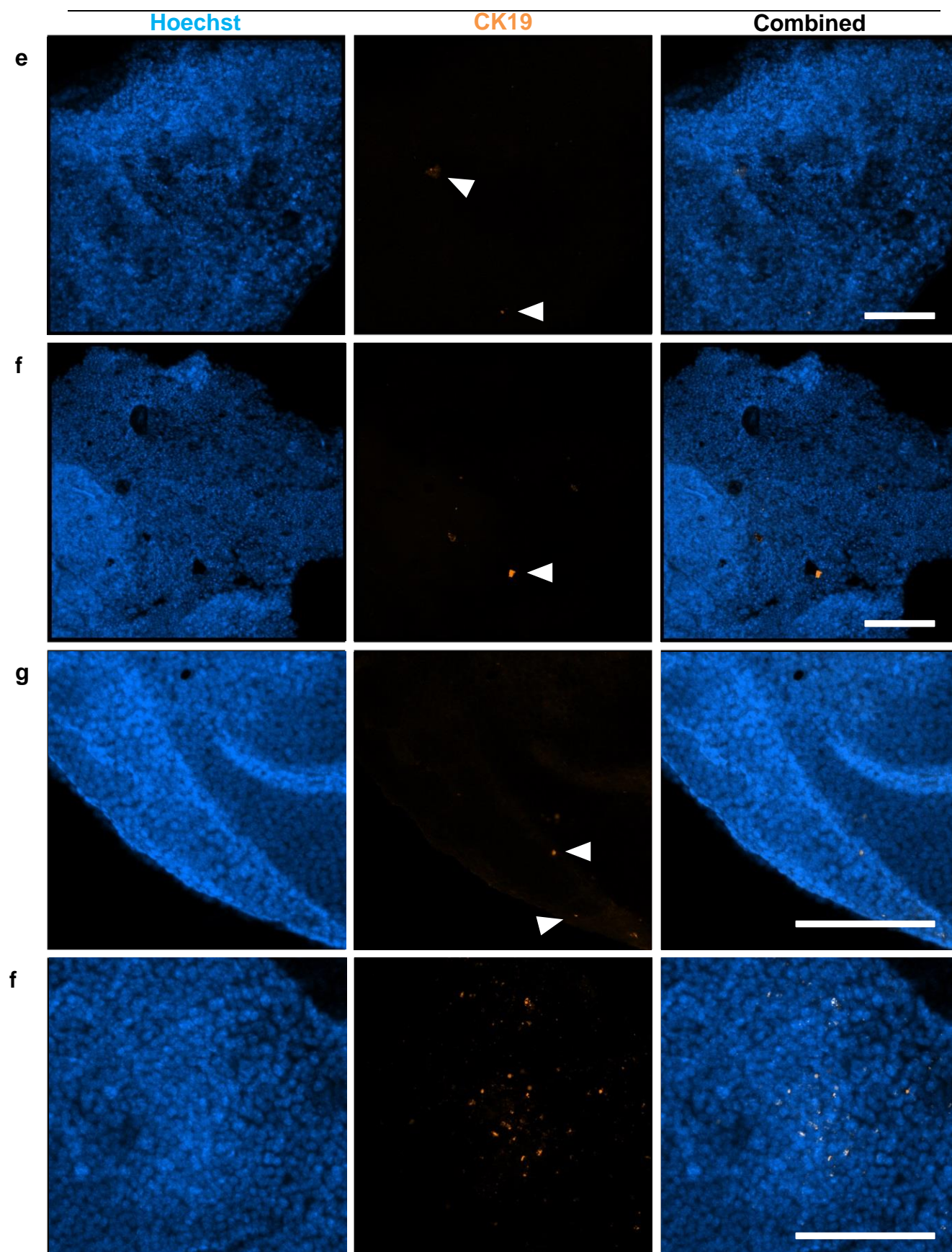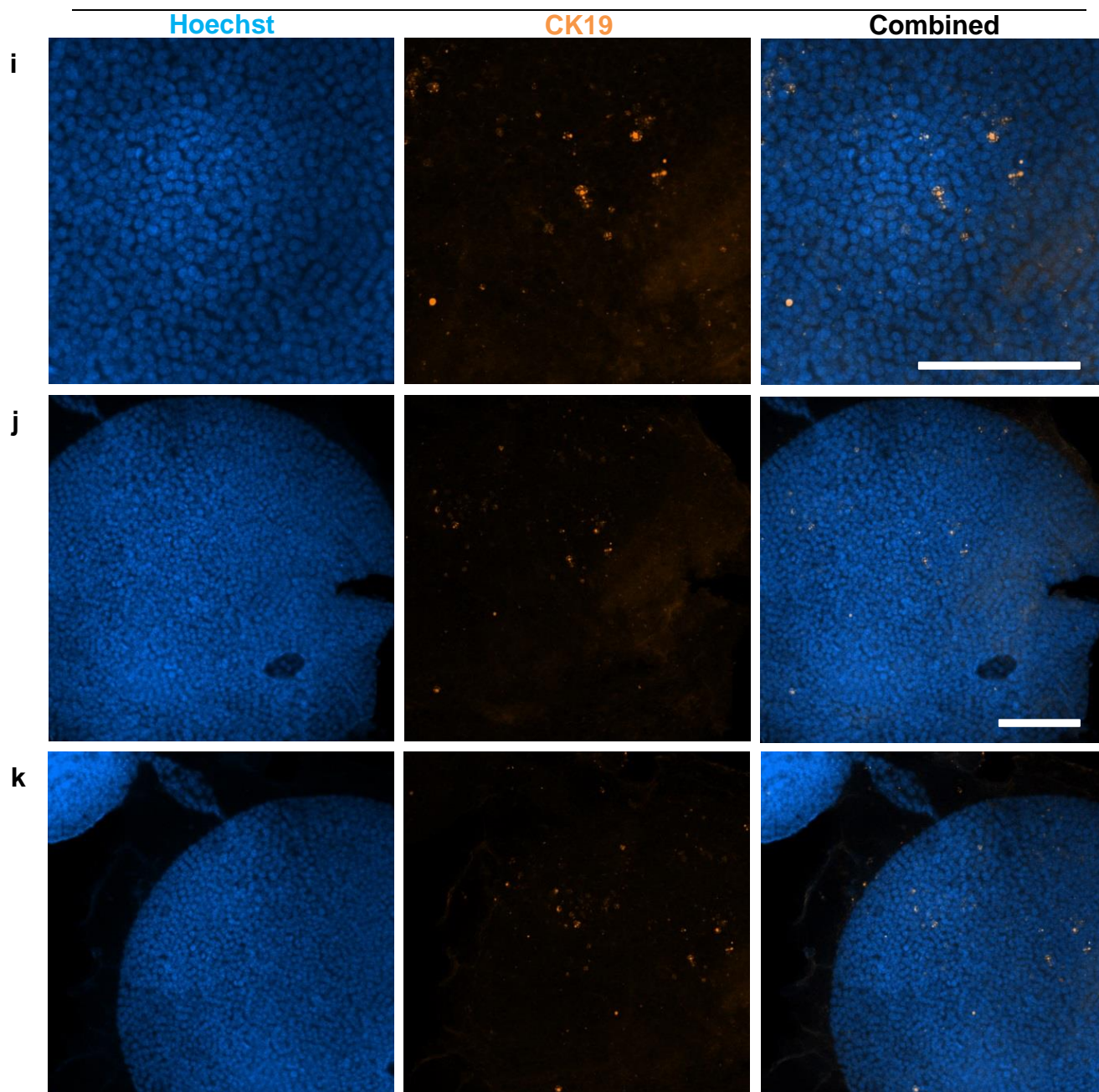
Figure 3.19 Immunofluorescent co-staining of CK19 and DNA in Differentiated and Non-differentiated Mouse Liver Organoids. a-f. Non-differentiated organoids expressing Cytokeratin 19 showed positive signal in only a few cells in each organoid (arrowhead in panel **a**, **c**, **d**, **e** and **f**). **g-k.** The differentiated organoids expressing CK19 also showed positive staining in a few cells in each as well (arrowhead in panel **g**). (Scale bar = 100 µm).

Hoechst	SOX9	Combined

Hoechst	SOX9	Combined
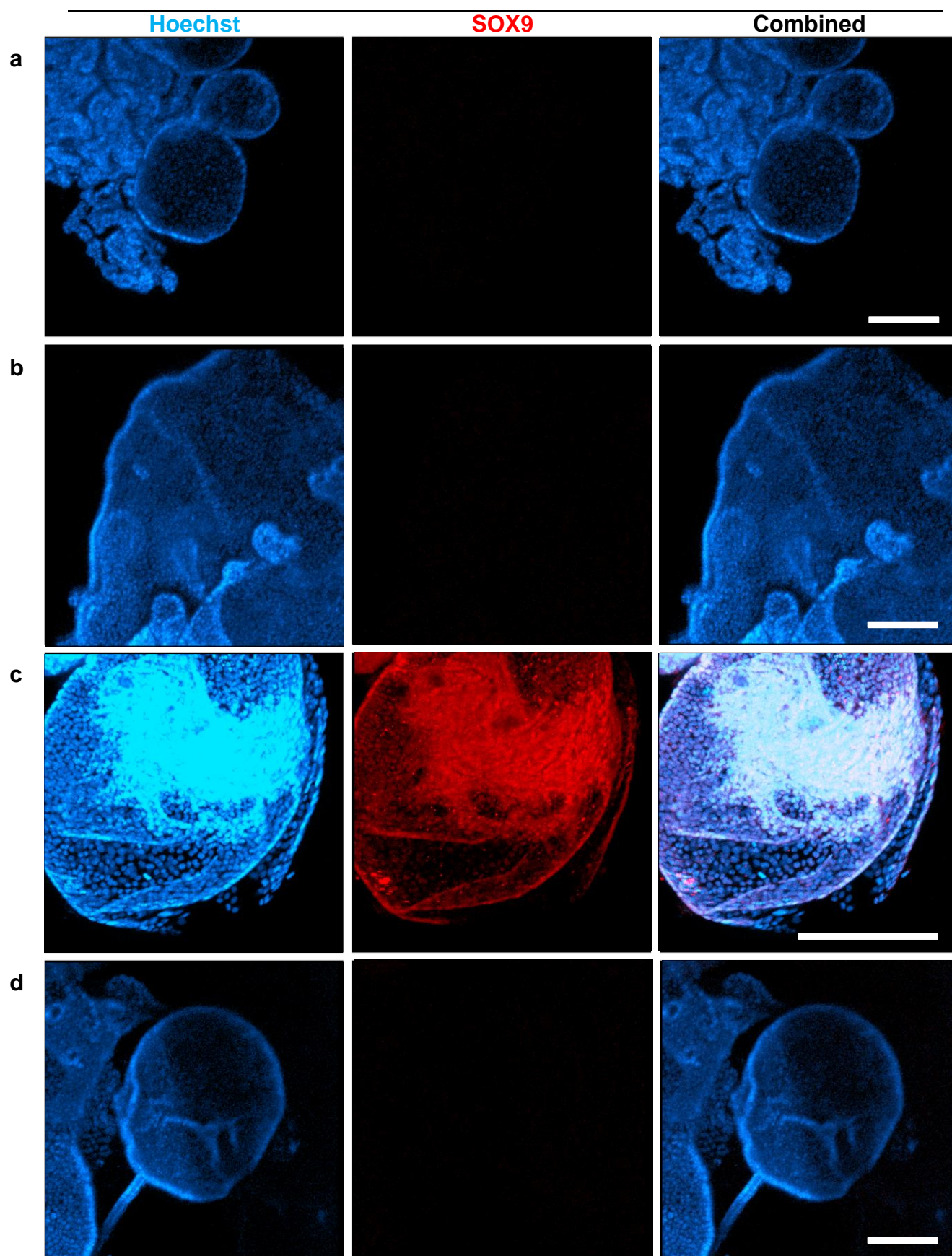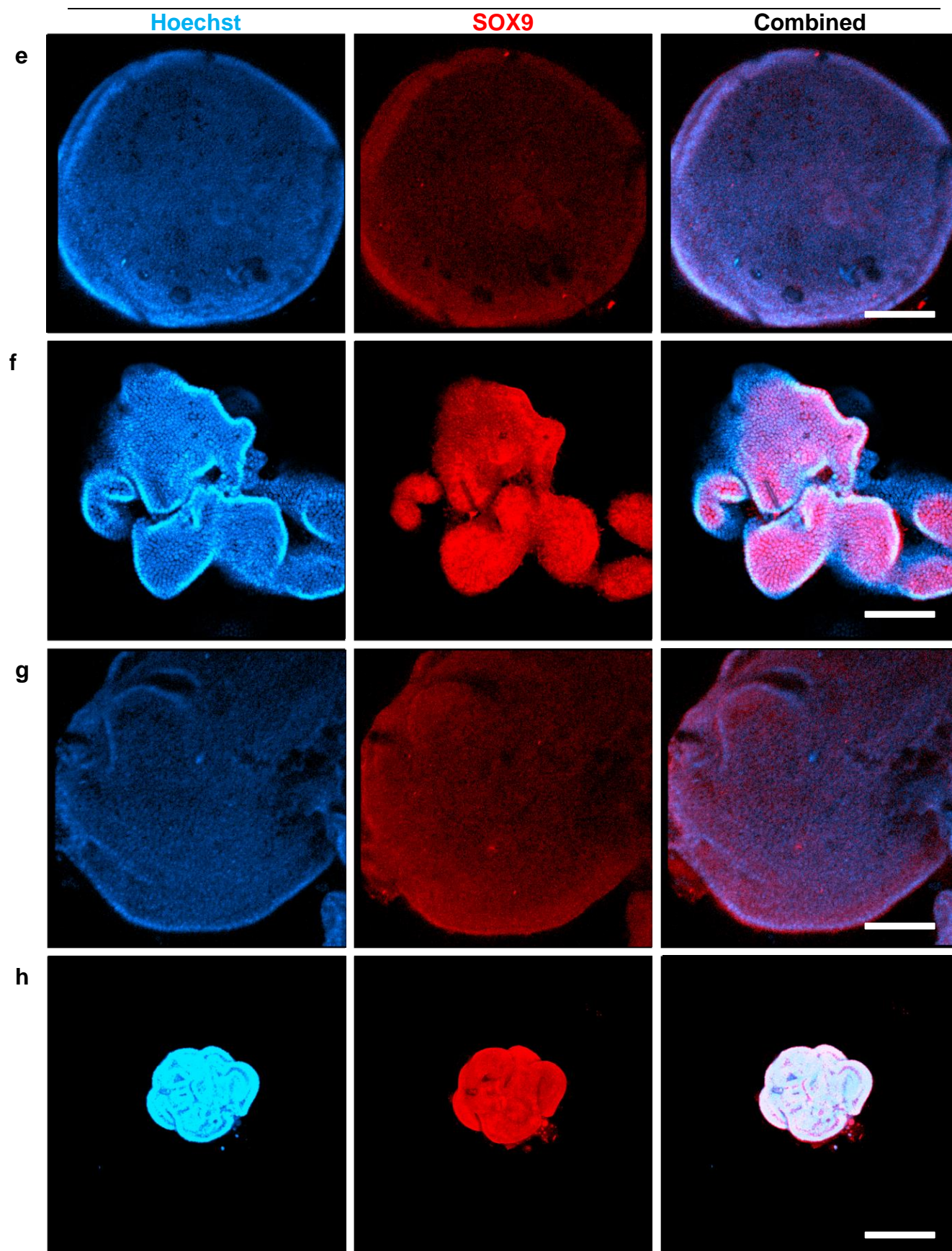
Figure 3.20 Immunofluorescent co-staining of SOX9 and DNA in Differentiated and Non-differentiated Mouse Liver Organoids. a-d. Non-differentiated organoids expressed the transcription factor SOX9 signal at very low levels in the cell membrane of all cells for most samples. **e-h.** The differentiated organoids expressed SOX9 signal at high levels in the cell membrane of all cells in the organoids. (Scale bar = 100 µm).

Hoechst	EpCAM	Combined
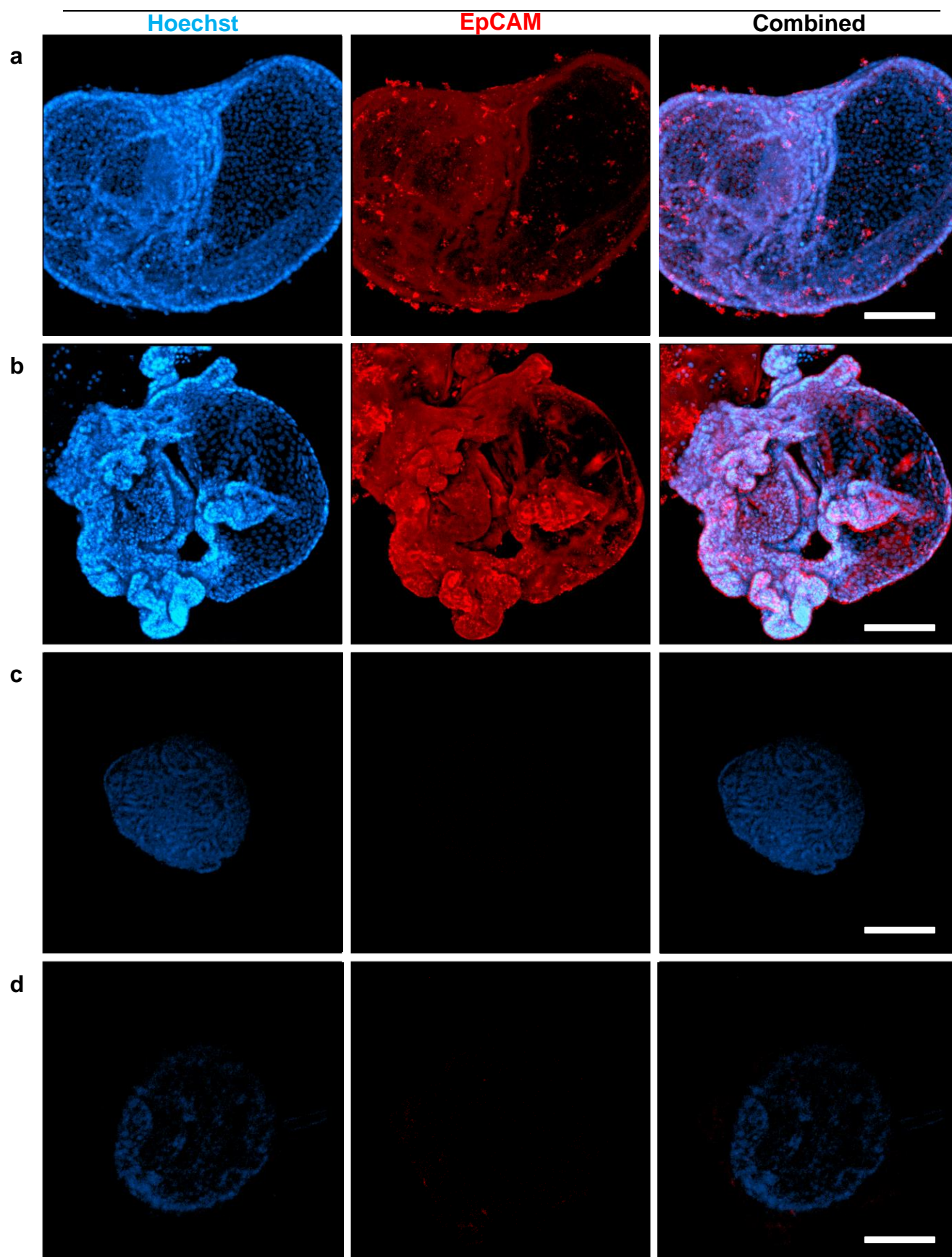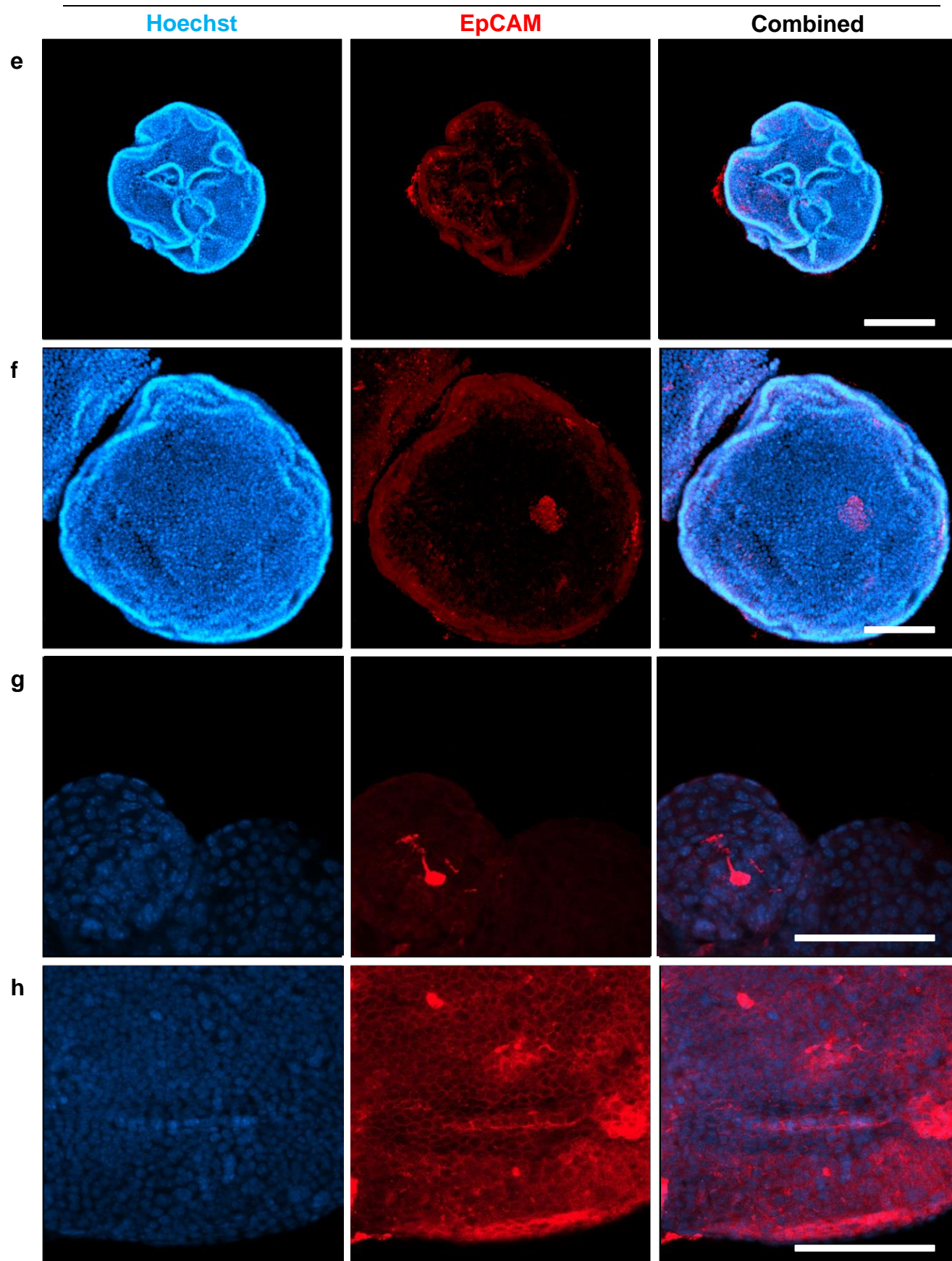
Figure 3.21 Immunofluorescent co-staining of EpCAM and DNA in Differentiated and Non-differentiated Mouse Liver Organoids. a-d. Non-differentiated organoids expressed the epithelial cell adhesion molecule staining signal at sporadically both between and on the cell membrane of cells with some samples showing no signal. **e-h.** The differentiated organoids express EpCAM staining at high levels for sample **h**, but sporadically in the cell membrane of some cells in the organoids. (Scale bar = 100 µm).
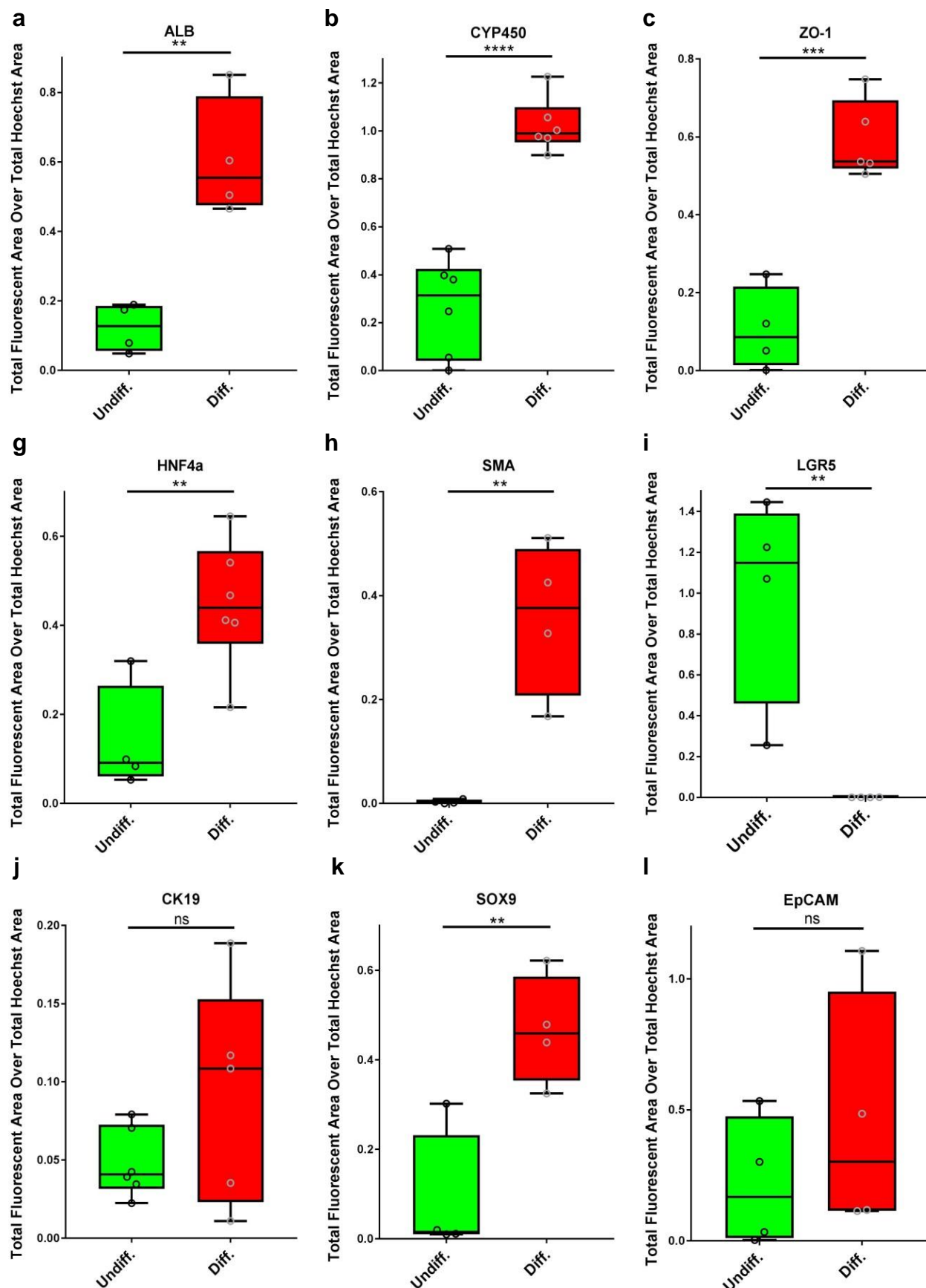
Figure 3.22 Immunofluorescent co-staining Quantification of Markers of liver Function. Ratio of total florescence area over total Hoechst stain area was measured in undifferentiated and differentiated organoids (n=4-6). Data were analysed using a one-way ANOVA to establish significant differences between the means of groups. * $p \leq 0.05$, ** $p \leq 0.01$, *** $p \leq 0.001$, **** $p \leq 0.0001$, ns $p > 0.05$. Error bars indicate ± standard error of the mean.

By comparing the total area of florescence of the immunolabelled proteins of interest to the total area of florescence of the Hoechst stain, a ratio of florescent signal could be used to compare the expression of proteins between differentiated and undifferentiated organoids. This method was used because other protein quantifying methods such as western blotting may not be expected to measure relative expression levels effectively because organoids cell cultures generally produce a very low yield. We identified that Albumin, Cytochrome p450, ZO-1, HNF4α, SMA-α and SOX-9 protein expression was significantly higher in the differentiated organoid, while LGR5 protein expression was significantly higher in the undifferentiated organoids.

Combined　　　　　　　　　　　**Hoechst LGR5 ZO-1**
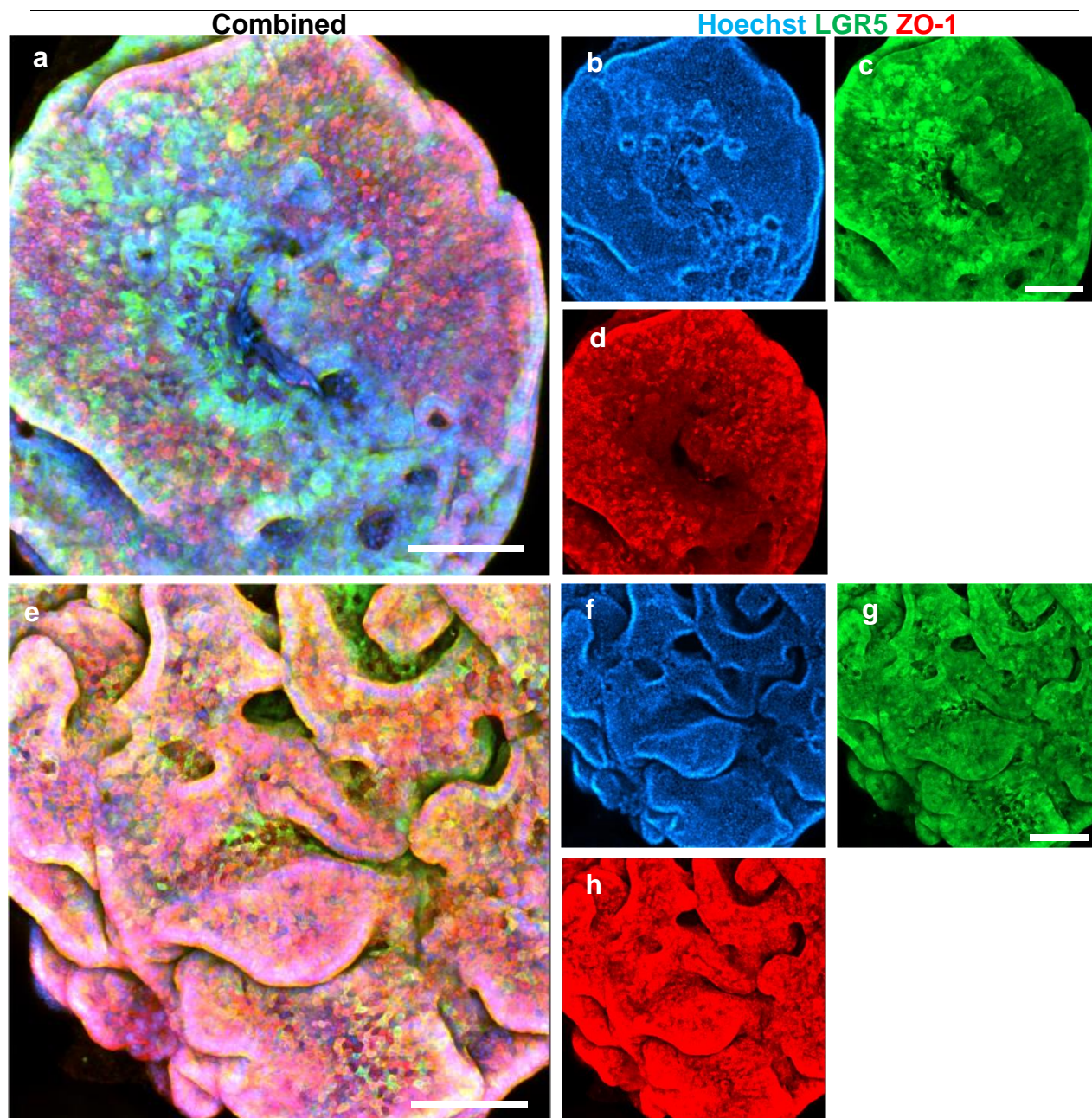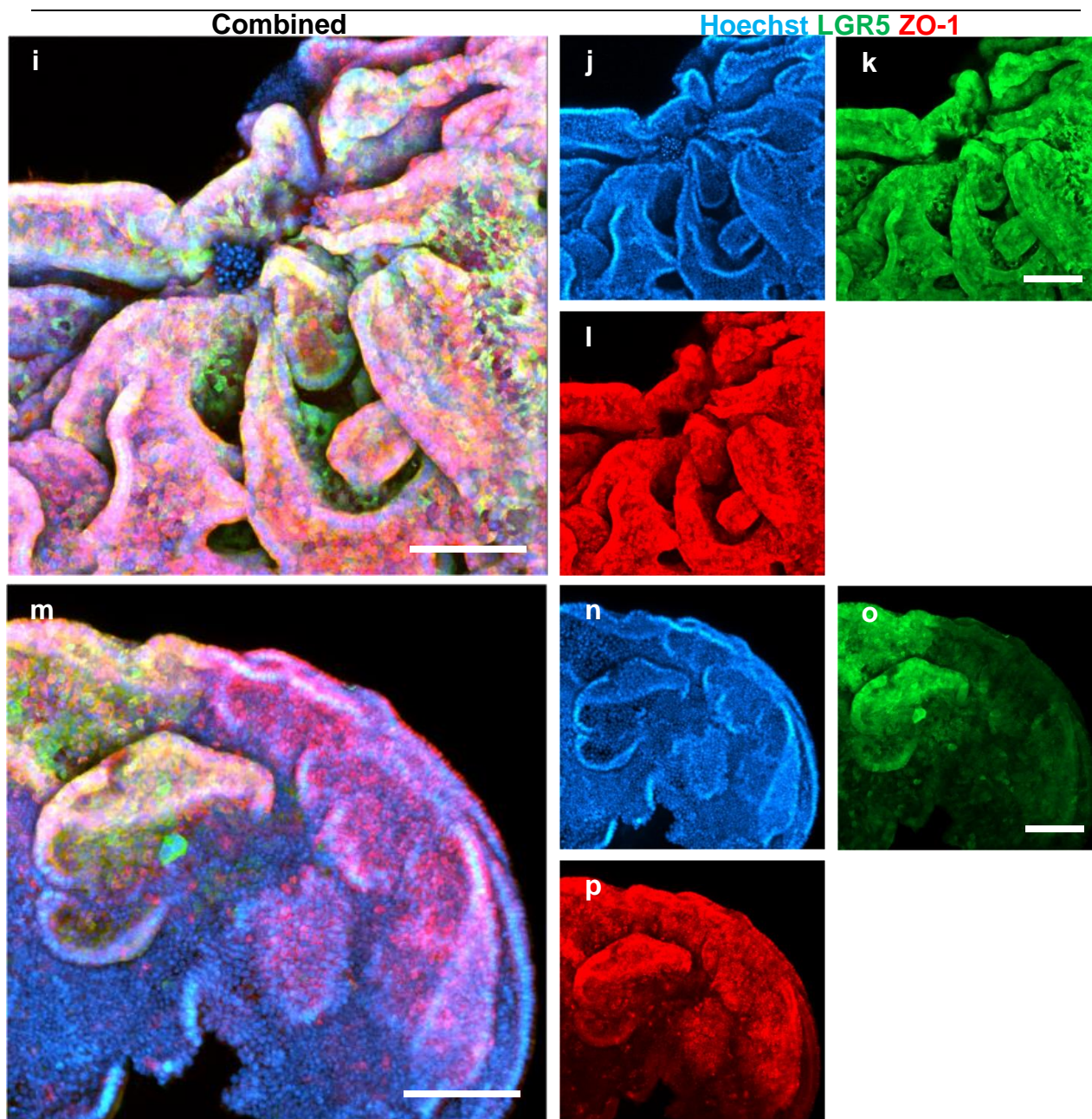
Figure 3.23 Immunofluorescent Co-staining of DNA, LGR5 and ZO-1 in Differentiated Mouse Liver Organoids using Confocal Laser Scanning Microscopy. Immunolabelling of differentiated organoids with LGR5 (Green), ZO-1 (Red) allows for the identification of different cell types within the organoids. (DNA is stained Blue) (Scale = 100 μm).

3.2.5 Light-Sheet Microscopy Analysis
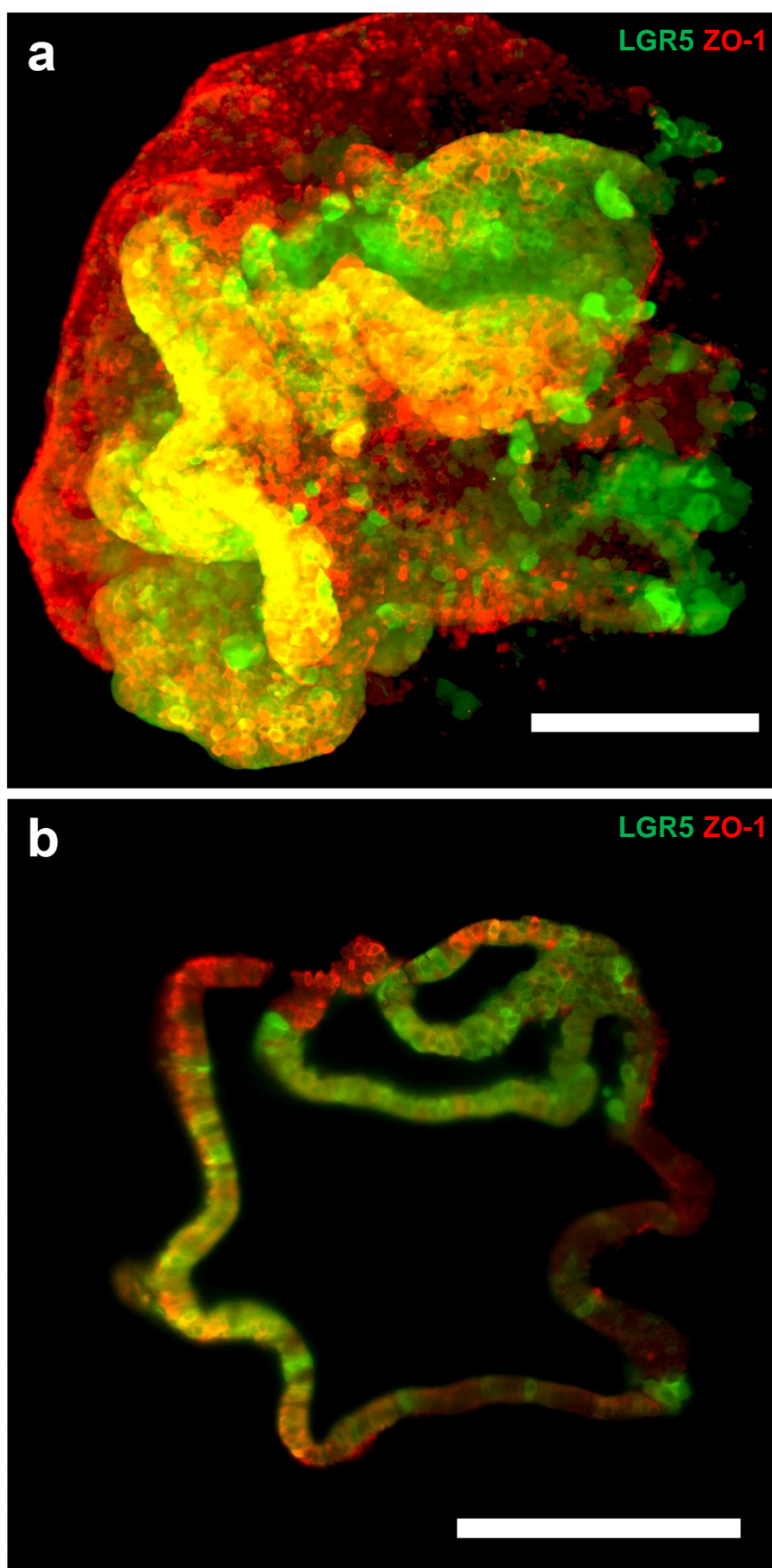
Figure 3.24 Immunofluorescent Co-staining of LGR5 and ZO-1 in Differentiated Mouse Liver Organoids using Light-Sheet microscopy. a. Immunolabelling of differentiated organoids to with LGR5 (Green) and ZO-1 (Red) allows for the identification of different cell types within the organoids (Scale = 200 μm). **b.** Cross-section of a single layer of the light-sheet image of the same sample (Scale = 100 µm).

Using confocal laser scanning microscopy and light-sheet microscopy of differentiated organoids that have been immunolabelled with multiply antibody markers of both liver differentiation and stemness. We were then able to identify multiple cell types in the same organoid.

3.3 DISCUSSION

The aim of the studies described in this chapter were to establish and characterise a mouse liver organoid cell culture model for investigating the interventions undertaken in the subsequent chapters. Using the established protocol (Broutier *et al* 2016) we observed ductal structures and single cells expand into organoids over the expected timeframe. These organoids displayed self-folding, budding and expansion to sizes more than 1000 µm. The cells did not divide within the organoids evenly as shown in Figure 3.11. This may be due to the different cell types within the organoids because organoids reflect the primary stem cell niche from which the cells are derived and differentiated *in vitro*; hence there will be cells within the organoids that were differentiated and others which retained a stem-cell like phenotype.

Gene expression analysis showed a shift in expression characteristic of a change from a liver stem-cell like phenotype to a differentiated hepatocyte phenotype and closely resembled to those in primary hepatocytes (Figure 3.12) (Huch *et al* 2013; Huch *et al* 2015; Broutier *et al* 2016). We found that characteristic markers of a primary liver stem cell-like phenotype *Mrp4*, *Lgr5*, *Ck19*, *Prom1*, *Ck7* and *Cd34* were downregulated during cell differentiation and correlated with the measured expression of primary hepatocytes, suggesting that cells in our liver organoid model had the capacity to differentiate into functional hepatocyte like phenotype (Huch *et al* 2013; Huch *et al* 2015; Broutier *et al* 2016). Consistent with this, we found that hepatocyte marker genes such as *Alb*, *Cyp3A11*, *G6pc*, *ZO-1*, *Hnf4α*, *Tbx3, Fah* and *Sox9* were upregulated during cell differentiation and correlated with the measured expression of primary hepatocytes.

Moreover, analysis of protein expression revealed a general change in cell phenotypes characteristic of transitioning from a stem cell-like phenotype to a hepatocyte phenotype (Figure 3.22) (Huch *et al* 2015; Broutier *et al* 2016). The changes we observed were however

heterogeneous, reflecting a general degree of variation between organoids within the same cultures. Nonetheless, it was particularly evident that protein expression of albumin from being undetectable to ubiquitous (Figure 3.13) and cytochrome p450 protein expression which changed from only being identified in a few cells to being numerous (Figure 3.14), confirming cellular differentiation of stem cells into a hepatocyte phenotype. Supporting this further we found that protein expression of a reliable cell surface marker, tight junction protein ZO-1 showed a very strong signal in differentiated hepatic phenotype and the level of expression was comparable to that of primary hepatocytes (Figure 3.15). Further, as expected, LGR5, a highly reliable cell surface marker of a primary liver stem-like phenotype (Huch *el al* 2013), showed intense staining in non-differentiated cells whereas its signal intensity was absent in the differentiated organoid cell culture with a few stem cell-like cells showing some positive staining (Figure 3.18e and h). Thus, these findings are consistent with published studies demonstrating the expression of hepatocellular markers during the development and differentiation of organoids (Huch *et al* 2013; Huch *et al* 2015; Broutier *et al* 2016).

By immunolabeling of LGR5 and ZO-1which represent cell surface markers of a stem cell-like phenotype and hepatocyte phenotype, respectively, I was able to observe the variation in cell type within the organoids (Figures 3.23 and 3.24). In line with this, the immunolabeling of cells in Figure 3.24b demonstrates the transition between stem cell-like cells (Green), and differentiated cells that are characteristic of a hepatic phenotype (Red). Similar to the hepatic stem cell niche, liver stem/progenitor cells continuously generated new hepatocytes in the portal field (Figure 1.8) which mature on their way to the central vein (Kordes and Häussinger 2013). Further, it can also be seen that the stem cell-like cells are dividing while the hepatocytes mostly remain undivided, thus supporting published studies (Kordes and Häussinger 2013).

Thus, the findings described in this chapter demonstrate that following the methods established in the literature (Broutier *et al* 2016), the organoids that have been developed accurately model

the morphological, gene expression and protein characteristics of mouse liver tissue *in vitro*. Therefore, we conclude that they are useful for the studies described in the following chapters on modelling of liver injury, fibrosis, and recovery.

CHAPTER 4

IN VITRO MODELLING OF LIVER INJURY AND FIBROSIS WITH 3D LIVER ORGANOIDS CO-CULTURED WITH HEPATIC STELLATE CELLS

CHAPTER 4

IN VITRO **MODELLING OF LIVER INJURY AND FIBROSIS WITH 3D LIVER ORGANOIDS CO-CULTURED WITH HEPATIC STELLATE CELLS**

KEY FINDINGS

1. The liver injury model in this chapter was a combination of mouse liver organoids and HSC cells. This model accurately represented certain aspects of liver injury *in vitro*.

2. Trans-differentiation of HSCs from a quiescent to a SMA-α positive activated phenotype was dependent on exposure to hepatocytes, TNF or TGF-β.

3. The liver injury model did not for the most part replicate an expected gene expression profile for liver injury or have differential collagen I expression.

4. Halofuginone treatment caused a reduction in HSC proliferation, although this did not cause an increase in hepatocyte survival.

5. Halofuginone suppresses *Col1a1*, *Mmp14* and *Timp2* under certain liver injury conditions.

CHAPTER 4 IN VITRO MODELLING OF LIVER INJURY AND FIBROSIS WITH 3D LIVER ORGANOIDS CO-CULTURED WITH HEPATIC STELLATE CELLS

4.1 BACKGROUND

In chapter 3 it was demonstrated that mouse liver organoids can accurately model liver tissue *in vitro*, representing liver parenchymal cells like hepatocytes. Liver injury usually occurs because of immune-mediated or direct injury to the hepatocytes. Hepatocytes release ROS and apoptotic bodies during the initiation of liver injury, which stimulate the activation of proinflammatory cytokines/immune cells and HSCs. This cell activation and the crosstalk between these cell populations is what defines liver injury, and the initiation and progression of fibrosis.

The fibrotic process is perpetuated by inflammatory cytokines such as TNF released by leukocytes that traffic to the damaged liver tissue, and growth factors such as TGF-β released by HSCs. These cytokines induce a cycle of inflammation, apoptosis, and proliferation, as well as the activation and proliferation of HSCs from a quiescent state to myofibroblastic phenotype, which produces ECM components like type I collagen. HIF-1α is also upregulated in macrophages and hepatocytes during injury, regulating genes that have been implicated in fibrosis.

The relevance of fibrosis for the progression of chronic liver diseases has generated interest in antifibrotic therapies for example for patients with NAFLD and/or NASH (Tacke and Weiskirchen, 2018). The small molecule Halofuginone, an analog of Febrifugine (Figure 4.1) which has been found to have anti-fibrotic properties, such as attenuating collagen α1(I) gene expression in rat and mouse models, as well as a reduction in the levels of collagen systhesis, resulting in complete resolution of the fibrosis. The ability of Halofuginone to elicit resolution of pre-existing fibrosis is partially due to its ability to reduce collagen synthesis and simultaneously to increase collagenase activity by augmenting synthesis of the TIMPs that regulate MMPs activity (Pines and Spector, 2015). Halofuginone was found to overcome TGF-

β-induced collagen synthesis in human and Tsk skin fibroblasts (Pines and Spector, 2015). In various fibrotic models no effect of Halofuginone was observed on expression of the TGF-β receptor gene or on TGF-β levels a finding that supports the hypothesis that the Halofuginone target is downstream in the TGF-β pathway. Halofuginone *in vitro* reduced Smad3 protein, inhibited TGF-β-dependent Smad3 phosphorylation and elevated expression of the inhibitory Smad7 in a variety of cell types, such as fibroblasts, HSCs and pancreatic stellate cells, tumour cells, and myoblasts (Pines and Spector, 2015).

As discussed in Chapter 1, newly designed *in vitro* models of liver disease need to satisfy the requirements of being high through put while still accurately replicating aspects of liver anatomy and metabolism. This thesis proposes combining organoid cell culture and an immortalised cell line to investigate the crosstalk between hepatocytes and HSCs, respectively. Such a model should satisfy the requirements for an effective *in vitro* model of that liver such as organotypic morphology, functions, interactions, the technical ease of use, ease of maintenance and throughput, all outlines in Table 1.1. These models have been used individually to study liver disease (Nantasanti *et al* 2016; Puche *et al* 2013), combining them should produce a more accurate representation of liver anatomy and metabolism, while still using conventional cell culture transwells that are commercially available and can be used for high through put experimentation.

I hypothesized that a mouse liver organoid culture combined with the mouse hepatic stellate cell line (JS1) (Guo *et al* 2009) in a transwell system (Figure 4.2a, using methods described in section 2.9) could accurately model the cellular crosstalk that occurs between injured hepatocytes and HSCs. The immune mediated liver injury could be modelled by treating the co-culture with TNF or TGF-β. Alternatively hypoxia can be used to induce hepatocyte injury directly and HIF-1α related fibrosis. To assess to capacity of this liver injury model to

accurately represent liver injury; morphology, cell viability, liver injury relevant gene expression and protein expression were assessed for both the organoid cell culture and the JS1 cell line. Halofuginone would be tested as an agent to reverse the liver injury phenotype (based on experiments by Huo *et al* 2015).

4.1.1 METHODS

Organoid and JS1 morphology was observed using contrast phase microscopy. Organoid culture viability was measured using a CellTiter-Glo® 3D cell viability assay and JS1 culture viability using an MTT assay. Gene expression for liver injury and fibrosis related genes such as *Col1a1* and *Fn1* were measured using RT-qPCR analysis of custom TaqMan[TM] Openarray assays. RNA was extracted from our cell culture samples using RNA column extraction. All RNA samples were tested for quality and integrity before being transcribed into cDNA for RT-qPCR analysis. HSC activation was observed by fixing and immunolabeling JS1 cells for SMA-α (Abcam 32575), fluorescently staining the cells using Alexa Fluor® 594 Goat anti-rabbit IgG (Invitrogen A-11037) antibody and an LSM 800 with Airyscan system (ZEISS) confocal microscope. HSC collagen I expression was observed by fixing and immunolabeling JS1 cells for collagen I (Abcam 21286). Four biological replicates were used per organoid group (that is 4 different primary liver organoid cultures from 4 different mouse clones). Four technical replicates were used per JS1 cell culture group.
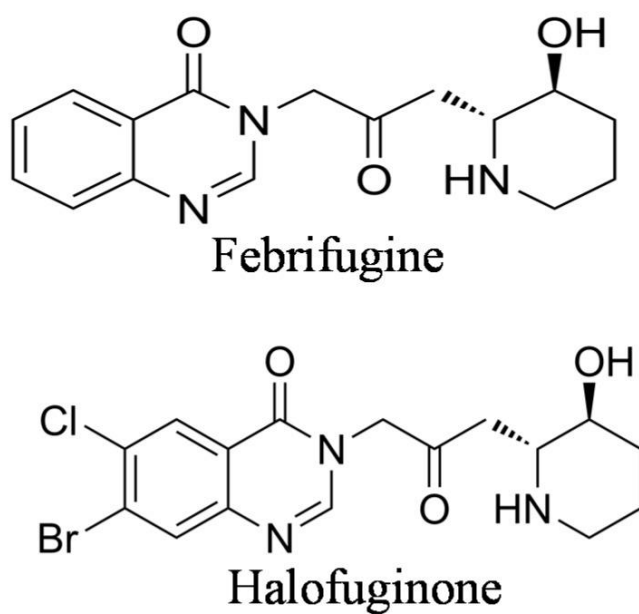
Figure 4.1 Chemical Structures of Febrifugine and Chemical Analogue Halofuginone.

(Pines and Spector, 2015)
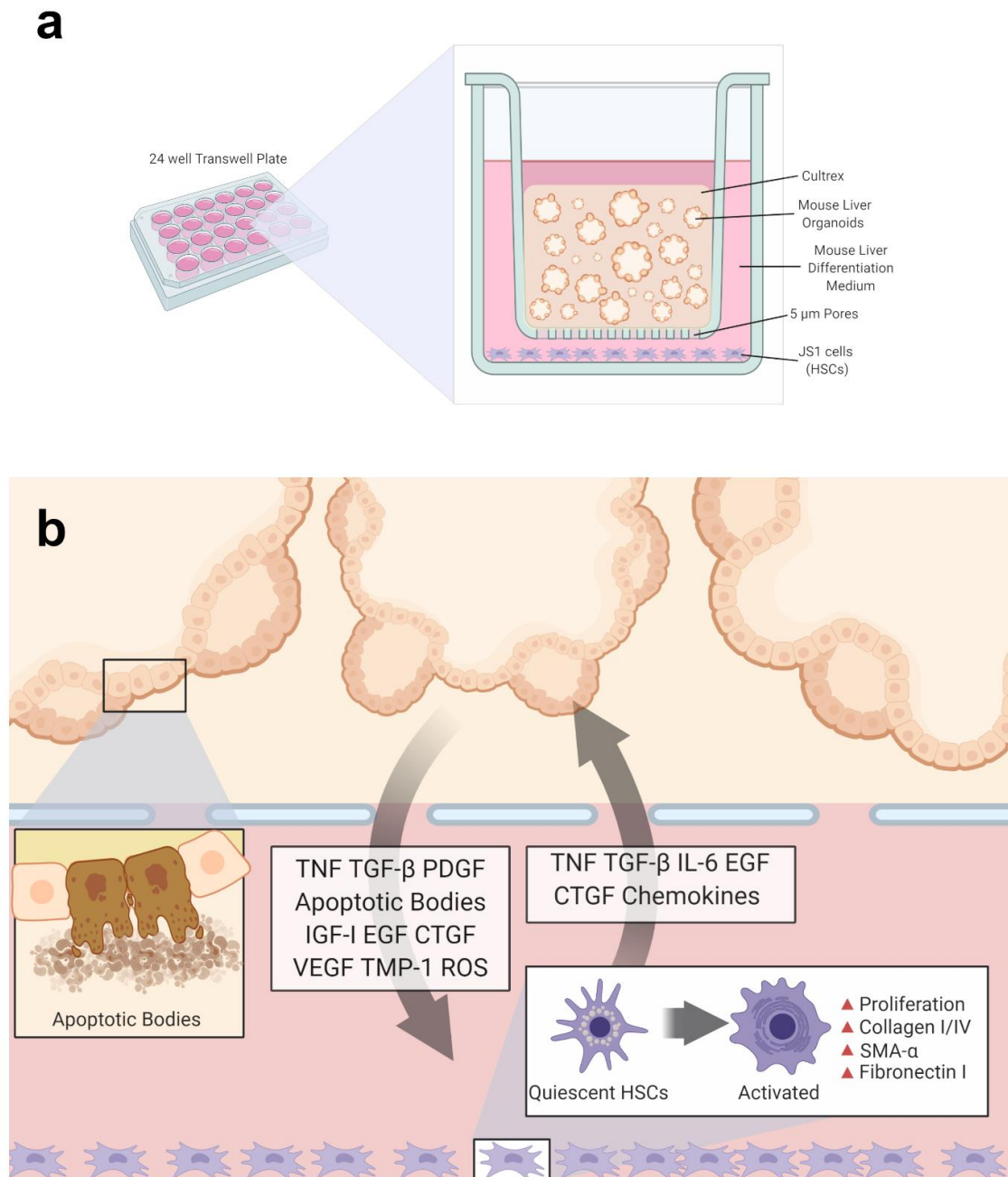
Figure 4.2 *In vitro* **Liver Injury Model Design a.** Mouse liver organoids and the JS1 cell line co-cultured in a transwell system in a 24 well cell culture plate. **b.** Diagram of the interactions expected to occur between the liver organoids and the JS1 cells which model liver injury, such as the release of fibrosis related cytokines, apoptotic bodies, ROS, as well as the activation of HSCs.

4.2 RESULTS
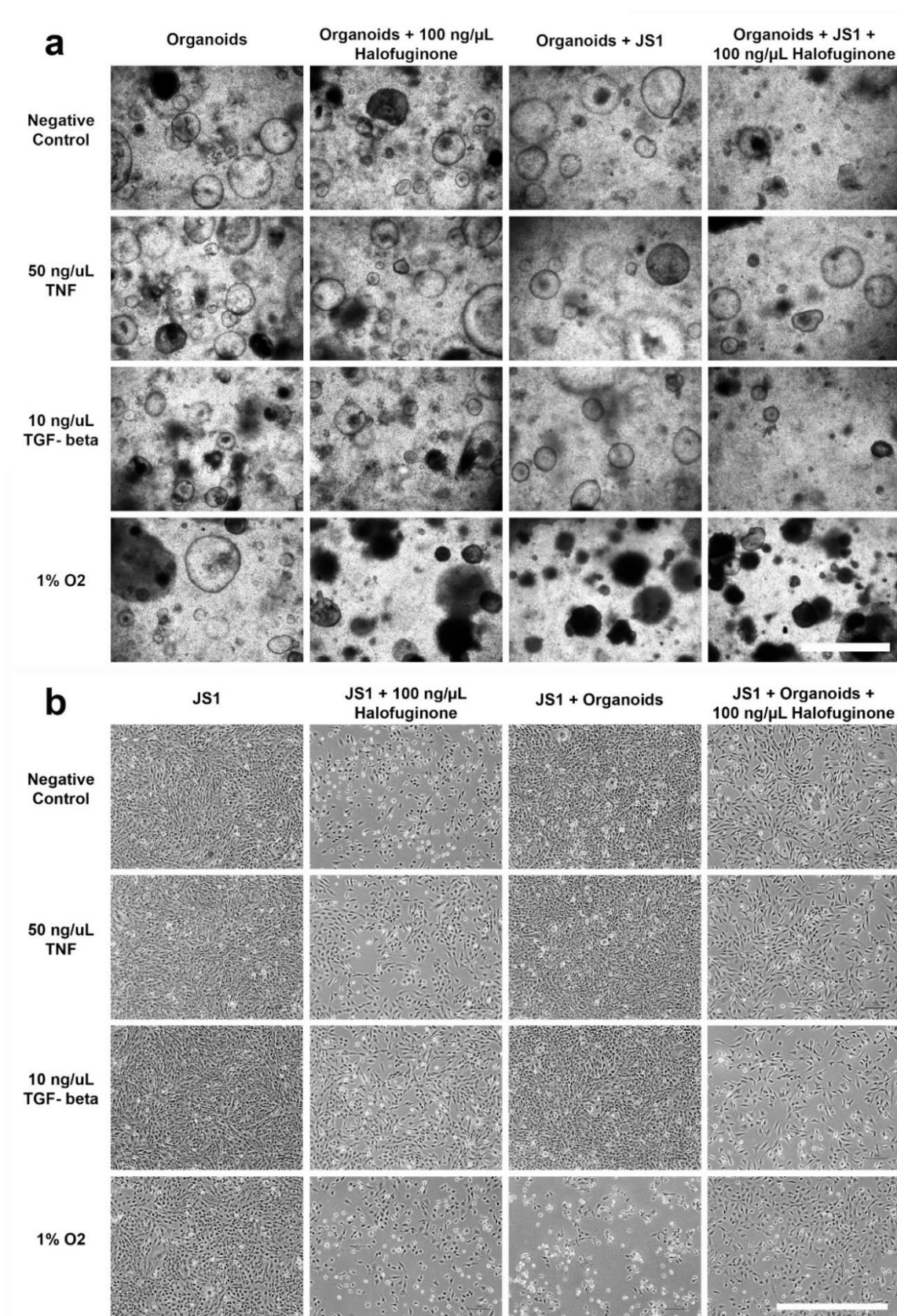
4.2.1 Contrast Phase Microscopy Analysis

Figure 4.3 Contrast Phase Microscopy Images of the Liver Injury Model a. Mouse liver organoids imaged within the insert of the transwell system after 48 hours of treatment. Each row represents a different treatment used to induce liver injury and the negative control group. Each column represents an organoid group treated with or without 100 ng/µL Halofuginone and/or in co-culture with the JS1 line (HSCs) (Scale = 500 µm). **b.** The JS1 cell line imaged in the bottom of the well of the transwell system after 48 hours of treatment. Each row represents a different treatment used to induce liver injury and the negative control group. Each column represents JS1 group treated with or without 100 ng/µL Halofuginone and/or in co-culture with the liver organoids (Scale = 1000 µm).

Co-culturing organoid with JS1 cells or treatment with TNF or TGF-β (Figure 4.3a) does not change the morphology of the organoids. Treatment with Halofuginone induces cell death and a loss of organoid morphology in both treated, co-cultured or control groups. Hypoxia treatment induces visible cell death and a loss of organoid shape in both co-culture and control groups. For the JS1 cells (Figure 4.3b) it was observed that they trans-differentiated to activated myofibroblasts in TNF, TGF-β and Halofuginone groups, as well as when co-cultured with organoids.

4.2.2 Cell Viability Analysis
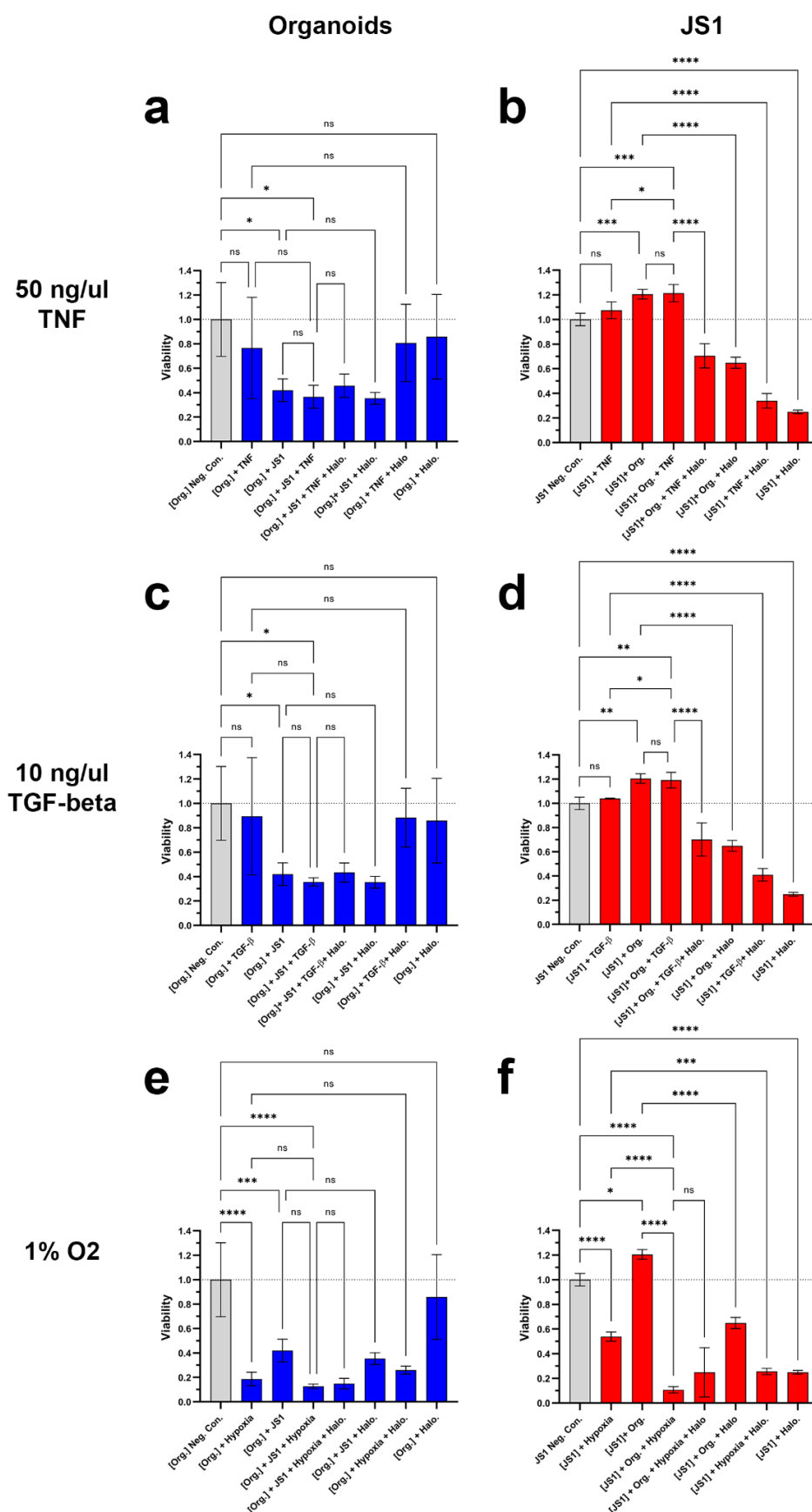
Figure 4.4 The Effects of Co-culturing, Inflammatory Cytokines, Hypoxia and Halofuginone on Liver Injury Model Viability. Cell viability of the organoid culture groups (Org.) (Blue) and the JS1 cell line groups (JS1) (Red) were measured after being treated with 50 ng/µL TNF (**a**, **b**), 10 ng/µL TGF-β (**c**, **d**) or 1 % O_2 (Hypoxia) (**e**, **f**) and then compared to the untreated negative control group (Neg. Con.) (Grey) (n=4) (in x-axis labels, '[ ]' indicates the culture in which viability was measured). The cell viability of the Org. and JS1 groups after co-culturing were measured individually and compared to the Neg. Con. (n=4). The cell viability or the co-cultures after being treated with 50 ng/µL TNF, 10 ng/µL TGF-β or 1 % O_2 were measured individually and compared to the Neg. Con. groups, the treatment only groups and the co-culture only groups (n=4). Every group was also compared to a treatment group with 100 ng/µL Halofuginone (Halo.) (n=4). Data were analysed using a one-way ANOVA to establish significant differences between the means of groups, and a post-hoc Holm-Šídák's multiple comparisons test for the pairwise comparison of the individual groups. * $p \leq 0.05$, ** $p \leq 0.01$, *** $p \leq 0.001$, **** $p \leq 0.0001$, ns $p > 0.05$. Error bars indicate mean ± the standard deviation.

TNF treatment groups and the relevant controls had significant variance within groups. TNF treatment decreased the mean viability of the organoid culture and increase the mean viability of the JS1 cell line, but neither changes were statistically significant ($p \leq 0.05$). Co-culturing of organoids and the JS1 cell line significantly decreased the mean viability of the organoid culture by more than 50%. On the other hand, the co-culturing caused a small but significant increase in the mean viability of the JS1 cell line (Figure 4.4). However, TNF treatment had no additive effect on the viability of either the organoids or the JS1 cells in the co-culture. Halofuginone treatment did not significantly change the mean viability of the organoid groups

compared to the relevant negative controls and did not prevent the reduction of viability of the organoids caused by co-culture with JS1 cells. However, as expected, Halofuginone treatment significantly decreased the mean viability of JS1 cells compared to the negative controls.

The results in the TGF-β treatment group were like those observed with TNF. TNF treatment had no additive effect on the viability of either the organoids or the JS1 cells in the co-culture.

TNF treated co-cultures, with Halofuginone treatment significantly decreased the mean viability of JS1 cells by more than 70% compared to the negative control group.

Hypoxic conditions induced by the application of 1% O_2 significantly decreased the mean viability of the organoid culture and the JS1 cells by more than 80% and 40%, respectively (Figure 4.4 panels e and f). Halofuginone on the other hand failed to prevent the reduction in the viability of organoids exposed to hypoxic condition. Unlike the co-cultures treated with either TNF or TGF-β treatment, the increased viability of JS1 cells co-cultured with the organoids under normoxic condition was drastically decreased by more than 80% when the cells were exposed to hypoxic condition.

4.2.3 RT-qPCR Analysis

Figure 4.5 *Col1a1* **Gene Expression Analysis of the Liver Injury Model.** *Col1a1* gene expression was measured for the Org. groups (n=4) and the JS1 groups (n=4) after treatment with 50 ng/µL TNF (**a**, **b**), 10 ng/µL TGF-β (**c**, **d**) or 1 % O2 (Hpx) (**e**, **f**). The gene expression of the Org. and JS1 groups after co-culturing were measured individually and compared to the Neg. Con (n=4). The gene expression or the co-cultures after being treated with 50 ng/µL TNF, 10 ng/µL TGF-β or 1 % O2 were measured individually and compared to the Neg. Con. groups, the treatment only groups and the co-culture only groups (n=4). Every group was also compared to a treatment group with 100 ng/µL Halo. group (n=4). Expression data was normalised to the *Hprt* housekeeper gene (n=4), and then normalised to the Neg. Con. group. Data was analysed using a one-way ANOVA to establish significant differences between the means of groups, and a post-hoc Holm-Šídák's multiple comparisons test for the pairwise comparison of the individual groups. * $p \leq 0.05$, ** $p \leq 0.01$, *** $p \leq 0.001$, **** $p \leq 0.0001$, ns $p > 0.05$. Error bars indicate mean ± the standard deviation.

There was no significant difference in the mean expression of *Col1a1* in the TNF treatment groups compared to the relevant controls. TNF treatment also did not cause a significant pairwise difference in mean *Col1a1* expression between any of the groups. On the other hand, 10 ng/µL TGF-β treatment caused a significant increase in *Col1a1* expression compared to the Neg. Control in the organoid groups, but this difference did not achieve a significant level in the JS1 groups. TGF-β treatment significantly increase *Col1a1* expression in the organoid treatment only group, but not in the co-culture only or co-culture with treatment groups. Halofuginone treatment of the TGF-β group did significantly decrease *Col1a1* expression. Further, Co-culture with JS1 cells or application of Halofuginone had no effect on *Col1a1* expression. In marked contrast, hypoxic condition induced by exposing the organoid to1 % O2

significantly increased ($p \leq 0.0001$) *Col1a1* expression compared to the Negative Control

group. However, although hypoxia increased *Col1a1* expression by nearly 5-fold compared to

Neg. Control group, the difference failed to achieve a significance. Exposure of the organoids

to 1 % O_2 did not affect *Col1a1* expression in the co-culture only or co-culture with treatment

groups. Interestingly, application of Halofuginone caused a small but significant reduction in

Col1a1 expression in the hypoxic group of organoids. None of the treatments influenced

Col1a1 expression in JS1 cells.
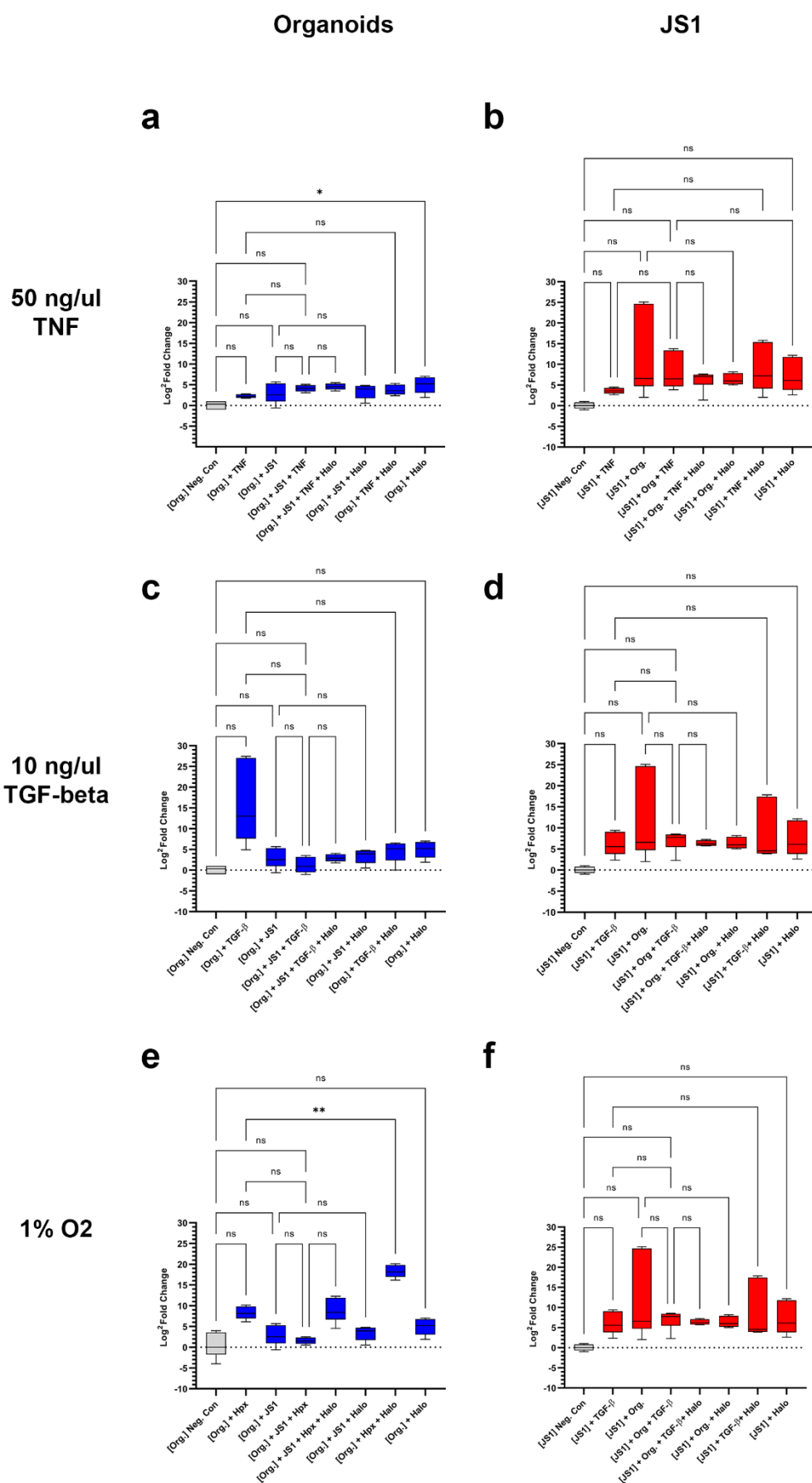
Organoids   **JS1**

Figure 4.6 *Col4a1* **Gene Expression Analysis of the Liver Injury Model.** *Col4a1* gene expression was measured for the Org. groups (n=4) and the JS1 groups (n=4) after treatment with 50 ng/µL TNF (**a**, **b**), 10 ng/µL TGF-β (**c**, **d**) or 1 % O2 (**e**, **f**). The gene expression of the Org. and JS1 groups after co-culturing were measured individually and compared to the Neg. Con (n=4). The gene expression or the co-cultures after being treated with 50 ng/µL TNF, 10 ng/µL TGF-β or 1 % O2 were measured individually and compared to the Neg. Con. groups, the treatment only groups and the co-culture only groups (n=4). Every group was also compared to a treatment group with 100 ng/µL Halo. group (n=4). Expression data were normalised to the *Hprt* housekeeper gene (n=4), and then normalised to the Neg. Con. group. Data were analysed using a one-way ANOVA to establish significant differences between the means of groups, and a post-hoc Holm-Šídák's multiple comparisons test for the pairwise comparison of the individual groups. * $p \leq 0.05$, ** $p \leq 0.01$, *** $p \leq 0.001$, **** $p \leq 0.0001$, ns $p > 0.05$. Error bars indicate mean ± the standard deviation.

The expression of *Col4a1* in response to 50 ng/µL TNF treatment was like that of *Col1a1* expression with TNF treatment groups and the relevant controls had no significant difference in the expression of *Col4a1* (Figure 4.6). There was however a small but significant increase in *Col4a1* expression in the organoids treated with Halofuginone alone compared to the Negative Control group. *Col4a1* expression increased due to 10 ng/µL TGF-β treatment in both the organoids and JS1 cells. However, the differences failed to achieve a significance. Hypoxia also had similar effects on *Col4a1* expression as in *Col1a1* expression; however, the expression in organoids alone did not reach significance (p>0.05). In contrast, application of Halofuginone further increased (p≤0.01) *Col4a1* expression compared to that of the organoids exposed to

hypoxia. None of the treatments had significantly affected *Col4a1* expression in JS1 cells

cultured alone or in co-culture with the organoids.

Organoids   **JS1**

Figure 4.7 *Fn1* Gene Expression Analysis of the Liver Injury Model. *Fn1* gene expression was measured for the Org. groups (n=4) and the JS1 groups (n=4) after treatment with 50 ng/µL TNF (**a**, **b**), 10 ng/µL TGF-β (**c**, **d**) or 1 % O2 (**e**, **f**). The gene expression of the Org. and JS1 groups after co-culturing were measured individually and compared to the Neg. Con (n=4). The gene expression or the co-cultures after being treated with 50 ng/µL TNF, 10 ng/µL TGF-β or 1 % O2 were measured individually and compared to the Neg. Con. groups, the treatment only groups and the co-culture only groups (n=4). Every group was also compared to a treatment group with 100 ng/µL Halo. group (n=4). Expression data were normalised to the *Hprt* housekeeper gene (n=4), and then normalised to the Neg. Con. group. Data were analysed using a one-way ANOVA to establish significant differences between the means of groups, and a post-hoc Holm-Šídák's multiple comparisons test for the pairwise comparison of the individual groups. * $p \leq 0.05$, ** $p \leq 0.01$, *** $p \leq 0.001$, **** $p \leq 0.0001$, ns $p > 0.05$. Error bars indicate mean ± the standard deviation.

TNF treatment groups and the relevant controls had a significant difference in the variance of the mean expression of *Fn1* for the organoid groups but not the JS1 groups. There was not a significant difference in mean gene expression with only TNF treatment or co-culturing, but there was a significant increase in mean gene expression of treatment and co-culturing together compared to the Negative Control group. The treatment and co-culturing group also had significant increases in mean gene expression compared to the treatment and co-culture only groups. There was also a significant decrease in the mean gene expression in the treatment and co-culture organoid group with Halofuginone treatment compared to just the treatment and co-culture group. 10 ng/µL TGF-β treatment groups and the relevant controls had a significant difference in the variance of the mean expression of *Fn1* for the organoid groups but not the

JS1 groups. There is a significant increase in the mean gene expression of *Fn1* in the organoid treatment group compared to the Negative Control group. There was also a significant decrease in the mean gene expression between the TGF-β treated co-culture group and the treatment only organoid group. No other pairwise comparisons were significantly different. 1 % O_2 treatment groups and the relevant controls had no significant difference in variance of mean *Fn1* expression between any of the groups. No pairwise comparisons were significantly different.

Figure 4.8 *Ctgf* Gene Expression Analysis of the Liver Injury Model. *Ctgf* gene expression was measured for the Org. groups (n=4) and the JS1 groups (n=4) after treatment with 50 ng/µL TNF (**a**, **b**), 10 ng/µL TGF-β (**c**, **d**) or 1 % O2 (**e**, **f**). The gene expression of the Org. and JS1 groups after co-culturing were measured individually and compared to the Neg. Con (n=4). The gene expression or the co-cultures after being treated with 50 ng/µL TNF, 10 ng/µL TGF-β or 1 % O2 were measured individually and compared to the Neg. Con. groups, the treatment only groups and the co-culture only groups (n=4). Every group was also compared to a treatment group with 100 ng/µL Halo. group (n=4). Expression data was normalised to the *Hprt* housekeeper gene (n=4), and then normalised to the Neg. Con. group. Data was analysed using a one-way ANOVA to establish significant differences between the means of groups, and a post-hoc Holm-Šídák's multiple comparisons test for the pairwise comparison of the individual groups. * $p \leq 0.05$, ** $p \leq 0.01$, *** $p \leq 0.001$, **** $p \leq 0.0001$, ns $p > 0.05$. Error bars indicate mean ± the standard deviation.

TNF treatment groups and the relevant controls had no significant difference in the variance of the mean expression of *Ctgf*. TNF treatment also did not cause a significant pairwise difference in mean *Ctgf* expression between any of the groups. 10 ng/µL TGF-β treatment groups and the relevant controls had no significant difference in the variance of the mean expression of *Ctgf*. TGF-β treatment also did not cause a significant pairwise difference in mean *Ctgf* expression between any of the groups. 1 % O_2 treatment groups and the relevant controls had a significant difference in the variance of the mean expression of *Ctgf* for the organoid groups but not the JS1 groups. No pairwise comparisons were significantly different.
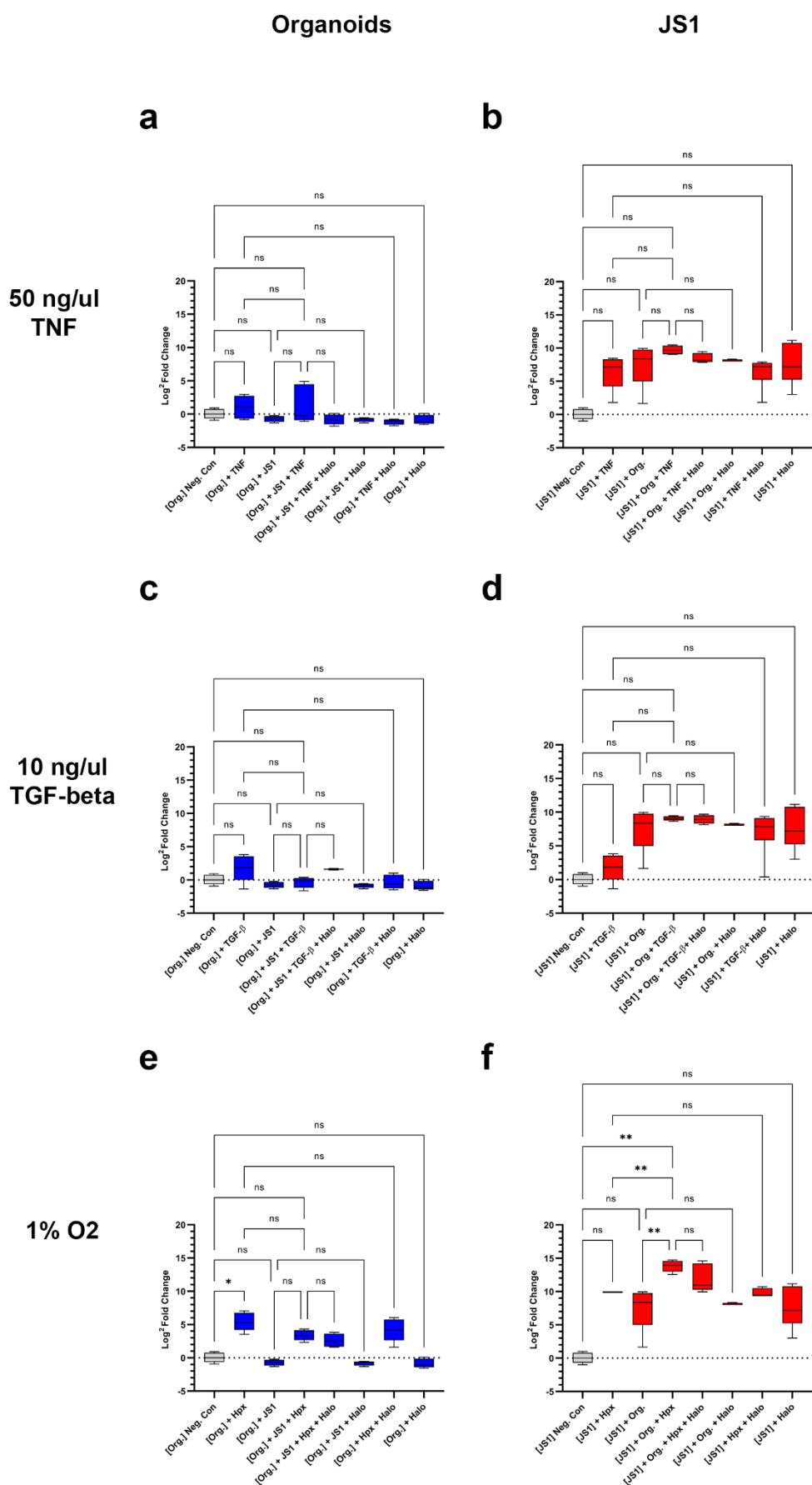
Figure 4.9 *Bsg* Gene Expression Analysis of the Liver Injury Model. *Bsg* gene expression was measured for the Org. groups (n=4) and the JS1 groups (n=4) after treatment with 50 ng/µL TNF (**a**, **b**), 10 ng/µL TGF-β (**c**, **d**) or 1 % O2 (**e**, **f**). The gene expression of the Org. and JS1 groups after co-culturing were measured individually and compared to the Neg. Con (n=4). The gene expression or the co-cultures after being treated with 50 ng/µL TNF, 10 ng/µL TGF-β or 1 % O2 were measured individually and compared to the Neg. Con. groups, the treatment only groups and the co-culture only groups (n=4). Every group was also compared to a treatment group with 100 ng/µL Halo. group (n=4). Expression data was normalised to the *Hprt* housekeeper gene (n=4), and then normalised to the Neg. Con. group. Data was analysed using a one-way ANOVA to establish significant differences between the means of groups, and a post-hoc Holm-Šídák's multiple comparisons test for the pairwise comparison of the individual groups. $* p \leq 0.05$, $** p \leq 0.01$, $*** p \leq 0.001$, $**** p \leq 0.0001$, ns $p > 0.05$. Error bars indicate mean ± the standard deviation.

TNF treatment groups and the relevant controls had no significant difference in the variance of the mean expression of *Bsg*. TNF treatment also did not cause a significant pairwise difference in mean *Bsg* expression between any of the groups. TGF-β treatment did not change the mean expression of *Bsg* for the organoid groups and the JS1 groups. TGF-β treatment did not cause a significant pairwise difference in mean *Bsg* expression between any of the groups. 1 % O_2 treatment caused a significant difference in the variance of the mean expression of *Bsg* for both organoid and JS1 groups. The organoid with treatment group had a significant increase in the mean expression of *Bsg* compared to the negative control group. The JS1 treatment and co-culture group had a significant increase in the mean expression compared to the negative control, but the treatment only and co-culture only groups did not have a significant increase

in mean expression. The JS1 treatment and co-culture group also had a significant increase in
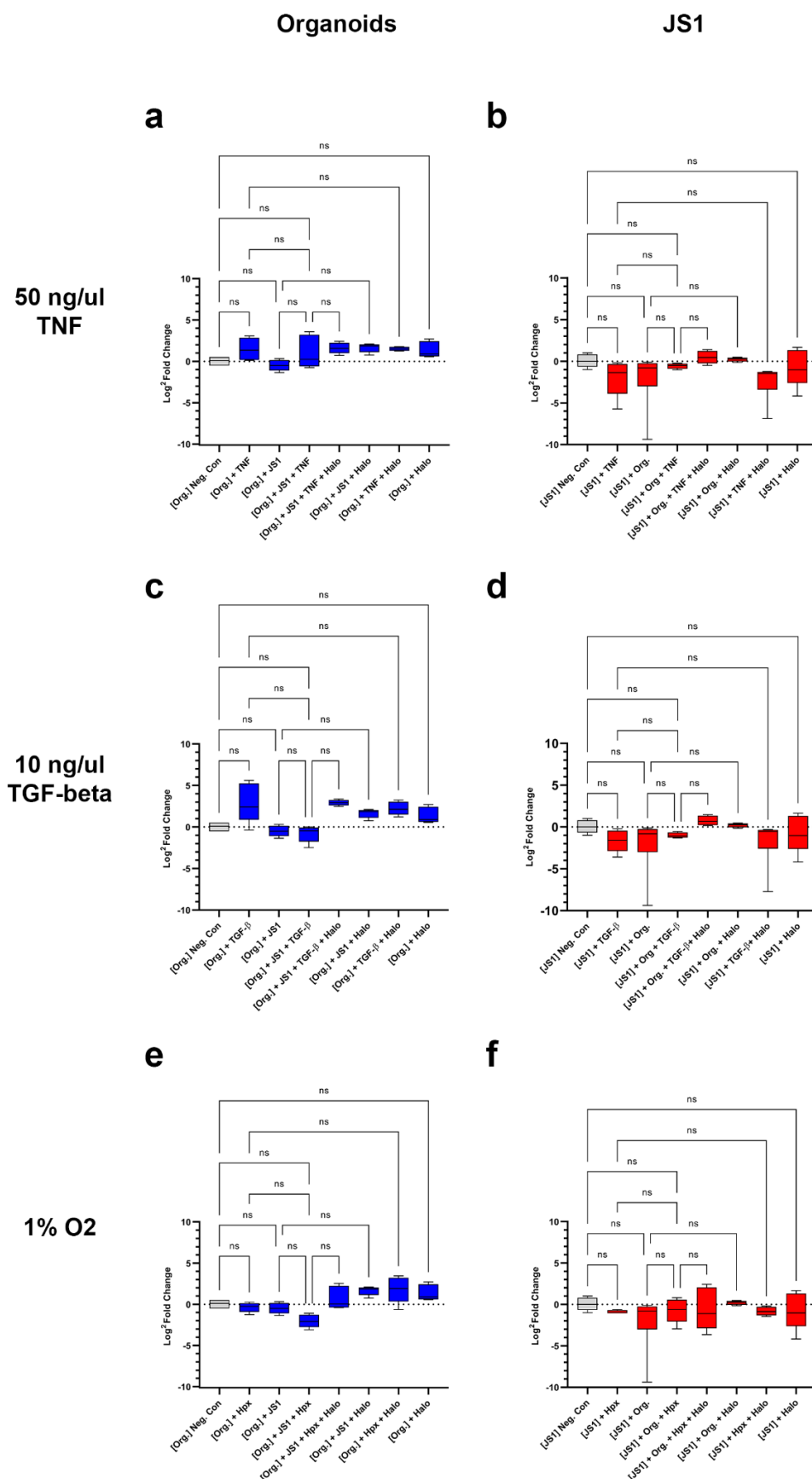
mean expression compared to the treatment only and co-culture only groups.

Figure 4.10 *Hif1a* Gene Expression Analysis of the Liver Injury Model. *Hif1a* gene expression was measured for the Org. groups (n=4) and the JS1 groups (n=4) after treatment with 50 ng/µL TNF (**a, b**), 10 ng/µL TGF-β (**c, d**) or 1 % O2 (**e, f**). The gene expression of the Org. and JS1 groups after co-culturing were measured individually and compared to the Neg. Con (n=4). The gene expression or the co-cultures after being treated with 50 ng/µL TNF, 10 ng/µL TGF-β or 1 % O2 were measured individually and compared to the Neg. Con. groups, the treatment only groups and the co-culture only groups (n=4). Every group was also compared to a treatment group with 100 ng/µL Halo. group (n=4). Expression data was normalised to the *Hprt* housekeeper gene (n=4), and then normalised to the Neg. Con. group. Data was analysed using a one-way ANOVA to establish significant differences between the means of groups, and a post-hoc Holm-Šídák's multiple comparisons test for the pairwise comparison of the individual groups. * $p \leq 0.05$, ** $p \leq 0.01$, *** $p \leq 0.001$, **** $p \leq 0.0001$, ns $p > 0.05$. Error bars indicate mean ± the standard deviation.

TNF treatment groups and the relevant controls had no significant difference in the variance of the mean expression of *Hif1a*. TNF treatment also did not cause a significant pairwise difference in mean *Hif1a* expression between any of the groups. 10 ng/µL TGF-β treatment groups and the relevant controls had no significant difference in the variance of the mean expression of *Hif1a*. TGF-β treatment also did not cause a significant pairwise difference in mean *Hif1a* expression between any of the groups. 1 % O$_2$ treatment groups and the relevant controls had no significant difference in the variance of the mean expression of *Hif1a*. Hypoxia treatment also did not cause a significant pairwise difference in mean *Hif1a* expression between any of the groups.
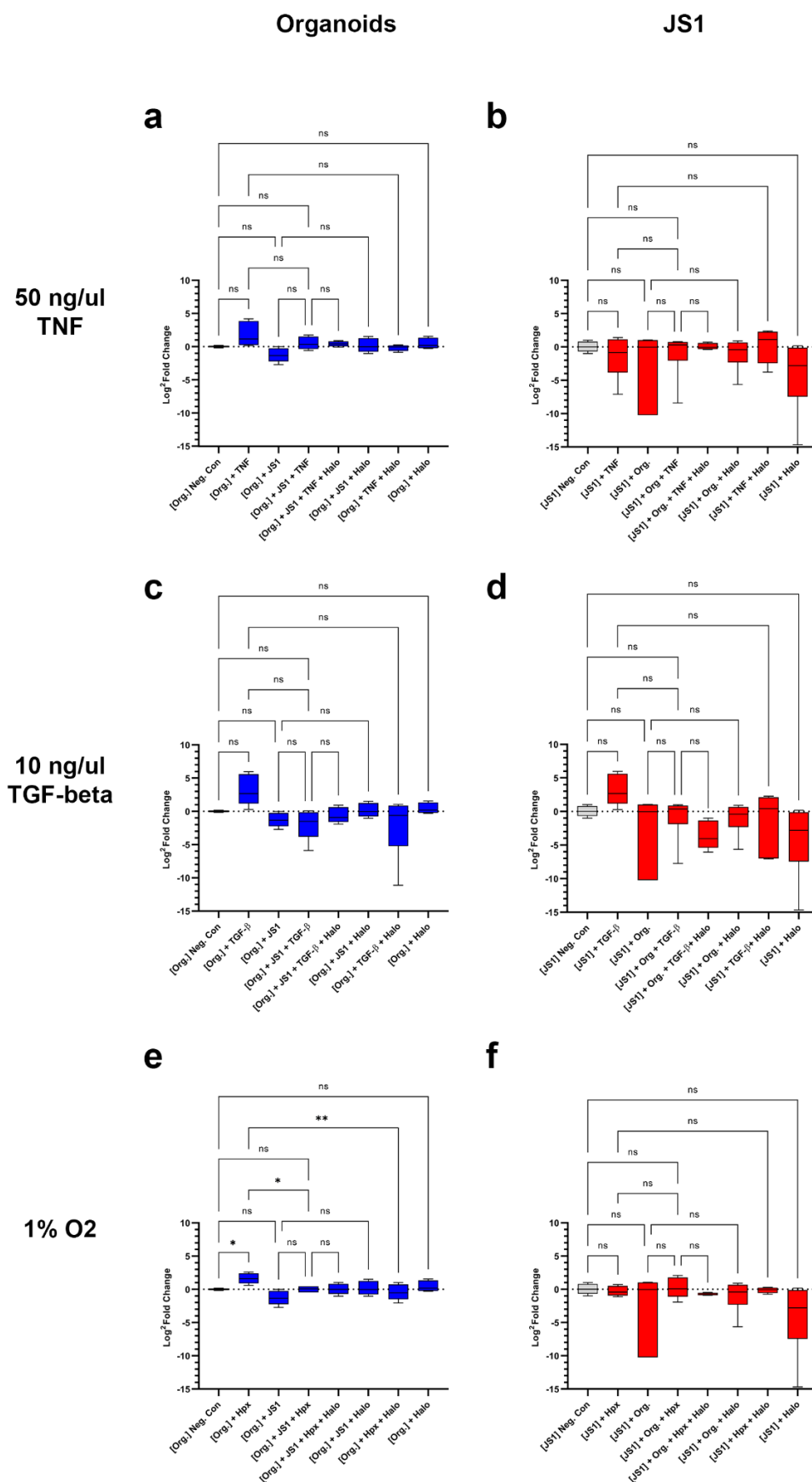
Figure 4.11 *Mmp14* Gene Expression Analysis of the Liver Injury Model. *Mmp14* gene expression was measured for the Org. groups (n=4) and the JS1 groups (n=4) after treatment with 50 ng/µL TNF (**a**, **b**), 10 ng/µL TGF-β (**c**, **d**) or 1 % O2 (**e**, **f**). The gene expression of the Org. and JS1 groups after co-culturing were measured individually and compared to the Neg. Con (n=4). The gene expression or the co-cultures after being treated with 50 ng/µL TNF, 10 ng/µL TGF-β or 1 % O2 were measured individually and compared to the Neg. Con. groups, the treatment only groups and the co-culture only groups (n=4). Every group was also compared to a treatment group with 100 ng/µL Halo. group (n=4). Expression data was normalised to the *Hprt* housekeeper gene (n=4), and then normalised to the Neg. Con. group. Data was analysed using a one-way ANOVA to establish significant differences between the means of groups, and a post-hoc Holm-Šídák's multiple comparisons test for the pairwise comparison of the individual groups. * $p \leq 0.05$, ** $p \leq 0.01$, *** $p \leq 0.001$, **** $p \leq 0.0001$, ns $p > 0.05$. Error bars indicate mean ± the standard deviation.

TNF treatment groups and the relevant controls had no significant difference in the variance of the mean expression of *Mmp14*. TNF treatment also did not cause a significant pairwise difference in mean *Mmp14* expression between any of the groups. 10 ng/µL TGF-β treatment groups and the relevant controls had no significant difference in the variance of the mean expression of *Mmp14*. TGF-β treatment also did not cause a significant pairwise difference in mean *Mmp14* expression between any of the groups. 1 % O_2 treatment groups and the relevant controls had a significant difference in the mean expression of *Mmp14* for the organoid groups, but not the JS1 groups. Hypoxia treatment significantly increased mean expression in the organoid group compared to the negative control group. The treatment compared to the co-culture group had a significant decrease in mean expression compared to the treatment only

group, and the addition of Halofuginone treatment also significantly decreased mean

expression compared to the treatment only group. For the other groups there were not

significant differences in gene expression.
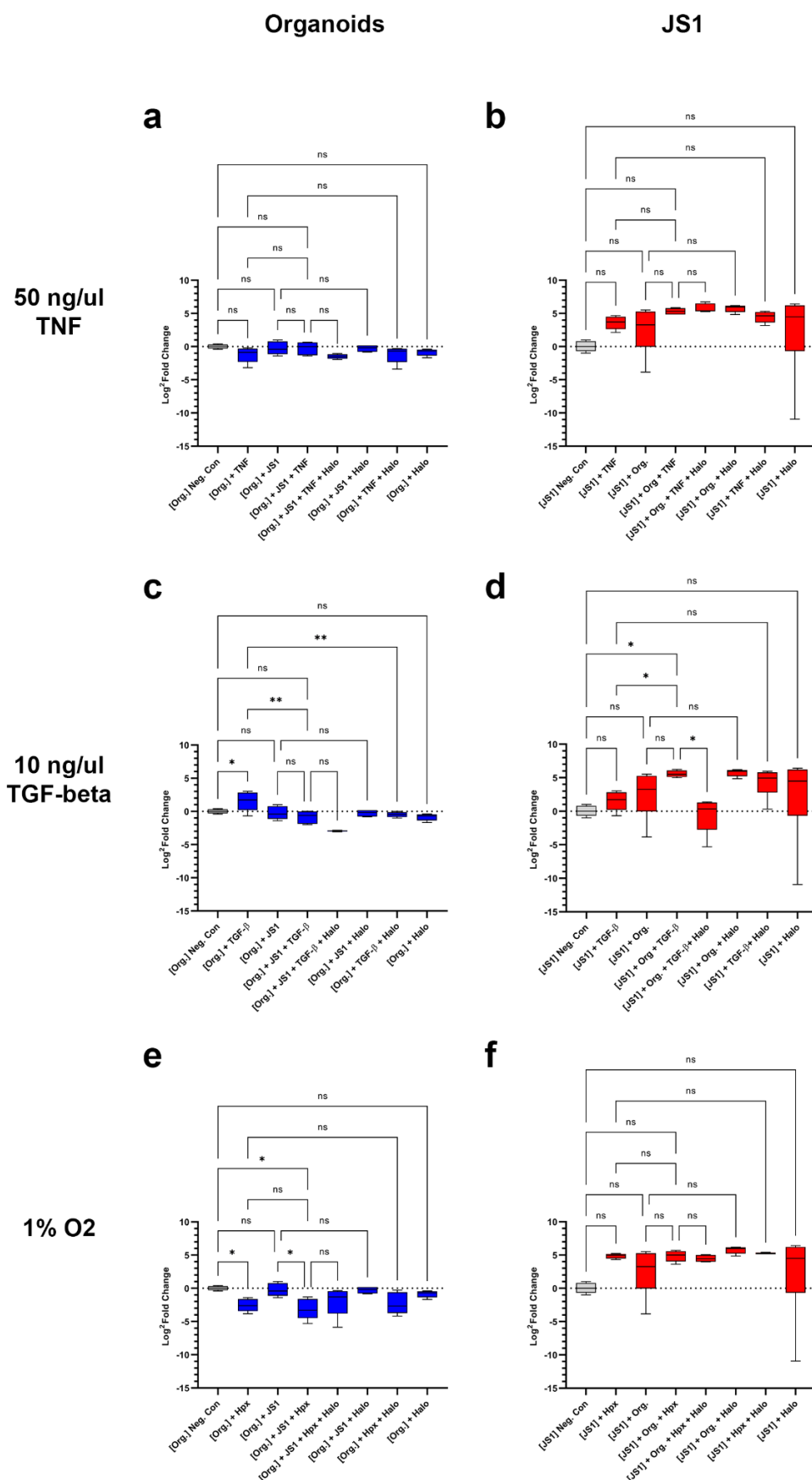
Figure 4.12 *Timp2* **Gene Expression Analysis of the Liver Injury Model.** *Timp2* gene expression was measured for the Org. groups (n=4) and the JS1 groups (n=4) after treatment with 50 ng/µL TNF (**a**, **b**), 10 ng/µL TGF-β (**c**, **d**) or 1 % O2 (**e**, **f**). The gene expression of the Org. and JS1 groups after co-culturing were measured individually and compared to the Neg. Con (n=4). The gene expression or the co-cultures after being treated with 50 ng/µL TNF, 10 ng/µL TGF-β or 1 % O2 were measured individually and compared to the Neg. Con. groups, the treatment only groups and the co-culture only groups (n=4). Every group was also compared to a treatment group with 100 ng/µL Halo. group (n=4). Expression data was normalised to the *Hprt* housekeeper gene (n=4), and then normalised to the Neg. Con. group. Data was analysed using a one-way ANOVA to establish significant differences between the means of groups, and a post-hoc Holm-Šídák's multiple comparisons test for the pairwise comparison of the individual groups. * $p \leq 0.05$, ** $p \leq 0.01$, *** $p \leq 0.001$, **** $p \leq 0.0001$, ns $p > 0.05$. Error bars indicate mean ± the standard deviation.
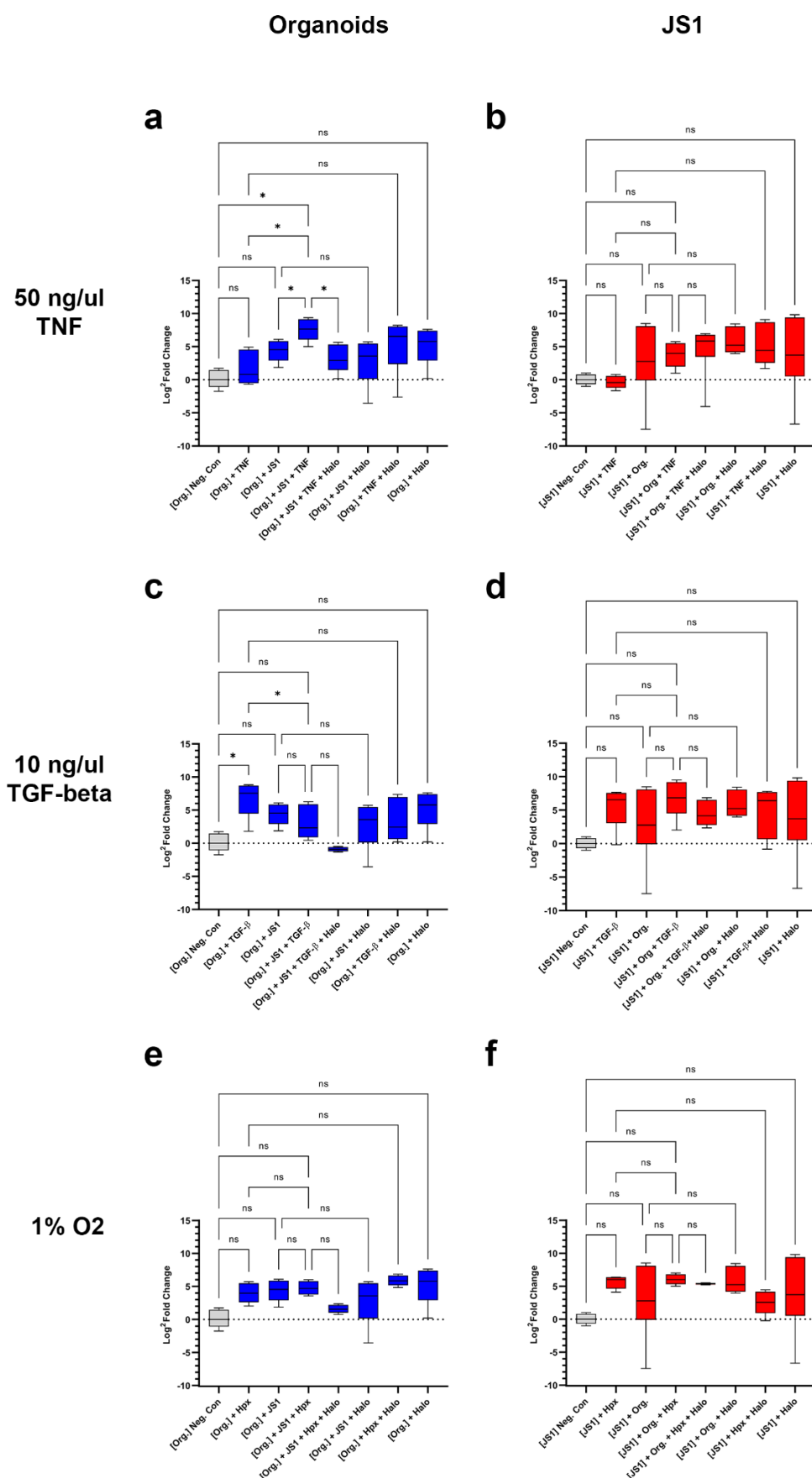
TNF treatment groups and the relevant controls did not have a significant difference in the mean expression of *Timp2* for the organoid groups or the JS1 groups. TNF treatment did not cause a significant pairwise difference in mean *Timp2* expression between any of the groups. 10 ng/µL TGF-β treatment groups and the relevant controls have a significant difference in the mean expression of *Timp2* for the organoid and JS1 groups. The organoid treatment group had a significant increase in mean expression over the negative control group. The organoid treatment + co-culture group as well at the organoid treatment with Halofuginone group had a significant decrease in mean expression compared to the treatment only group. The JS1 treatment + co-culture group had a significant increase in mean expression compared to the treatment only and negative control groups. The treatment and co-culture group with

Halofuginone treatment also had a significant decrease in mean expression compared to the

treatment and co-culture group.
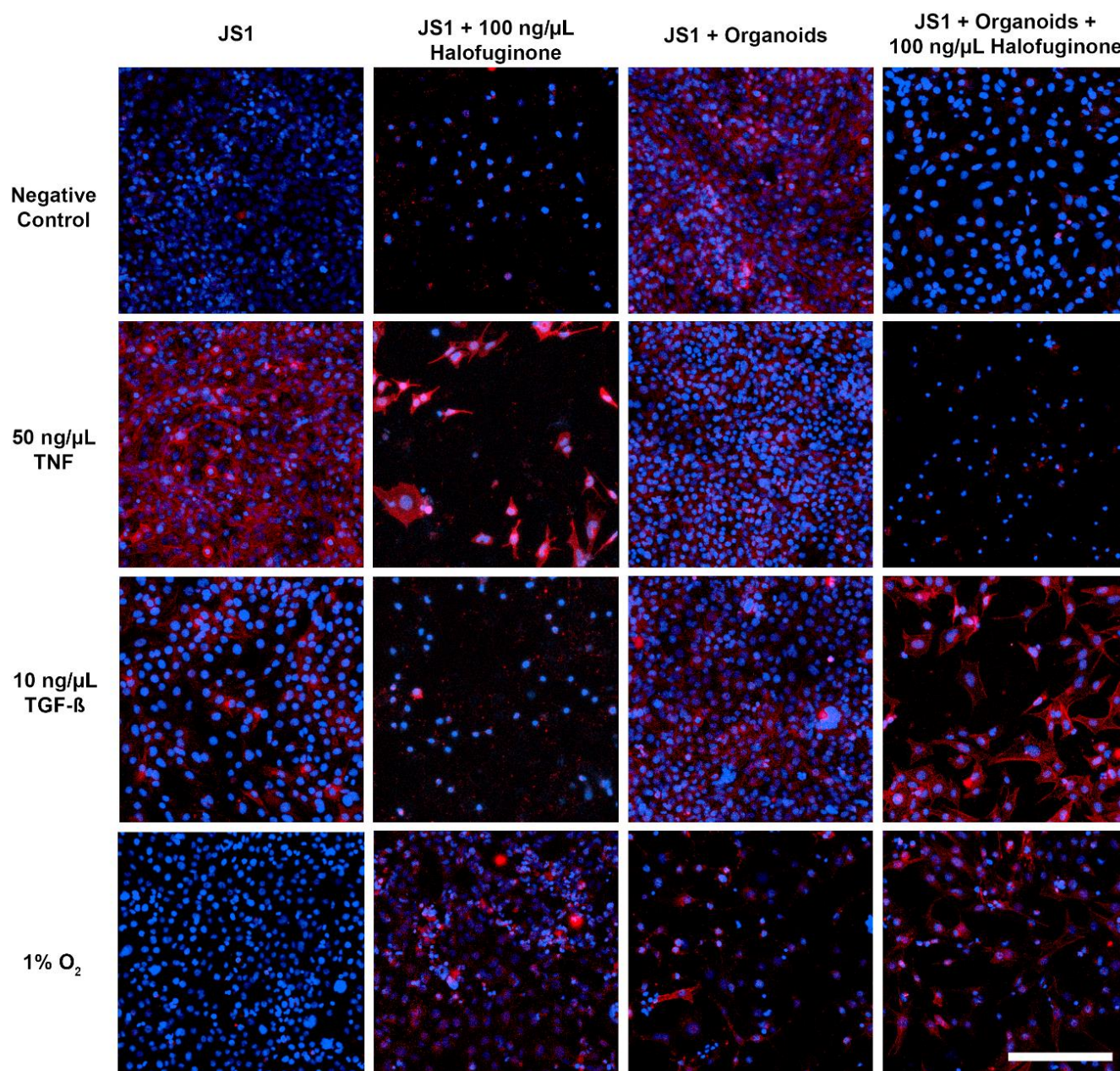
4.2.4 Confocal Laser Scanning Microscopy Analysis

Figure 4.13 Immunofluorescent co-staining of SMA-α and DNA on JS1 cells for Analysis of Liver Injury Model. JS1 cells co-stained for SMA-α (Red) and DNA (Blue). The JS1 cell line imaged in the bottom of the well of the trans-well system after 48 hours of treatment. Each row represents a different treatment used to induce liver injury and the negative control group. Each column represents JS1 group treated with or without 100 ng/µL Halofuginone and/or in co-culture with the liver organoids (Scale bar = 100 µm).

The JS1 cells alone express SMA-α, although the amount of expression is greatest in JS1 cells treated only with 50 ng/µL TNF (Figure 4.13). Expression is also high when JS1 cells are co-cultured with organoids and lowest in the culture under hypoxic conditions. Halofuginone supresses SMA-α, but this may be a product of the reduction in cell numbers, because the expression is still high in TNF and Halofuginone treated cells. TGF-β treated cells also have an increase in expression, but not as high as for TNF.
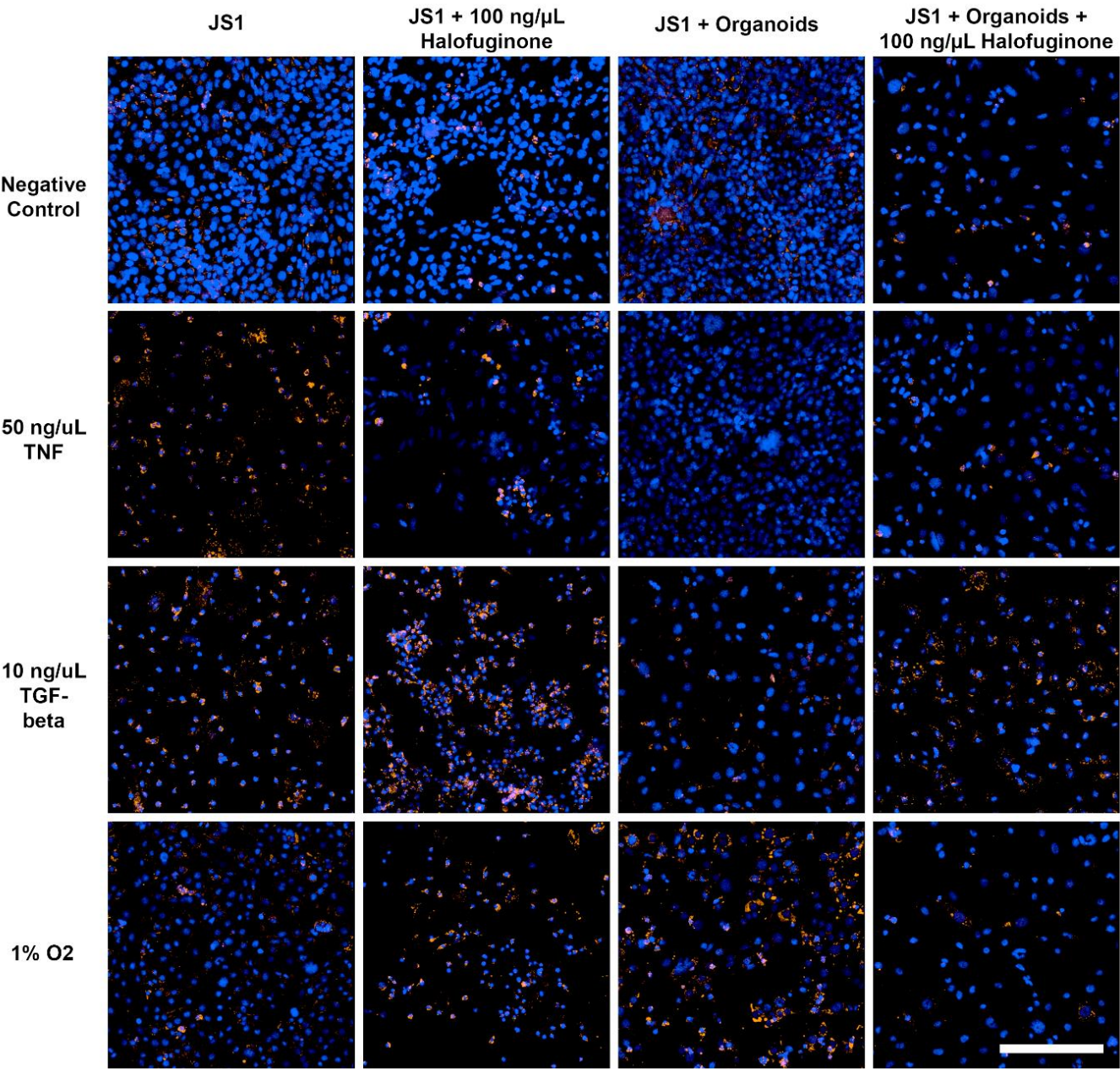
Figure 4.14 Immunofluorescent co-staining of Collagen I and DNA on JS1 cells for Analysis of Liver Injury Model. JS1 cells co-stained for Col I (Orange) and DNA (Blue). The JS1 cell line imaged in the bottom of the well of the trans-well system after 48 hours of treatment. Each row represents a different treatment used to induce liver injury and the negative control group. Each column represents JS1 group treated with or without 100 ng/µL Halofuginone and/or in co-culture with the liver organoids (Scale bar = 100 µm).

The JS1 cells (Figure 4.14) express collagen I in all experimental groups with limited differential expression in response to various treatments or with co-culture with organoids, any observable differences between the groups were inconclusive.

4.3 Discussion

The liver injury model in this chapter which combined mouse liver organoids with HSC cells did accurately represent certain aspects of liver injury *in vitro*. These include a direct damage to primary hepatocytes by cytokine dependent HSC signalling, and the proliferation and trans-differentiation of HSCs when exposed to hepatocytes, or cytokines TNF and TGF-β. Halofuginone treatment also caused a reduction in HSC proliferation and supress genes *Col1a1*, *Mmp14* and *Timp2*, although this did not cause an increase in hepatocyte survival.

Trans-differentiation of HSCs from a quiescent to a SMA-α positive activated phenotype was dependent on exposure to hepatocyte, TNF or TGF-β. Hepatocyte exposure was also the dependent factor for significant HSC proliferation. This models the hepatocyte/HSC inflammatory response which is usually initiated by apoptotic bodies and ROS release by hepatocytes and is emblematic of liver injury initiation (Tu *et al* 2015).

The liver injury model did not for the most part replicate the expected gene expression of liver injury. Most notable was the lack of differential HSC gene expression of *Col1a1* and *Col4a1* which encode for collagens I and IV and are typical of a fibrotic ECM phenotype *in vivo* (Robinson *et al* 2016; Iredale and Guha 2007; Tsuchida and Friedman 2017). Collagen I protein expression was observed in all HSC groups by immunofluorescences (Figure 4.14), but the increase in mean gene expression of both collagen genes (*Col1a1* and *Col4a1*, Figures 4.5 and 4.6) were not found to be statistically significant.

To better characterise the transcriptional profile this *in vitro* model I pursued transcriptional profiling described in Chapter 5 on the impact of TNF treatment on the organoids/JS1 co-culture. This was because TNF is a potent inflammatory cytokine signal produced from Kupffer cells and would substitute the role of inflammatory cells in liver injury and hence trigger

multiple signalling pathways involved in inflammation, proliferation, and apoptosis (Yang and Seki 2015).

Hypoxic conditions altered the morphology of the organoids, losing their round appearance and filling the internal lumen. Hypoxia reduced organoid viability, but the effect on viability was not significant when co-cultured with JS1 cells, suggesting that HSCs may be protective to hepatocytes under hypoxic conditions. Hypoxia increased *Col1a1, Bsg* and *Mmp14* expression in organoids, and reduced *Timp2* expression in organoids both in co-culture with JS1 and without, hence hypoxia suppresses the expression of inhibitors of the matrix metalloproteinases, thus promoting tissue fibrogenesis. This phenotype models some aspects of hypoxia induced acute liver injury (Roth and Copple 2015).

Halofuginone treatment did not significantly change organoid morphology or viability of the culture, suggesting the hepatocytes in the culture were resistant to the effects of drug toxicity at this concentration. Halofuginone suppresses *Col1a1* gene expression in TGF-β and hypoxia treated hepatocytes. Halofuginone increases the gene expression of *Col4a1* in hepatocytes, but this is supressed by HSCs. Halofuginone suppresses fibronectin I gene expression in hepatocytes that are exposed to inflammatory cytokines like TNF and signals from HSCs. Halofuginone suppresses matrix metalloproteinase gene expression in hepatocytes during hypoxia related liver injury. Halofuginone suppresses inhibitors of the matrix metalloproteinases gene expression in hepatocytes that are activated by TGF-β. This suggests that Halofuginone selectively inhibits HSC proliferation and genetic markers of liver fibrosis.

While some aspects of liver injury were replicated *in vitro*, many key genetic and protein markers of liver injury were not differentially expressed in the present model. The findings also suggest that future models for liver injury should integrate zonation for a more accurate representation of the liver lobe, by applying an oxygen gradient across the cell culture

(Jungermann & Kietzmann, 2000). Different instigators of hepatic injury could also be applied as opposed to inflammatory cytokines or hypoxia, such as lipid overloading as similar to what is observed in NASH (Sepanlou *et al* 2020; Tu *et al* 2015), or toxin induced injury such as Aflatoxin (Tu *et al* 2015), or the use of hepatotropic infectious pathogens, particularly HBV and HCV which cause the majority of chronic liver disease (Tu *et al* 2015). These changes could produce a more representative *in vitro* model of liver jury.

CHAPTER 5

TRANSCRIPTIONAL PROFILING ANALYSIS OF THE *IN VITRO* MODELLING OF LIVER INJURY AND FIBROSIS

CHAPTER 5

TRANSCRIPTIONAL PROFILING ANALYSIS OF THE *IN VITRO* MODELLING OF LIVER INJURY AND FIBROSIS

KEY FINDINGS

1. TNF treatment induced unique phenotypes in the liver organoids and HSCs.

2. Gene expression characteristics of the liver injury initiation phase were upregulated by TNF treatment in our model.

3. Gene sets related to the interferon gamma response inflammation, hypoxia, and apoptosis were positively enriched in each cell population by TNF treatment.

4. Collagen I was downregulated in HSCs with the upregulated TNF response, hence crosstalk between the liver injury phenotype organoid tissues and the HSCs did not induce a fibrous phenotype.

CHAPTER 5 TRANSCRIPTIONAL PROFILING ANALYSIS OF THE IN VITRO MODELLING OF LIVER INJURY AND FIBROSIS

5.1 BACKGROUND

In Chapter 4 we described and designed an *in vitro* model of liver disease and demonstrated that it was partially representative of key aspects of fibrotic liver injury. In this chapter we will analyse the transcriptional profile of the TNF treated liver organoids/JS1 cell co-culture as described in Chapter 4 using transcriptional profiling. This was pursued to better characterise the gene expression phenotypes in each cell population in this *in vitro* model of liver injury.

The TNF treated organoid/JS1 cell co-culture model was chosen because as a dominant pro inflammatory cytokine TNF can represent the intercellular interactions which occur during the progression of liver injury (Tu *et al* 2015), that is the inflammatory signals being released at the initiation of injury by inflammatory cells stimulating an injury phenotype in hepatocytes which initiates the activation and proliferation of HSCs. For reference the liver injury phenotype we are in part replicating *in vitro* is summarised in Figures 1.14 and 1.15 in Chapter 1.

5.1.1 METHODS

RNA was extracted from our cell culture samples using RNA column extraction. All RNA samples were tested for quality and integrity before being analysed. Three biological replicates were used per organoid group (that is 3 different primary liver organoid cultures from 3 different mouse clones, not 3 different passages from the same culture). Three technical replicates were used per JS1 cell culture group.

Samples were sequenced using custom Multiplex bulk RNA sequencing developed by Dr. Trevor Wilson at the medical genomics facility of the Hudson Institute of Medical Research at Monash University, Melbourne, Australia. Bioinformatic analysis of the raw data was initially accomplished in R by A/Prof. David Powell using a pipeline developed at the Monash

Bioinformatics Platform at Monash University, Melbourne, Australia, and visualised using the software Degust.

Hierarchical Cluster Analysis was achieved using the "VoomNormalize", "HierarchicalClustering" and "HierarchicalClusteringViewer" modules on the open-source computational biology software GenePattern Version v3.9.11-rc.5 b234 (Reich *et al* 2006). Protein-Protein interaction analysis was achieved using the STRING software Version 11.0. Gene Set Enrichment Analysis (GSEA) was achieved using the "GSEAPreranked" module on GenePattern Version v3.9.11-rc.5 b234.

To satisfy our aim to use transcriptional profiling to characterise the gene expression of our model and assess its accuracy as a model of liver injury *in vitro*, we hypothesised that by using multiplex bulk RNA sequencing we will be able to determine the range and quantity of all differential expression in our organoids and JS1 cells. We will identify these differentially expressing genes.

We will identify of these differentially expressing genes, and variables that likely affect differential expression using overlapping analysis, and then characterise expected protein interactions and pathway activation by Protein-Protein interaction analysis. We can also discover common biological pathways that are being enriched in our model using gene set enrichment analysis (GSEA) (Subramanian *et al* 2005). This will give us a clear picture of the gene expression phenotypes being represented in cell populations of this *in vitro* model.

We expect to discover differentially expressed genes dependent on TNF treatment and cell co-culturing, like interferons, interleukins, ROS related genes, inflammatory cytokines, NFκB, apoptosis, ECM genes especially collagen I, specific growth factors like PDGF, VEGF and CTGF, proliferations signalling, hedgehog signalling, Periostin and cell death genes (Tu *et al* 2015; Robinson *et al* 2016; Tsuchida and Friedman, 2017; Luedde *et al* 2014; Amara *et al*

2015; Yang and Seki 2015; Saile *et al* 1999). We also expect to discovery pathways and gene

sets related to these genes to be activated and enriched. By doing so we will also get a good

understanding of the intercellular interacts between the cell populations.

5.2 RESULTS

Experimental Groups Details	Experimental Groups Labels	Name of Samples within each Group
Mouse Liver Organoid Negative Control Group	**Org Neg Con**	1-OrgNegCon5395_N701 2-OrgNegCon5434_N702 3-OrgNegCon4716_N703
Mouse Liver Organoid Group Co-cultured with JS1 Cells	**Org + JS1**	7-Org5395JS1B_N707 8-Org5434JS1C_N710 9-Org4716JS1D_N711
Mouse Liver Organoid Group Treated with TNF	**Org + TNF**	13-Org5395TNF_N716 14-Org5434TNF_N718 15-Org4716TNF_N719
Mouse Liver Organoid Group Co-cultured with JS1 Cells and Treated with TNF	**Org + JS1 + TNF**	19-Org5395JS1BTNF_N723 20-Org5434JS1CTNF_N724 21-Org4716JS1DTNF_N726
JS1 Negative Control Group	**JS1 Neg Con**	4-JS1NegConB_N704 5-JS1NegConC_N705 6-JS1NegConD_N706
JS1 Cells Co-cultured with Mouse Liver Organoids	**JS1 + Org**	10-JS1BOrg5395_N712 11-JS1COrg5434_N714 12-JS1DOrg4716_N715
JS1 Cells Treated with TNF	**JS1 + TNF**	16-JS1BTNF_N720 17-JS1CTNF_N721 18-JS1DTNF_N722
JS1 Cells Co-cultured with Mouse Liver Organoids and Treated with TNF	**JS1 + Org + TNF**	22-JS1BOrg5395TNF_N727 23-JS1COrg5434TNF_N728 24-JS1DOrg4716TNF_N729

Table 5.1 Table for Referencing which Samples Belong to Which Group. The nomenclature used for the samples: (#-) number between 1-24 before a hyphen is for referencing which RNA aliquot this sample was. (Org) when first in the name means it was an organoid RNA sample, but if it was second in the name it means the sample was co-cultured with organoids. (JS1) when first means it was a JS1 cell line RNA sample, but if it was second in the name it means the sample was co-cultured with JS1 cells. (NegCon) means this sample

was a negative control sample. (####) the 4 digit number is the number of the mouse the

corresponding organoid was derived from. (B-D) the letters B through D are the technical

replicate from the JS1 cell line. (TNF) means the sample was treated with 50 ng/µL of TNF.

(_N###) is the sequencing reference number.

5.2.1 Quality Control Analysis for Organoid Samples
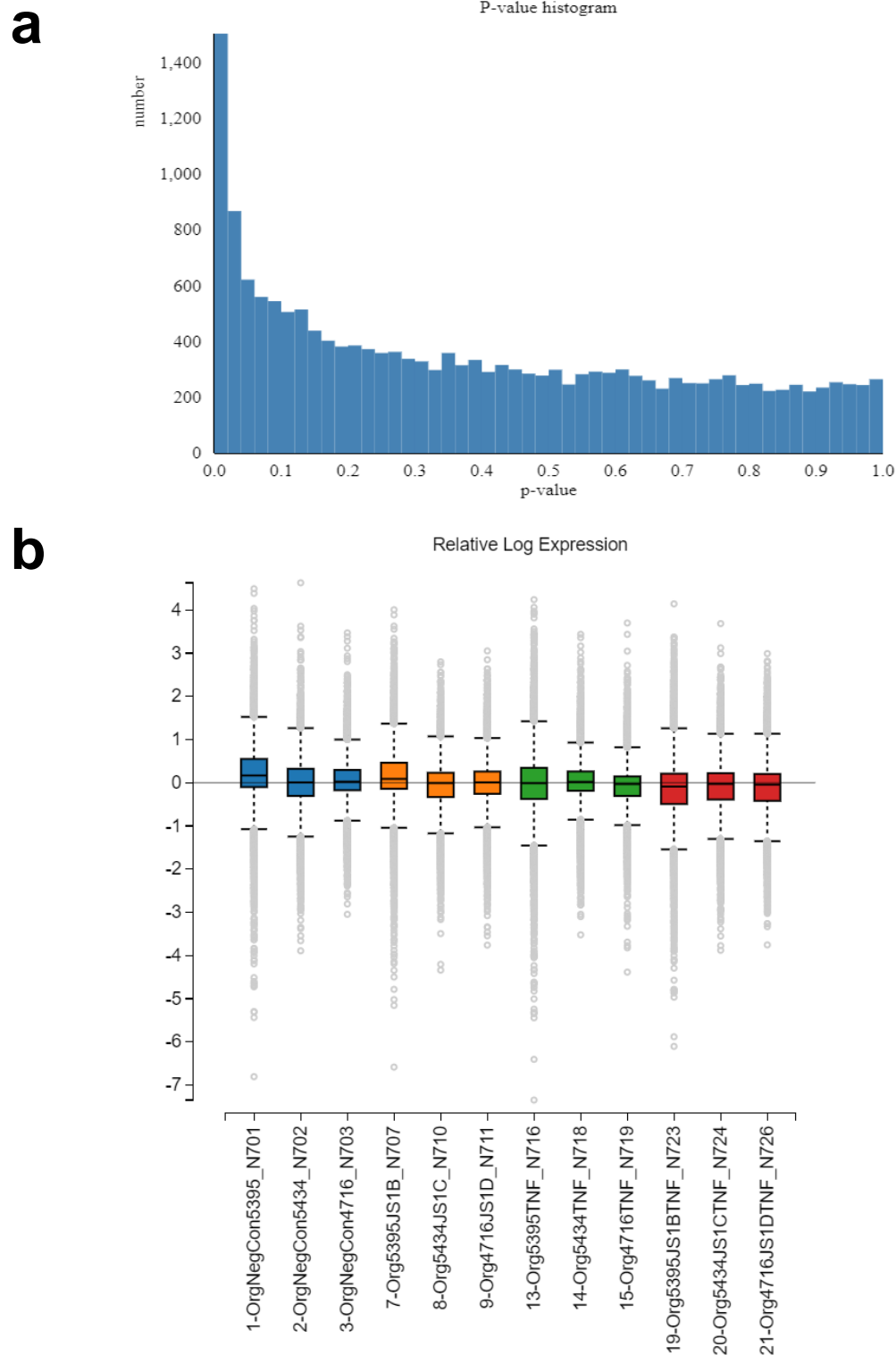
Figure 5.1 Quality Control Analysis of Organoid Samples a. p-Value histogram quantifying all organoid sample genes measured over the calculated probability of a null hypothesis (p-value). **b.** Relative Log gene Expression boxplot of each sample measured.
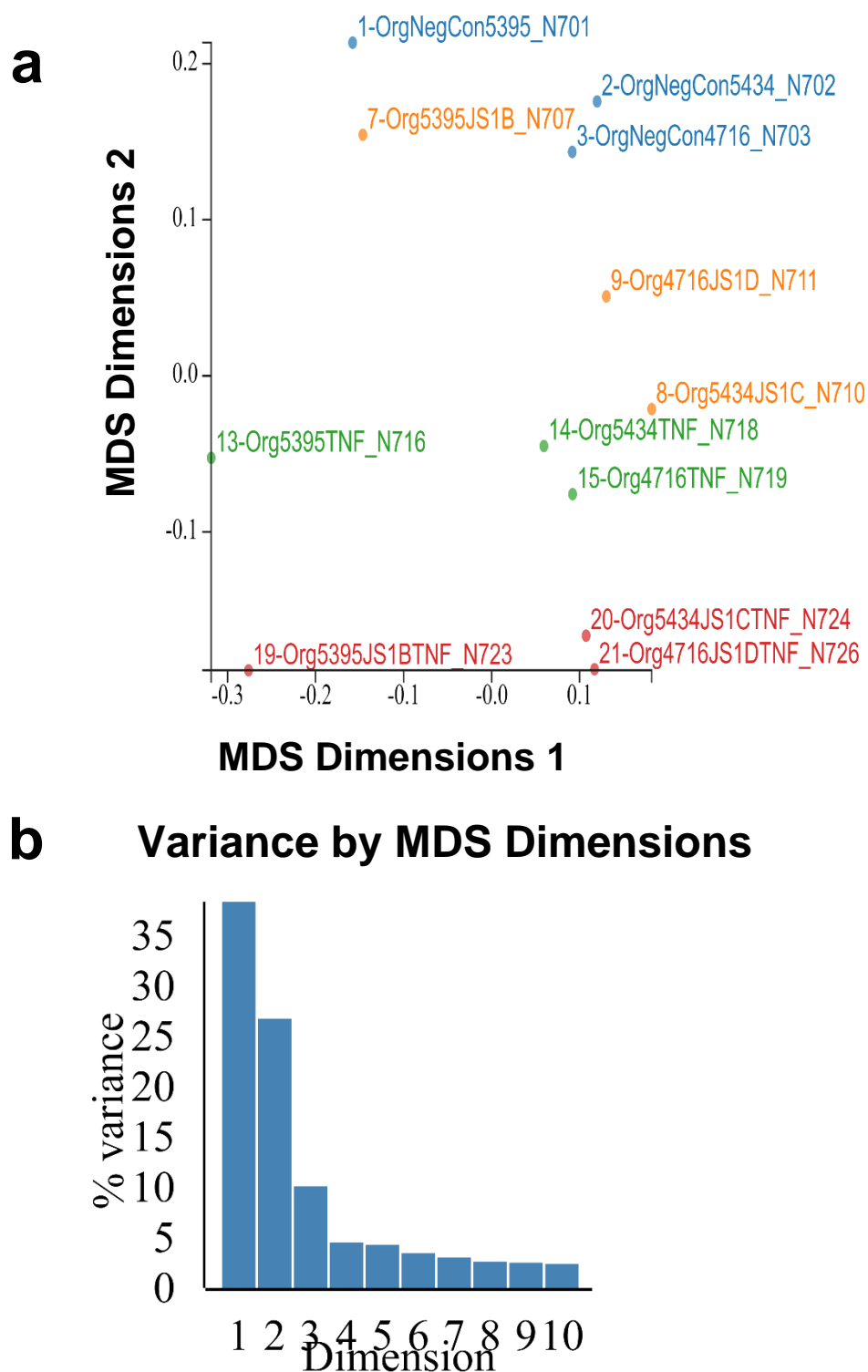
Figure 5.2 Multidimensional Analysis of Organoid Samples a. Multidimensional scaling (MDS) plot of each measured organoid sample. **b.** Histogram representing the percentage variance between the first 10 dimensions of the MDS plot.

217

The p-Value histogram (Figure 5.1a) indicated an anti-conservative trend. The relative Log expression boxplot (Figure 5.1b) of our samples were consistent, with the means around zero. The multidimensional scaling (Figure 5.2a) found that there were some variances between the samples within each group, the percentage variances across the first 10 dimensions are represented in Figure 5.2b.

5.2.2 Gene Expression Analysis for Organoid Samples
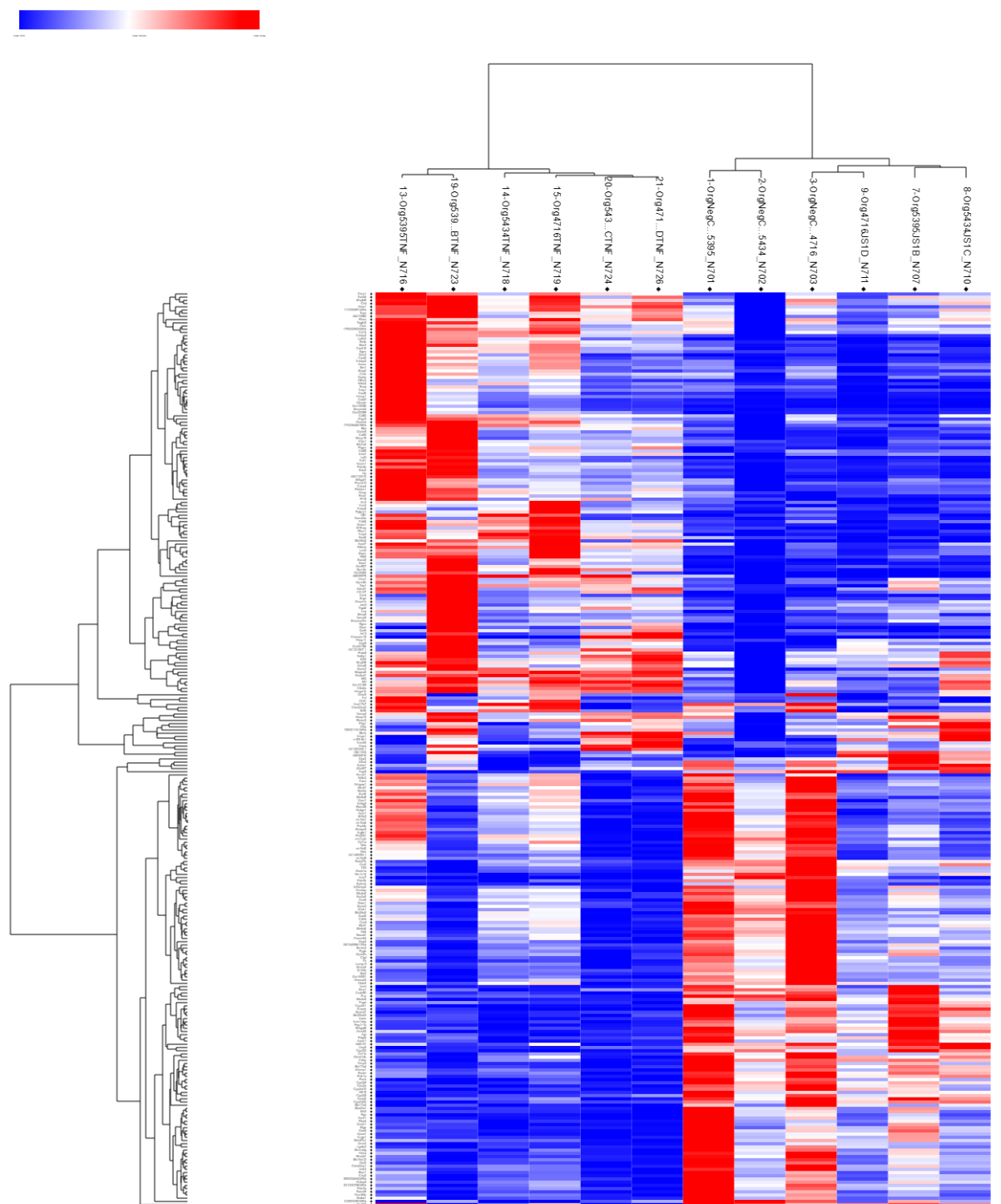
Figure 5.3 Hierarchical Cluster Analysis. Hierarchical clustering of organoid samples and the significantly differentially expressed genes of each sample. Relative increases in gene expression are labelled red and relative decreases in genes expression are labelled blue. Only genes with a false discovery rate (FDR) cut-off of ≤ 0.05 are represented.

Hierarchical cluster analysis suggests a high degree of similarity between the organoid negative control group and the organoid co-cultured group, and a high degree of similarity between the Organoid TNF treated group and the Organoid co-cultured TNF treated group. This divides the samples into two distinct transcriptional profiles dependent on TNF treatment.
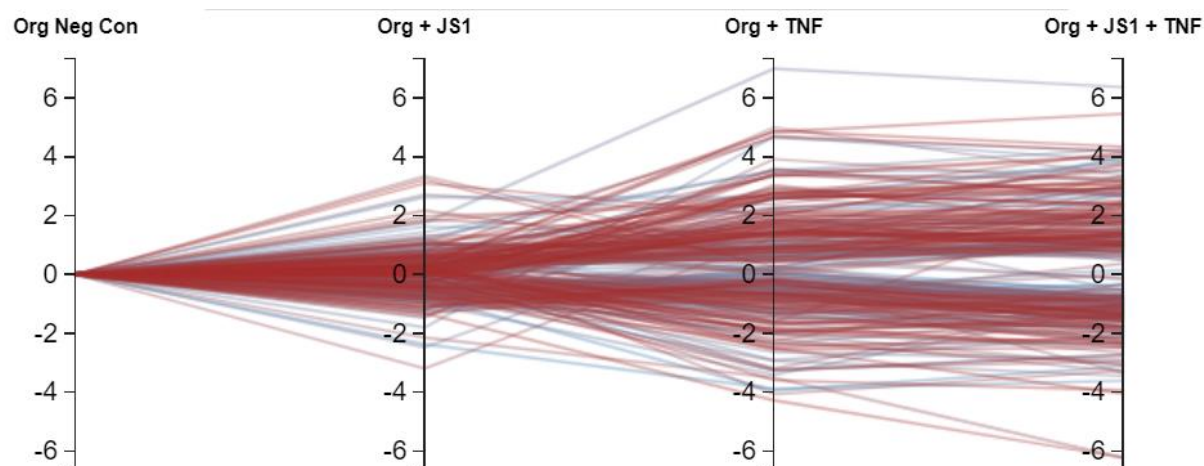
Figure 5.4 Parallel Coordinate Analysis of Organoid Samples. Parallel coordinate graph of each organoid group gene expression measured relative to the negative control group, each line is a gene, and the y-coordinate is the log fold change of each group. Only genes with an FDR cut-off of ≤ 0.05 are represented.

The parallel coordinate analysis suggests that there is a greater amount of variance in differential expression for the organoid groups treated with TNF ranging from a log change of 6-fold compared to the negative control, than the co-culture only group compared to the negative control. This group only had a variance in differentially expression ranging from a log change of 3-fold.
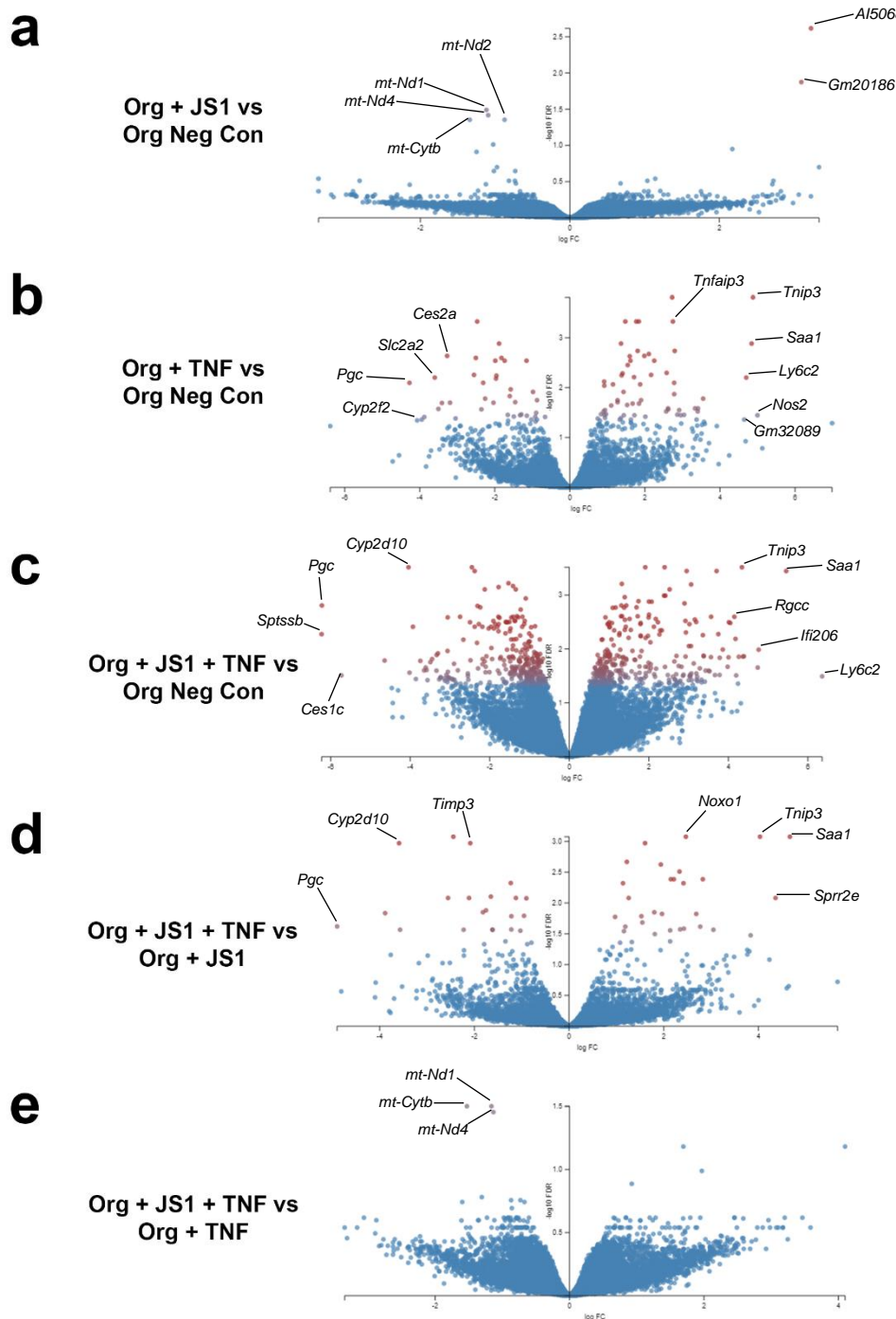
Figure 5.5 Volcano Plot of Organoid Gene Expression Log-fold Change and Statistical Significance (-log10 FDR). Points with an FDR cut-off > 0.05 are blue and point with an FDR cut-off ≤ 0.05 are red. Some genes on the extremes of significance and log-fold change in gene expression have been labelled **a.** Relative gene expression of the Organoid/JS1 coculture compared to the negative control group. **b.** Relative gene expression of the Organoid/TNF

treatment culture compared to the negative control group. **c.** Relative gene expression of the

Organoid/JS1 coculture group treated with TNF, compared to the negative control group. **d.**

Relative gene expression of the Organoid/JS1 coculture group treated with TNF, compared to

the Organoid/JS1 coculture group. **e.** Relative gene expression of the Organoid/JS1 coculture

group treated with TNF, compared to the Organoid/TNF treatment culture group.

The volcano plots represent the number of significant differentially expressing genes as well

as non-differentially expressing genes between organoid groups, the largest number being

between the organoids co-cultured with JS1 cells and treated with TNF compared to the

organoid negative control group.
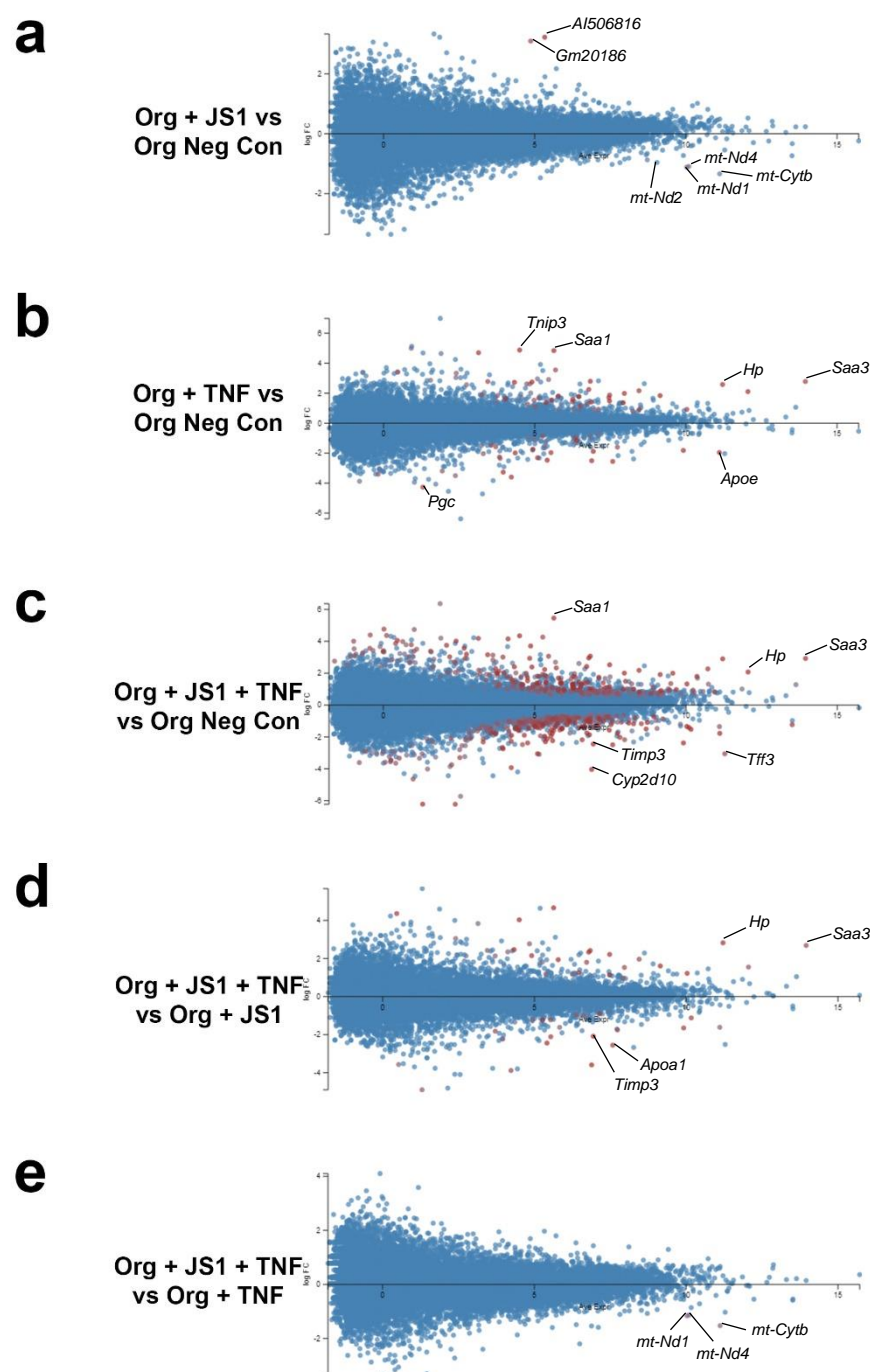
Figure 5.6 MA Ratio Intensity Plot of Organoid Gene Expression Log-Fold Change and Mean Average Expression. Points with an FDR cut-off > 0.05 are blue and points with an FDR cut-off ≤ 0.05 are red. Some genes on the extremes of mean average expression and log-fold change in gene expression have been labelled **a.** Relative gene expression of the Organoid/JS1 coculture compared to the negative control group. **b.** Relative gene expression

of the Organoid/TNF treatment culture compared to the negative control group. **c.** Relative gene expression of the Organoid/JS1 coculture group treated with TNF, compared to the negative control group. **d.** Relative gene expression of the Organoid/JS1 coculture group treated with TNF, compared to the Organoid/JS1 coculture group. **e.** Relative gene expression of the Organoid/JS1 coculture group treated with TNF, compared to the Organoid/TNF treatment culture group.

The log-fold change in expression of all the organoid genes between each of the groups clustered around zero on the MA plots, hence we can assume that the gene expression analysis has been correctly normalised for the samples and the measured relative changes are correct.

Figure 5.7 Common and Unique Gene Expression in Organoids. Venn diagram for

quantifying significant organoid differential gene expression between groups and overlapping

across group. Only genes with an FDR cut-off of ≤ 0.05 were quantified. Not all overlapping

could be represented by a Venn diagram, hence use the Table 5.2 for all discovered overlapping

between groups.

Overlapping Analysis Groups	Number of Significant Genes within each overlapping group set
Org + JS1 vs Org Neg Con	6
Org + TNF vs Org Neg Con	108
Org + JS1 + TNF vs Org Neg Con	703
Org + JS1 + TNF vs Org + JS1	57
Org + JS1 + TNF vs Org + TNF	3
Org + JS1 vs Org Neg Con: Org + TNF vs Org Neg Con	0
Org + JS1 vs Org Neg Con: Org + JS1 + TNF vs Org Neg Con	2
Org + TNF vs Org Neg Con: Org + JS1 + TNF vs Org Neg Con	48
Org + JS1 vs Org Neg Con: Org + TNF vs Org Neg Con: Org + JS1 + TNF vs Org Neg Con	1
Org + JS1 vs Org Neg Con: Org + JS1 + TNF vs Org + JS1	0
Org + TNF vs Org Neg Con: Org + JS1 + TNF vs Org + JS1	0
Org + JS1 vs Org Neg Con: Org + TNF vs Org Neg Con: Org + JS1 + TNF vs Org + JS1	0
Org + JS1 + TNF vs Org Neg Con: Org + JS1 + TNF vs Org + JS1	11
Org + JS1 vs Org Neg Con: Org + JS1 + TNF vs Org Neg Con: Org + JS1 + TNF vs Org + JS1	0
Org + TNF vs Org Neg Con: Org + JS1 + TNF vs Org Neg Con: Org + JS1 + TNF vs Org + JS1	**46**
Org + JS1 vs Org Neg Con: Org + TNF vs Org Neg Con: Org + JS1 + TNF vs Org Neg Con: Org + JS1 + TNF vs Org + JS1	0
Org + JS1 vs Org Neg Con: Org + JS1 + TNF vs Org + TNF	0
Org + TNF vs Org Neg Con: Org + JS1 + TNF vs Org + TNF	0
Org + JS1 vs Org Neg Con: Org + TNF vs Org Neg Con: Org + JS1 + TNF vs Org + TNF	0
Org + JS1 + TNF vs Org Neg Con: Org + JS1 + TNF vs Org + TNF	0
Org + JS1 vs Org Neg Con: Org + JS1 + TNF vs Org Neg Con: Org + JS1 + TNF vs Org + TNF	**3**
Org + TNF vs Org Neg Con: Org + JS1 + TNF vs Org Neg Con: Org + JS1 + TNF vs Org + TNF	0
Org + JS1 vs Org Neg Con: Org + TNF vs Org Neg Con: Org + JS1 + TNF vs Org Neg Con: Org + JS1 + TNF vs Org + TNF	0
Org + JS1 + TNF vs Org + JS1: Org + JS1 + TNF vs Org + TNF	0
Org + JS1 vs Org Neg Con: Org + JS1 + TNF vs Org + JS1: Org + JS1 + TNF vs Org + TNF	0
Org + TNF vs Org Neg Con: Org + JS1 + TNF vs Org + JS1: Org + JS1 + TNF vs Org + TNF	0
Org + JS1 vs Org Neg Con: Org + TNF vs Org Neg Con: Org + JS1 + TNF vs Org + JS1: Org + JS1 + TNF vs Org + TNF	0
Org + JS1 + TNF vs Org Neg Con: Org + JS1 + TNF vs Org + JS1: Org + JS1 + TNF vs Org + TNF	0
Org + JS1 vs Org Neg Con: Org + JS1 + TNF vs Org Neg Con: Org + JS1 + TNF vs Org + JS1: Org + JS1 + TNF vs Org + TNF	0
Org + TNF vs Org Neg Con: Org + JS1 + TNF vs Org Neg Con: Org + JS1 + TNF vs Org + JS1: Org + JS1 + TNF vs Org + TNF	0
Org + JS1 vs Org Neg Con: Org + TNF vs Org Neg Con: Org + JS1 + TNF vs Org Neg Con: Org + JS1 + TNF vs Org + JS1: Org + JS1 + TNF vs Org + TNF	0

Table 5.2 Organoid Differential Gene Expression Overlapping Analysis. Table for quantifying the number of significant organoid differential gene expression between groups and all discovered overlapping differential expression. Only genes with an FDR cut-off of ≤ 0.05 were quantified.

From overlapping analysis of all the significant differentially expressed genes, 3 genes in the organoid samples were discovered to be differentially expressed dependent on co-culturing them with JS1 cells (Table 5.3) and 46 genes were discovered to be differentially expressed dependent on treating of the samples with TNF (Table 5.4).

Gene Name	Ensembl Gene ID	Org Neg. Con.	Org + JS1	Org + JS1 + TNF	FDR cut-off	Ave. Expr.	P value
mt-Nd1	ENSMUSG00000064341	0	-1.115604271	-1.345356884	0.001310894	10.02657442	1.38E-06
mt-Nd4	ENSMUSG00000064363	0	-1.092465279	-1.415025943	0.001309657	10.09818615	1.26E-06
mt-Cytb	ENSMUSG00000064370	0	-1.338844759	-1.777529687	0.001354232	11.1174536	1.53E-06

Table 5.3 Differentially Expressed Organoid Genes Dependent on Co-culturing with JS1 Cells. List of the 3 organoid genes discovered by overlapping analysis to be JS1 cell co-culture dependent (Table 5.2 bold and underlined). Only genes with differentially expression between groups dependent on co-culturing with JS1 cells and had an FDR cut-off of ≤ 0.05 were included. List includes Gene Name, the Ensembl genome browser ID code, group mean gene expression fold-change compared to the negative control group, the FDR cut-off, Average gene expression and P value. Genes ranked in descending order by log-fold gene expression of organoids co-cultured with JS1 cells treated with TNF. Group mean gene expression fold-change colour scaled red for an increase and blue for a decrease.
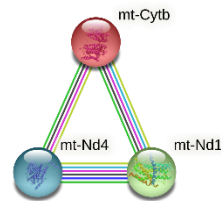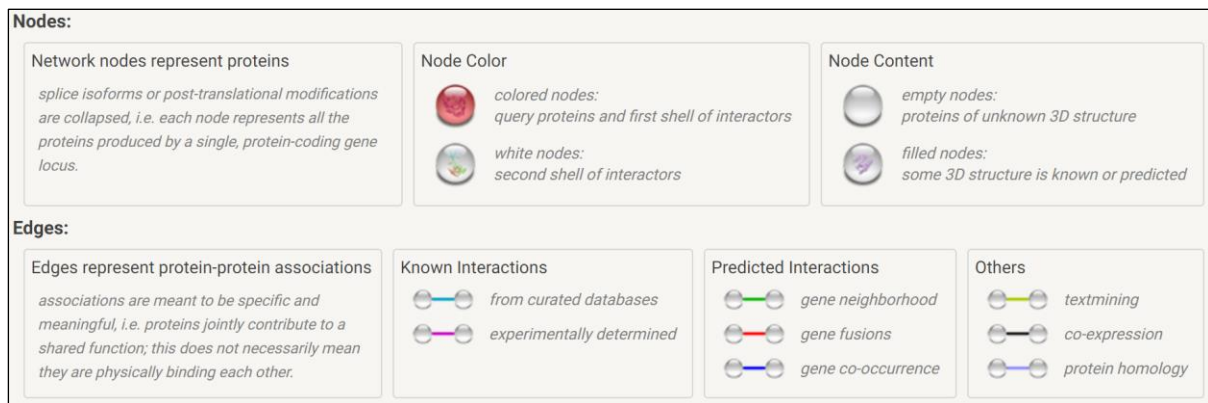
Figure 5.8 Protein-Protein Interaction Analysis of Organoid Genes Dependent on Co-culturing with JS1 Cells a. Protein-protein interaction map translated from of all significant differentially expressed organoid genes dependent on co-culturing with JS1 cells discovered by overlapping analysis. **b.** Legend for the protein-protein interaction map.

The JS1 cell dependent protein interaction phenotype was a downregulation of a pathway involving the NADH-ubiquinone oxidoreductase chain 1 (*mt-Nd1*) and 4 (*mt-Nd4*), with Cytochrome b (*mt-Cytb*).

Gene Name	Ensembl Gene ID	Org Neg. Con.	Org + TNF	Org + JS1 + TNF	FDR cut-off	Ave. Expr.	P value
Saa1	ENSMUSG00000074115	0	4.843736508	5.4554565	0.000631939	5.632629688	2.74035E-07
Tnip3	ENSMUSG00000044162	0	4.880555222	4.342632311	0.000232709	4.500380542	2.62755E-08
Ly6c2	ENSMUSG00000022584	0	4.700939198	4.181178849	0.005981054	3.139972303	1.92469E-05
Sprr2e	ENSMUSG00000055030	0	3.414748197	4.050084721	0.006461929	0.463021166	2.84554E-05
Susd2	ENSMUSG00000006342	0	3.335654048	4.014014817	0.006353819	2.404195521	2.63403E-05
Spns3	ENSMUSG00000020798	0	2.566661728	3.192548687	0.006353819	2.746507687	2.72619E-05
Ptges	ENSMUSG00000050737	0	2.7809088	3.157389199	0.005176081	3.4475627	1.47487E-05
Vcam1	ENSMUSG00000027962	0	2.794532391	3.064973284	0.000782948	6.837779031	5.74625E-07
Cd52	ENSMUSG00000000682	0	2.249456926	2.952272717	0.000669846	6.787271725	4.24124E-07
Pde4b	ENSMUSG00000028525	0	2.615830886	2.933265973	0.008993358	4.835259759	4.66801E-05
Saa3	ENSMUSG00000040026	0	2.778912893	2.92182976	0.004933132	13.95219844	1.17521E-05
Hp	ENSMUSG00000031722	0	2.579636549	2.898374592	0.002093003	11.21282156	3.07221E-06
Slpi	ENSMUSG00000017002	0	1.873664483	2.523417538	0.001551239	7.477451891	2.07422E-06
Srgn	ENSMUSG00000020077	0	1.410284009	2.416849547	0.002957195	6.71910864	4.55308E-06
Noxo1	ENSMUSG00000019320	0	2.726996301	2.397381753	0.000232709	4.328488222	2.15343E-08
Tnfaip3	ENSMUSG00000019850	0	2.745980725	2.383644085	0.000631939	4.908381045	2.97242E-07
Pglyrp1	ENSMUSG00000030413	0	2.165472557	2.17542918	0.004130106	8.44877673	7.69455E-06
Lcn2	ENSMUSG00000026822	0	2.10462348	2.071558618	0.001268863	12.05168205	1.41E-06
Hmga1b	ENSMUSG00000078249	0	1.438242968	2.004749145	0.005176081	3.740325138	1.49913E-05
Mpdz	ENSMUSG00000028402	0	1.985126494	2.00285495	0.001268863	7.963752292	1.50961E-06
Nfkbia	ENSMUSG00000021025	0	1.837314493	1.911496587	0.000295249	9.146500126	5.00055E-08
Relb	ENSMUSG00000002983	0	1.806958784	1.690444017	0.001268863	5.783068922	1.57596E-06
Plscr1	ENSMUSG00000032369	0	1.769376465	1.433308943	0.000669846	6.454684437	4.22314E-07
Birc3	ENSMUSG00000032000	0	1.379664405	1.398558416	0.004243764	5.374399071	8.23556E-06
Atox1	ENSMUSG00000018585	0	0.917806629	1.322052803	0.001247397	10.03145764	1.26761E-06
Itgav	ENSMUSG00000027087	0	1.595527612	1.26250216	0.003047741	6.256579094	5.26838E-06
Cxcl16	ENSMUSG00000018920	0	1.478673514	1.165359415	0.000669846	7.473569875	4.538E-07
Ier3	ENSMUSG00000003541	0	1.404558315	1.02664812	0.006017675	6.873548718	2.28806E-05
Cd44	ENSMUSG00000005087	0	1.363367576	1.009083582	0.001551239	7.928818422	2.10183E-06
St3gal5	ENSMUSG00000056091	0	-1.154015034	-0.801089323	0.004933132	6.392801352	1.19757E-05
Bcam	ENSMUSG00000002980	0	-0.660311141	-0.859497072	0.008674424	7.145191234	4.35851E-05
Sparcl1	ENSMUSG00000029309	0	-1.73731506	-1.028992795	0.004959941	4.939141049	1.23328E-05
Polr1a	ENSMUSG00000049553	0	-0.874353828	-1.222350336	0.00426843	5.264235142	9.20923E-06
Apoe	ENSMUSG00000002985	0	-1.956153847	-1.355205725	0.007006339	11.10645463	3.16438E-05
Klf15	ENSMUSG00000030087	0	-1.986631985	-1.459722724	0.004243764	4.352661791	8.38546E-06
Gas6	ENSMUSG00000031451	0	-1.600545834	-1.776541862	0.006017675	7.734051722	2.17887E-05
Slc17a4	ENSMUSG00000021336	0	-1.576305661	-1.807918102	0.006017675	3.710130522	2.0891E-05
Cyp4b1	ENSMUSG00000028713	0	-1.96813539	-1.96942796	0.005129119	5.536625854	1.38993E-05
Ppp1r1b	ENSMUSG00000061718	0	-2.469148758	-2.126106928	0.000631939	5.411938173	2.60172E-07
Ttr	ENSMUSG00000061808	0	-1.822169189	-2.379406752	0.000631939	9.916320116	3.21089E-07
Timp3	ENSMUSG00000020044	0	-1.886040423	-2.449186652	0.000554816	6.936318056	1.2529E-07
Apoa1	ENSMUSG00000032083	0	-2.554096187	-2.495909922	0.00426843	7.578997148	9.39811E-06
Ces2a	ENSMUSG00000055730	0	-3.27058384	-2.74683571	0.002056431	3.956551105	2.90243E-06
Slc2a2	ENSMUSG00000027690	0	-3.598877884	-3.932155394	0.005098156	4.226660227	1.35275E-05
Cyp2d10	ENSMUSG00000094806	0	-2.505171232	-4.042775766	0.000631939	6.883966448	2.40823E-07
Pgc	ENSMUSG00000023987	0	-4.273207992	-6.221264971	0.002957195	1.297601902	4.74E-06

Table 5.4 Differentially Expressed Organoid Genes Dependent on TNF Treatment. List of 46 organoid genes discovery by overlapping analysis to be TNF dependent (Table 5.2 bold and underlined). Only genes with differentially expression between groups dependent on TNF treatment and had an FDR cut-off of ≤ 0.05 were included. List includes Gene Name, the Ensembl genome browser ID code, group mean gene expression compared to the negative control group, the FDR cut-off, Average gene expression and P value. Genes ranked in descending order by log-fold gene expression of organoids co-cultured with JS1 cells treated with TNF. Group mean gene expression fold-change colour scaled red for an increase and blue

for a decrease. A solid black outside border indicates organoid genes that have also been

implicated in liver injury (see Chapter 1).

**Figure 5.9 Protein-Protein Interaction Analysis of Organoid Genes Dependent on TNF
Treatment a.** Protein-protein interaction map translated from of all significant differentially
expressed organoid genes dependent on TNF treatment discovered by overlapping analysis. **b.**
Legend for the protein-protein interaction map.

CHAPTER 5 TRANSCRIPTIONAL PROFILING ANALYSIS OF THE IN VITRO MODELLING OF LIVER INJURY AND FIBROSIS

The TNF dependent protein interaction phenotype (Figure 5.9) contained clusters of interactions around the upregulated Tumour necrosis factor alpha-induced protein 3 (*Tnfaip3*), TNFAIP3-interacting protein 3 (*Tnip3*), the Baculoviral IAP repeat-containing protein 3 (*birc3*), and NFκB inhibitor alpha (*Nfkbia*), which are expected interaction induced in a TNF response pathway (Wullaert *et al* 2007). This cluster interacts with the cell surface receptors Integrin alpha-V (*Itgav*) and CD44 (*Cd44*) via the Vascular cell adhesion protein 1 (*Vcam1/ VCAM1*).

Gene Name	Ensembl Gene ID	Org Neg. Con.	Org + JS1	Org + TNF	Org + JS1 + TNF	FDR cut-off	Ave. Expr.	P value
Tnfaip3	ENSMUSG00000019850	0	0.234004125	2.745980725	2.383644085	0.000332339	4.908381045	1.23E-07
Mmp8	ENSMUSG00000005800	0	0.812860559	1.317486817	2.267922773	0.028100685	10.72293822	0.0002899
Mmp19	ENSMUSG00000025355	0	0.108670077	1.235114289	1.919595014	0.014527296	5.263418674	9.02E-05
Mif	ENSMUSG00000033307	0	0.546170274	1.003631011	1.492125638	0.028100685	8.000793526	0.0002919
Timp1	ENSMUSG00000001131	0	0.406045489	1.272132681	1.421087168	0.009280965	6.751800861	3.98E-05
Tnfaip2	ENSMUSG00000021281	0	-0.235986239	1.71136375	1.075594164	0.002746117	7.452857837	7.19E-06
Pdgfd	ENSMUSG00000032006	0	0.3902	-1.10023	-0.50225	0.028885	4.853792	0.000308
Tnf	ENSMUSG00000024401	0	-2.466938867	1.749267041	-0.535930365	0.038700309	0.918695547	0.0004892
Ctgf	ENSMUSG00000019997	0	-0.60375	-1.19089	-1.86537	0.016046	6.810967	0.000107
Timp3	ENSMUSG00000020044	0	-0.362819518	-1.886040423	-2.449186652	0.000324176	6.936318056	9.15E-08

Table 5.5 Organoid Genes of Interest. List of significantly measured organoid genes, that have also been implicated in liver injury (see Chapter 1). Only genes with an FDR cut-off of ≤ 0.05 were included. List includes Gene Name, the Ensembl genome browser ID code, group mean gene expression compared to the negative control group, the FDR cut-off, Average gene expression and P value. Genes ranked in descending order by log-fold gene expression of organoids co-cultured with JS1 cells treated with TNF. Group mean gene expression fold-change colour scaled red for an increase and blue for a decrease.

5.2.3 Gene Set Enrichment Analysis for Organoid Samples

REGULATED GENE SETS (Org + JS1 vs Org Neg Con)	NES	FDR q-val	LEADING EDGE
HALLMARK_INTERFERON_GAMMA_RESPONSE	2.559112	0	tags=48%, list=16%, signal=56%
HALLMARK_ALLOGRAFT_REJECTION	2.503522	0	tags=46%, list=18%, signal=55%
HALLMARK_INTERFERON_ALPHA_RESPONSE	2.44003	0	tags=51%, list=16%, signal=60%
HALLMARK_TNFA_SIGNALING_VIA_NFKB	2.372104	0	tags=37%, list=13%, signal=42%
HALLMARK_IL6_JAK_STAT3_SIGNALING	2.231522	0	tags=51%, list=17%, signal=61%
HALLMARK_INFLAMMATORY_RESPONSE	2.178336	0	tags=41%, list=17%, signal=49%
HALLMARK_HYPOXIA	2.036037	0	tags=42%, list=19%, signal=52%
HALLMARK_APOPTOSIS	1.794519	0.001427	tags=32%, list=15%, signal=37%
HALLMARK_MYC_TARGETS_V1	1.794177	0.001268	tags=28%, list=13%, signal=32%
HALLMARK_OXIDATIVE_PHOSPHORYLATION	1.731076	0.001689	tags=44%, list=25%, signal=57%
HALLMARK_KRAS_SIGNALING_UP	1.665966	0.003528	tags=31%, list=17%, signal=37%
HALLMARK_IL2_STAT5_SIGNALING	1.641323	0.004006	tags=25%, list=12%, signal=28%
HALLMARK_COMPLEMENT	1.602066	0.005853	tags=26%, list=17%, signal=31%
HALLMARK_P53_PATHWAY	1.522196	0.013926	tags=25%, list=14%, signal=28%
HALLMARK_ANGIOGENESIS	1.520432	0.013318	tags=15%, list=5%, signal=15%
HALLMARK_REACTIVE_OXYGEN_SPECIES_PATHWAY	1.421166	0.029486	tags=30%, list=10%, signal=33%
HALLMARK_EPITHELIAL_MESENCHYMAL_TRANSITION	1.415132	0.029644	tags=30%, list=19%, signal=36%
HALLMARK_UV_RESPONSE_UP	1.410064	0.029291	tags=36%, list=24%, signal=47%
HALLMARK_MTORC1_SIGNALING	1.386696	0.035066	tags=30%, list=20%, signal=37%
HALLMARK_PROTEIN_SECRETION	1.359813	0.042663	tags=23%, list=14%, signal=27%
HALLMARK_COAGULATION	1.343117	0.047391	tags=32%, list=17%, signal=38%
HALLMARK_GLYCOLYSIS	1.303801	0.06141	tags=26%, list=17%, signal=31%
HALLMARK_E2F_TARGETS	1.30029	0.061255	tags=23%, list=18%, signal=28%
HALLMARK_PANCREAS_BETA_CELLS	1.126211	0.234812	tags=36%, list=10%, signal=40%
HALLMARK_ESTROGEN_RESPONSE_EARLY	-1.2855	0.195612	tags=29%, list=21%, signal=36%
HALLMARK_UV_RESPONSE_DN	-1.35739	0.121232	tags=21%, list=12%, signal=24%
HALLMARK_BILE_ACID_METABOLISM	-1.36622	0.13521	tags=31%, list=20%, signal=38%
HALLMARK_WNT_BETA_CATENIN_SIGNALING	-1.4604	0.065655	tags=40%, list=22%, signal=51%
HALLMARK_HEDGEHOG_SIGNALING	-1.64108	0.012242	tags=63%, list=26%, signal=85%
HALLMARK_MITOTIC_SPINDLE	-1.64537	0.018049	tags=27%, list=15%, signal=31%
HALLMARK_NOTCH_SIGNALING	-1.7653	0.004876	tags=40%, list=11%, signal=45%

Table 5.6 Enriched Gene Sets when Comparing Organoids Co-cultured with JS1 Cells and the Organoid Negative Control Group. NES = Normalised Enrichment Score. FDR q-val = False Discovery Rate Q Value. tags = The percentage of gene hits before (for positive ES) or after (for negative ES) the peak in the running enrichment score. This gives an indication of the percentage of genes contributing to the enrichment score. list = The percentage of genes in the ranked gene list before (for positive ES) or after (for negative ES) the peak in the running enrichment score. This gives an indication of where in the list the enrichment score is attained. signal = The enrichment signal strength that combines the two previous statistics. Only gene

sets with an FDR q-value of ≥ 0.25 were included. A solid black outside border indicates

organoid gene sets that have also been implicated in liver injury (see Chapter 1).

REGULATED GENE SETS (Org + TNF vs Org Neg Con)	NES	FDR q-val	LEADING EDGE
HALLMARK_INTERFERON_GAMMA_RESPONSE	2.704874	0	tags=47%, list=10%, signal=51%
HALLMARK_INFLAMMATORY_RESPONSE	2.676826	0	tags=53%, list=14%, signal=61%
HALLMARK_TNFA_SIGNALING_VIA_NFKB	2.60217	0	tags=40%, list=12%, signal=44%
HALLMARK_ALLOGRAFT_REJECTION	2.564354	0	tags=48%, list=15%, signal=56%
HALLMARK_IL6_JAK_STAT3_SIGNALING	2.533489	0	tags=49%, list=10%, signal=54%
HALLMARK_INTERFERON_ALPHA_RESPONSE	2.444017	0	tags=47%, list=10%, signal=52%
HALLMARK_E2F_TARGETS	2.080794	0	tags=42%, list=19%, signal=52%
HALLMARK_MYC_TARGETS_V1	2.05725	0	tags=42%, list=22%, signal=53%
HALLMARK_APOPTOSIS	2.035986	0	tags=27%, list=9%, signal=29%
HALLMARK_G2M_CHECKPOINT	1.968317	0	tags=41%, list=19%, signal=50%
HALLMARK_COMPLEMENT	1.920423	0	tags=25%, list=11%, signal=28%
HALLMARK_MTORC1_SIGNALING	1.827582	0.000381	tags=42%, list=22%, signal=52%
HALLMARK_KRAS_SIGNALING_UP	1.813835	0.0006	tags=29%, list=11%, signal=32%
HALLMARK_UV_RESPONSE_UP	1.774392	0.001104	tags=31%, list=18%, signal=37%
HALLMARK_IL2_STAT5_SIGNALING	1.741766	0.001891	tags=30%, list=15%, signal=35%
HALLMARK_CHOLESTEROL_HOMEOSTASIS	1.735694	0.00201	tags=14%, list=3%, signal=14%
HALLMARK_MYC_TARGETS_V2	1.726803	0.002129	tags=44%, list=22%, signal=56%
HALLMARK_HYPOXIA	1.716179	0.002258	tags=44%, list=24%, signal=57%
HALLMARK_ANGIOGENESIS	1.661108	0.004576	tags=21%, list=5%, signal=22%
HALLMARK_EPITHELIAL_MESENCHYMAL_TRANSITION	1.625629	0.006708	tags=20%, list=9%, signal=21%
HALLMARK_P53_PATHWAY	1.56188	0.010458	tags=31%, list=17%, signal=37%
HALLMARK_GLYCOLYSIS	1.447642	0.029289	tags=32%, list=22%, signal=41%
HALLMARK_PROTEIN_SECRETION	1.435883	0.031409	tags=40%, list=28%, signal=55%
HALLMARK_ANDROGEN_RESPONSE	1.313972	0.084498	tags=24%, list=14%, signal=28%
HALLMARK_MITOTIC_SPINDLE	1.218783	0.171181	tags=28%, list=19%, signal=34%
HALLMARK_UNFOLDED_PROTEIN_RESPONSE	1.214867	0.169454	tags=32%, list=25%, signal=42%
HALLMARK_APICAL_JUNCTION	1.19649	0.185582	tags=16%, list=12%, signal=19%
HALLMARK_COAGULATION	1.192807	0.184138	tags=16%, list=7%, signal=17%
HALLMARK_SPERMATOGENESIS	1.182533	0.190287	tags=31%, list=18%, signal=37%
HALLMARK_FATTY_ACID_METABOLISM	-1.21607	0.233817	tags=18%, list=13%, signal=21%
HALLMARK_KRAS_SIGNALING_DN	-1.24245	0.231412	tags=29%, list=17%, signal=35%
HALLMARK_MYOGENESIS	-1.33611	0.134082	tags=28%, list=19%, signal=34%
HALLMARK_HEDGEHOG_SIGNALING	-1.41368	0.083742	tags=22%, list=4%, signal=23%
HALLMARK_XENOBIOTIC_METABOLISM	-1.73712	0.005621	tags=28%, list=12%, signal=31%
HALLMARK_BILE_ACID_METABOLISM	-1.76782	0.009121	tags=29%, list=15%, signal=34%

Table 5.7 Enriched Gene Sets when Comparing Organoids Treated with TNF and the Organoid Negative Control Group. NES = Normalised Enrichment Score. FDR q-val = False Discovery Rate Q Value. tags = The percentage of gene hits before (for positive ES) or after (for negative ES) the peak in the running enrichment score. This gives an indication of the percentage of genes contributing to the enrichment score. list = The percentage of genes in the ranked gene list before (for positive ES) or after (for negative ES) the peak in the running

enrichment score. This gives an indication of where in the list the enrichment score is attained.

signal = The enrichment signal strength that combines the two previous statistics. Only gene sets with an FDR q-value of ≥ 0.25 were included. A solid black outside border indicates organoid gene sets that have also been implicated in liver injury (see Chapter 1).

REGULATED GENE SETS (Org + JS1 + TNF vs Org Neg Con)	NES	FDR q-val	LEADING EDGE
HALLMARK_INTERFERON_GAMMA_RESPONSE	2.54678	0	tags=48%, list=16%, signal=56%
HALLMARK_ALLOGRAFT_REJECTION	2.499805	0	tags=46%, list=18%, signal=55%
HALLMARK_INTERFERON_ALPHA_RESPONSE	2.486044	0	tags=51%, list=16%, signal=60%
HALLMARK_TNFA_SIGNALING_VIA_NFKB	2.374335	0	tags=37%, list=13%, signal=42%
HALLMARK_IL6_JAK_STAT3_SIGNALING	2.228324	0	tags=51%, list=17%, signal=61%
HALLMARK_INFLAMMATORY_RESPONSE	2.165525	0	tags=41%, list=17%, signal=49%
HALLMARK_HYPOXIA	2.079022	0	tags=42%, list=19%, signal=52%
HALLMARK_APOPTOSIS	1.806679	0.000921	tags=32%, list=15%, signal=37%
HALLMARK_MYC_TARGETS_V1	1.776904	0.001369	tags=28%, list=13%, signal=32%
HALLMARK_OXIDATIVE_PHOSPHORYLATION	1.74629	0.001877	tags=44%, list=25%, signal=57%
HALLMARK_KRAS_SIGNALING_UP	1.638911	0.005594	tags=31%, list=17%, signal=37%
HALLMARK_IL2_STAT5_SIGNALING	1.625773	0.005731	tags=25%, list=12%, signal=28%
HALLMARK_COMPLEMENT	1.599687	0.006726	tags=26%, list=17%, signal=31%
HALLMARK_P53_PATHWAY	1.540264	0.011288	tags=25%, list=14%, signal=28%
HALLMARK_ANGIOGENESIS	1.527115	0.011931	tags=15%, list=5%, signal=15%
HALLMARK_REACTIVE_OXYGEN_SPECIES_PATHWAY	1.450494	0.023211	tags=30%, list=10%, signal=33%
HALLMARK_EPITHELIAL_MESENCHYMAL_TRANSITION	1.438111	0.025525	tags=30%, list=19%, signal=36%
HALLMARK_UV_RESPONSE_UP	1.38695	0.03789	tags=36%, list=24%, signal=47%
HALLMARK_MTORC1_SIGNALING	1.383326	0.037011	tags=30%, list=20%, signal=37%
HALLMARK_PROTEIN_SECRETION	1.370242	0.038488	tags=23%, list=14%, signal=27%
HALLMARK_COAGULATION	1.340706	0.047106	tags=32%, list=17%, signal=38%
HALLMARK_GLYCOLYSIS	1.304545	0.06278	tags=26%, list=17%, signal=31%
HALLMARK_E2F_TARGETS	1.295463	0.064124	tags=23%, list=18%, signal=28%
HALLMARK_PANCREAS_BETA_CELLS	1.146703	0.198136	tags=36%, list=10%, signal=40%
HALLMARK_ESTROGEN_RESPONSE_EARLY	-1.29058	0.19023	tags=29%, list=21%, signal=36%
HALLMARK_UV_RESPONSE_DN	-1.34076	0.141152	tags=21%, list=12%, signal=24%
HALLMARK_BILE_ACID_METABOLISM	-1.38213	0.115829	tags=31%, list=20%, signal=38%
HALLMARK_WNT_BETA_CATENIN_SIGNALING	-1.4743	0.057062	tags=40%, list=22%, signal=51%
HALLMARK_MITOTIC_SPINDLE	-1.64802	0.011243	tags=27%, list=15%, signal=31%
HALLMARK_HEDGEHOG_SIGNALING	-1.65664	0.016245	tags=63%, list=26%, signal=85%
HALLMARK_NOTCH_SIGNALING	-1.71795	0.014551	tags=40%, list=11%, signal=45%

Table 5.8 Enriched Gene Sets when Comparing Organoids Co-cultured with JS1 Cells Treated with TNF and the Organoid Negative Control Group. NES = Normalised Enrichment Score. FDR q-val = False Discovery Rate Q Value. tags = The percentage of gene hits before (for positive ES) or after (for negative ES) the peak in the running enrichment score. This gives an indication of the percentage of genes contributing to the enrichment score. list = The percentage of genes in the ranked gene list before (for positive ES) or after (for negative ES) the peak in the running enrichment score. This gives an indication of where in the list the enrichment score is attained. signal = The enrichment signal strength that combines the two previous statistics. Only gene sets with an FDR q-value of ≥ 0.25 were included. A solid black

outside border indicates organoid gene sets that have also been implicated in liver injury (see

Chapter 1).

REGULATED GENE SETS (Org + JS1 + TNF vs Org + JS1)	NES	FDR q-val	LEADING EDGE
HALLMARK_INFLAMMATORY_RESPONSE	2.584149	0	tags=40%, list=13%, signal=45%
HALLMARK_ALLOGRAFT_REJECTION	2.521901	0	tags=43%, list=14%, signal=49%
HALLMARK_TNFA_SIGNALING_VIA_NFKB	2.486881	0	tags=28%, list=6%, signal=29%
HALLMARK_IL6_JAK_STAT3_SIGNALING	2.404634	0	tags=43%, list=11%, signal=47%
HALLMARK_INTERFERON_GAMMA_RESPONSE	2.367241	0	tags=37%, list=14%, signal=43%
HALLMARK_INTERFERON_ALPHA_RESPONSE	2.236498	0	tags=43%, list=19%, signal=54%
HALLMARK_APOPTOSIS	1.844003	0.000921	tags=27%, list=12%, signal=31%
HALLMARK_COMPLEMENT	1.811855	0.001421	tags=19%, list=8%, signal=21%
HALLMARK_E2F_TARGETS	1.657884	0.006556	tags=37%, list=22%, signal=47%
HALLMARK_HYPOXIA	1.601357	0.009797	tags=28%, list=15%, signal=32%
HALLMARK_ANGIOGENESIS	1.571911	0.011352	tags=21%, list=6%, signal=22%
HALLMARK_UV_RESPONSE_UP	1.563681	0.011357	tags=15%, list=7%, signal=16%
HALLMARK_KRAS_SIGNALING_UP	1.558367	0.011049	tags=15%, list=4%, signal=16%
HALLMARK_P53_PATHWAY	1.488621	0.019994	tags=34%, list=22%, signal=43%
HALLMARK_MYC_TARGETS_V1	1.471638	0.022077	tags=37%, list=25%, signal=49%
HALLMARK_REACTIVE_OXYGEN_SPECIES_PATHWAY	1.431037	0.030372	tags=30%, list=10%, signal=33%
HALLMARK_EPITHELIAL_MESENCHYMAL_TRANSITION	1.385808	0.040208	tags=16%, list=8%, signal=17%
HALLMARK_IL2_STAT5_SIGNALING	1.345208	0.053937	tags=20%, list=11%, signal=22%
HALLMARK_CHOLESTEROL_HOMEOSTASIS	1.315238	0.065754	tags=13%, list=4%, signal=13%
HALLMARK_G2M_CHECKPOINT	1.246537	0.110371	tags=31%, list=20%, signal=38%
HALLMARK_GLYCOLYSIS	1.155236	0.212318	tags=20%, list=14%, signal=23%
HALLMARK_MTORC1_SIGNALING	1.130396	0.238892	tags=26%, list=19%, signal=31%
HALLMARK_ADIPOGENESIS	-1.18571	0.239834	tags=19%, list=15%, signal=22%
HALLMARK_APICAL_SURFACE	-1.19278	0.2443	tags=23%, list=7%, signal=24%
HALLMARK_XENOBIOTIC_METABOLISM	-1.223	0.208965	tags=26%, list=17%, signal=30%
HALLMARK_ANDROGEN_RESPONSE	-1.22962	0.213835	tags=38%, list=24%, signal=49%
HALLMARK_PEROXISOME	-1.23921	0.216875	tags=31%, list=19%, signal=38%
HALLMARK_HEME_METABOLISM	-1.27694	0.175062	tags=17%, list=13%, signal=20%
HALLMARK_FATTY_ACID_METABOLISM	-1.29358	0.166859	tags=21%, list=11%, signal=23%
HALLMARK_ESTROGEN_RESPONSE_LATE	-1.32677	0.14111	tags=24%, list=15%, signal=28%
HALLMARK_HEDGEHOG_SIGNALING	-1.36032	0.118386	tags=30%, list=16%, signal=35%
HALLMARK_UV_RESPONSE_DN	-1.36399	0.132674	tags=31%, list=22%, signal=40%
HALLMARK_WNT_BETA_CATENIN_SIGNALING	-1.39225	0.120461	tags=40%, list=19%, signal=50%
HALLMARK_PANCREAS_BETA_CELLS	-1.48061	0.063809	tags=18%, list=5%, signal=19%
HALLMARK_ESTROGEN_RESPONSE_EARLY	-1.57672	0.034979	tags=26%, list=16%, signal=31%
HALLMARK_NOTCH_SIGNALING	-1.64414	0.025552	tags=40%, list=19%, signal=49%
HALLMARK_BILE_ACID_METABOLISM	-1.74432	0.018865	tags=36%, list=20%, signal=45%

Table 5.9 Enriched Gene Sets when Comparing Organoids Co-cultured with JS1 Cells Treated with TNF and Organoids Co-cultured with JS1 Cells. NES = Normalised Enrichment Score. FDR q-val = False Discovery Rate Q Value. tags = The percentage of gene hits before (for positive ES) or after (for negative ES) the peak in the running enrichment score. This gives an indication of the percentage of genes contributing to the enrichment score. list =

The percentage of genes in the ranked gene list before (for positive ES) or after (for negative ES) the peak in the running enrichment score. This gives an indication of where in the list the enrichment score is attained. signal = The enrichment signal strength that combines the two previous statistics. Only gene sets with an FDR q-value of ≥ 0.25 were included. A solid black outside border indicates organoid gene sets that have also been implicated in liver injury (see Chapter 1).

REGULATED GENE SETS (Org + JS1 + TNF vs Org + TNF)	NES	FDR q-val	LEADING EDGE
HALLMARK_OXIDATIVE_PHOSPHORYLATION	1.939864	0.002216	tags=32%, list=16%, signal=38%
HALLMARK_XENOBIOTIC_METABOLISM	1.685938	0.009922	tags=31%, list=19%, signal=38%
HALLMARK_HYPOXIA	1.648575	0.010943	tags=33%, list=17%, signal=40%
HALLMARK_ADIPOGENESIS	1.594575	0.013156	tags=23%, list=13%, signal=26%
HALLMARK_REACTIVE_OXYGEN_SPECIES_PATHWAY	1.336039	0.112437	tags=28%, list=17%, signal=33%
HALLMARK_COAGULATION	1.277712	0.158789	tags=25%, list=18%, signal=31%
HALLMARK_INFLAMMATORY_RESPONSE	-1.21878	0.246186	tags=31%, list=26%, signal=41%
HALLMARK_TNFA_SIGNALING_VIA_NFKB	-1.23526	0.230099	tags=22%, list=16%, signal=26%
HALLMARK_MTORC1_SIGNALING	-1.31423	0.125764	tags=23%, list=18%, signal=28%
HALLMARK_UV_RESPONSE_DN	-1.37042	0.080283	tags=29%, list=20%, signal=36%
HALLMARK_E2F_TARGETS	-1.38174	0.078054	tags=30%, list=21%, signal=38%
HALLMARK_ESTROGEN_RESPONSE_EARLY	-1.40553	0.065906	tags=27%, list=20%, signal=33%
HALLMARK_PI3K_AKT_MTOR_SIGNALING	-1.41103	0.068388	tags=32%, list=22%, signal=41%
HALLMARK_TGF_BETA_SIGNALING	-1.42616	0.065723	tags=28%, list=20%, signal=35%
HALLMARK_MYC_TARGETS_V2	-1.45224	0.057122	tags=26%, list=16%, signal=31%
HALLMARK_ANDROGEN_RESPONSE	-1.53961	0.024196	tags=34%, list=19%, signal=41%
HALLMARK_NOTCH_SIGNALING	-1.55569	0.023787	tags=43%, list=22%, signal=55%
HALLMARK_WNT_BETA_CATENIN_SIGNALING	-1.58689	0.019757	tags=60%, list=33%, signal=89%
HALLMARK_HEDGEHOG_SIGNALING	-1.5873	0.024697	tags=30%, list=14%, signal=34%
HALLMARK_G2M_CHECKPOINT	-1.90252	0.000928	tags=53%, list=29%, signal=74%
HALLMARK_CHOLESTEROL_HOMEOSTASIS	-1.94587	0.000907	tags=38%, list=16%, signal=44%
HALLMARK_MITOTIC_SPINDLE	-2.06814	0	tags=51%, list=26%, signal=68%

Table 5.10 Enriched Gene Sets when Comparing Organoids Co-cultured with JS1 Cells Treated with TNF and Organoids Treated with TNF. NES = Normalised Enrichment Score. FDR q-val = False Discovery Rate Q Value. tags = The percentage of gene hits before (for positive ES) or after (for negative ES) the peak in the running enrichment score. This gives an indication of the percentage of genes contributing to the enrichment score. list = The percentage of genes in the ranked gene list before (for positive ES) or after (for negative ES) the peak in the running enrichment score. This gives an indication of where in the list the enrichment score is attained. signal = The enrichment signal strength that combines the two previous statistics. Only gene sets with an FDR q-value of ≥ 0.25 were included. A solid black outside border indicates organoid gene sets that have also been implicated in liver injury (see Chapter 1).

CHAPTER 5 TRANSCRIPTIONAL PROFILING ANALYSIS OF THE IN VITRO MODELLING OF LIVER INJURY AND FIBROSIS

NAME	Org + JS1 vs Org Neg Con	Org + TNF vs Org Neg Con	Org + JS1 + TNF vs Org Neg Con	Org + JS1 + TNF vs Org + JS1	Org + JS1 + TNF vs Org + TNF
HALLMARK_INTERFERON_GAMMA_RESPONSE	2.5591118	2.7048738	2.54678	2.3672414	
HALLMARK_ALLOGRAFT_REJECTION	2.5035217	2.5643535	2.4998047	2.5219014	
HALLMARK_INTERFERON_ALPHA_RESPONSE	2.4400303	2.4440165	2.4860437	2.2364976	
HALLMARK_TNFA_SIGNALING_VIA_NFKB	2.3721037	2.6021702	2.3743353	2.4868805	-1.2352579
HALLMARK_IL6_JAK_STAT3_SIGNALING	2.2315216	2.5334888	2.2283235	2.4046335	
HALLMARK_INFLAMMATORY_RESPONSE	2.178336	2.6768258	2.1655247	2.5841486	-1.2187831
HALLMARK_HYPOXIA	2.036037	1.7161791	2.0790215	1.6013566	1.6485753
HALLMARK_APOPTOSIS	1.7945192	2.0359862	1.806679	1.8440032	
HALLMARK_MYC_TARGETS_V1	1.79417	2.05725	1.7769035	1.4716381	
HALLMARK_OXIDATIVE_PHOSPHORYLATION	1.731076	-1.2424474	1.7462904		1.9398642
HALLMARK_KRAS_SIGNALING_DN	1.6659662	1.7417663	1.6257734	1.3452076	
HALLMARK_IL2_STAT5_SIGNALING	1.641323	1.9204228	1.5996867	1.8118554	
HALLMARK_COMPLEMENT	1.6020663	1.5618796	1.5402644	1.486211	
HALLMARK_P53_PATHWAY	1.5221955	1.6611075	1.527115	1.5719112	
HALLMARK_ANGIOGENESIS	1.5204319	1.4211664	1.4504936	1.431037	-1.3360394
HALLMARK_REACTIVE_OXYGEN_SPECIES_PATHWAY	1.4211664	1.6256292	1.4381112	1.3858079	
HALLMARK_EPITHELIAL_MESENCHYMAL_TRANSITION	1.415132	1.7743915	1.3869501	1.5636808	
HALLMARK_UV_RESPONSE_UP	1.410064	1.827582	1.383326	1.1303961	-1.3142254
HALLMARK_MTORC1_SIGNALING	1.3866956	1.4358826	1.3702415		
HALLMARK_PROTEIN_SECRETION	1.3598125	1.1928065	1.3407058		1.2777115
HALLMARK_COAGULATION	1.3431171	1.4476416	1.3045449	1.1552355	
HALLMARK_GLYCOLYSIS	1.303801	2.080794	1.2954625	1.6578842	-1.3817412
HALLMARK_E2F_TARGETS	1.3002895		1.1467026	-1.4806076	
HALLMARK_PANCREAS_BETA_CELLS	1.1262113				
HALLMARK_ESTROGEN_RESPONSE_EARLY	-1.2854978		-1.290576	-1.5767205	-1.4055271
HALLMARK_UV_RESPONSE_DN	-1.3573864		-1.3407611	-1.3639873	-1.3704182
HALLMARK_BILE_ACID_METABOLISM	-1.366219	-1.7678248	-1.3821256	-1.7443225	
HALLMARK_WNT_BETA_CATENIN_SIGNALING	-1.460431	-1.7371234	-1.4743024	-1.3922471	-1.5868919
HALLMARK_HEDGEHOG_SIGNALING	-1.6410805	-1.4136829	-1.6566366	-1.3603172	-1.5872995
HALLMARK_MITOTIC_SPINDLE	-1.6453673	1.218783	-1.6480198		-2.0681443
HALLMARK_NOTCH_SIGNALING	-1.7652994		-1.717951	-1.6441399	-1.5556949
HALLMARK_G2M_CHECKPOINT		1.9683167	1.2465374		-1.9025155
HALLMARK_KRAS_SIGNALING_UP		1.8138347	1.5583673	1.6389109	
HALLMARK_CHOLESTEROL_HOMEOSTASIS		1.7356938	1.3152376		-1.9458736
HALLMARK_MYC_TARGETS_V2		1.726803			-1.4522351
HALLMARK_ANDROGEN_RESPONSE		1.3139716		-1.2296187	-1.5396069
HALLMARK_UNFOLDED_PROTEIN_RESPONSE		1.2148665			
HALLMARK_APICAL_JUNCTION		1.1964903			
HALLMARK_SPERMATOGENESIS		1.1825325			
HALLMARK_FATTY_ACID_METABOLISM		-1.2160684			
HALLMARK_MYOGENESIS		-1.3361124			
HALLMARK_ADIPOGENESIS				-1.2935793	1.5945746
HALLMARK_APICAL_SURFACE				-1.1857072	
HALLMARK_XENOBIOTIC_METABOLISM				-1.1927772	1.6859378
HALLMARK_PEROXISOME				-1.2229954	
HALLMARK_HEME_METABOLISM				-1.2392057	
HALLMARK_ESTROGEN_RESPONSE_LATE				-1.2769412	
HALLMARK_DNA_REPAIR				-1.3267686	
HALLMARK_PI3K_AKT_MTOR_SIGNALING					-1.4110316
HALLMARK_TGF_BETA_SIGNALING					-1.4261559

Table 5.11 Gene Set Enrichment Analysis of Significant Differentially Expressed Gene Sets Between Organoid Groups. Ranking the hallmark gene sets from the Mouse_ENSEMBL_Gene_ID_Human_Orthologs_MSigDB.v7.2.chip data base on normalised enrichment score between all the organoid experimental groups. All enrichment scores are for gene sets that had an FDR q-value ≥ 0.25. Group normalised enrichment score colour scaled red for a positive normalised enrichment score and blue for a negative normalised enrichment score. A solid black outside border indicates organoid gene sets that have also been implicated in liver injury (see Chapter 1).

Using GSEA on significant differentially expressing genes we identified JS1 cell dependent positive gene set enrichment that are important to liver injury (Tables 5.6-5.11), such as the hallmarks of Hypoxia (Roth and Copple 2015), the ROS pathway (Tu *et al* 2015), and coagulation (Robinson *et al* 2016), as well as negative gene set enrichment for the hallmarks of hedgehog signalling and notch signalling (Tsuchida and Friedman 2017). There was also TNF treatment dependent positive gene set enrichment for the hallmarks of the interferon gamma response (Sherlock & Dooley, 2002; Tu *et al* 2015), TNF signalling via NFκB, IL-6/JAK/STAT3 signalling (Yang and Seki 2015; Luedde *et al* 2014), the inflammatory response, hypoxia, and apoptosis. While there was a TNF dependent negative gene set enrichment for the hallmarks of Hedgehog signalling (Tsuchida and Friedman 2017).

5.2.4 Quality Control Analysis for JS1 Samples
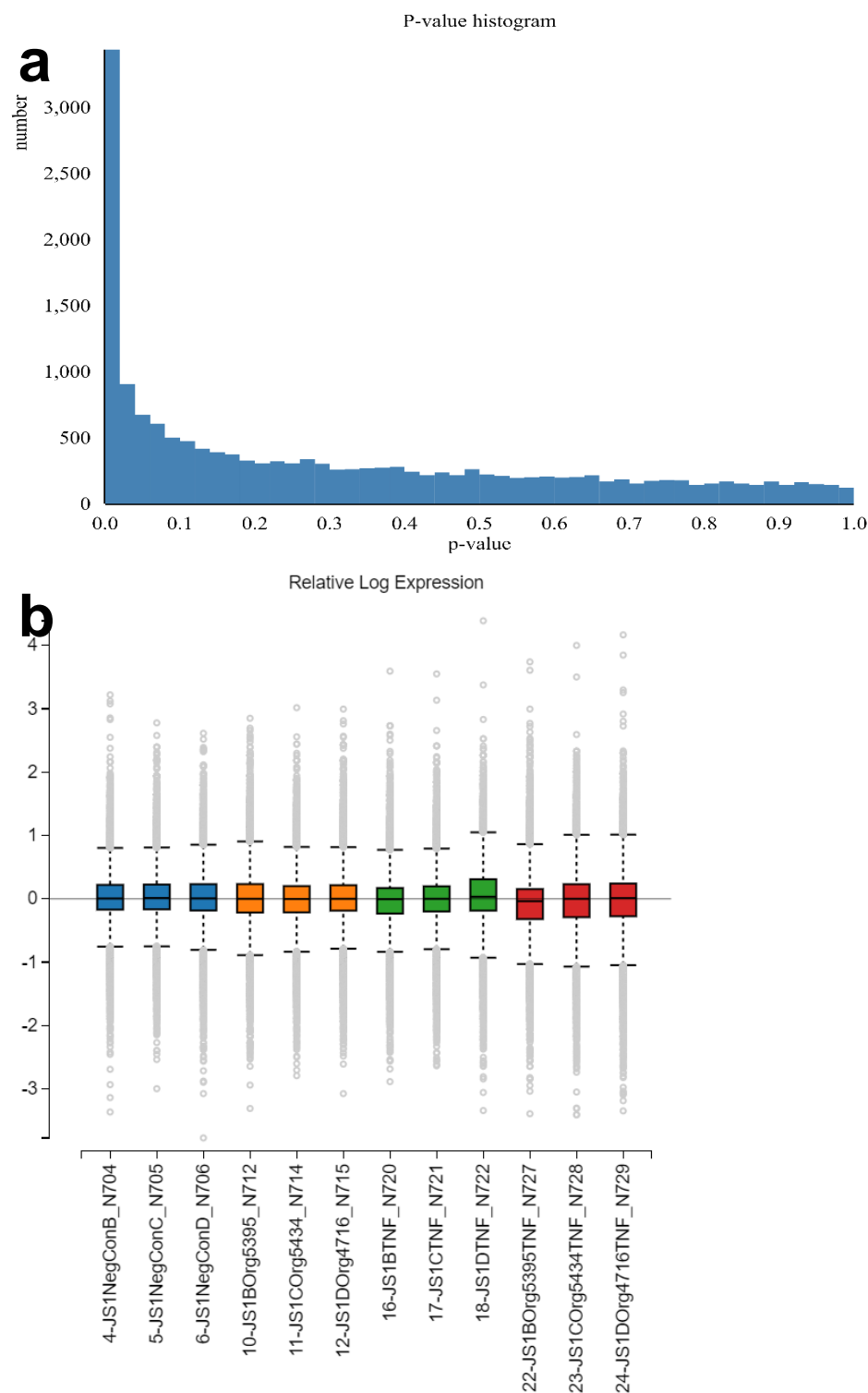
Figure 5.10 Quality Control Analysis of JS1 Cell Samples a. p-Value histogram quantifying all gene expression data from JS1 Samples measured over the calculated probability of a null hypothesis (p-value). **b.** Relative Log gene Expression boxplot of each sample measured.

245

a

b Variance by MDS Dimensions
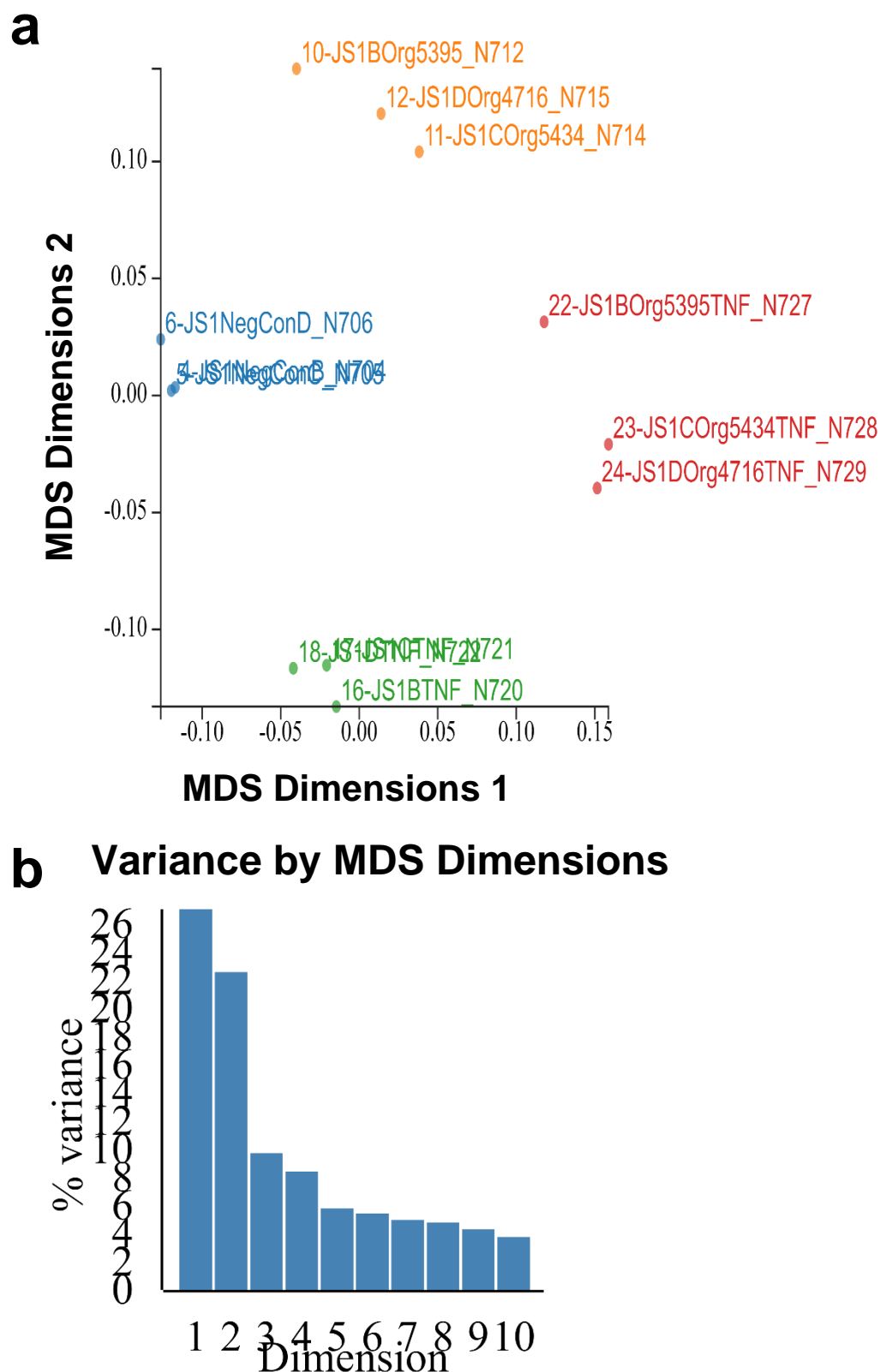
Figure 5.11 Multidimensional Analysis of JS1 cell Samples a. Multidimensional scaling

(MDS) plot of each measured organoid sample. **b.** Histogram representing the percentage

variance between the first 10 dimensions of the MDS plot.

**5.2.5 Gene Expression Analysis
for JS1 Samples**

a
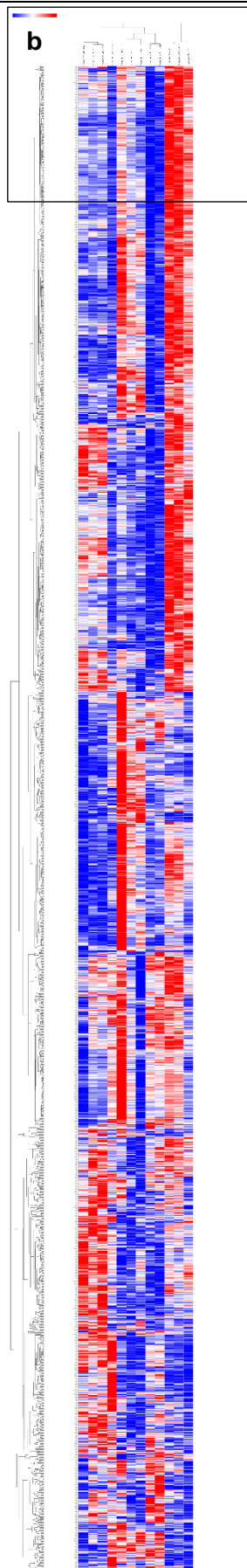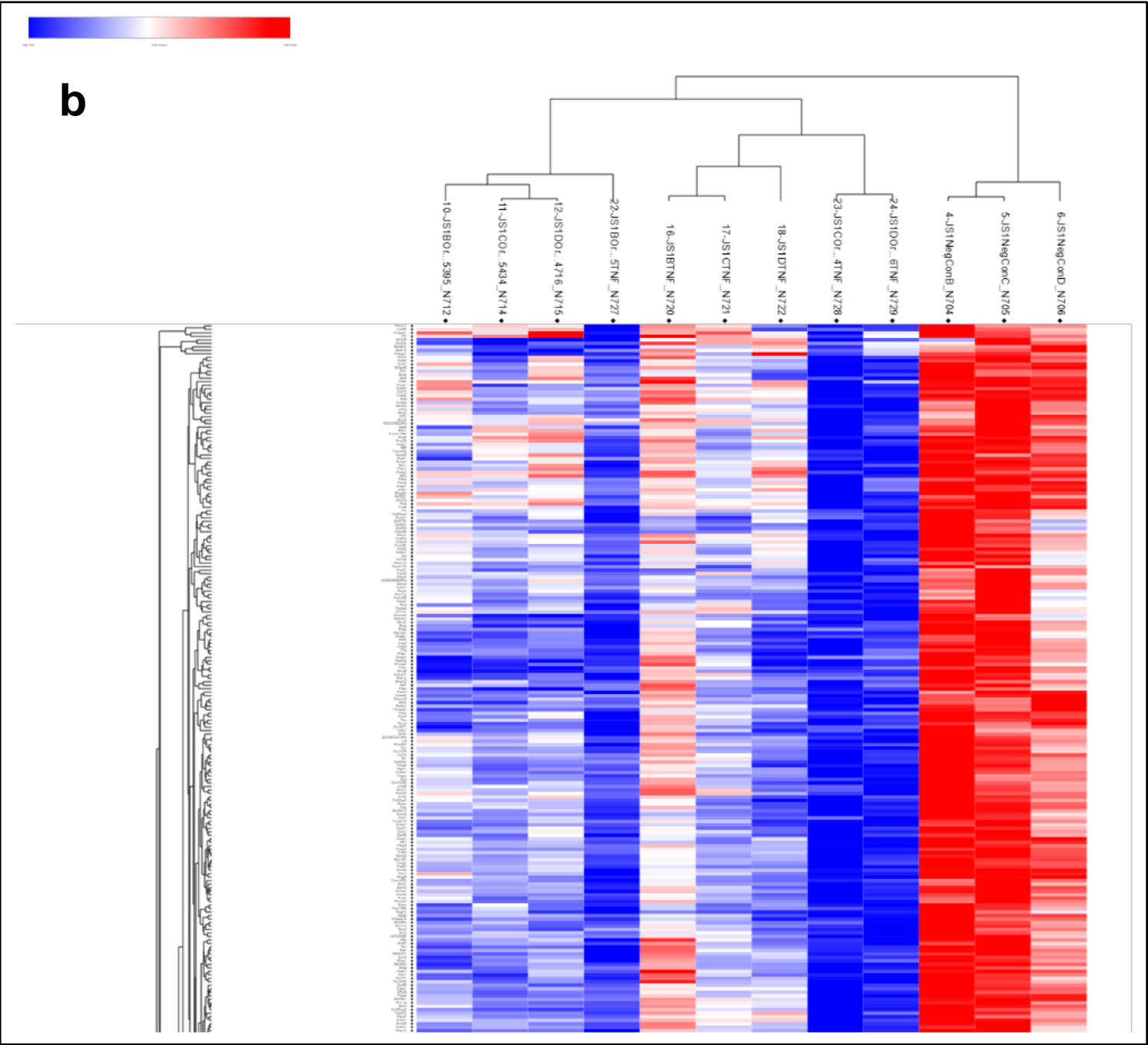
b

Figure 5.12 Hierarchical Cluster Analysis. a. Hierarchical clustering of JS1 samples and the significantly differentially expressed genes of each sample. **b.** Subsection of hierarchical cluster for identifying column labels. Relative increases in gene expression are labelled red and relative decreases in genes expression are labelled blue. Only genes with an FDR cut-off of $\leq$ 0.05 are represented.

Hierarchical cluster analysis suggests a the JS1 cell divided into three distinct phenotypes, that is the negative control phenotype, The co-culture phenotype and the TNF treated phenotype. The co-culture with TNF treatment phenotype grouped with the TNF treated or co-culture only phenotypes.
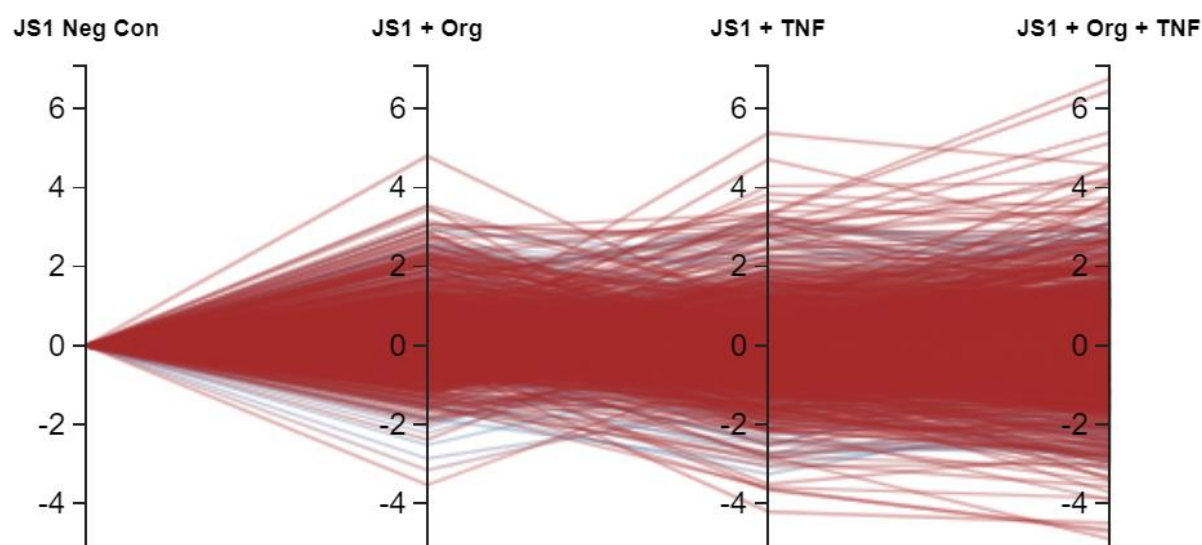
Figure 5.13 Parallel Coordinate Analysis of JS1 Cell Samples. Parallel coordinate graph of
each JS1 group relative to the negative control group, each line is a gene and the y-coordinate
is the log fold change of each group. Only genes with an FDR cut-off of ≤ 0.05 are represented.

The parallel coordinate analysis suggests that there is a greater amount of variance in
differential expression for the JS1 cell groups co-cultured with organoids and treated with TNF
ranging from a log change of greater than 6-fold compared to the negative control, than the co-
culture only group and the TNF only group compared to the negative control. These groups
only had a variance in differentially expression ranging from a log change of greater than 4-
fold.
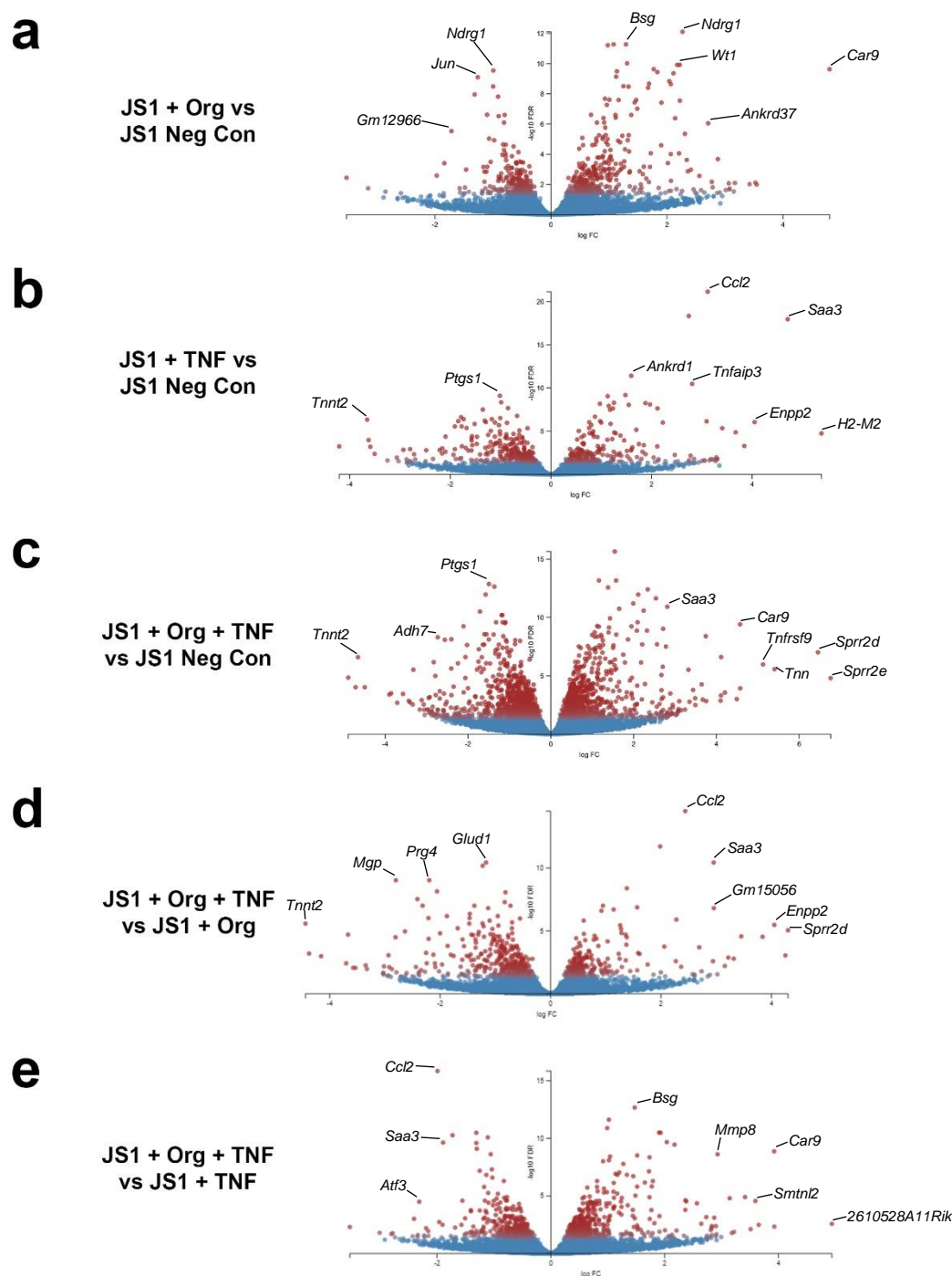
Figure 5.14 Volcano plot of JS1 gene expression log-fold change and statistical significance (-log^{10} FDR). Points with an FDR cut-off > 0.05 are blue and points with an FDR cut-off ≤ 0.05 are red. **a.** Relative gene expression of the JS1/Organoid coculture compared to the negative control group. **b.** Relative gene expression of the JS1/TNF treatment culture

compared to the negative control group. **c.** Relative gene expression of the JS1/Organoid coculture group treated with TNF, compared to the negative control group. **d.** Relative gene expression of the JS1/Organoid coculture group treated with TNF, compared to the JS1/Organoid coculture group. **e.** Relative gene expression of the JS1/Organoid coculture group treated with TNF, compared to the TNF/Organoid treatment culture group.

The volcano plots represent the number of significant differentially expressing genes as well as non-differentially expressing genes between JS1 cell groups, the largest number being 1982 significant differentially expressed genes between the JS1 cells co-cultured with organoids and treated with TNF compared to the organoid negative control group.
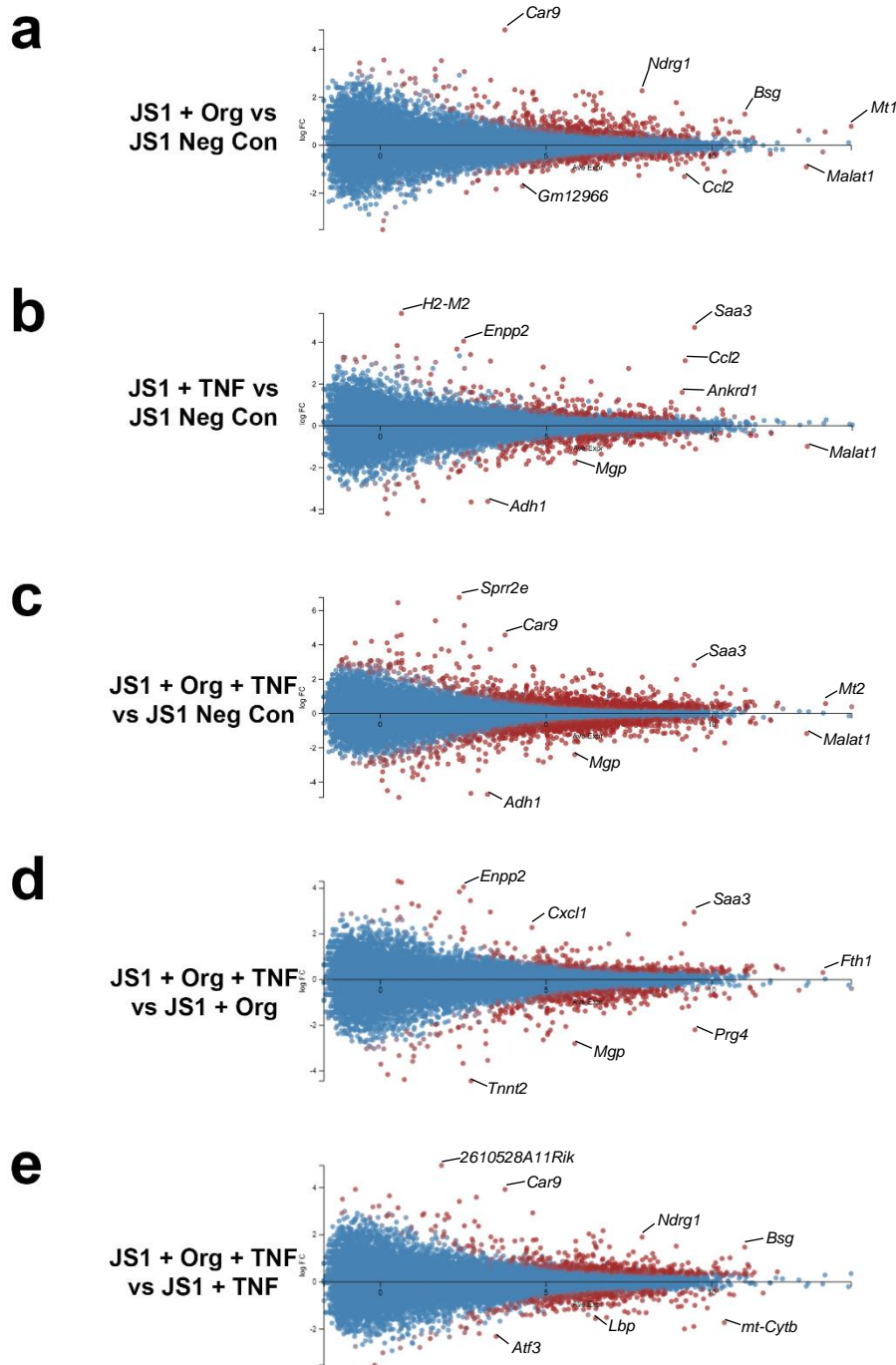
Figure 5.15 MA Ratio Intensity Plot of JS1 Cell Gene Expression Log-Fold Change and Mean Average Expression. Points with an FDR cut-off > 0.05 are blue and point with an FDR cut-off ≤ 0.05 are red. Some genes on the extremes of mean average expression and log-fold change in gene expression have been labelled **a.** Relative gene expression of the JS1/Organoid coculture compared to the negative control group. **b.** Relative gene expression of the JS1/TNF treatment culture compared to the negative control group. **c.** Relative gene expression of the

JS1/Organoid coculture group treated with TNF, compared to the negative control group. **d.** Relative gene expression of the JS1/Organoid coculture group treated with TNF, compared to the JS1/Organoid coculture group. **e.** Relative gene expression of the JS1/Organoid coculture group treated with TNF, compared to the JS1/TNF treatment culture group.

The log-fold change in expression of all the JS1 cell genes between each of the groups clustered around zero on the MA plots, hence we can assume that the gene expression analysis has been correctly normalised for the samples and the measured relative changes are correct. Some genes on the extremes of mean average expression and log-fold change in gene expression like *Bsg*, *Saa3* and *Car9*, were observed to be common between groups analysed.
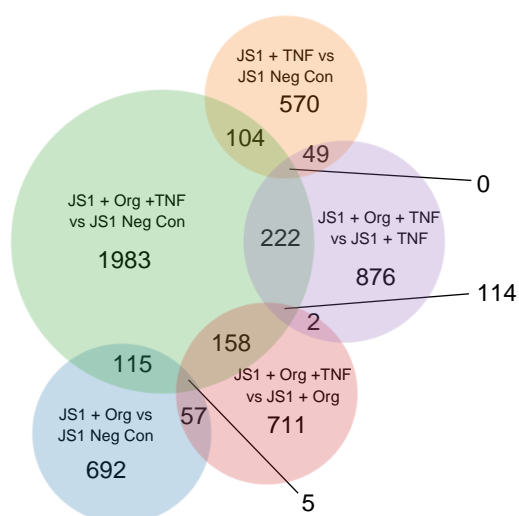
Figure 5.16 Common and Unique Gene Expression in JS1 Cells. Venn diagram for quantifying significant JS1 gene expression within groups and overlapping between group. Only genes with an FDR cut-off of ≤ 0.05 were quantified. Not all overlapping could be represented by a Venn diagram, hence use the Table 5.12 for all discovered overlapping between groups.

Overlapping Analysis Groups	Number of Significant Genes within each over lapping group set
JS1 + Org vs JS1 Neg Con	692
JS1 + TNF vs JS1 Neg Con	570
JS1 + Org + TNF vs JS1 Neg Con	1983
JS1 + Org + TNF vs JS1 + Org	711
JS1 + Org + TNF vs JS1 + TNF	876
JS1 + TNF vs JS1 Neg Con: JS1 + Org + TNF vs JS1 Neg Con	104
JS1 + Org vs JS1 Neg Con: JS1 + TNF vs JS1 Neg Con: JS1 + Org + TNF vs JS1 Neg Con	37
JS1 + Org vs JS1 Neg Con:JS1 + Org + TNF vs JS1 + Org	57
JS1 + TNF vs JS1 Neg Con: JS1 + Org + TNF vs JS1 + Org	14
JS1 + Org vs JS1 Neg Con: JS1 + TNF vs JS1 Neg Con: JS1 + Org + TNF vs JS1 + Org	1
JS1 + Org + TNF vs JS1 Neg Con: JS1 + Org + TNF vs JS1 + Org	158
JS1 + Org vs JS1 Neg Con: JS1 + Org + TNF vs JS1 Neg Con: JS1 + Org + TNF vs JS1 + Org	5
JS1 + TNF vs JS1 Neg Con: JS1 + Org +TNF vs JS1 Neg Con: JS1 + Org + TNF vs JS1 + Org	**153**
JS1 + Org vs JS1 Neg Con: JS1 + TNF vs JS1 Neg Con: JS1 + Org + TNF vs JS1 Neg Con: JS1 + Org + TNF vs JS1 + Org	25
JS1 + Org vs JS1 Neg Con: JS1 + Org + TNF vs JS1 + TNF	19
JS1 Neg Con vs JS1 + TNF: JS1 + TNF vs JS1 + Org + TNF	49
JS1 + Org vs JS1 Neg Con: JS1 + TNF vs JS1 Neg Con: JS1 + Org + TNF vs JS1 + TNF	3
JS1 + Org + TNF vs JS1 Neg Con: JS1 + Org + TNF vs JS1 + TNF	222
JS1 + Org vs JS1 Neg Con: JS1 + Org + TNF vs JS1 Neg Con: JS1 + Org + TNF vs JS1 + TNF	**202**
JS1 + TNF vs JS1 Neg Con: JS1 + Org + TNF vs JS1 Neg Con: JS1 + Org + TNF vs JS1 + TNF	0
JS1 + Org vs JS1 Neg Con: JS1 + TNF vs JS1 Neg Con: JS1 + Org + TNF vs JS1 Neg Con: JS1 + Org + TNF vs JS1 + TNF	10
JS1 + Org + TNF vs JS1 + Org: JS1 + Org + TNF vs JS1 + TNF	2
JS1 + Org vs JS1 Neg Con: JS1 + Org + TNF vs JS1 + Org: JS1 + Org + TNF vs JS1 + TNF	4
JS1 + TNF vs JS1 Neg Con: JS1 + Org vs JS1 + Org + TNF: JS1 + Org + TNF vs JS1 + TNF	3
JS1 + Org vs JS1 Neg Con: JS1 + TNF vs JS1 Neg Con: JS1 + Org + TNF vs JS1 + Org: JS1 + Org + TNF vs JS1 + TNF	2
JS1 + Org + TNF vs JS1 Neg Con: JS1 + Org + TNF vs JS1 + Org: JS1 + Org + TNF vs JS1 + TNF	114
JS1 + Org vs JS1 Neg Con: JS1 + Org + TNF vs JS1 Neg Con: JS1 + Org + TNF vs JS1 + Org: JS1 + Org + TNF vs JS1 + TNF	18
JS1 + TNF vs JS1 Neg Con: JS1 + Org + TNF vs JS1 Neg Con: JS1 + Org + TNF vs JS1 + Org: JS1 + Org + TNF vs JS1 + TNF	23
JS1 + Org vs JS1 Neg Con: JS1 + TNF vs JS1 Neg Con: JS1 + Org + TNF vs JS1 Neg Con: JS1 + Org + TNF vs JS1 + Org: JS1 + Org + TNF vs JS1 + TNF	24

Table 5.12 JS1 Differential Gene Expression Overlapping Analysis. Table for quantifying the number of significant JS1 gene expression within groups and all discovered overlapping differential expression. Only genes with an FDR cut-off of ≤ 0.05 were quantified.

CHAPTER 5 TRANSCRIPTIONAL PROFILING ANALYSIS OF THE IN VITRO MODELLING OF LIVER INJURY AND FIBROSIS

From overlapping analysis of all the significant differentially expressed genes, 202 genes in the JS1 cell samples were discovered to be differentially expressed dependent on co-culturing them with organoids (Table 5.13) and 153 genes were discovered to be differentially expressed dependent on treating of the samples with TNF (Table 5.14).

Gene Name	Ensembl Gene ID	JS1 Neg. Con.	JS1 + Org	JS1 + Org + TNF	FDR cut-off	Ave. Expr.	P value
Car9	ENSMUSG00000028463	0	4.802920715	4.572272153	2.87939E-11	3.762642744	3.302E-14
2610528A11Rik	ENSMUSG00000096001	0	3.523040974	3.751505283	0.001388087	1.845757918	5.396E-05
Cd52	ENSMUSG00000000682	0	3.012015953	3.669131322	0.002029707	0.273889064	8.748E-05
Stmn2	ENSMUSG00000027500	0	2.456745497	3.64258484	0.000173194	2.06731712	3.795E-06
Lamb3	ENSMUSG00000026639	0	3.170476045	3.349147178	0.001549021	1.651282169	6.23E-05
Slc16a3	ENSMUSG00000025161	0	2.485625224	3.101899952	0.002896821	0.659846761	0.0001411
Prelid2	ENSMUSG00000056671	0	2.309080613	2.780130656	3.73003E-08	4.058128858	1.775E-10
Mmp8	ENSMUSG00000005800	0	2.140652542	2.713573567	1.44039E-09	4.599038214	3.304E-12
Apln	ENSMUSG00000037010	0	2.34009661	2.671797342	8.67861E-06	2.845199002	1.032E-07
Ppp1r3b	ENSMUSG00000046794	0	2.260032134	2.624942757	0.003937131	1.317368034	0.000206
Fabp4	ENSMUSG00000062515	0	2.110812597	2.539478349	2.09335E-12	6.296532283	1.516E-15
Pirb	ENSMUSG00000058818	0	2.066428138	2.451502341	0.003042675	1.533090126	0.0001506
Ppp1r3c	ENSMUSG00000067279	0	2.77204976	2.379756725	0.004218391	0.900318608	0.0002251
Sprr2g	ENSMUSG00000046203	0	1.56109155	2.27403092	0.000151595	2.794435033	3.194E-06
Bnip3	ENSMUSG00000078566	0	2.176695603	2.242451596	4.14715E-12	6.656458246	3.755E-15
Egln3	ENSMUSG00000035105	0	2.22185748	2.2076993	3.77E-09	4.613215642	1.024E-11
Sprr2f	ENSMUSG00000050635	0	1.855375865	2.198092611	0.00167096	2.003851007	6.919E-05
Ndrg1	ENSMUSG00000005125	0	2.265740591	2.111918314	5.95685E-14	7.899059158	1.438E-17
Ankrd37	ENSMUSG00000050914	0	2.709749273	2.08714952	8.20505E-07	3.33504746	6.885E-09
Gm16439	ENSMUSG00000072594	0	2.359100771	2.084316178	0.000650087	2.264228654	1.97E-05
Egln1	ENSMUSG00000031987	0	2.065734624	2.077693081	2.00299E-10	5.896859376	3.627E-13
Bhlhe41	ENSMUSG00000030256	0	2.410813072	2.069104887	0.000582874	1.9167009	1.731E-05
Tyrobp	ENSMUSG00000030579	0	1.64586407	2.02902088	0.005951134	1.877480735	0.0003506
Fam162a	ENSMUSG00000003955	0	1.770465692	1.991552116	2.77369E-12	8.929527165	2.177E-15
Smtnl2	ENSMUSG00000045667	0	2.065319604	1.833543501	3.90494E-05	2.898480728	6.105E-07
Bhlhe40	ENSMUSG00000030103	0	1.903807311	1.75068063	1.11828E-08	4.702356382	4.118E-11
4930447F24Rik	ENSMUSG00000102224	0	1.643022716	1.721367399	0.000771404	2.770269783	2.538E-05
Mgarp	ENSMUSG00000037161	0	1.352237311	1.648018912	5.51426E-05	4.419137231	9.121E-07
Pgm2	ENSMUSG00000025791	0	1.441727333	1.579961248	1.41094E-09	6.429170569	3.151E-12
Chil3	ENSMUSG00000040809	0	2.040373012	1.548697649	1.506E-09	6.456668404	3.636E-12
Gbe1	ENSMUSG00000022707	0	1.263449614	1.546733401	4.64359E-06	4.414200701	5.102E-08
Pdk1	ENSMUSG00000006494	0	1.673143287	1.513424738	1.41094E-09	6.518486628	3.087E-12
mt-Tm	ENSMUSG00000064344	0	1.230075135	1.502874811	4.95995E-08	6.7218698	2.545E-10
Sprr1a	ENSMUSG00000050359	0	1.323108029	1.471142949	4.28598E-07	5.573200469	3.119E-09
Aldoart1	ENSMUSG00000059343	0	1.357741558	1.449365569	0.002835184	2.771241321	0.0001359
Pgk1	ENSMUSG00000062070	0	1.149533311	1.441524404	3.81748E-05	4.399685149	5.945E-07
Pfkl	ENSMUSG00000020277	0	1.337343798	1.405294749	1.8522E-10	7.494443255	3.242E-13
Snai1	ENSMUSG00000042821	0	1.238605276	1.388093307	0.00701761	2.693764738	0.0004315
Bsg	ENSMUSG00000023175	0	1.292334747	1.38318493	7.94039E-14	10.99709742	2.397E-17
Tnfsf9	ENSMUSG00000035678	0	1.60057182	1.364464512	0.00033905	3.472732673	8.76E-06
Dusp6	ENSMUSG00000019960	0	1.690719755	1.316256645	1.92367E-09	6.161071094	4.857E-12
Gys1	ENSMUSG00000003865	0	1.275922501	1.280788156	6.39687E-06	6.914314981	7.221E-08
Cys1	ENSMUSG00000062563	0	1.583331544	1.238102778	0.001637807	3.050263441	6.743E-05
Slpi	ENSMUSG00000017002	0	0.895682937	1.226697109	1.01193E-08	7.907428782	3.665E-11
Clybl	ENSMUSG00000025545	0	1.114606436	1.199521795	1.78767E-08	7.000926523	7.338E-11
Bnip3l	ENSMUSG00000022051	0	0.942847454	1.174357813	3.39327E-08	6.696524813	1.557E-10
Aldoa	ENSMUSG00000030695	0	0.978835434	1.1613871	4.17475E-14	10.55314529	7.56E-18
Ldha	ENSMUSG00000063229	0	1.007088574	1.15889727	4.00309E-10	10.11708482	7.491E-13
Grhpr	ENSMUSG00000035637	0	0.818449955	1.150589779	2.81441E-06	5.922966951	2.854E-08
Ccdc58	ENSMUSG00000075229	0	0.712759077	1.145710108	8.03536E-05	5.734259543	1.431E-06
Lox	ENSMUSG00000024529	0	1.468863548	1.142230596	2.16866E-08	6.718705858	9.295E-11
Mxi1	ENSMUSG00000025025	0	1.016342551	1.122460092	9.63638E-06	4.990051317	1.169E-07
Gpi1	ENSMUSG00000036427	0	1.123247384	1.11984107	6.63794E-11	8.267573584	9.617E-14
mt-Ti	ENSMUSG00000064342	0	0.896250537	1.091916703	0.004286988	3.655027281	0.0002316
Gm1840	ENSMUSG00000043192	0	1.216780097	1.08191592	0.000381258	4.30040609	1.013E-05
Jmjd6	ENSMUSG00000056962	0	0.889817919	1.077578113	1.05876E-07	7.084642867	6.136E-10
P4ha2	ENSMUSG00000018906	0	0.935095384	1.06474889	4.01898E-08	7.71869603	1.941E-10
Gm7336	ENSMUSG00000078636	0	0.802070783	1.027727429	1.4094E-06	6.908280327	1.268E-08
Cebpd	ENSMUSG00000071637	0	1.38356253	1.024867937	2.73726E-07	5.38132427	1.801E-09

Gene Name	Ensembl Gene ID	JS1 Neg. Con.	JS1 + Org	JS1 + Org + TNF	FDR cut-off	Ave. Expr.	P value
Ddit3	ENSMUSG00000025408	0	0.855393805	1.006644414	0.000129437	6.082123361	2.618E-06
Casp6	ENSMUSG00000027997	0	0.711426712	1.005717596	0.000134108	5.489442101	2.744E-06
Tpi1	ENSMUSG00000023456	0	0.79124759	0.997666719	4.46556E-09	9.288718369	1.267E-11
Plekha2	ENSMUSG00000031557	0	0.772728808	0.99592518	4.08397E-06	6.16580546	4.388E-08
Gm9790	ENSMUSG00000044330	0	1.007902027	0.994871327	0.000193392	6.053737632	4.424E-06
Amz2	ENSMUSG00000020610	0	0.674734794	0.987017633	1.4206E-05	6.319866003	1.852E-07
Kdm4b	ENSMUSG00000024201	0	0.967208649	0.96975067	0.000930807	4.461134082	3.265E-05
Hk1	ENSMUSG00000037012	0	1.025146544	0.966451494	1.25515E-05	6.437768873	1.599E-07
Eno1	ENSMUSG00000063524	0	0.962089175	0.938796864	8.24853E-09	8.150571383	2.788E-11
Snhg5	ENSMUSG00000097195	0	0.625942265	0.914124251	0.000344013	5.428796591	8.95E-06
Pafah1b3	ENSMUSG00000005447	0	0.553547294	0.909597458	9.26567E-05	6.077615503	1.712E-06
Nampt	ENSMUSG00000020572	0	0.748529232	0.909444506	3.3957E-05	6.228513948	5.125E-07
Tpd52	ENSMUSG00000027506	0	0.58671391	0.904770949	0.000487529	5.103144928	1.354E-05
Eif1b	ENSMUSG00000006941	0	0.865952103	0.904661057	0.000188013	5.66296408	4.245E-06
P4ha1	ENSMUSG00000019916	0	0.930225853	0.892136685	3.72203E-09	8.016021704	9.886E-12
Plod2	ENSMUSG00000032374	0	0.995363349	0.885724235	0.000165613	5.612304522	3.569E-06
Eno1b	ENSMUSG00000059040	0	0.904496269	0.880785272	5.89961E-08	7.923333232	3.134E-10
Vhl	ENSMUSG00000033933	0	1.1163223	0.87315524	0.000318626	4.887613372	8.044E-06
Soat1	ENSMUSG00000026600	0	0.949424677	0.870506686	4.47464E-06	6.520856691	4.889E-08
Htra1	ENSMUSG00000006205	0	0.519437937	0.85568655	0.000380713	6.649211221	1.007E-05
Pim1	ENSMUSG00000024014	0	0.698275036	0.854231174	0.000191545	6.20871152	4.348E-06
Ccng2	ENSMUSG00000029385	0	0.785621731	0.821189238	0.007721121	4.8333193	0.0004889
Rsbn1	ENSMUSG00000044098	0	0.613579932	0.815785264	0.002939973	5.053992782	0.0001445
Me2	ENSMUSG00000024556	0	0.68941178	0.80949237	0.000815971	5.958291122	2.763E-05
Tmem45a	ENSMUSG00000022754	0	1.155864507	0.809149402	1.4206E-05	5.915992554	1.851E-07
Txnip	ENSMUSG00000038393	0	0.763436666	0.803653142	0.000683003	7.106192388	2.127E-05
Krt19	ENSMUSG00000020911	0	0.761616707	0.801055827	0.005125636	4.879987632	0.0002902
Pla2g15	ENSMUSG00000031903	0	0.664221788	0.780929927	0.00612741	4.772694034	0.0003647
Gpr146	ENSMUSG00000044197	0	0.821650615	0.779512532	0.006838817	4.604858941	0.0004174
Trappc6a	ENSMUSG00000002043	0	0.652146192	0.770789691	9.57729E-05	6.581538702	1.798E-06
Pcdh9	ENSMUSG00000055421	0	0.518828276	0.763315846	0.001106209	6.0606734	4.033E-05
Isg20	ENSMUSG00000039236	0	0.901564896	0.738794781	0.000561976	6.111798841	1.645E-05
Tigd2	ENSMUSG00000049232	0	0.596176605	0.732068688	0.001013699	6.014796455	3.647E-05
Vim	ENSMUSG00000026728	0	0.689271938	0.724141762	1.48147E-08	10.13149032	5.733E-11
Gm15710	ENSMUSG00000084111	0	0.450248976	0.721871874	0.00013317	6.575872721	2.717E-06
Rdm1	ENSMUSG00000010362	0	0.916542564	0.70142053	0.000263912	6.007239521	6.325E-06
Mfge8	ENSMUSG00000030605	0	0.488443428	0.692262456	0.000111485	7.228108034	2.18E-06
Prrc1	ENSMUSG00000024594	0	0.537464562	0.687434168	0.002922981	5.902398357	0.0001427
Nsmce1	ENSMUSG00000030750	0	0.466622343	0.684990918	0.000317075	7.301128581	7.962E-06
Gm6988	ENSMUSG00000113198	0	0.520089461	0.67025477	0.000191602	7.126844316	4.372E-06
Dusp4	ENSMUSG00000031530	0	0.996879999	0.665244048	0.000256129	5.279683929	6.084E-06
Gtf2e2	ENSMUSG00000031585	0	0.76041015	0.659874709	9.4994E-06	6.984389433	1.144E-07
Kdelr3	ENSMUSG00000010830	0	0.408781105	0.658618085	0.00066809	6.852013747	2.045E-05
Spidr	ENSMUSG00000041974	0	0.588110282	0.641988423	0.007467442	5.243266185	0.0004647
Lyz2	ENSMUSG00000069516	0	0.550391152	0.61785532	0.002572939	6.473269283	0.0001211
Hdac5	ENSMUSG00000008855	0	0.648948511	0.607943617	0.000341349	6.307690811	8.86E-06
Mrrf	ENSMUSG00000026887	0	0.547810705	0.597762247	0.014654249	5.205843735	0.0011305
Rps25	ENSMUSG00000009927	0	0.466096994	0.595003223	0.000894955	7.568207157	3.106E-05
Alkbh5	ENSMUSG00000042650	0	0.780605365	0.593098728	7.15838E-06	7.660267531	8.34E-08
Pkm	ENSMUSG00000032294	0	0.5519251	0.58304406	1.96493E-06	10.19602771	1.85E-08
Rps25-ps1	ENSMUSG00000067344	0	0.410484121	0.567021859	0.000237752	8.00567179	5.612E-06
Seh1l	ENSMUSG00000079614	0	0.508778535	0.55024221	0.0025122	6.185457431	0.0001177
Ubl4a	ENSMUSG00000015290	0	0.468150128	0.535661322	0.001978924	7.045244792	8.402E-05
Pdpn	ENSMUSG00000028583	0	0.642720196	0.527029853	0.00088744	9.139794814	3.064E-05
Socs3	ENSMUSG00000053113	0	0.602718509	0.525769113	0.007663984	5.760759154	0.0004828
Pfkp	ENSMUSG00000021196	0	0.590887672	0.519313018	0.012083809	6.089502015	0.0008627
Hspa8	ENSMUSG00000015656	0	0.40269752	0.516867554	0.000100338	9.28606508	1.922E-06
St13	ENSMUSG00000022403	0	0.30398048	0.514636943	0.00017392	8.796065572	3.853E-06

Gene Name	Ensembl Gene ID	JS1 Neg. Con.	JS1 + Org	JS1 + Org + TNF	FDR cut-off	Ave. Expr.	P value
Rnf126	ENSMUSG00000035890	0	0.529975947	0.509438249	0.016245383	6.433478086	0.0013131
Ndufv3	ENSMUSG00000024038	0	0.493751627	0.500197353	0.000115635	9.586094623	2.269E-06
Vdac1	ENSMUSG00000020402	0	0.440382638	0.490719478	0.002576978	7.802656871	0.0001215
Anxa2	ENSMUSG00000032231	0	0.48393996	0.489903003	6.92197E-05	10.19626309	1.22E-06
Tmem263	ENSMUSG00000060935	0	0.443384878	0.459576736	0.001501757	7.649856712	5.983E-05
Asph	ENSMUSG00000028207	0	0.421975505	0.453269662	0.015833802	6.972705293	0.001254
Spc24	ENSMUSG00000074476	0	0.420327422	0.450562728	0.016377614	7.139761131	0.0013248
Prdx5	ENSMUSG00000024953	0	0.368764192	0.441919258	0.000451626	9.04682994	1.235E-05
Ecm1	ENSMUSG00000028108	0	0.447308553	0.433930699	0.002205394	7.634811874	9.853E-05
G2e3	ENSMUSG00000035293	0	0.504258333	0.412673005	0.006204419	6.726681269	0.00037
Ncaph2	ENSMUSG00000008690	0	0.353429321	0.396419425	0.00890346	8.422716907	0.0005896
Trim59	ENSMUSG00000034317	0	0.407478503	0.388722039	0.021136193	6.529997505	0.0018411
Adipor1	ENSMUSG00000026457	0	0.419190439	0.383406203	0.006280448	7.630787732	0.0003765
Golt1b	ENSMUSG00000030245	0	0.37179892	0.380509447	0.015941766	7.153194325	0.0012654
Snx3	ENSMUSG00000019804	0	0.318551798	0.364559758	0.012702534	8.489600987	0.0009209
Mbnl2	ENSMUSG00000022139	0	0.363364565	0.3354579	0.007979335	8.535675869	0.0005091
Sept_2	ENSMUSG00000026276	0	0.418722122	0.322167331	0.001990384	9.198210459	8.483E-05
Npepps	ENSMUSG00000001441	0	0.349659453	0.295504307	0.027564246	8.487554274	0.0026323
Tubb5	ENSMUSG00000001525	0	0.540634865	0.291105624	1.23316E-05	10.81879016	1.563E-07
Arpc2	ENSMUSG00000006304	0	0.266046999	0.251410001	0.023873318	9.561112509	0.0021645
Nme1	ENSMUSG00000037601	0	-0.304924809	-0.258110617	0.026540767	9.216700256	0.0025041
Pdia6	ENSMUSG00000020571	0	-0.346179921	-0.329135654	0.003269853	9.721513235	0.0001648
Hnrnpm	ENSMUSG00000059208	0	-0.345967737	-0.364931976	0.01683794	8.119237756	0.0013742
Ets2	ENSMUSG00000022895	0	-0.499092436	-0.414787174	0.021608997	5.875349181	0.0019084
Ddx5	ENSMUSG00000020719	0	-0.347575074	-0.445430999	0.000931693	9.023319447	3.284E-05
Lrrc59	ENSMUSG00000020869	0	-0.481377023	-0.450542525	0.00701761	8.189380342	0.0004316
Msmo1	ENSMUSG00000031604	0	-0.443547508	-0.456786599	0.001127261	8.14618401	4.13E-05
Trim26	ENSMUSG00000024457	0	-0.486170888	-0.469881577	0.027042403	5.928159243	0.0025688
Calm1	ENSMUSG00000001175	0	-0.32860449	-0.474035552	0.002221984	10.15583468	0.0001006
Scd2	ENSMUSG00000025203	0	-0.56112458	-0.481369411	3.0377E-05	9.36942561	4.456E-07
Hif1a	ENSMUSG00000021109	0	-0.380034334	-0.49201384	0.001476556	7.764831804	5.864E-05
Ddx21	ENSMUSG00000020075	0	-0.601936337	-0.514201339	0.000149483	7.746201412	3.122E-06
Hspa5	ENSMUSG00000026864	0	-0.301957486	-0.542459134	0.000169442	10.53967423	3.682E-06
Rrs1	ENSMUSG00000061024	0	-0.687674181	-0.548242505	0.000496459	6.393159882	1.391E-05
Dhx9	ENSMUSG00000042699	0	-0.547369758	-0.556006315	0.001249497	6.304009742	4.744E-05
Sqle	ENSMUSG00000022351	0	-0.308423452	-0.582153579	0.000126987	7.960485572	2.56E-06
Mrpl20	ENSMUSG00000029066	0	-0.501802878	-0.589370757	0.000562206	7.412949544	1.653E-05
Pnisr	ENSMUSG00000028248	0	-0.780786259	-0.610564064	8.60062E-05	6.557394957	1.547E-06
Txlna	ENSMUSG00000053841	0	-0.49615268	-0.620923676	0.001551364	6.811667534	6.256E-05
Akap8	ENSMUSG00000024045	0	-0.650357082	-0.623457983	0.00121438	6.040215082	4.552E-05
Sirt7	ENSMUSG00000025138	0	-0.606678613	-0.630888594	0.008217813	5.388365472	0.0005288
Plpp1	ENSMUSG00000021759	0	-0.367892187	-0.657818884	0.000142135	7.87440961	2.943E-06
Filip1l	ENSMUSG00000043336	0	-0.980051747	-0.669007811	1.18298E-05	6.482292297	1.485E-07
Psph	ENSMUSG00000029446	0	-0.673782658	-0.684949811	0.000139525	6.875078498	2.88E-06
mt-Nd2	ENSMUSG00000064345	0	-0.423352342	-0.685653816	9.12791E-05	8.39803541	1.675E-06
Gpatch4	ENSMUSG00000028069	0	-0.659619349	-0.699901277	0.000932368	5.68435173	3.292E-05
Slc7a1	ENSMUSG00000041313	0	-0.46966408	-0.70466119	0.000941639	6.544312471	3.331E-05
Mir99ahg	ENSMUSG00000090386	0	-0.90057637	-0.724900782	0.022526601	4.588207007	0.002018
Gata6	ENSMUSG00000005836	0	-0.388309176	-0.726487773	6.08905E-05	7.437058916	1.048E-06
Ap3d1	ENSMUSG00000020198	0	-0.496840486	-0.731525013	0.000179485	6.793373589	3.998E-06
Sh3bgrl	ENSMUSG00000031246	0	-0.516369417	-0.741391046	0.000108675	6.64249522	2.106E-06
Ccdc86	ENSMUSG00000024732	0	-0.4978465	-0.746749677	0.001937317	5.68229669	8.174E-05
Mvk	ENSMUSG00000041939	0	-0.737296603	-0.754961296	9.88174E-05	6.175979602	1.885E-06
Creld2	ENSMUSG00000023272	0	-0.410719098	-0.775908377	0.000132241	7.521561803	2.69E-06
Arf2	ENSMUSG00000062421	0	-0.446329725	-0.8140375	0.000316403	6.164207092	7.907E-06
Zfp771	ENSMUSG00000054716	0	-0.533114648	-0.816783967	0.002090158	5.202229965	9.11E-05
Skiv2l	ENSMUSG00000040356	0	-0.535319567	-0.818050936	0.000809997	5.784640561	2.733E-05
Slc1a5	ENSMUSG00000001918	0	-0.527755861	-0.828493582	0.000715365	6.257301959	2.271E-05
Dnajb11	ENSMUSG00000004460	0	-0.5508239	-0.841745602	2.44281E-05	6.961290655	3.495E-07
Ier5	ENSMUSG00000056708	0	-0.66437509	-0.847322699	0.009145909	5.03641082	0.0006084

Gene Name	Ensembl Gene ID	JS1 Neg. Con.	JS1 + Org	JS1 + Org + TNF	FDR cut-off	Ave. Expr.	P value
Wdr6	ENSMUSG00000066357	0	-0.685738226	-0.848254983	0.000824771	5.107873667	2.803E-05
Lss	ENSMUSG00000033105	0	-0.810163727	-0.849053404	5.13718E-06	7.001265346	5.768E-08
Calr	ENSMUSG00000003814	0	-0.778454588	-0.877399394	9.87507E-07	9.753136979	8.465E-09
Aacs	ENSMUSG00000029482	0	-0.473934396	-0.878309703	3.23565E-05	6.418672806	4.805E-07
Gcat	ENSMUSG00000006378	0	-0.586501092	-0.879848395	3.53583E-05	6.608359134	5.421E-07
Ppp1r15a	ENSMUSG00000040435	0	-1.099436842	-0.900273874	0.000327845	4.89930048	8.411E-06
Mbd1	ENSMUSG00000024561	0	-0.590154993	-0.919171038	6.86807E-06	6.619896841	7.851E-08
Srsf5	ENSMUSG00000021134	0	-1.067820338	-0.947449861	2.67479E-06	5.815891637	2.664E-08
Snapc5	ENSMUSG00000032398	0	-0.584885314	-0.990964886	0.000186937	6.010941287	4.198E-06
Slc35b1	ENSMUSG00000020873	0	-0.591880427	-0.997446253	6.63875E-07	7.522086875	5.41E-09
Abca7	ENSMUSG00000035722	0	-0.52040716	-1.011243913	0.000316403	5.447761885	7.898E-06
Cycs	ENSMUSG00000063694	0	-0.824950405	-1.040631369	0.000481822	4.912000868	1.332E-05
Mat2a	ENSMUSG00000053907	0	-0.673615272	-1.063679494	1.16348E-07	6.965199252	6.813E-10
Trp53inp2	ENSMUSG00000038375	0	-0.837474763	-1.087829719	1.674E-06	6.061733665	1.556E-08
Neurl3	ENSMUSG00000047180	0	-1.189496097	-1.103922038	0.024266394	2.83978276	0.0022163
Klf6	ENSMUSG00000000078	0	-0.997252297	-1.106232511	1.00516E-10	8.785310331	1.638E-13
Klf4	ENSMUSG00000003032	0	-0.786318297	-1.253963719	5.74578E-08	7.37210035	3.018E-10
Jun	ENSMUSG00000052684	0	-1.262197085	-1.322416875	5.11068E-11	7.804011332	6.479E-14
Rhob	ENSMUSG00000054364	0	-0.867515271	-1.395036024	2.99958E-05	5.314230818	4.382E-07
Mir22hg	ENSMUSG00000085148	0	-1.112186297	-1.406416175	9.3104E-05	4.544146843	1.725E-06
Gm24289	ENSMUSG00000088254	0	-1.48304413	-1.528843747	0.005275823	2.93428899	0.0003003
Gm12966	ENSMUSG00000070729	0	-1.715841181	-1.715781681	4.13487E-07	4.293709268	2.92E-09
Dusp8	ENSMUSG00000037887	0	-1.969813277	-1.762935149	0.000977555	2.600360444	3.491E-05
Atf3	ENSMUSG00000026628	0	-1.839233879	-2.000761942	6.01504E-05	3.496074032	1.024E-06
mt-Tc	ENSMUSG00000064349	0	-3.524837261	-3.402152604	0.001031461	0.074522075	3.73E-05

Table 5.13 Differentially Expressed JS1 Genes Dependent on Co-culturing with Organoids. List of the 202 JS1 genes discovery by overlapping analysis to be Organoid co-culture dependent (Table 5.12 bold and underlined). Only genes with differentially expression between groups dependent on co-culturing with JS1 cells and had an FDR cut-off of ≤ 0.05 were included. List includes Gene Name, the Ensembl genome browser ID code, group mean gene expression fold-change compared to the negative control group, the FDR cut-off, Average gene expression and P value. Genes ranked in descending order by log-fold gene expression of JS1 cells co-cultured with organoids treated with TNF. Group mean gene expression fold-change colour-scaled red for an increase and blue for a decrease. A solid black outside border indicates JS1 genes that have also been implicated in liver injury (see Chapter 1).

a

b

Nodes:

Network nodes represent proteins	Node Color	Node Content
splice isoforms or post-translational modifications are collapsed, i.e. each node represents all the proteins produced by a single, protein-coding gene locus.	*colored nodes: query proteins and first shell of interactors*	*empty nodes: proteins of unknown 3D structure*
	white nodes: second shell of interactors	*filled nodes: some 3D structure is known or predicted*

Edges:

Edges represent protein-protein associations	Known Interactions	Predicted Interactions	Others
associations are meant to be specific and meaningful, i.e. proteins jointly contribute to a shared function; this does not necessarily mean they are physically binding each other.	*from curated databases*	*gene neighborhood*	*textmining*
	experimentally determined	*gene fusions*	*co-expression*
		gene co-occurrence	*protein homology*

Figure 5.17 Protein-Protein Interaction Analysis of JS1 Genes Dependent on Organoid Co-culturing a. Protein-protein interaction map translated from of all significant differentially expressed organoid genes. **b.** Legend for the protein-protein interaction map.

The organoid co-culture dependent HSC protein interaction phenotype observed was focused on upregulated proteins Phosphoglycerate kinase 1 (*Pgk1*), Fructose-bisphosphate aldolase A (*Aldoa*), Lactate dehydrogenase A (*Ldha*), Triosephosphate isomerase (*Tpi1*), ATP-dependent 6-phosphofructokinase platelet type (*Pfkp*), and Alpha-enolase (*Eno1*) were clustered together by multiply protein-protein interaction in this phenotype.

Gene Name	Ensembl Gene ID	JS1 Neg. Con.	JS1 + TNF	JS1 + Org + TNF	FDR cut-off	Ave. Expr.	P value
H2-M2	ENSMUSG00000016283	0	5.377039036	4.575124563	8.67745E-06	0.638343669	1.04E-07
Kcnh1	ENSMUSG00000058248	0	2.926529765	4.206201294	0.000813681	-0.259174547	2.69E-05
Enpp2	ENSMUSG00000022425	0	4.048009521	4.115232639	6.68074E-08	2.511144013	3.43E-10
U90926	ENSMUSG00000029409	0	2.857663379	3.490574254	0.005765316	0.654637626	0.000333
Traf1	ENSMUSG00000026875	0	3.84208275	3.4864071	0.000192381	0.509300406	4.46E-06
Pik3r5	ENSMUSG00000020901	0	2.773160088	3.43793324	0.000294787	1.150480707	7.54E-06
Slc16a2	ENSMUSG00000033965	0	3.404923155	3.324426701	6.66939E-07	2.717062143	4.99E-09
Serpinb2	ENSMUSG00000062345	0	3.671002666	2.886002965	9.89024E-06	2.307532147	1.2E-07
1500009L16Rik	ENSMUSG00000087651	0	2.461379992	2.712073521	0.000749843	1.526062493	2.44E-05
Kcnj15	ENSMUSG00000062609	0	2.275888033	2.560188644	0.005817764	0.708198676	0.000337
Nav3	ENSMUSG00000020181	0	1.709778542	1.975113984	0.001161028	2.504841092	4.23E-05
Arhgap22	ENSMUSG00000063506	0	1.618294708	1.959287056	2.14921E-05	3.480379483	2.92E-07
Gpr176	ENSMUSG00000040133	0	1.819695603	1.948633796	0.000354078	2.464217713	9.32E-06
Pcolce2	ENSMUSG00000015354	0	1.509228682	1.910066395	4.47564E-05	3.62966526	7.24E-07
Hmga1	ENSMUSG00000046711	0	1.349937655	1.656699945	0.000302027	3.40565258	7.76E-06
Abcb1b	ENSMUSG00000028970	0	1.481056695	1.651569641	6.36188E-12	6.634818967	6.14E-15
Hmga1b	ENSMUSG00000078249	0	1.192574051	1.597394528	0.000179078	4.060340868	4.12E-06
Steap4	ENSMUSG00000012428	0	1.382114802	1.465080433	2.75374E-06	5.055449606	2.63E-08
Ces2e	ENSMUSG00000031886	0	1.206835724	1.433209943	0.006542271	3.138647402	0.000393
Birc3	ENSMUSG00000032000	0	1.45491856	1.376837558	3.40391E-05	3.989615467	5.22E-07
AU020206	ENSMUSG00000097415	0	1.12085686	1.21700303	0.001112803	4.796847905	3.96E-05
Nfkbie	ENSMUSG00000023947	0	1.696316375	1.191803256	7.39545E-06	3.844264012	8.75E-08
Relb	ENSMUSG00000002983	0	1.185195563	1.187040032	1.5784E-07	5.599524145	9.72E-10
Gpr137b	ENSMUSG00000021306	0	1.59408298	1.184908598	0.001552924	2.72801253	6.09E-05
Edn1	ENSMUSG00000021367	0	0.961898304	1.118431284	5.71721E-05	5.649948804	9.91E-07
Fas	ENSMUSG00000024778	0	1.545877016	1.111708281	8.00844E-06	5.315810611	2.9E-11
Cdc42ep5	ENSMUSG00000063838	0	0.968975343	1.110333655	0.004982217	3.473374767	0.000276
Csf1	ENSMUSG00000014599	0	1.252291337	1.096024717	1.21476E-09	7.168256915	2.71E-12
Nfkbia	ENSMUSG00000021025	0	1.127815453	1.058653357	1.07075E-10	8.756548911	1.62E-13
Micall2	ENSMUSG00000036718	0	0.825872585	1.026213693	0.000572615	5.039817767	1.71E-05
Abcb1a	ENSMUSG00000040584	0	0.927409343	0.884951999	0.000717316	4.758171458	2.3E-05
App	ENSMUSG00000022892	0	0.550680563	0.805261773	3.60522E-05	7.028023764	5.75E-07
Dram1	ENSMUSG00000020057	0	0.955176034	0.798945363	0.001051674	4.765778714	3.68E-05
C1s1	ENSMUSG00000038521	0	1.121891518	0.792312764	0.000106813	4.716015655	2.1E-06
Psmd10	ENSMUSG00000031429	0	0.83982914	0.785213207	2.58765E-06	6.284608644	2.39E-08
Ly6a	ENSMUSG00000075602	0	0.802029553	0.776808694	3.04536E-07	9.580937308	1.99E-09
Cdk6	ENSMUSG00000040274	0	0.999981415	0.754135009	8.131E-07	7.787915613	6.35E-09
Gopc	ENSMUSG00000019861	0	0.809166156	0.754026012	0.001813063	5.102802457	7.49E-05
P2rx4	ENSMUSG00000029470	0	0.70430031	0.749391661	0.00498836	4.813218361	0.000277
Tnfaip2	ENSMUSG00000021281	0	0.661036766	0.734639672	0.000667577	5.584026739	2.11E-05
Rnd1	ENSMUSG00000054855	0	0.756406692	0.699221018	0.015283398	4.831753872	0.001202
Maged2	ENSMUSG00000025268	0	0.506434714	0.627282778	0.003421349	6.081006544	0.000172
C3	ENSMUSG00000024164	0	0.761138867	0.620440517	4.8836E-07	8.906769018	3.33E-09
Ccnd1	ENSMUSG00000070348	0	0.759760279	0.603221666	2.67729E-06	8.577106861	2.52E-08
Mvp	ENSMUSG00000030681	0	0.653094774	0.596026331	0.001261662	5.92658416	4.71E-05
Gm10275	ENSMUSG00000069682	0	0.427829274	0.567245874	0.00049169	7.993816778	1.4E-05
Pde4b	ENSMUSG00000028525	0	0.853911082	0.535086952	5.5036E-05	6.336682098	9.36E-07
Gng12	ENSMUSG00000036402	0	0.340734619	0.523200201	0.000417993	8.5955428	1.14E-05
B2m	ENSMUSG00000060802	0	0.769524788	0.491079314	2.20032E-05	10.28922009	3.03E-07
C1qbp	ENSMUSG00000018446	0	0.442166678	0.482907405	0.000805294	7.677822181	2.65E-05
Mrpl38	ENSMUSG00000020775	0	0.536993185	0.454575782	0.000505243	7.185845925	1.45E-05
Tomm70a	ENSMUSG00000022752	0	0.533643292	0.430593053	0.009196207	6.097804599	0.000621
Sh3bp5	ENSMUSG00000021892	0	0.650937167	0.362795676	0.000436519	6.711605442	1.21E-05
Pank3	ENSMUSG00000018846	0	-0.350251458	-0.298388656	0.021384261	7.455906264	0.001907
Ahnak	ENSMUSG00000069833	0	-0.402749488	-0.353505324	0.011382709	10.10147491	0.00081
Wwp1	ENSMUSG00000041058	0	-0.402178972	-0.356544516	0.002569412	8.313445937	0.000118
Bcl2l1	ENSMUSG00000007659	0	-0.407253711	-0.365797901	0.009960049	7.677549988	0.000687
Nt5c3	ENSMUSG00000029780	0	-0.532927131	-0.378463281	0.005466577	6.217549475	0.000311
Psap	ENSMUSG00000004207	0	-0.461960007	-0.3834302	0.003936776	8.167542094	0.000205

Gene Name	Ensembl Gene ID	JS1 Neg. Con.	JS1 + TNF	JS1 + Org + TNF	FDR cut-off	Ave. Expr.	P value
Nnmt	ENSMUSG00000032271	0	-0.57353832	-0.417564514	0.000179078	8.147085081	4.12E-06
Acaa2	ENSMUSG00000036880	0	-0.639095986	-0.420065702	0.003696827	5.932909003	0.00019
AI506816	ENSMUSG00000105987	0	-0.368575128	-0.432936023	0.000208418	11.1638338	4.97E-06
Mras	ENSMUSG00000032470	0	-0.461617218	-0.461595592	0.011297231	6.458159262	0.000801
Klf13	ENSMUSG00000052040	0	-0.434740881	-0.492110358	0.00064516	7.810354881	2.01E-05
Bgn	ENSMUSG00000031375	0	-0.627613339	-0.494087712	4.71367E-06	8.430219475	5.26E-08
Abcg2	ENSMUSG00000029802	0	-0.540419811	-0.495241626	0.007413015	6.441102382	0.000465
Sparc	ENSMUSG00000018593	0	-0.466121733	-0.512960804	2.09512E-07	11.15244309	1.33E-09
Tex2	ENSMUSG00000040548	0	-0.556163849	-0.513108689	0.028190733	5.73651699	0.002764
Smtn	ENSMUSG00000020439	0	-0.578504169	-0.527572742	0.001950501	6.482769388	8.18E-05
Efr3a	ENSMUSG00000015002	0	-0.461502649	-0.539792486	0.000421476	7.817545881	1.15E-3
Pdcd4	ENSMUSG00000024975	0	-0.872168476	-0.573733318	7.27105E-05	6.592632978	1.33E-06
Col1a1	ENSMUSG00000001506	0	-0.468960266	-0.579040267	0.001161028	11.31176286	4.23E-05
Hlx	ENSMUSG00000039377	0	-0.851022277	-0.58503362	0.001703995	5.676575881	6.87E-05
Tnrc6c	ENSMUSG00000025571	0	-0.634824717	-0.608773855	0.000955169	6.138563774	3.25E-05
Lurap1l	ENSMUSG00000048706	0	-0.510829771	-0.619121967	0.001730324	6.613618939	7.02E-05
Ebp	ENSMUSG00000031168	0	-0.437271708	-0.635500689	0.000122869	7.338392279	2.48E-06
4931406P16Rik	ENSMUSG00000066571	0	-0.542782601	-0.635549829	0.001813063	6.13201721	7.48E-05
Nid2	ENSMUSG00000021806	0	-0.570067444	-0.638370293	0.002447559	6.365194032	0.000111
S100a16	ENSMUSG00000074457	0	-0.783495976	-0.652192352	0.000708803	7.372423833	2.26E-05
Mindy3	ENSMUSG00000026767	0	-0.758743356	-0.664848059	9.72027E-05	6.120975121	1.85E-06
Matn2	ENSMUSG00000022324	0	-0.608642088	-0.665992958	0.000586515	6.312259532	1.76E-05
Emilin1	ENSMUSG00000029163	0	-0.528722986	-0.673220364	0.002759268	6.11991067	0.00013
Rapgef5	ENSMUSG00000041992	0	-0.456635573	-0.692464267	0.001154654	6.677481912	4.18E-05
Zbtb20	ENSMUSG00000022708	0	-0.528351033	-0.696493457	2.13552E-05	7.705921605	2.89E-07
Cavin2	ENSMUSG00000045954	0	-0.672399632	-0.74382322	4.61926E-09	10.11846659	1.39E-11
Ypel5	ENSMUSG00000039770	0	-0.661753049	-0.752726572	0.000257688	6.452308518	6.5E-06
Tmem205	ENSMUSG00000040883	0	-0.611447367	-0.763286979	0.001279313	6.47609087	4.79E-05
Lifr	ENSMUSG00000054263	0	-0.722549679	-0.768995056	0.000607036	5.654567773	1.85E-05
Cdc42ep3	ENSMUSG00000036533	0	-0.752046532	-0.789421051	2.82942E-05	6.263981671	4.24E-07
Atoh8	ENSMUSG00000037621	0	-0.809349	-0.791011481	0.006388672	4.82219271	0.000379
Mmd	ENSMUSG00000003948	0	-0.603601303	-0.792123236	0.001786699	5.26893337	7.33E-05
Gpm6a	ENSMUSG00000031517	0	-0.530140681	-0.802756444	5.45539E-05	6.721336659	9.19E-07
Arsb	ENSMUSG00000042082	0	-0.862466176	-0.8130197	0.000143806	5.566994287	3.09E-06
Igsf3	ENSMUSG00000042035	0	-0.558747869	-0.829203888	0.000123944	6.804034326	2.51E-06
Ces2g	ENSMUSG00000031877	0	-0.459413939	-0.830318718	4.29133E-05	6.819442972	6.91E-07
Mical2	ENSMUSG00000038244	0	-1.014788959	-0.864701137	4.24885E-06	6.073632712	4.57E-08
Rab7	ENSMUSG00000079477	0	-0.569552043	-0.864888845	4.81125E-08	8.383867253	2.32E-10
Id1	ENSMUSG00000042745	0	-0.683875799	-0.877777729	0.000131113	6.258929057	2.71E-06
Car5b	ENSMUSG00000031373	0	-0.850015121	-0.882702904	0.008170391	4.202184621	0.000533
Nt5e	ENSMUSG00000032420	0	-1.293025407	-0.892302622	0.003914936	3.781847966	0.000203
Sesn1	ENSMUSG00000038332	0	-0.783660634	-0.911945973	0.000163639	5.110509359	3.67E-06
Cxcl12	ENSMUSG00000061353	0	-0.56128366	-0.949138435	0.000569356	7.010413396	1.69E-05
Mgll	ENSMUSG00000033174	0	-1.197187605	-0.967846092	0.00010302	5.033984426	2.01E-06
Npy4r	ENSMUSG00000048337	0	-0.793695413	-0.972105256	0.000955524	5.445105173	3.26E-05
Cyp39a1	ENSMUSG00000023963	0	-1.294112602	-0.983570469	5.48784E-07	5.395865614	3.91E-09
Igfbp4	ENSMUSG00000017493	0	-0.684581424	-0.999472141	2.09512E-07	6.96828709	1.33E-09
Usp2	ENSMUSG00000032010	0	-1.303983894	-1.008604762	0.000528082	4.890532588	1.53E-05
Nav1	ENSMUSG00000009418	0	-0.560170458	-1.01421752	3.46763E-05	6.008286705	5.48E-07
Jcad	ENSMUSG00000033960	0	-0.865052801	-1.026193947	0.00011016	6.740212082	2.18E-06
Clca3a1	ENSMUSG00000056025	0	-0.695188558	-1.034376162	0.000136222	6.083103772	2.89E-06
Glul	ENSMUSG00000026473	0	-0.89015321	-1.045111827	1.42486E-06	7.870573598	1.24E-08
Itga1	ENSMUSG00000042284	0	-0.819614832	-1.141791154	0.001464924	4.27384701	5.63E-05
Upk3b	ENSMUSG00000042985	0	-1.409390986	-1.151897642	0.003103913	3.64515462	0.000153
Tmem108	ENSMUSG00000042757	0	-1.162732007	-1.162923685	0.000482249	4.052549215	1.36E-05
Plce1	ENSMUSG00000024998	0	-0.88768348	-1.194668426	3.42628E-05	5.025687021	5.29E-07
Gas1	ENSMUSG00000052957	0	-1.247924696	-1.204138553	6.12038E-06	5.72267169	7.13E-08
Pkhd1l1	ENSMUSG00000038725	0	-1.252755393	-1.24312972	0.001678808	3.999755255	6.73E-05
Cfh	ENSMUSG00000026365	0	-1.112484996	-1.243736181	5.50967E-08	6.179776025	2.75E-10

Gene Name	Ensembl Gene ID	JS1 Neg. Con.	JS1 + TNF	JS1 + Org + TNF	FDR cut-off	Ave. Expr.	P value
Spry2	ENSMUSG00000022114	0	-1.01569948	-1.246875135	0.000195567	5.653864869	4.6E-06
S100a4	ENSMUSG00000001020	0	-0.916913475	-1.260354629	1.39374E-05	6.930063333	1.79E-07
Igfbp6	ENSMUSG00000023046	0	-0.90548152	-1.266074987	4.0929E-07	6.78852491	2.73E-09
Cobll1	ENSMUSG00000034903	0	-0.88635408	-1.291553585	9.31477E-08	6.214332169	5.23E-10
Kcnab1	ENSMUSG00000027827	0	-0.679984251	-1.291582337	6.82364E-05	5.033346971	1.22E-06
Nrp1	ENSMUSG00000025810	0	-0.884454886	-1.307901175	0.000195567	5.043288924	4.6E-06
Bambi	ENSMUSG00000024232	0	-1.394507685	-1.312729091	0.012905517	2.643740892	0.000953
Fmo2	ENSMUSG00000040170	0	-1.585050552	-1.324968148	0.013400732	2.712472233	0.001002
Htra3	ENSMUSG00000029096	0	-1.05519515	-1.42681861	0.005131402	3.583256787	0.000287
Ppp2r2b	ENSMUSG00000024500	0	-0.923046182	-1.50410741	0.00064092	3.60611591	1.99E-05
Mertk	ENSMUSG00000014361	0	-1.784880402	-1.526503373	0.007146196	2.231661989	0.000445
Clec11a	ENSMUSG00000004473	0	-1.469359711	-1.555566142	7.39545E-06	3.954378595	8.72E-08
Nkain4	ENSMUSG00000027574	0	-1.011305876	-1.610308277	4.59004E-08	5.945679799	2.19E-10
Fmod	ENSMUSG00000041559	0	-0.94561511	-1.619579932	6.11268E-06	4.529822367	7.08E-08
Cdh11	ENSMUSG00000031673	0	-1.315187934	-1.64126189	1.21909E-08	5.858987042	4.78E-11
Zhx3	ENSMUSG00000035877	0	-1.006072164	-1.665886923	6.56109E-07	5.960233518	4.87E-09
Fbln5	ENSMUSG00000021186	0	-1.676800246	-1.676525183	7.96969E-07	4.467847267	6.16E-09
Prelp	ENSMUSG00000041577	0	-1.194343848	-1.737988563	7.24487E-08	5.593593609	3.85E-10
Tshz2	ENSMUSG00000047907	0	-1.578270567	-1.827556101	0.000340326	3.562250219	8.9E-06
Actn3	ENSMUSG00000006457	0	-2.212653264	-1.979656104	0.000640836	2.347221281	1.99E-05
Slc1a3	ENSMUSG00000005360	0	-1.842248837	-2.062673427	5.62749E-08	4.396120803	2.85E-10
Plagl1	ENSMUSG00000019817	0	-1.475002993	-2.064745951	1.47812E-05	3.705775756	1.91E-07
4930481A15Rik	ENSMUSG00000086938	0	-1.692854346	-2.34821374	7.31169E-05	3.179033924	1.34E-06
Mgp	ENSMUSG00000030218	0	-1.785545414	-2.403560447	4.4365E-09	5.861952092	1.26E-11
Fat4	ENSMUSG00000046743	0	-1.816939782	-2.516236607	0.00226116	1.732053742	9.9E-05
Ptn	ENSMUSG00000029838	0	-1.734923761	-2.559616253	5.81856E-09	5.130530169	1.86E-11
Plekha6	ENSMUSG00000041757	0	-2.164202659	-2.683105287	0.000695074	2.384615912	2.21E-05
Agtr2	ENSMUSG00000068122	0	-3.504344121	-2.727480438	0.002278523	0.148945808	9.99E-05
Hs3st1	ENSMUSG00000051022	0	-2.095354416	-2.790760206	4.26542E-06	3.181709402	4.61E-08
Ifi27l2b	ENSMUSG00000021208	0	-1.578719473	-2.82819877	9.3883E-07	4.916358977	7.65E-09
Itga8	ENSMUSG00000026768	0	-2.812607171	-3.059942027	0.0093878	-0.419290394	0.000638
Tdo2	ENSMUSG00000028011	0	-2.343187721	-3.430703511	0.001990176	1.004270618	8.39E-05
St8sia1	ENSMUSG00000030283	0	-2.933588012	-3.569106808	0.000229626	1.125031538	5.65E-06
Scrg1	ENSMUSG00000031610	0	-4.208360574	-4.495709649	6.53097E-05	0.222460711	1.17E-06
Tnnt2	ENSMUSG00000026414	0	-3.652558448	-4.658708681	4.59004E-08	2.73475506	2.19E-10

Table 5.14 Differentially Expressed JS1 Genes Dependent on TNF Treatment. List of the
153 JS1 genes discovery by overlapping analysis to be TNF treatment dependent (Table 5.12
bold and underlined). Only genes with differentially expression between groups dependent on
TNF treatment and had an FDR cut-off of ≤ 0.05 were included. List includes Gene Name, the
Ensembl genome browser ID code, group mean gene expression fold-change compared to the
negative control group, the FDR cut-off, Average gene expression and P value. Genes ranked
in descending order by log-fold gene expression of JS1 cells co-cultured with organoids treated
with TNF. Group mean gene expression fold-change colour-scaled red for an increase and blue
for a decrease. A solid black outside border indicates JS1 genes that have also been implicated
in liver injury (see Chapter 1).

Figure 5.18 Protein-Protein Interaction Analysis of JS1 Genes Dependent on TNF Treatment a. Protein-protein interaction map translated from of all significant differentially expressed organoid genes. **b.** Legend for the protein-protein interaction map.

The TNF dependent HSC protein interaction phenotype had a cluster of interactions between upregulated TNF and NFκB related proteins such as TNF receptor-associated factor 1 (*Traf1*), Tumor necrosis factor alpha-induced protein 2 (*Tnfaip2*), Baculoviral IAP repeat-containing protein 3 (*Birc3*), Transcription factor RelB (*Relb*), NFκB inhibitor α and ε (*Nfkbia* and *Nfkbie*).

Gene Name	Ensembl Gene ID	JS1 Neg. Con.	JS1 + Org	JS1 + TNF	JS1 + Org + TNF	FDR cut-off	Ave. Expr.	P value
Tnn	ENSMUSG00000026725	0	2.710575189	3.040300498	5.403832259	2.54E-05	1.665403697	5.08E-07
Tnfrsf9	ENSMUSG00000028965	0	3.065399888	2.746094597	5.126205806	1.01E-05	2.537080303	1.71E-07
Lamb3	ENSMUSG00000026639	0	3.170476045	1.234929087	3.349147178	0.001523913	1.651282169	8.22E-05
Mmp9	ENSMUSG00000017737	0	1.725208257	2.783905227	2.927154498	0.028265136	0.466640942	0.0035677
Mmp8	ENSMUSG00000005800	0	2.140652542	-0.216943946	2.713573567	1.42E-11	4.599038214	2.77E-14
Il15ra	ENSMUSG00000023206	0	0.219192404	2.124171771	1.798276371	0.009615484	1.201217252	0.0008498
Tnfaip3	ENSMUSG00000019850	0	0.416400029	2.80675295	1.789995146	6.40E-12	4.904137809	1.08E-14
Bsg	ENSMUSG00000023175	0	1.292334747	-0.090905606	1.38318493	2.97E-16	10.99709742	8.97E-20
Tnfsf9	ENSMUSG00000035678	0	1.60057182	-0.374656898	1.364464512	6.92E-06	3.472732673	1.07E-07
Igfbp7	ENSMUSG00000036256	0	-0.094264897	0.859635943	1.197922501	0.000976329	3.53976823	4.68E-05
Actn1	ENSMUSG00000015143	0	-0.506431526	0.733153825	1.063930407	0.007853434	6.8954782	0.0006552
Tnfaip8	ENSMUSG00000062210	0	0.454246285	0.688619736	0.962747817	0.000265214	5.580661011	9.05E-06
Vegfa	ENSMUSG00000023951	0	0.511314588	0.144229468	0.898772097	0.010740272	4.249787868	0.0009855
Srgn	ENSMUSG00000020077	0	-0.06017215	-0.763785976	0.841192146	0.019904111	2.216674583	0.002218
Tnfaip2	ENSMUSG00000021281	0	-0.29828602	0.661036766	0.734639672	3.18E-06	5.584026739	4.24E-08
Sdc4	ENSMUSG00000017009	0	0.712679208	0.414205085	0.43531463	7.14E-05	9.420805515	1.84E-06
Vcan	ENSMUSG00000021614	0	0.510880219	0.627749433	0.385351739	0.000315869	7.556010468	1.13E-05
Adipor1	ENSMUSG00000026457	0	0.419190439	-0.160676864	0.383406203	8.45E-05	7.630787732	2.29E-06
Nfkb1	ENSMUSG00000028163	0	-0.067922112	0.770986434	0.332161933	0.000742081	5.470224167	3.37E-05
Col5a2	ENSMUSG00000026042	0	0.227567	-0.26048	0.205964	0.002272	7.779756	0.000135
Actb	ENSMUSG00000029580	0	0.589639203	0.039835298	0.122291367	0.000253951	12.63125256	8.58E-06
Igf1r	ENSMUSG00000005533	0	0.307687744	-0.25207272	0.080444076	0.027411411	5.78248493	0.0034186
Hspg2	ENSMUSG00000028763	0	-0.109989631	0.498529025	0.078523982	0.026587618	5.792595893	0.0032725
Il17rc	ENSMUSG00000030281	0	-0.309088078	0.285113732	0.066514583	0.026325825	5.315683846	0.0032307
Ddr2	ENSMUSG00000026674	0	-0.206731299	0.288876818	-0.008588037	0.007891211	7.061320606	0.0006598
Tnfaip1	ENSMUSG00000017615	0	-0.312118936	0.119729265	-0.014996955	0.014344052	7.667399644	0.0014278
Vegfd	ENSMUSG00000031380	0	0.361030321	-0.385960653	-0.308380491	0.000622846	5.905247879	2.63E-05
Tgfbr3	ENSMUSG00000029287	0	0.174087584	-0.335998991	-0.313101655	0.019202161	5.831058209	0.0021235
Tnfrsf12a	ENSMUSG00000023905	0	-0.202739765	0.054137348	-0.346161717	0.010302081	8.034991665	0.0009303
Pdgfc	ENSMUSG00000028019	0	0.437170348	-0.617549705	-0.347335532	0.000370176	4.744352502	1.37E-05
Col4a6	ENSMUSG00000031273	0	0.394203	-0.30879	-0.53653	0.000224	5.164005	7.34E-06
Agrn	ENSMUSG00000041936	0	-0.663913722	0.572561768	-0.548381764	0.000170135	4.092234609	5.21E-06
Col1a1	ENSMUSG00000001506	0	0.105967	-0.46896	-0.57904	3.46E-05	11.31176	7.26E-07
Col5a1	ENSMUSG00000026837	0	-0.32303	-0.01466	-0.59591	0.001651	6.658558	9.11E-05
Col4a2	ENSMUSG00000031503	0	-0.18014	-0.10217	-0.71175	1.10E-05	8.161402	1.89E-07
Col4a1	ENSMUSG00000031502	0	-0.34655	-0.20959	-0.71749	7.76E-06	8.55769	1.24E-07
Igf1	ENSMUSG00000020053	0	0.368342495	-0.882490154	-0.791686211	0.000608276	3.846294167	2.54E-05
Igfbp4	ENSMUSG00000017493	0	-0.281984043	-0.684581424	-0.999472141	1.87E-07	6.96828709	1.70E-09
Igfbp6	ENSMUSG00000023046	0	-0.247408614	-0.90548152	-1.266074987	1.69E-07	6.78852491	1.48E-09
Col3a1	ENSMUSG00000026043	0	-0.71576	-0.54329	-1.34093	1.14E-06	9.221817	1.31E-08
Ogn	ENSMUSG00000021390	0	-0.903005787	-0.815723894	-1.344081565	0.000106563	4.753099301	2.98E-06
Fmod	ENSMUSG00000041559	0	0.062444762	-0.94561511	-1.619579932	2.13E-07	4.529822367	2.01E-09
Prelp	ENSMUSG00000041577	0	0.318603641	-1.194343848	-1.737988563	8.35E-11	5.593593609	2.17E-13
Actn3	ENSMUSG00000006457	0	0.115577801	-2.212653264	-1.979656104	4.25E-05	2.347221281	9.33E-07
Col4a4	ENSMUSG00000067158	0	0.888095	-1.93751	-2.78067	6.79E-08	2.492742	5.21E-10

Table 5.15 JS1 Genes of Interest. List of significantly measured JS1 genes, that have also
been implicated in liver injury (see Chapter 1). Only genes with an FDR cut-off of ≤ 0.05 were
included. List includes Gene Name, the Ensembl genome browser ID code, group mean gene
expression compared to the negative control group, the FDR cut-off, Average gene expression
and P value.

5.2.6 Gene Set Enrichment Analysis for JS1 Samples

REGULATED GENE SETS (JS1 + Org vs JS1 Neg Con)	NES	FDR q-val	LEADING EDGE
HALLMARK_HYPOXIA	2.588361	0	tags=39%, list=5%, signal=41%
HALLMARK_GLYCOLYSIS	2.295275	0	tags=24%, list=7%, signal=25%
HALLMARK_KRAS_SIGNALING_UP	1.74007	0.010759	tags=26%, list=11%, signal=29%
HALLMARK_PROTEIN_SECRETION	1.687451	0.01566	tags=20%, list=11%, signal=22%
HALLMARK_MTORC1_SIGNALING	1.674177	0.015356	tags=12%, list=2%, signal=12%
HALLMARK_EPITHELIAL_MESENCHYMAL_TRANSITION	1.662779	0.014346	tags=26%, list=9%, signal=28%
HALLMARK_IL2_STAT5_SIGNALING	1.628525	0.020039	tags=30%, list=16%, signal=35%
HALLMARK_UV_RESPONSE_DN	1.608813	0.021604	tags=21%, list=9%, signal=23%
HALLMARK_COAGULATION	1.463214	0.080195	tags=16%, list=8%, signal=17%
HALLMARK_COMPLEMENT	1.455158	0.078393	tags=33%, list=21%, signal=42%
HALLMARK_HEDGEHOG_SIGNALING	1.414854	0.1028	tags=22%, list=7%, signal=23%
HALLMARK_TNFA_SIGNALING_VIA_NFKB	1.360897	0.151014	tags=23%, list=9%, signal=25%
HALLMARK_TGF_BETA_SIGNALING	1.336496	0.169418	tags=25%, list=9%, signal=27%
HALLMARK_APICAL_SURFACE	1.3022	0.206244	tags=50%, list=26%, signal=68%
HALLMARK_SPERMATOGENESIS	1.299244	0.196431	tags=42%, list=25%, signal=56%
HALLMARK_HEME_METABOLISM	1.282204	0.208013	tags=18%, list=13%, signal=21%
HALLMARK_ESTROGEN_RESPONSE_EARLY	1.277131	0.203031	tags=12%, list=8%, signal=13%
HALLMARK_APICAL_JUNCTION	1.242177	0.24828	tags=28%, list=17%, signal=34%
HALLMARK_REACTIVE_OXYGEN_SPECIES_PATHWAY	-1.30773	0.169263	tags=23%, list=8%, signal=25%
HALLMARK_UNFOLDED_PROTEIN_RESPONSE	-1.37317	0.130249	tags=23%, list=12%, signal=26%
HALLMARK_XENOBIOTIC_METABOLISM	-1.46368	0.090629	tags=29%, list=16%, signal=33%
HALLMARK_CHOLESTEROL_HOMEOSTASIS	-2.06957	0	tags=37%, list=8%, signal=40%

Table 5.16 Enriched Gene Sets when Comparing JS1 Cells Co-cultured with Organoids and the JS1 Cells Negative Control Group. NES = Normalised Enrichment Score. FDR q-val = False Discovery Rate Q Value. tags = The percentage of gene hits before (for positive ES) or after (for negative ES) the peak in the running enrichment score. This gives an indication of the percentage of genes contributing to the enrichment score. list = The percentage of genes in the ranked gene list before (for positive ES) or after (for negative ES) the peak in the running enrichment score. This gives an indication of where in the list the enrichment score is attained. signal = The enrichment signal strength that combines the two previous statistics. Only gene sets with an FDR q-value of ≥ 0.25 were included. A solid black outside border indicates organoid gene sets that have also been implicated in liver injury (see Chapter 1).

REGULATED GENE SETS (JS1 + TNF vs JS1 Neg Con)	NES	FDR q-val	LEADING EDGE
HALLMARK_TNFA_SIGNALING_VIA_NFKB	2.757703	0	tags=32%, list=5%, signal=33%
HALLMARK_INTERFERON_GAMMA_RESPONSE	2.743647	0	tags=45%, list=10%, signal=49%
HALLMARK_INFLAMMATORY_RESPONSE	2.597618	0	tags=44%, list=11%, signal=48%
HALLMARK_ALLOGRAFT_REJECTION	2.56012	0	tags=43%, list=11%, signal=48%
HALLMARK_INTERFERON_ALPHA_RESPONSE	2.483423	0	tags=44%, list=10%, signal=48%
HALLMARK_MYC_TARGETS_V1	2.399555	0	tags=46%, list=17%, signal=54%
HALLMARK_IL6_JAK_STAT3_SIGNALING	2.267468	0	tags=44%, list=12%, signal=49%
HALLMARK_MYC_TARGETS_V2	1.925181	0.001	tags=47%, list=14%, signal=55%
HALLMARK_UV_RESPONSE_UP	1.694152	0.008759	tags=18%, list=7%, signal=19%
HALLMARK_UNFOLDED_PROTEIN_RESPONSE	1.681027	0.008742	tags=28%, list=14%, signal=33%
HALLMARK_WNT_BETA_CATENIN_SIGNALING	1.629448	0.01324	tags=24%, list=10%, signal=26%
HALLMARK_COMPLEMENT	1.615895	0.014221	tags=23%, list=12%, signal=26%
HALLMARK_APOPTOSIS	1.49355	0.033553	tags=16%, list=4%, signal=16%
HALLMARK_KRAS_SIGNALING_UP	1.469746	0.038894	tags=17%, list=7%, signal=18%
HALLMARK_IL2_STAT5_SIGNALING	1.41791	0.053957	tags=17%, list=7%, signal=18%
HALLMARK_HYPOXIA	1.391207	0.062127	tags=27%, list=11%, signal=30%
HALLMARK_TGF_BETA_SIGNALING	1.317667	0.107372	tags=17%, list=5%, signal=18%
HALLMARK_P53_PATHWAY	1.258663	0.157924	tags=12%, list=7%, signal=13%
HALLMARK_HEDGEHOG_SIGNALING	1.211184	0.203835	tags=13%, list=5%, signal=14%
HALLMARK_ESTROGEN_RESPONSE_EARLY	1.208937	0.196519	tags=14%, list=7%, signal=14%
HALLMARK_PEROXISOME	1.189303	0.21572	tags=14%, list=7%, signal=15%
HALLMARK_HEME_METABOLISM	-1.18097	0.231478	tags=34%, list=20%, signal=42%
HALLMARK_UV_RESPONSE_DN	-1.19514	0.225663	tags=16%, list=7%, signal=17%
HALLMARK_COAGULATION	-1.26774	0.144647	tags=21%, list=7%, signal=22%
HALLMARK_ESTROGEN_RESPONSE_LATE	-1.27886	0.145733	tags=23%, list=13%, signal=26%
HALLMARK_OXIDATIVE_PHOSPHORYLATION	-1.27996	0.158719	tags=19%, list=13%, signal=22%
HALLMARK_FATTY_ACID_METABOLISM	-1.29744	0.153686	tags=13%, list=7%, signal=14%
HALLMARK_KRAS_SIGNALING_DN	-1.29882	0.170288	tags=16%, list=8%, signal=18%
HALLMARK_SPERMATOGENESIS	-1.29975	0.192635	tags=20%, list=18%, signal=24%
HALLMARK_EPITHELIAL_MESENCHYMAL_TRANSITION	-1.36573	0.132181	tags=16%, list=4%, signal=17%
HALLMARK_CHOLESTEROL_HOMEOSTASIS	-1.4624	0.063256	tags=43%, list=21%, signal=53%
HALLMARK_ADIPOGENESIS	-1.48521	0.065269	tags=25%, list=13%, signal=28%
HALLMARK_MYOGENESIS	-1.506	0.069685	tags=33%, list=17%, signal=39%
HALLMARK_XENOBIOTIC_METABOLISM	-1.53529	0.076553	tags=21%, list=9%, signal=22%
HALLMARK_BILE_ACID_METABOLISM	-1.61899	0.068853	tags=26%, list=16%, signal=31%

Table 5.17 Enriched Gene Sets when Comparing JS1 Cells Treated with TNF and the JS1 Cells Negative Control Group. NES = Normalised Enrichment Score. FDR q-val = False Discovery Rate Q Value. tags = The percentage of gene hits before (for positive ES) or after (for negative ES) the peak in the running enrichment score. This gives an indication of the percentage of genes contributing to the enrichment score. list = The percentage of genes in the ranked gene list before (for positive ES) or after (for negative ES) the peak in the running

enrichment score. This gives an indication of where in the list the enrichment score is attained.

signal = The enrichment signal strength that combines the two previous statistics. Only gene sets with an FDR q-value of $\geq$ 0.25 were included. A solid black outside border indicates organoid gene sets that have also been implicated in liver injury (see Chapter 1).

REGULATED GENE SETS (JS1 + Org + TNF vs JS1 Neg Con)	NES	FDR q-val	LEADING EDGE
HALLMARK_HYPOXIA	2.318305	0	tags=34%, list=6%, signal=35%
HALLMARK_ALLOGRAFT_REJECTION	2.274519	0	tags=34%, list=11%, signal=37%
HALLMARK_MYC_TARGETS_V1	2.050398	0	tags=34%, list=15%, signal=40%
HALLMARK_GLYCOLYSIS	2.016537	0	tags=25%, list=9%, signal=27%
HALLMARK_TNFA_SIGNALING_VIA_NFKB	1.970641	0	tags=30%, list=6%, signal=31%
HALLMARK_INFLAMMATORY_RESPONSE	1.883468	0.000649	tags=26%, list=8%, signal=28%
HALLMARK_INTERFERON_GAMMA_RESPONSE	1.849374	0.000937	tags=26%, list=11%, signal=29%
HALLMARK_IL6_JAK_STAT3_SIGNALING	1.781395	0.001864	tags=29%, list=7%, signal=31%
HALLMARK_MYC_TARGETS_V2	1.521907	0.032737	tags=35%, list=21%, signal=44%
HALLMARK_COMPLEMENT	1.510904	0.031515	tags=21%, list=10%, signal=23%
HALLMARK_MTORC1_SIGNALING	1.475418	0.039359	tags=12%, list=2%, signal=12%
HALLMARK_IL2_STAT5_SIGNALING	1.42948	0.056041	tags=14%, list=6%, signal=15%
HALLMARK_KRAS_SIGNALING_UP	1.401804	0.065447	tags=27%, list=13%, signal=31%
HALLMARK_PROTEIN_SECRETION	1.386712	0.06837	tags=15%, list=13%, signal=17%
HALLMARK_WNT_BETA_CATENIN_SIGNALING	1.333022	0.100581	tags=12%, list=4%, signal=12%
HALLMARK_P53_PATHWAY	1.273888	0.151786	tags=11%, list=4%, signal=12%
HALLMARK_UV_RESPONSE_UP	1.240282	0.183374	tags=12%, list=9%, signal=13%
HALLMARK_SPERMATOGENESIS	1.233967	0.18069	tags=35%, list=22%, signal=45%
HALLMARK_INTERFERON_ALPHA_RESPONSE	1.227117	0.178314	tags=22%, list=13%, signal=25%
HALLMARK_OXIDATIVE_PHOSPHORYLATION	1.181525	0.235312	tags=27%, list=17%, signal=32%
HALLMARK_ESTROGEN_RESPONSE_EARLY	-1.36176	0.097729	tags=21%, list=10%, signal=23%
HALLMARK_MYOGENESIS	-1.37665	0.099212	tags=19%, list=7%, signal=20%
HALLMARK_ESTROGEN_RESPONSE_LATE	-1.37939	0.116057	tags=19%, list=11%, signal=22%
HALLMARK_EPITHELIAL_MESENCHYMAL_TRANSITION	-1.38976	0.13359	tags=21%, list=6%, signal=22%
HALLMARK_KRAS_SIGNALING_DN	-1.43945	0.108035	tags=16%, list=10%, signal=18%
HALLMARK_XENOBIOTIC_METABOLISM	-1.7063	0.008647	tags=25%, list=13%, signal=29%
HALLMARK_CHOLESTEROL_HOMEOSTASIS	-1.95992	0	tags=38%, list=11%, signal=43%

Table 5.18 Enriched Gene Sets when Comparing JS1 Cells Co-cultured with Organoids and Treated with TNF and the JS1 Cells Negative Control Group. NES = Normalised Enrichment Score. FDR q-val = False Discovery Rate Q Value. tags = The percentage of gene hits before (for positive ES) or after (for negative ES) the peak in the running enrichment score. This gives an indication of the percentage of genes contributing to the enrichment score. list = The percentage of genes in the ranked gene list before (for positive ES) or after (for negative ES) the peak in the running enrichment score. This gives an indication of where in the list the enrichment score is attained. signal = The enrichment signal strength that combines the two previous statistics. Only gene sets with an FDR q-value of ≥ 0.25 were included. A solid black outside border indicates organoid gene sets that have also been implicated in liver injury (see Chapter 1).

REGULATED GENE SETS (JS1 + Org + TNF vs JS1 + Org)	NES	FDR q-val	LEADING EDGE
HALLMARK_MYC_TARGETS_V1	2.547739	0	tags=44%, list=16%, signal=51%
HALLMARK_ALLOGRAFT_REJECTION	2.448726	0	tags=34%, list=12%, signal=39%
HALLMARK_INTERFERON_GAMMA_RESPONSE	2.284833	0	tags=25%, list=8%, signal=26%
HALLMARK_TNFA_SIGNALING_VIA_NFKB	2.251427	0	tags=27%, list=8%, signal=28%
HALLMARK_INFLAMMATORY_RESPONSE	2.043359	0	tags=22%, list=7%, signal=24%
HALLMARK_IL6_JAK_STAT3_SIGNALING	1.955681	0.000175	tags=19%, list=4%, signal=20%
HALLMARK_MYC_TARGETS_V2	1.933789	0.000335	tags=39%, list=18%, signal=47%
HALLMARK_UV_RESPONSE_UP	1.66004	0.008491	tags=16%, list=7%, signal=17%
HALLMARK_UNFOLDED_PROTEIN_RESPONSE	1.407685	0.067613	tags=20%, list=12%, signal=22%
HALLMARK_P53_PATHWAY	1.360089	0.088703	tags=15%, list=7%, signal=16%
HALLMARK_PEROXISOME	1.350718	0.086469	tags=15%, list=8%, signal=16%
HALLMARK_OXIDATIVE_PHOSPHORYLATION	1.346755	0.081552	tags=41%, list=23%, signal=52%
HALLMARK_REACTIVE_OXYGEN_SPECIES_PATHWAY	1.296974	0.11187	tags=15%, list=6%, signal=16%
HALLMARK_WNT_BETA_CATENIN_SIGNALING	1.296576	0.103879	tags=18%, list=12%, signal=20%
HALLMARK_COMPLEMENT	1.280723	0.109753	tags=18%, list=8%, signal=20%
HALLMARK_INTERFERON_ALPHA_RESPONSE	1.266336	0.112961	tags=9%, list=3%, signal=9%
HALLMARK_PI3K_AKT_MTOR_SIGNALING	-1.20111	0.228602	tags=33%, list=22%, signal=42%
HALLMARK_TGF_BETA_SIGNALING	-1.21967	0.211156	tags=25%, list=10%, signal=28%
HALLMARK_HEDGEHOG_SIGNALING	-1.28283	0.140859	tags=13%, list=1%, signal=13%
HALLMARK_APICAL_SURFACE	-1.30517	0.126352	tags=32%, list=8%, signal=35%
HALLMARK_ANDROGEN_RESPONSE	-1.31836	0.121922	tags=17%, list=6%, signal=18%
HALLMARK_HYPOXIA	-1.34061	0.108969	tags=25%, list=13%, signal=28%
HALLMARK_KRAS_SIGNALING_DN	-1.3561	0.10376	tags=17%, list=12%, signal=20%
HALLMARK_HEME_METABOLISM	-1.393	0.082922	tags=21%, list=15%, signal=25%
HALLMARK_BILE_ACID_METABOLISM	-1.3988	0.086377	tags=31%, list=16%, signal=37%
HALLMARK_APICAL_JUNCTION	-1.42922	0.070884	tags=25%, list=14%, signal=29%
HALLMARK_NOTCH_SIGNALING	-1.4347	0.075702	tags=39%, list=16%, signal=47%
HALLMARK_ESTROGEN_RESPONSE_EARLY	-1.48414	0.053217	tags=29%, list=15%, signal=34%
HALLMARK_ESTROGEN_RESPONSE_LATE	-1.50263	0.048967	tags=26%, list=13%, signal=29%
HALLMARK_XENOBIOTIC_METABOLISM	-1.52364	0.048025	tags=25%, list=13%, signal=29%
HALLMARK_COAGULATION	-1.57914	0.029297	tags=23%, list=11%, signal=26%
HALLMARK_MYOGENESIS	-1.63931	0.018855	tags=20%, list=8%, signal=22%
HALLMARK_EPITHELIAL_MESENCHYMAL_TRANSITION	-1.69836	0.012345	tags=25%, list=9%, signal=27%
HALLMARK_UV_RESPONSE_DN	-1.80348	0.003868	tags=32%, list=15%, signal=37%

Table 5.19 Enriched Gene Sets when Comparing JS1 Cells Co-cultured with Organoids and Treated with TNF and JS1 Cells Co-cultured with Organoids. NES = Normalised Enrichment Score. FDR q-val = False Discovery Rate Q Value. tags = The percentage of gene hits before (for positive ES) or after (for negative ES) the peak in the running enrichment score. This gives an indication of the percentage of genes contributing to the enrichment score. list = The percentage of genes in the ranked gene list before (for positive ES) or after (for negative ES) the peak in the running enrichment score. This gives an indication of where in the list the

enrichment score is attained. signal = The enrichment signal strength that combines the two

previous statistics. Only gene sets with an FDR q-value of ≥ 0.25 were included. A solid black

outside border indicates organoid gene sets that have also been implicated in liver injury (see

Chapter 1).

REGULATED GENE SETS (JS1 + Org + TNF vs JS1 + TNF)	NES	FDR q-val	LEADING EDGE
HALLMARK_HYPOXIA	2.455016	0	tags=38%, list=5%, signal=40%
HALLMARK_GLYCOLYSIS	2.203855	0	tags=30%, list=10%, signal=33%
HALLMARK_SPERMATOGENESIS	1.689778	0.017088	tags=39%, list=21%, signal=50%
HALLMARK_OXIDATIVE_PHOSPHORYLATION	1.679544	0.013663	tags=22%, list=13%, signal=25%
HALLMARK_PROTEIN_SECRETION	1.660566	0.013802	tags=44%, list=25%, signal=58%
HALLMARK_MTORC1_SIGNALING	1.581389	0.026078	tags=16%, list=4%, signal=16%
HALLMARK_ADIPOGENESIS	1.371609	0.158397	tags=16%, list=12%, signal=18%
HALLMARK_FATTY_ACID_METABOLISM	1.318817	0.210601	tags=20%, list=16%, signal=24%
HALLMARK_REACTIVE_OXYGEN_SPECIES_PATHWAY	1.296878	0.222597	tags=38%, list=14%, signal=44%
HALLMARK_E2F_TARGETS	1.294155	0.204596	tags=26%, list=15%, signal=29%
HALLMARK_IL2_STAT5_SIGNALING	1.259002	0.238217	tags=27%, list=18%, signal=33%
HALLMARK_MYC_TARGETS_V2	-1.21267	0.202326	tags=47%, list=23%, signal=61%
HALLMARK_P53_PATHWAY	-1.36077	0.073859	tags=20%, list=7%, signal=21%
HALLMARK_APOPTOSIS	-1.38124	0.068051	tags=20%, list=9%, signal=22%
HALLMARK_EPITHELIAL_MESENCHYMAL_TRANSITION	-1.39313	0.067232	tags=21%, list=10%, signal=23%
HALLMARK_XENOBIOTIC_METABOLISM	-1.5087	0.027532	tags=29%, list=14%, signal=34%
HALLMARK_CHOLESTEROL_HOMEOSTASIS	-1.53932	0.023029	tags=41%, list=20%, signal=51%
HALLMARK_KRAS_SIGNALING_DN	-1.54021	0.025777	tags=23%, list=17%, signal=28%
HALLMARK_ALLOGRAFT_REJECTION	-1.55895	0.025223	tags=16%, list=6%, signal=17%
HALLMARK_IL6_JAK_STAT3_SIGNALING	-1.62488	0.016891	tags=15%, list=4%, signal=15%
HALLMARK_UNFOLDED_PROTEIN_RESPONSE	-1.65175	0.015115	tags=22%, list=7%, signal=23%
HALLMARK_INFLAMMATORY_RESPONSE	-1.79146	0.004273	tags=19%, list=8%, signal=21%
HALLMARK_TNFA_SIGNALING_VIA_NFKB	-1.95445	0	tags=26%, list=7%, signal=27%
HALLMARK_INTERFERON_GAMMA_RESPONSE	-2.19496	0	tags=34%, list=10%, signal=37%
HALLMARK_INTERFERON_ALPHA_RESPONSE	-2.206	0	tags=49%, list=15%, signal=58%

**Table 5.20 Enriched Gene Sets when Comparing JS1 Cells Co-cultured with Organoids
and Treated with TNF and JS1 Cells Treated with TNF.** NES = Normalised Enrichment
Score. FDR q-val = False Discovery Rate Q Value. tags = The percentage of gene hits before
(for positive ES) or after (for negative ES) the peak in the running enrichment score. This gives
an indication of the percentage of genes contributing to the enrichment score. list = The
percentage of genes in the ranked gene list before (for positive ES) or after (for negative ES)
the peak in the running enrichment score. This gives an indication of where in the list the
enrichment score is attained. signal = The enrichment signal strength that combines the two
previous statistics. Only gene sets with an FDR q-value of ≥ 0.25 were included. A solid black
outside border indicates organoid gene sets that have also been implicated in liver injury (see
Chapter 1).

NAME	JS1 + Org vs JS1 Neg Con	JS1 + TNF vs JS1 Neg Con	JS1 + Org + TNF vs JS1 Neg Con	JS1 + Org + TNF vs JS1 + Org	JS1 + Org + TNF vs JS1 + TNF
HALLMARK_HYPOXIA	2.5883608	1.3912073	2.3183053	-1.3406054	2.455016
HALLMARK_GLYCOLYSIS	2.2952745		2.016537		2.203855
HALLMARK_KRAS_SIGNALING_UP	1.74007	1.4697464	1.4018039		
HALLMARK_PROTEIN_SECRETION	1.6874509		1.3867115		1.6605663
HALLMARK_MTORC1_SIGNALING	1.674177		1.4754177		1.5813885
HALLMARK_EPITHELIAL_MESENCHYMAL_TRANSITION	1.6627791	-1.365734	-1.3897558	-1.6983601	-1.3931324
HALLMARK_IL2_STAT5_SIGNALING	1.628525	1.4179097	1.4294797		1.259002
HALLMARK_UV_RESPONSE_DN	1.6088134	-1.1951408		-1.8034837	
HALLMARK_COAGULATION	1.4632137	-1.2677385		-1.5791386	
HALLMARK_COMPLEMENT	1.4551575	1.615895	1.5109044	1.2807225	
HALLMARK_HEDGEHOG_SIGNALING	1.4148539	1.211843		-1.2828263	-1.9544467
HALLMARK_TNFA_SIGNALING_VIA_NFKB	1.3608973	2.7577026	1.9706413	2.251427	
HALLMARK_TGF_BETA_SIGNALING	1.336496	1.3176672		-1.2196728	
HALLMARK_APICAL_SURFACE	1.3021998			-1.3051665	
HALLMARK_SPERMATOGENESIS	1.2992443	-1.2997515	1.2339666		1.6897776
HALLMARK_HEME_METABOLISM	1.282204	-1.1809733	-1.3929952		
HALLMARK_ESTROGEN_RESPONSE_EARLY	1.2771306	1.2089368	-1.3617613	-1.4841444	
HALLMARK_APICAL_JUNCTION	1.242177		-1.4292166		
HALLMARK_REACTIVE_OXYGEN_SPECIES_PATHWAY	-1.3077272		1.2969736		1.2968783
HALLMARK_UNFOLDED_PROTEIN_RESPONSE	-1.3731663	1.6810268	1.4076847		-1.6517506
HALLMARK_XENOBIOTIC_METABOLISM	-1.4636842	-1.5352875	-1.7063006	-1.5236372	-1.5086958
HALLMARK_CHOLESTEROL_HOMEOSTASIS	-2.0695689	-1.462404	-1.9599239		-1.5393178
HALLMARK_INTERFERON_GAMMA_RESPONSE		2.7436466	1.8493735	2.284833	-2.1949646
HALLMARK_INFLAMMATORY_RESPONSE		2.5976179	1.8834683	2.0433588	-1.7914569
HALLMARK_ALLOGRAFT_REJECTION		2.5601196	2.2745185	2.4487257	-1.5589542
HALLMARK_INTERFERON_ALPHA_RESPONSE		2.4834228	1.2271174	1.2663363	-2.2060015
HALLMARK_MYC_TARGETS_V1		2.3995545	2.0503976	2.5477388	
HALLMARK_IL6_JAK_STAT3_SIGNALING		2.267468	1.7813954	1.9556814	-1.624813
HALLMARK_MYC_TARGETS_V2		1.925181	1.5219069	1.9337891	-1.2126703
HALLMARK_UV_RESPONSE_UP		1.6941516	1.240282	1.6600395	
HALLMARK_WNT_BETA_CATENIN_SIGNALING		1.6294484	1.3330215	1.2965757	
HALLMARK_APOPTOSIS		1.4935504	1.2738878		-1.3812388
HALLMARK_P53_PATHWAY		1.2586626	1.3600891		-1.3607725
HALLMARK_PEROXISOME		1.1893027	1.3507183		
HALLMARK_ESTROGEN_RESPONSE_LATE		-1.2788633	-1.3793933	-1.502628	
HALLMARK_OXIDATIVE_PHOSPHORYLATION		-1.2799611	1.1815245	1.3467546	1.6795442
HALLMARK_FATTY_ACID_METABOLISM		-1.2974393			1.3188168
HALLMARK_KRAS_SIGNALING_DN		-1.298824	-1.4394473	-1.3561016	-1.5402122
HALLMARK_ADIPOGENESIS		-1.4852113			1.3716091
HALLMARK_MYOGENESIS		-1.5059961	-1.3766514	-1.6393077	
HALLMARK_BILE_ACID_METABOLISM		-1.6189902		-1.3988008	
HALLMARK_E2F_TARGETS					1.294155
HALLMARK_PI3K_AKT_MTOR_SIGNALING				-1.2011107	
HALLMARK_ANDROGEN_RESPONSE				-1.318363	
HALLMARK_NOTCH_SIGNALING			-1.4346999		
HALLMARK_ANGIOGENESIS					
HALLMARK_DNA_REPAIR					
HALLMARK_G2M_CHECKPOINT					
HALLMARK_MITOTIC_SPINDLE					
HALLMARK_PANCREAS_BETA_CELLS					

Table 5.21 Gene Set Enrichment Analysis of Significant Differentially Expressed Gene Sets Between JS1 cell Groups. Ranking the hallmark gene sets from the Mouse_ENSEMBL_Gene_ID_Human_Orthologs_MSigDB.v7.2.chip data base on normalised enrichment score between all the organoid experimental groups. All enrichment scores are for gene sets that had an FDR q-value ≥ 0.25. Group normalised enrichment score colour scaled red for a positive normalised enrichment score and blue for a negative normalised enrichment score. A solid black outside border indicates organoid gene sets that have also been implicated in liver injury (see Chapter 1).

Using GSEA on significant differentially expressing genes we identified organoid co-culture dependent positive gene set enrichment that are important to liver injury (Tables 5.16-5.21), such as the hallmarks of Hypoxia (Roth and Copple 2015). There was also TNF treatment dependent positive gene set enrichment for the hallmarks of the TNF signalling via NFκB (Yang and Seki 2015; Luedde *et al* 2014), the interferon gamma response (Sherlock & Dooley, 2002; Tu *et al* 2015), the inflammatory response and IL-6/JAK/STAT3 signalling (Yang and Seki 2015; Robinson *et al* 2016).

5.3 Discussion

The TNF treated liver organoid/JS1 cell model did have differential gene expression and enriched gene sets related to the TNF response, the inflammatory pathway, apoptosis, and gene sets related to interferon gamma and hypoxia. In liver organoids and HSCs this was dependent on TNF treatment, and there was limited evidence of a liver injury phenotype being upregulated in our tissue caused by co-culturing the two cell populations.

Quality control analysis of the organoid samples found an anti-conservative trend from the p-Value histogram (Figure 5.1a), meaning the that the p-values for the non-significant samples are evenly distributed and the significant data is grouped close to zero (as would be expected from a non-random data set, where you reject the null-hypothesis); meaning that the analysis used to find significance appears be giving us a natural and valid probability distribution. The relative Log expression boxplot of our samples were consistent (Figure 5.1b); hence there was technical consistency in the handling and quality of our samples. There were variances between our organoid samples within groups as indicated by the multidimensional scaling analysis (Figure 5.2a and b), this could be explained by heterogeneity of cell types within the organoids themselves which has been demonstrated in Figures 3.23 and 3.24. Hierarchical clustering analysis (Figure 5.3) found more dissimilarity between the groups caused by TNF treatment; hence TNF has a greater effect on the liver organoid gene expression phenotype than co-culturing the organoids with JS1 cells.

Analysis of the significant differentially expressing genes between our organoid groups found that the greatest range and quantity of differential expression was between the organoid co-culture group treated with TNF and the negative control group (Figure 5.5) with 703 significant differentially expressed genes. MA ratio intensity plot analysis of differential expression (Figure 5.6) found that the log-fold change in expression of all the organoid genes between

each of the groups clustered around zero, hence we can assume that the gene expression analysis has been correctly normalised for the samples and the measured relative changes are correct.

Overlapping analysis of the significant differentially expressing genes between organoid groups (Figure 5.7 and Table 5.2) discovered 3 common genes whose expression was depended on co-culturing the organoid with JS1 cells and 46 common genes whose expression was dependent on TNF treatment. Of these discovered TNF dependent genes, *Tnfaip3* and *Timp3* have been previously implicated in liver injury (see Chapter 1). There were no common genes dependent of both JS1 co-culturing and TNF treatment (Table 5.2).

The *Tnfaip3* (tumor necrosis factor, alpha-induced protein 3) gene was upregulated and the *Timp3* (tissue inhibitor of metalloproteinase 3) gene was downregulated. The function of the coded protein from the *Tnfaip3* gene is an actin cytoskeleton-organizing protein that plays a role in the formation of cell projections, and is required for actin polymerization at immunological synapses (IS) and for the recruitment of the chemokine receptor CXCR4 to IS (Song *et al* 1996; Jung *et al* 2015). The *Tnfaip3* gene would be expected to be upregulated during liver injury. The function of the coded protein from the *Timp3* gene is as a secreted protein that complexes with metalloproteinases (such as collagenases) and irreversibly inactivates them by binding to their catalytic zinc cofactor. This may form part of a tissue-specific acute response to remodelling stimuli (Fan and Kassiri 2020). The *Timp3* gene would be expected to be upregulated during liver injury. From all the significant differentially expressing genes 10 genes have been implicated in liver injury, their relative differential expression to the negative control group was summarised in Table 5.5.

CHAPTER 5 TRANSCRIPTIONAL PROFILING ANALYSIS OF THE IN VITRO MODELLING OF LIVER INJURY AND FIBROSIS

The expected interactions of the coded proteins from the discovered differentially expressing genes dependent on co-culturing with JS1 cells or TNF treatment were described using protein-protein interaction maps (Figures 5.8 and 5.9).

The JS1 cell dependent protein interaction phenotype (Figure 5.8) was a downregulation of a pathway involving the NADH-ubiquinone oxidoreductase chain 1 (*mt-Nd1*) and 4 (*mt-Nd4*), with Cytochrome b (*mt-Cytb*), which are all part of the mitochondrial membrane respiratory chain (Chomyn *et al* 1985), hence JS1 co-culturing suppresses the expression of a few functions related to the mitochondrial membrane.

The TNF dependent protein interaction phenotype (Figure 5.9) contained clusters of interactions around the upregulated Tumour necrosis factor alpha-induced protein 3 (*Tnfaip3*), TNFAIP3-interacting protein 3 (*Tnip3*), the Baculoviral IAP repeat-containing protein 3 (*birc3*), and NFκB inhibitor alpha (*Nfkbia*), which are expected interaction induced in a TNF response pathway (Wullaert *et al* 2007). This cluster interacts with the cell surface receptors Integrin alpha-V (*Itgav*) and CD44 (*Cd44*) via the Vascular cell adhesion protein 1 (*Vcam1*/ VCAM1). These receptors interact with the upregulated secretory granule proteoglycan core protein Serglycin (*Srgn*) which plays a role in cytotoxic cell granule-mediated apoptosis and regulates the secretion of TNF (Zernichow *et al* 2006). The upregulated VCAM1 is also important in cell-cell recognition and plays a pathophysiologic role both in immune responses and in leukocyte emigration to sites of inflammation (Cook-Mills *et al* 2011). The protein VCAM1 also interacts with upregulated Antileukoproteinase (*Slpi*) via Haptoglobin (*Hp*), which play a role in regulating the activation of NFκB and inflammatory responses (Mulligan *et al* 2000; Klimenkova *et al* 2014). Hence the TNF dependent organoid protein interaction phenotype had expected activated pathways related to liver injury like TNF response,

inflammation, and apoptosis, but not related to chemokines, or specific growth factors that related to HSC cell signalling (Tu *et al* 2015).

Using GSEA on significant differentially expressing genes we identified JS1 cell dependent positive gene set enrichment that are important to liver injury (Tables 5.6-5.11), such as the hallmarks of Hypoxia (Roth and Copple 2015), the ROS pathway (Tu *et al* 2015), and coagulation (Robinson *et al* 2016), as well as negative gene set enrichment for the hallmarks of hedgehog signalling and notch signalling (Tsuchida and Friedman 2017). There was also TNF treatment dependent positive gene set enrichment for the hallmarks of the interferon gamma response (Sherlock & Dooley, 2002; Tu *et al* 2015), TNF signalling via NFκB, IL-6/JAK/STAT3 signalling (Yang and Seki 2015; Luedde *et al* 2014), the inflammatory response, hypoxia, and apoptosis. While there was a TNF dependent negative gene set enrichment for the hallmarks of Hedgehog signalling (Tsuchida and Friedman 2017). Hence the organoids in our model are replicating many important biological pathways of the liver injury response.

Quality control analysis my JS1 cell samples found an anti-conservative trend from the p-Value histogram (Figure 5.10a); hence we can assume a significant hypothesis from our data. The relative Log expression boxplot of our samples were consistent (Figure 5.10b); hence we can assume technical consistency in the handling and quality of our samples. There was group clustering by the JS1 cells samples within groups as indicated by the multidimensional scaling analysis (Figure 5.11a and b), hence we can assume low variances between samples. Hierarchical clustering analysis of the JS1 cell samples (Figure 5.12) suggests that co-culturing or TNF treatment of the JS1 cells each influence JS1 cell phenotype, and that the combining of co-culturing with TNF treatment is not dissimilar from these two phenotypes, hence combining co-culturing and TNF treatment does not lead to a more distinctive phenotype.

CHAPTER 5 TRANSCRIPTIONAL PROFILING ANALYSIS OF THE IN VITRO MODELLING OF LIVER INJURY AND FIBROSIS

Analysis of the significant differentially expressing genes between our JS1 cell groups found that the greatest range and quantity of differential expression was between the JS1 cells co-culture group treated with TNF and the negative control group (Figure 5.13 and 5.14) with 1982 significant differentially expressed genes. MA ratio intensity plot analysis of differential expression found that the log-fold change in expression of all the organoid genes between each of the groups clustered around zero, hence we can assume that the gene expression analysis has been correctly normalised for the samples and the measured relative changes are correct.

Overlapping analysis of the significant differentially expression genes between JS1 cell groups (Figure 5.16 and Table 5.12) discovered 202 genes whose expression was depended on co-culturing the JS1 cells with organoids and 153 genes whose expression was dependent on TNF treatment. Of these discovered genes 5 of the co-culturing dependent genes have been implicated in liver injury (see Chapter 1). *Lamb3*, *Mmp8*, *Bsg*, *Tnfsf9* and *Adipor1* were all upregulated dependent on the JS1 cell samples being co-cultured with organoids (Table 5.13).

Of these discovered genes 7 of the TNF dependent gene have been implicated in liver injury. *Tnfaip2* was upregulated while, *Col1a1*, *Igfbp4*, *Igfbp6*, *Fmod*, *Prelp*, and *Actn3* were all downregulated (Table 5.14). From all the significant differentially expressing genes 45 genes have been implicated in liver injury, their relative differential expression to the negative control group was summarised in Table 5.15.

The expected interactions of the coded proteins from the discovered differentially expressing genes dependent on co-culturing with organoids or TNF treatment were described using protein-protein interaction maps (Figures 5.17 and 5.18), to illustrate the discovered phenotypes.

The organoid co-culture dependent HSC protein interaction phenotype observed was focused on key upregulated glycolysis proteins and not upregulated liver injury related protein

interactions. Upregulated proteins Phosphoglycerate kinase 1 (*Pgk1*), Fructose-bisphosphate aldolase A (*Aldoa*), Lactate dehydrogenase A (*Ldha*), Triosephosphate isomerase (*Tpi1*), ATP-dependent 6-phosphofructokinase platelet type (*Pfkp*), and Alpha-enolase (*Eno1*) were clustered together by multiply protein-protein interaction in this phenotype and are all central to glycolysis (Bollong *et al* 2018; Rodriguez-Almazan *et al* 2008; Hang *et al* 2018). Hence glucose metabolism pathways were upregulated when HSCs were exposed to organoids and not key injury pathways.

The TNF dependent HSC protein interaction phenotype had a cluster of interactions between upregulated TNF and NFκB related proteins such as TNF receptor-associated factor 1 (*Traf1*), Tumor necrosis factor alpha-induced protein 2 (*Tnfaip2*), Baculoviral IAP repeat-containing protein 3 (*Birc3*), Transcription factor RelB (*Relb*), NFκB inhibitor α and ε (*Nfkbia* and *Nfkbie*) all of which are associated with TNF and NFκB (Lavorgna *et al* 2009; Hayden and Ghosh 2014). Hence this HSC phenotype had upregulation of TNF/NFκB related pathways, while Collagen I (*Col1a1*) and proteins that interact with Collagen I were downregulated. Proteins like SPARC (*Sparc*), Biglycan (*Bgn*), Integrin alpha-1 (*Itga1*), Cadherin-11 (*Cdh11*) and Matrix Gla protein (*Mgp*). Hence in this HSC phenotype the collagen I pathways were downregulated with the upregulated TNF response which has been observed *in vitro* (Saile *et al* 1999; Yang and Seki 2015), and the inclusion of organoids in co-culture did not lead to a more fibrous phenotype (Table 5.15) as would be necessary in a liver injury model (Tu *et al* 2015; Yang and Seki 2015).

Using GSEA on significant differentially expressing genes we identified organoid co-culture dependent positive gene set enrichment that are important to liver injury (Tables 5.16-5.21), such as the hallmarks of Hypoxia (Roth and Copple 2015). There was also TNF treatment dependent positive gene set enrichment for the hallmarks of the TNF signalling via NFκB

(Yang and Seki 2015; Luedde *et al* 2014), the interferon gamma response (Sherlock & Dooley, 2002; Tu *et al* 2015), the inflammatory response and IL-6/JAK/STAT3 signalling (Yang and Seki 2015; Robinson *et al* 2016). Hence the HSCs in our model are replicating important biological pathways of the liver injury response.

Hepatocyte death, inflammation, fibrosis, and the upregulation of profibrogenic factor TNF (Figure 1.19) (Yang and Seki 2015; Luedde *et al* 2014), are characteristics of the initiation phase liver injury. The initiation phase is perpetuated by TNF production, which results in the activation of resident HSCs into fibrogenic myofibroblasts (Yang and Seki 2015). In our model TNF treatment induced unique phenotypes in the liver organoids and HSCs (Figure 5.3 and 512), activating pathways related to liver injury like TNF response, inflammation, and apoptosis, but not related to chemokines, or specific growth factors that related to HSC cell signalling (Tu *et al* 2015), and enriching gene sets in each cell population related to the interferon gamma response inflammation, hypoxia, and apoptosis. That said collagen I was downregulated in HSCs with the upregulated TNF response, hence crosstalk between the liver injury phenotype organoid tissues and the HSCs did not induce a fibrous phenotype as observed *in vivo* during liver injury (Tu *et al* 2015; Yang and Seki 2015).

CHAPTER 6

ULTRASTRUCTURE MAPPING AND CHARACTERISATION OF LIVER ORGANOIDS USING SCALABLE HIGH RESOLUTION FIELD EMISSION SCANNING ELECTRON MICROSCOPY

CHAPTER 6

ULTRSTRUCTURE MAPPING AND CHARACTERISATION OF LIVER ORGANOIDS USING SCALABLE HIGH RESOLUTION FIELD EMISSION SCANNING ELECTRON MICROSCOPY (HRSEM)

KEY FINDINGS

1. We demonstrated a novel method for characterising the topology and ultrastructure of organoids using chemical tissue processing and HRSEM.

2. HRSEM allows for wide area (500 x 500 μm^2) imaging of samples to ensure the discovery of regions of interests at similar resolution to TEM.

3. HRSEM is a low-cost system that is not limited by sample thickness (~ 120-250 nm thickness) or by electron beam damage to delicate structures.

4. HRSEM also can be combined easily with CLEM.

5. Organoid differentiation causes little change to topological morphology.

6. The cell ultrastructure of organoids was not as uniform or typically hexagonally shaped as hepatocytes are *in vivo*.

7. We observed multiple features of liver organoid cell ultrastructure including signs of cell stress, such as abundant lysosomes, autophagy, and apoptosis.

CHAPTER 6 ULTRSTRUCTURE MAPPING AND CHARACTERISATION OF LIVER ORGANOIDS USING SCALABLE HIGH RESOLUTION FIELD EMISSION SCANNING ELECTRON MICROSCOPY

6.1 BACKGROUND

Organogenesis, tissue homeostasis, and organ function are the culmination of highly coordinated molecular and structural interactions between our tissues and cells. Studying the dynamics of these essential interactions and how they are altered by developmental disease, degenerative conditions, and cancer represents a significant technical challenge (Rios and Clevers 2018). *In vivo* animal models while incredibly informative only approximate the genetic, cellular, and physiological context of humans, and *in vitro* two-dimensional (2D) cultures can be compromised by an artificial environment and a lack of cell-to-cell crosstalk. These limitations have driven the development of advances in new three-dimensional (3D) *in vitro* organoid models that comprise several cell types that develop from stem cells or organ progenitors and self-organise through cell sorting and spatially restricted lineage commitment, similar to organogenesis *in vivo* (Lancaster & Knoblich 2014; Kim *et al* 2020). The practical realisation of 3D in vitro models has established organoid biology as a rapidly emerging field of investigation that is a product of and is advantageous to our understanding of stem cell fate initiation and cellular differentiation (Clevers 2016).

The past decade has seen the emergence of a new era for volume or 3D imaging with novel microscopic approaches that allows scalable microscopic to high resolution correlative imaging of tissue and cells, an essential requirement for probing the complexity of organoids (Rios and Clevers 2018). This is generally achieved at the microscale level using various iterations of light microscopy including confocal laser scanning, multi-photon, super-resolution, and light-sheet achieving subcellular resolutions (Dekkers *et al* 2019). While optical microscopy has been useful for understanding organoid structures, light microscopes are limited in resolution by the physical restraints of the visible light spectrum, hence there is a minimal resolvable distance that light microscopes can observe. This problem can be overcome using an electron

beam as opposed to visible light, because the wavelength of an electron is inversely proportional to its velocity, which can be modulated by controlling the applied voltage on the electron beam. Hence with an electron microscope significantly lesser resolvable distances are achievable and the major limitation to resolution becomes radiation damage applied to observe a sample as opposed to wavelength or numerical aperture (Alberts *et al* 2008).

Using Transmission Electron Microscopy (TEM) samples are dehydrated, permeated with a monomeric resin and polymerized to form a solid block of plastic, the block is then thinly sliced and placed on a copper grid in the path of an electron beam. As electrons pass through the sample, contrast is detectable as electron-dense materials will scatter electrons more than less dense materials. While providing the highest resolution TEM is usually more expensive and technically more difficult than other approaches such as Scanning Electron Microscopy (SEM) and up to 25% of large samples can be unobservable due to the copper grid used for TEM (Alberts *et al* 2008). Scanning Electron Microscopy uses electrons that are scattered or emitted from the specimen's surface. This is achieved by fixing, drying, and coating the specimen with a thin layer of heavy metals and finally scanning the specimen with a very narrow beam of electrons (Alberts *et al* 2008). The quantity of electrons scattered or emitted as this primary beam bombards each successive point of the metallic surface is measured and used to control the intensity of a second beam, which moves in synchrony with the primary beam and forms an image on a computer monitor. In this way, a highly enlarged image of the surface is constructed. This technique provides a great depth of field; moreover, since the amount of electron scattering depends on the angle of the surface relative to the beam, the image contains highlights and shadows that give it a three-dimensional appearance (Alberts *et al* 2008).

Field Emission Scanning Electron Microscopy (FESEM) uses a field emission gun which is a type of electron gun with a sharply pointed Müller-type emitter held at several kilovolts

negative potential relative to a nearby electrode, so that there is sufficient potential gradient at the emitter surface to cause field electron emission (Orloff 2008). In electron microscopes, a field emission gun produces a smaller more coherent electron beam, with up to three orders of magnitude greater current density or brightness than conventional thermionic emitters. This results in a significantly improved signal-to-noise ratio and spatial resolution (Orloff 2008).

Most organoid studies have used TEM to detail ultrastructural characteristics. Examples of this include observing the ultrastructure of cells in airway organoids (Sachs *et al* 2019), the ultrastructure of vascular enhancement in kidney organoids (Homan *et al* 2019), identifying cellular differentiation in canine intestinal organoids (Kramer *et al* 2020), the glomerular ultrastructure of kidney organoids including the positive identification of podocytes (Xinaris *et al* 2016; van den Berg *et al* 2018). TEM has also been, used for characterising the infectivity and viral life cycle of SARS-CoV-2 in human intestinal organoids (Lamers *et al* 2020) and therapies that inhibit SARS-CoV-2 infection in blood vessel organoids and kidney organoids (Monteil *et al* 2020).

To satisfy a proportion of the 2nd aim of this thesis, which was to characterise the capacity of organoids to model liver characteristics *in vitro* by observing morphological markers, we developed novel methods of High Resolution field emission Scanning Electron Microscopy (HRSEM) to observe the topology of undifferentiated and differentiated organoids as described in chapter 3 and compared them to the topology of cyto-spun primary mouse hepatocytes. This process led us to test the limitations of HRSEM for organoid ultrastructure analysis, which became the 4th aim of this thesis. We hypothesised that we can use HRSEM to generate high quality micrographs with similar resolutions to TEM but with a larger field of view by adapting methods developed previously (Figure 6.1) for large area pathology samples (Cohen Hyams *et al* 2020). We also hypothesised that the primary liver organoids would topologically be similar

to extracted primary hepatocytes and contain the same ultrastructural features as liver tissue *in vivo*.

We observed the topology and ultrastructure of mouse liver organoids during organoid expansion and differentiation, as well as from organoids co-cultured with the hepatic stellate cell line JS1 cells, TNF treatment or hypoxia. We also demonstrated that HRSEM can be used with correlative light-electron microscopy (CLEM) a technique whereby an ultrathin section prepared for electron microscopy is fluorescently labelled and imaged for both light microscopy and electron microscopy to localise specific markers in the ultrastructure of the sample (de Boer *et al* 2015).

The wide-area capacity of HRSEM allows for the identification of rare events of immunolabelled proteins of interest within the ultrastructure of organoids (Figure 6.2). This requires some chemical etching of cut sections, and immunolabeling using quantum dot nanocrystals (QDs) using techniques discussed previously (Killingsworth *et al* 2012; Killingsworth & Bobryshev 2016). At this point immunofluorescence was observed and correlated with HRSEM images of the same sample using image analysis software Adobe® Photoshop.

CHAPTER 6 ULTRSTRUCTURE MAPPING AND CHARACTERISATION OF LIVER ORGANOIDS USING SCALABLE HIGH RESOLUTION FIELD EMISSION SCANNING ELECTRON MICROSCOPY

6.1.1 METHODS

The results in this chapter were the product of collaboration between the author of this thesis, microscopist Dr. Tzipi Cohen Hyams and pathologist A/Prof. Murray Killingsworth from the Ingham Institute Microscopy Laboratory, New South Wales Health Pathology and UNSW Sydney, Australia. Electron microscopy and carbon coating was performed by Dr. Tzipi Cohen Hyams, and the embedding and cutting of samples was performed by A/Prof. Murray Killingsworth. All other methods and analysis were performed by the author of this thesis.
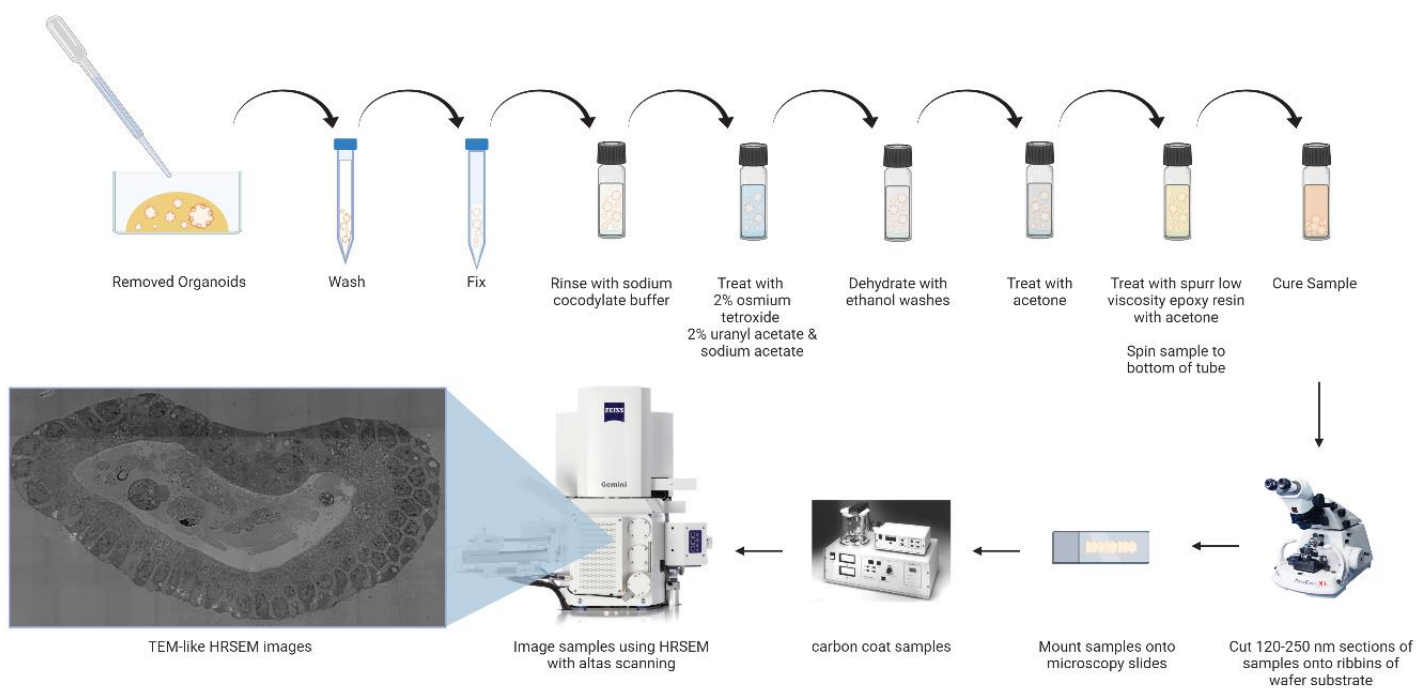
Figure 6.1 Visual Diagram of the HRSEM Tissue Processing Methods for Organoids.

Flow diagram for reference describing the methods of washing, fixing, treating, dehydrating, curing, cutting, mounting, coating, and imaging organoids for HRSEM.

**Figure 6.2 Visual Diagram of the CLEM with HRSEM Tissue Processing Methods for
Organoids.** Flow diagram for reference describing the methods of washing, fixing, treating,
dehydrating, curing, cutting, mounting, Primary and secondary staining, immunofluorescent
imaging, coating, and HRSEM imaging.

CHAPTER 6 ULTRSTRUCTURE MAPPING AND CHARACTERISATION OF LIVER ORGANOIDS USING SCALABLE HIGH RESOLUTION FIELD EMISSION SCANNING ELECTRON MICROSCOPY

6.2 RESULTS

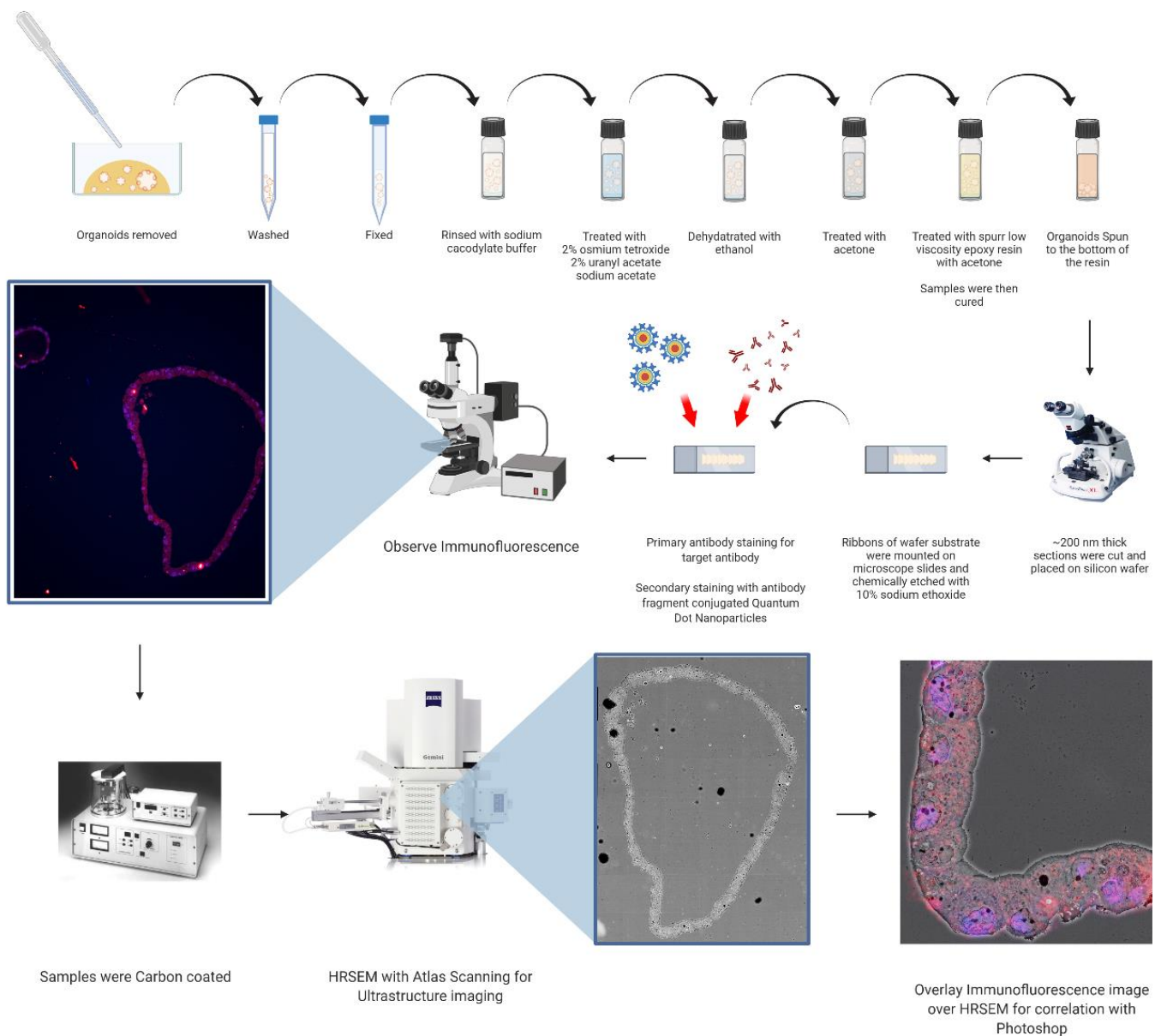To characterise the topological morphology of our organoids before and after differentiation to satisfy Aim 2 of this thesis, this was in order to observe whether the morphology was a product of liver organoid differentiation, and hence characteristic of liver organoid tissue differentiation. We used topographical HRSEM on undifferentiated (Figure 6.3), differentiated (Figure 6.4) and primary mouse hepatocytes as a differentiation positive control (Figure 6.5). To characterise the cellular ultrastructure of our organoids we used HRSEM of chemically treated organoids and compared them to the ultrastructure of mouse liver sections which acted as a positive control (Figures 6.6 and 6.7). We then observed the utility of HRSEM by comparing its capacity to capture wide area images of our organoid samples with no loss of ROIs compared to TEM (Figure 6.8). We also observed to utility of HRSEM to capture wide area (500 x 500 μm^2) images and rescan samples for 1 nm^2 per pixel resolutions for observing organelles (Figure 6.8). Finally, we used HRSEM and CLEM to observe the ultrastructure characteristics of organoids under different conditions, to characterise how these conditions change organoid ultrastructure (Figures 6.9 – 6.12).

6.2.1 Topographical Analysis
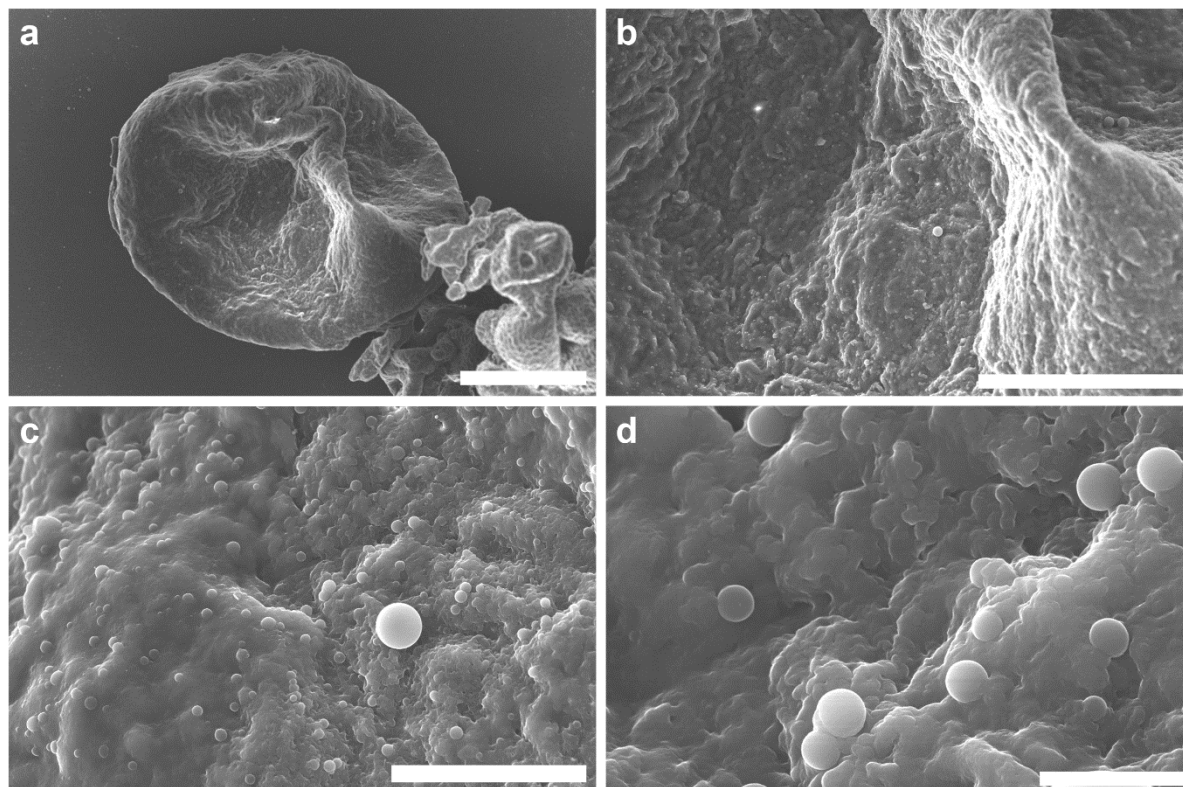
Figure 6.3 Undifferentiated Organoid Topographical HRSEM Imaging. A.
Undifferentiated mouse liver organoid mounted on a glass microscopy slide. Scale = 100 µm.
b. Surface of undifferentiated mouse liver organoid. Scale = 50 µm. **c** and **d.** Exosomes being
secreted on the surface of the organoid. Scales = 10 µm and 2 µm.

Using the methods of organoid generation as described in Chapters 2 and 3, we generated
undifferentiated organoids which appear crumpled with a ruff topology. Structurally they all
look deflated which may be a result of fixation and dehydration deflating the organoids
collapsing the inside of the internal lumen. There is also the ubiquitous secretion of exosomes
ranging from 500 nm – 2 µm in diameter. What we did not observe were hepatocyte microvilli
or 294holangiocytes cilium which are characteristic of these cell types.
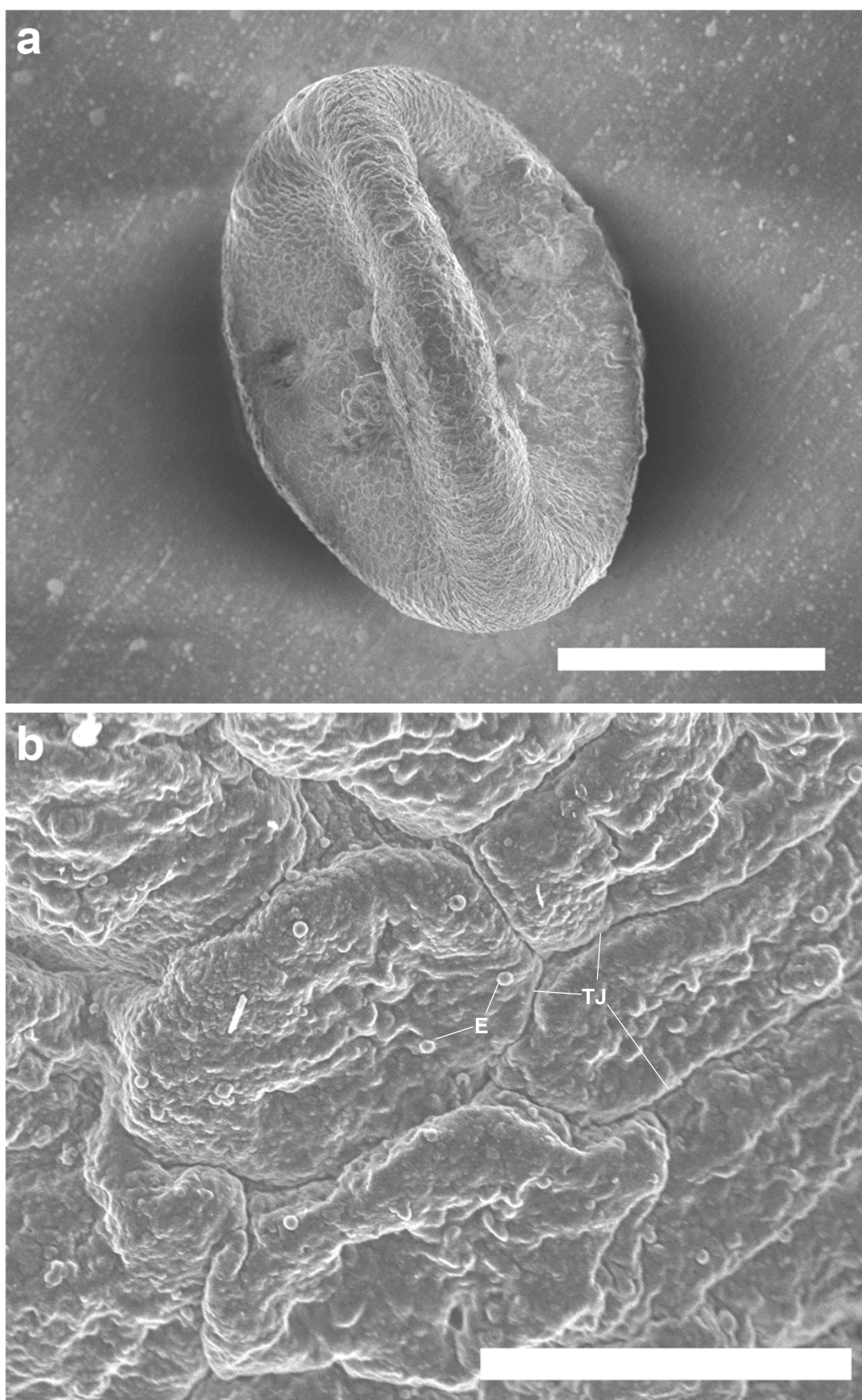
Figure 6.4 Differentiated Organoid Topographical HRSEM Imaging. A. Differentiated mouse liver organoid mounted on a glass microscopy slide. Scale = 100 µm. **b.** Surface of Differentiated mouse liver organoid. There are exosomes € being secreted by these organoids as well as clear demarcation of individual cells caused by observable tight junctions (TJ). Scale = 5 µm.

Differentiated organoids appear to have many of the same characteristic as undifferentiated organoids with exosome secretion, a crumpled, ruff topology and deflation, although this differentiated organoid (Figure 6.4) did have creases that may be demarcating the borders between cells as the shapes they create are the right size for defining individual cells bound together by hepatocyte tight junctions. This characteristic did not appear in all the differentiated organoids (not shown), as there was variation in size, topology roughness and the presences or lack of creases.
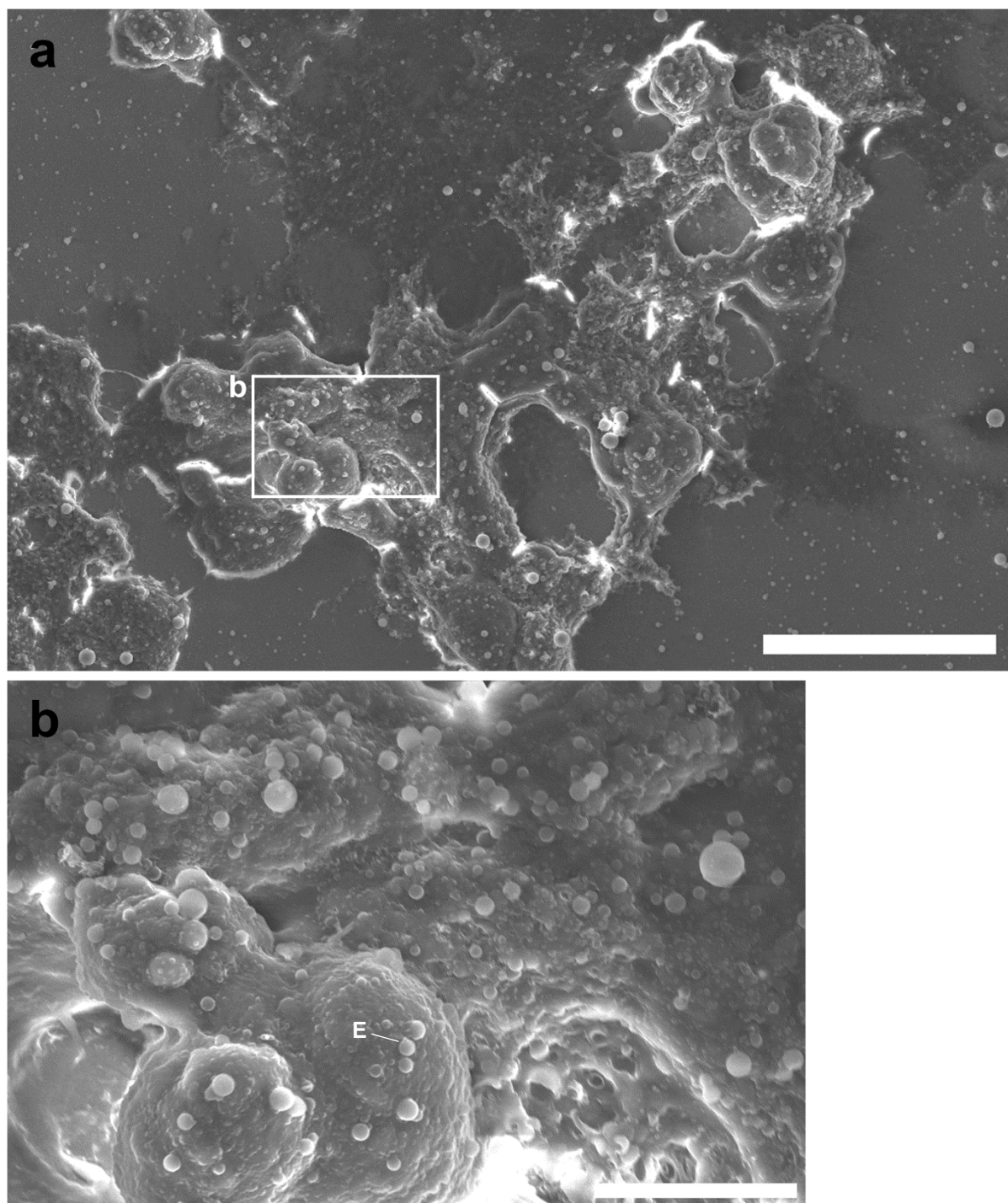
Figure 6.5 Primary Hepatocyte Topographical HRSEM Imaging. A. Primary mouse hepatocytes cyto-spun onto a poly lysine coverslip then mounted on a glass microscopy slide. Scale = 50 µm. **b.** Surface of primary mouse hepatocytes. There are exosomes € being secreted by these cells. Scale = 10 µm.

CHAPTER 6 ULTRSTRUCTURE MAPPING AND CHARACTERISATION OF LIVER ORGANOIDS USING SCALABLE HIGH RESOLUTION FIELD EMISSION SCANNING ELECTRON MICROSCOPY

Primary hepatocytes were morphologically closely resemble both undifferentiated and differentiated organoids with a ruff topology and exosome secretion. This being consistent with all the samples in each group is probably the result of the fixation and dehydration process.

6.2.2 Cross-Sectional Analysis
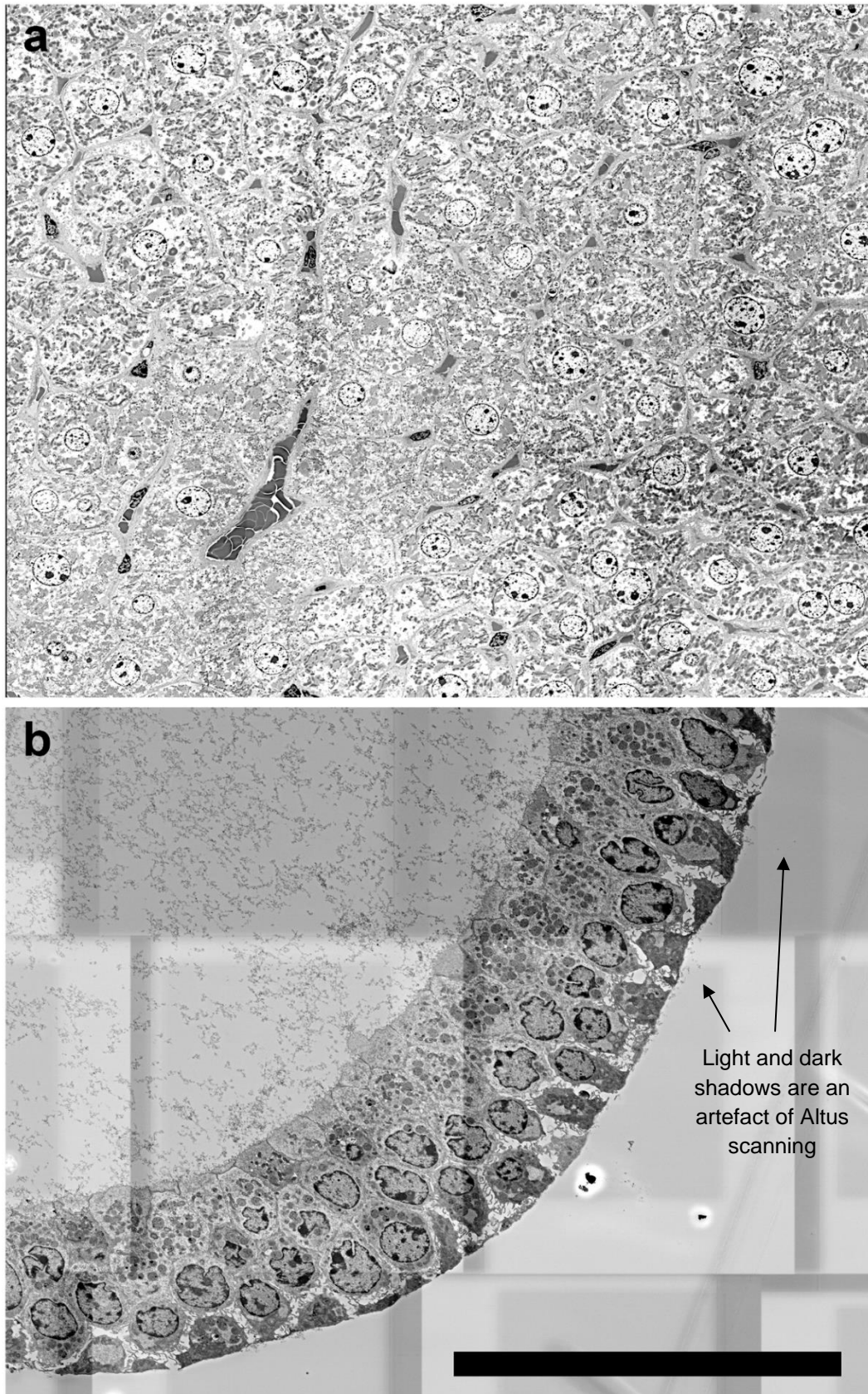
Light and dark shadows are an artefact of Altus scanning

Figure 6.6 Ultrastructure Anatomy of Mouse Liver Section Compared to a Mouse Liver Organoid. a. Ultrastructure of a cut sections from a mouse liver **b.** Ultrastructure of a mouse liver organoid. The organoids contain cells which face the internal hollow lumen and cells that face the exterior (Light and dark shadows are an artefact of Altus scanning, indicated by arrows). Scale = 50 µm.

Ultrastructure analysis of the cells in a section of mouse liver tissue compared to a differentiated liver organoid found that the primary tissue cells appear more uniform, with rounded nucleoli and a larger cytoplasm to nucleus ratio and hexagonal shape. The cells within the structure of the organoid appear to have different morphology depending on whether they were positioned on the internal lumen of the organoid or exposed to the external space. Cells on the inside contained more lysosomes and were smaller, while cells on the outside were larger and had a greater proportion of the volume of the cell taken up by the nucleus. Also, there appeared to be variation between organoid within the same cultures under the same conditions. this includes variations such as whether the organoid's anatomy was made from multilayers of cells or a single layer of cells. Light and dark shadows are an artefact of Altus scanning, as the samples are scanned in sections to make a whole image.
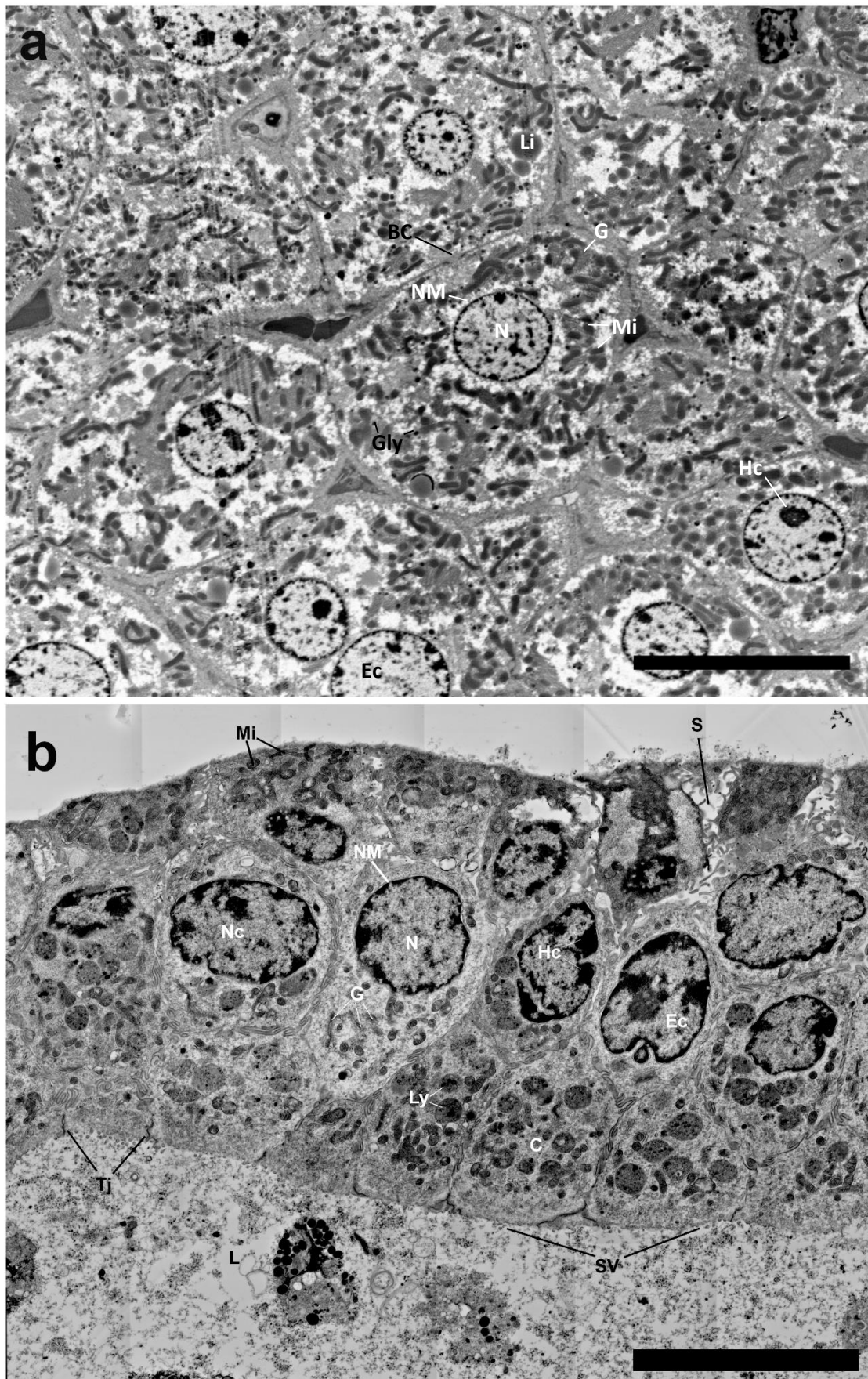
Figure 6.7 Cellular Ultrastructure of Organoid Samples Imaged using HRSEM a. Cell ultrastructure of a mouse liver section. Scale = 5 µm. **b.** Cell utrastructure of a differentiatied mouse liver organoid. Scale = 5 µm. Nucleus (N), nucleolus (Nc), heterochromatin (Hc), euchromatin (Ec), Nuclear membrane (NM), cytoplasm (C), mitochondria (Mi), Golgi apparatus (G), Billiary canaliculus (BC), Glycogen (Gly), Lipid droplet (Li), tight-junctions (Tj), lysosomes (Ly), intercellular spatium (S), secretory vesicle (SV) and organoid lumen (L).

Cells from mouse liver sections are populated with abundant mitochondria and an even spread of glycogen. These cells also have lipid droplets and biliary canaliculus. The nucleoli in the cells of our organoids are not rounded and take up the majority of the space in each cell. The cells that border the internal lumen of the organoid are full or lysosomes, a sign of autophagy. Cells that border the external space of the culture have intercellular spatium openings between cells. Tight junctions and intercellular locking are present in the cells of the organoid, as well as the accumulation of debris in the internal lumen likely secreted from cells.
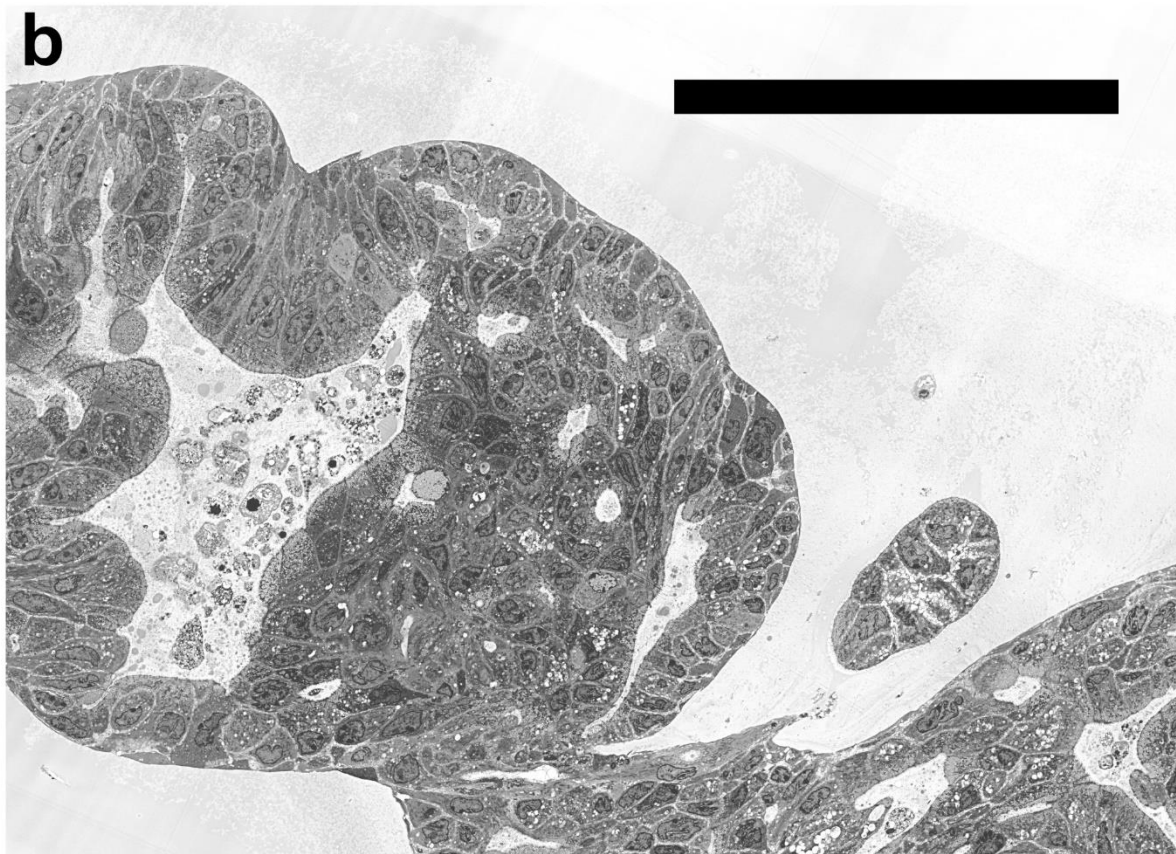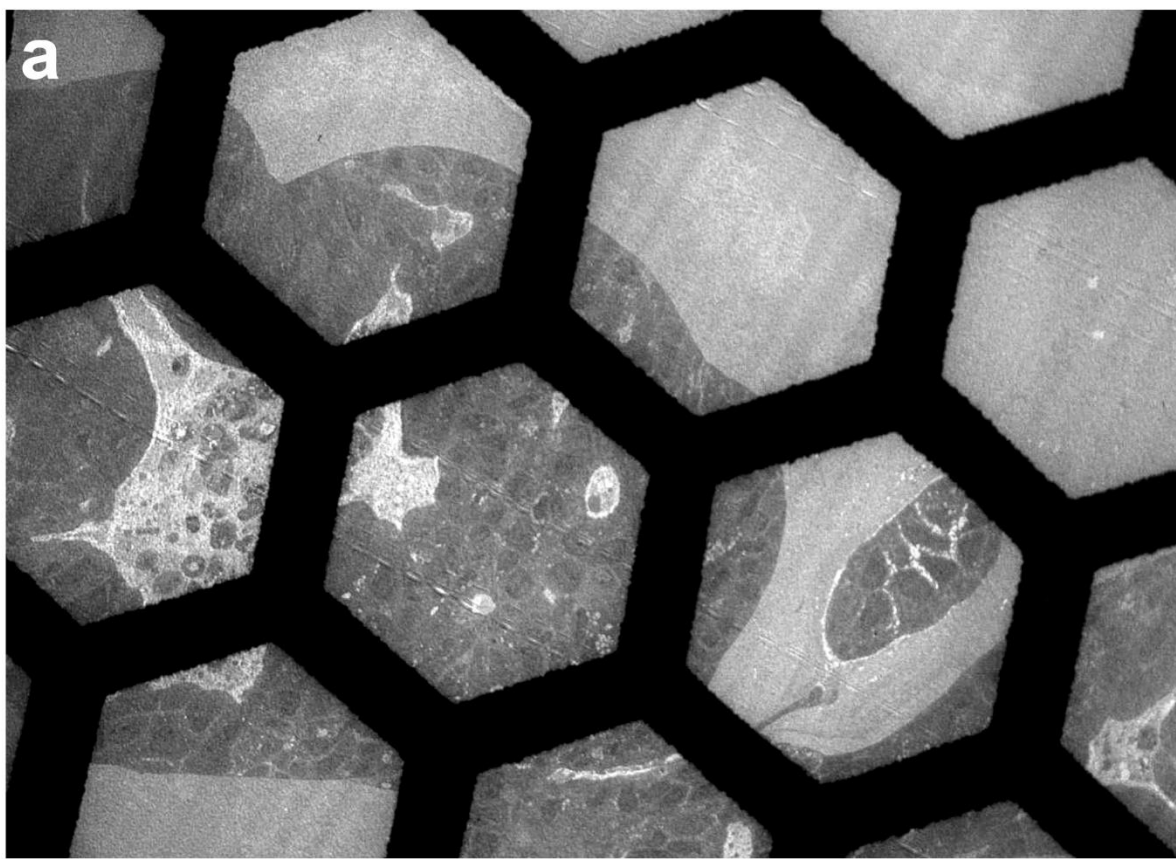
Figure 6.8 Demonstrating the Loss of Information Which Occurs When Using TEM Compared to HRSEM for Imaging Wide-Area Samples a. Liver organoid mounted on copper grid imaged using TEM. **b.** HRSEM imaging with an Atlas scan generator of a correlating cut section of the same liver organoid. Scale = 100 µm

We demonstrate the utility of HRSEM compared to TEM when it comes to large scale imaging without the loss of information. We cut two different sections of the same mouse liver organoid sample that nearly correlate, then we imaged one with conventional TEM and the other using HRSEM. The TEM sample (Figure 6.7a) required mounting on a copper grid to prevent the ~100 nm thick sample from tearing or folding, but also allows the transmission of electrons through the sample for high resolution imaging. The HRSEM sample (Figure 6.7b) on the other hand was cut ~200 nm thick and mounted onto a silicon wafer substrate and a glass microscopy slide. Figure 6.7a is not a representative of the best resolution TEM microscopes can attain. This figure is an indicative of the amount of information that is lost in wide-area samples like organoids.

Figure 6.9 Scalable High-Resolution Imaging of Mouse Liver Organoid Ultrastructure using HRSEM and Rescanning of ROIs for Nano-scale Resolution. a. Monolayer cross section of organoid imaged using HRSEM with an Atlas scan generator. Scale = 50 µm. **b-d.** Rescanning of ROI on the sample using HRSEM for higher resolution to observe cell organelle ultrastructure at high resolution. (Mv) microvilli, (Mi) mitochondria, (LD) lipid droplets, (N) nucleus, (Hc) heterochromatin, (Nc) nucleolus, (NM) nuclear membrane, (Ly) lysosome, (G) Golgi apparatus, (LB) lamellar body. **b.** Scale = 1 µm. **c.** Scale = 1 µm. **d.** Scale = 500 nm.

Our HRSEM method with Atlas scanning meant we could image a wide area (500 x 500 µm^2) of tissue, such as this organoid cell monolayer (Figure 6.9a) and allowing for a scalable overview of the sample corresponding to microscale light microscopy but with the added utility to "zoom in" to ROIs for key ultrastructural features and rescan these areas at resolutions as high as 1 nm^2 per pixel (Figure 6.9d). At this scale cell organelle ultrastructures are clearly visible and subcellular morphology can be analysed. In figure 6.9 we could easily distinguish individual cells, the cell nucleus and their features including finer features like the nuclear membrane with its' pores. Microvilli are a feature of these liver organoids but only appear on the internal lumen facing side of these cells. Other features observed include extracellular vesicles, mitochondria, lysosomes, lipid droplets and the Golgi apparatus (Figure 6.9d).
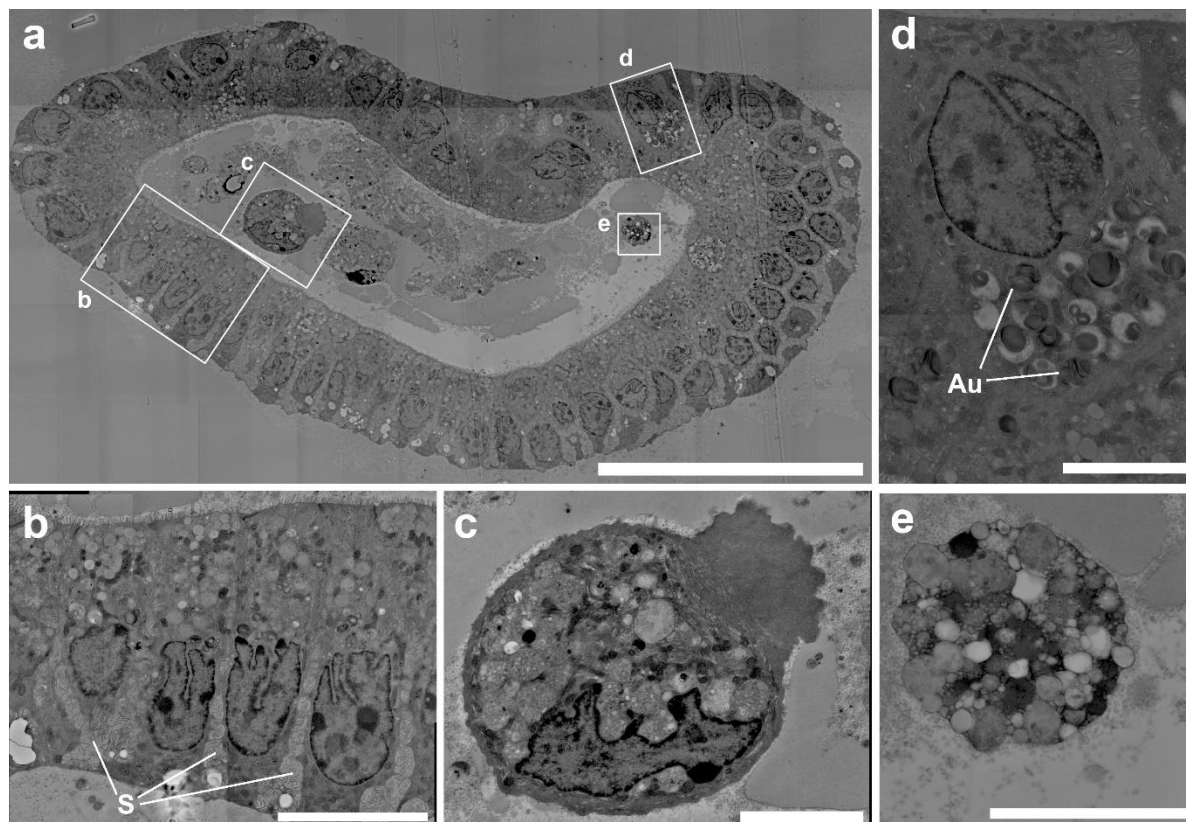
Figure 6.10 Liver Organoid Sample Co-cultured with Hepatic Stellate Cells Displayed Ultrastructural Characteristics of Autophagy and Apoptosis, as Well as the Opening of the Intercellular Spatium. a. Liver organoid co-cultured for 48 hours with immortalised hepatic stellate cells JS1 cells, imaged using HRSEM with an Atlas scan generator. Scale = 50 µm. **b.** Distinct intercellular space (S) opening between cells along with the release of extracellular vesicles. Scale = 10 µm. **c.** Late stage apoptosis of cell ejected into the internal lumen of the liver organoid. Scale = 5 µm. **d.** Autophagy (Au) of cell organelles. Scale = 5 µm. **e.** Late stage apoptosis of cell ejected into the lumen of liver organoid. Scale = 5 µm.
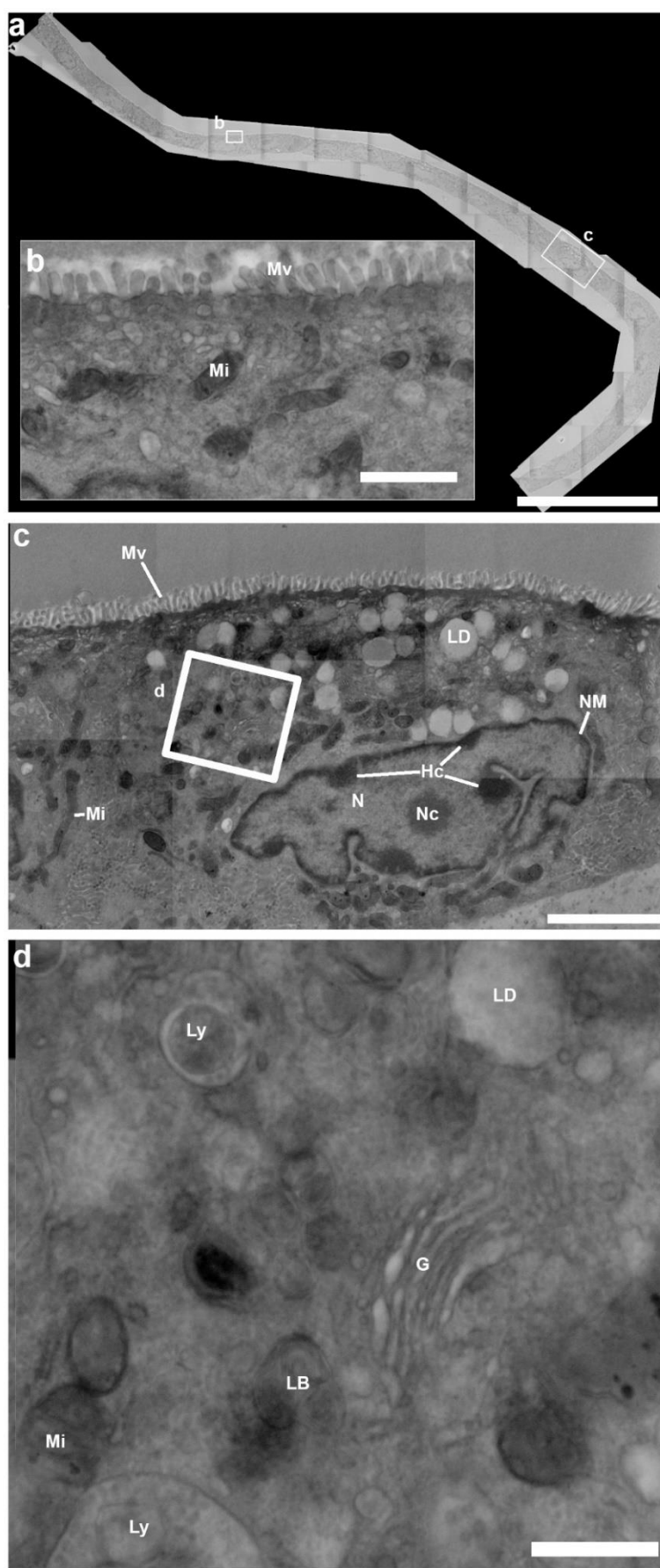
CHAPTER 6 ULTRSTRUCTURE MAPPING AND CHARACTERISATION OF LIVER ORGANOIDS USING SCALABLE HIGH RESOLUTION FIELD EMISSION SCANNING ELECTRON MICROSCOPY

We co-cultured our mouse liver organoids with a hepatic stellate cell line (JS1 cells), myofibroblastic cell type in the liver for 48 hours to induce an injury response (see Chapter 4). This initiated various stages of autophagy (Figure 6.10d) within the cells of the organoid and apoptosis (Figures 6.10c and 6.10e) within cells ejected into the internal lumen of the organoid. We also observed an atypical opening of the intercellular space (Figure 6.10b) between the cells.
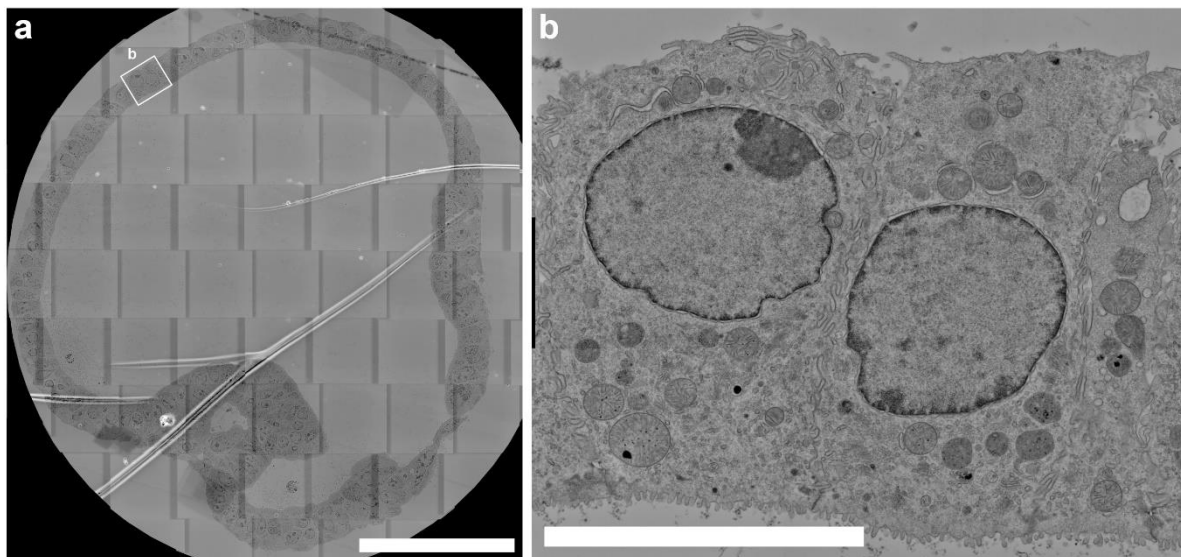
Figure 6.11 Liver organoid cultured for 48 hours with 50 ng / mL TNF displayed atypical organelle ultrastructure a. Liver organoid imaged using HRSEM with an Atlas scan generator. Scale = 100 µm. **b.** Cells within the organoid displaying atypical round nuclei and mitochondria as well as closed junctions between all cells. Scale = 5 µm.

Differentiated mouse liver organoids exposed to 50 ng / mL tumour necrosis factor (TNF) for 48 hours (See Chapter 4) to induce an injury response (Figure 6.11). This sample can be compared to the typical differentiated control mouse organoid ultrastructure (Figure 6.6 b). The ultrastructure of these organoids consistently displayed rounded mitochondria and nuclei across the entire organoid. The intercellular space between the cells were also tightly closed (Figure 6.11b).
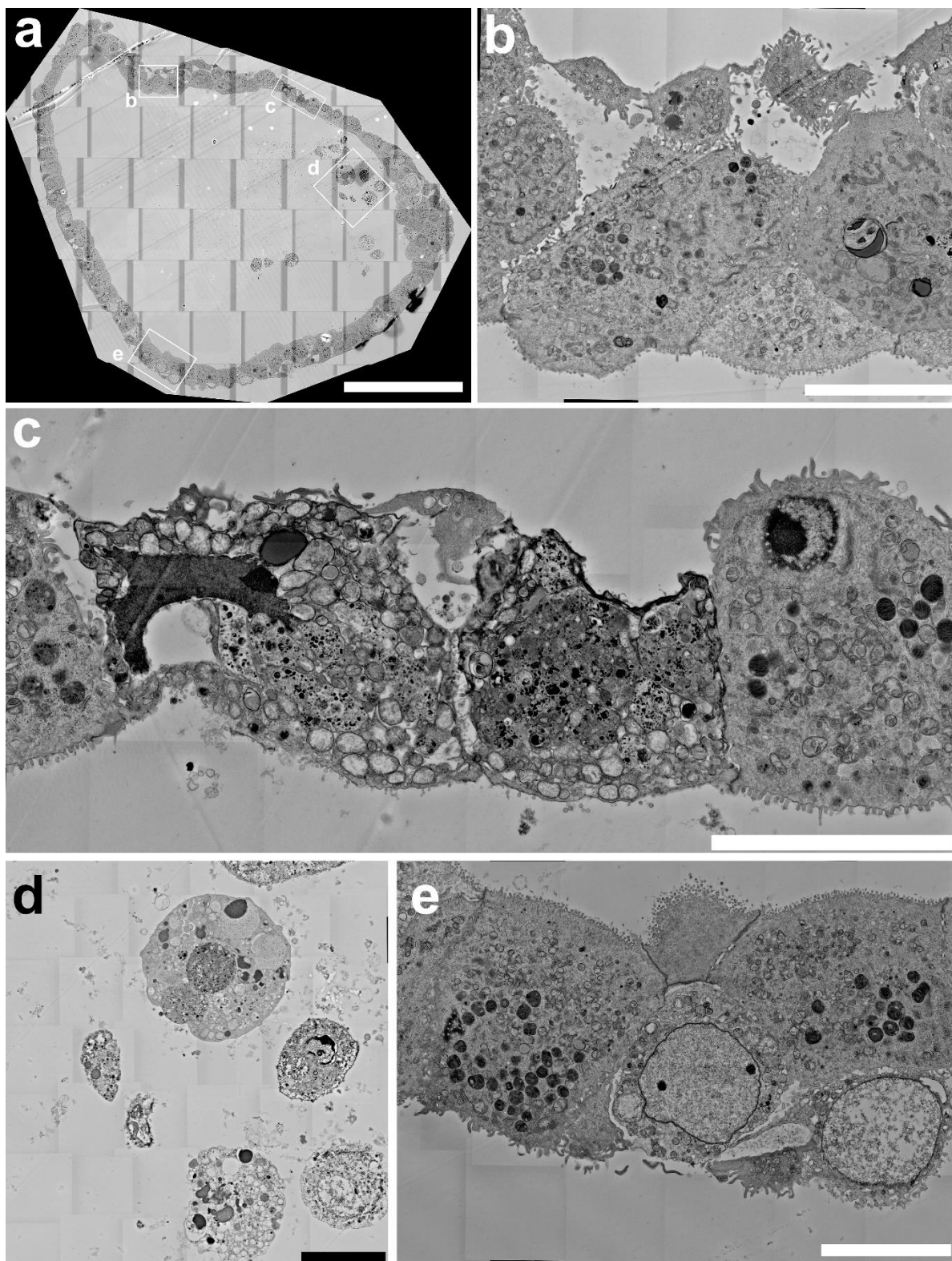
Figure 6.12. Liver organoid cultured for 48 hours with 1 % O$_2$ displaying cellular stress.

Liver organoids cultures under hypoxic conditions imaged using HRSEM with an Atlas scan generator, display atypical cytoplasm organisation with autophagy (b, e) and apoptosis (c,d). **a.** Scale = 100 µm. **b.** Scale = 10 µm. **c.** Scale = 10 µm. **d.** Scale = 10 µm. **e.** Scale = 10 µm.

Mouse liver organoids exposed to hypoxic (1% O$_2$) culture conditions for 48 hours display a drastically unorganised cytoplasm with clear signs of autophagy (Figures 5b and 5e) as well as apoptosis within the body of the organoids (Figure 6.12c) and in cells ejected into the organoid lumen (Figure 6.12d).

6.2.3 Correlative Light Electron Microscopy Analysis
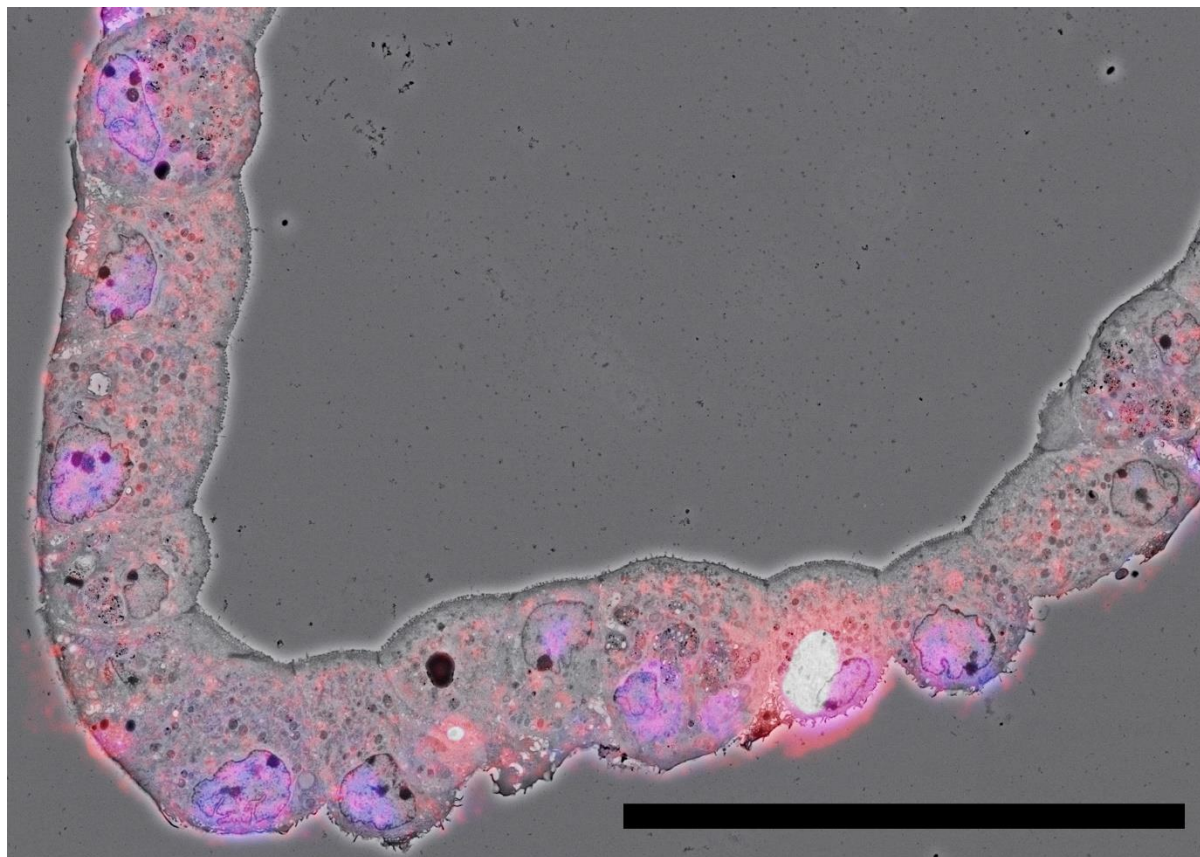
Figure 6.13 Liver Organoid Cultured for 48 hours with 1% O$_2$ Displaying Cellular Stress.

Imaged using CLEM, organoid immunolabelled for lysosomes with LAMP2 (red) and DNA stained (blue) with DAPI (Scale = 50 µm).

We were able to immunolabel the lysosome-associated membrane protein 2 (LAMP2) and fluorescently localize lysosomes within the ultrastructure of our liver organoids along with DNA staining (Figure 6.13) using the methods we developed (Figure 6.2). The red signal from the FAB2 antibody fragment conjugated quantum dot nanoparticles tend to localise within a range of 10-20 nm from their tagged protein of interest. This is because of the length of the primary and secondary antibodies factors into the location of the signal relative to the proteins of interest.

6.3 DISCUSSION

In this chapter we demonstrate a valuable new method for characterising the topology and ultrastructure of organoids using chemical tissue processing and HRSEM. We found that our organoids are very similar to primary hepatocytes and there was limited change in morphology caused by differentiation. We were also able to demonstrate the advantages of contemporary HRSEMs using over existing TEM methods for ultrastructure analysis. HRSEM allows for comprehensive imaging of samples to ensure the discovery of ROIs at similar resolution to TEM. In addition, HRSEM can also be combined easily with CLEM.

HRSEM is a low-cost system that is not limited by sample thickness (~ 120-250 nm thickness) or by electron beam damage to delicate structures. Samples can be mounted on silicon wafers or Indium-Tin-Oxide coverslips, enabling sample preservation and re-imaging which is an improvement on delicate TEM ultrathin sections (~ 100 nm thick) that are easily damaged by handling. This was possible because we used new generation HRSEM instruments which have reduced constraints on specimen size and final image resolution, allowing more flexibility to sample preparation techniques and imaging (Kuwajima *et al* 2013; Cohen Hyams *et al* 2020).

As indicated earlier TEM is more expensive and difficult to use than HRSEM and as we demonstrated a significant proportion of TEM samples are unobservable (see Figure 6.8), because of the necessity of mounting TEM samples on a metal grid for imaging (Cohen Hyams *et al* 2020). Our technique can achieve a wide area (500 x 500 μm^2) "google earth" view of samples with ultrastructure resolutions as small as 1 nm^2 per pixel (Figure 6.9), without the technical difficulties associated with cryogenic freezing or mounting samples onto metal grids. Changes in organoid ultrastructure can be easily defined using HRSEM and with

immunofluorescent labelling using quantum dot nanoparticles (Figure 6.13), proteins of interest within ROIs can also be observed.

The cell ultrastructure of our organoid was not as uniform or typically hexagonally shaped as hepatocytes are *in vivo* (Figure 6.7). While we can observe many of the organelles present in the organoid cells the proportion of the cytoplasm to the nucleus is much lower than that observed in our liver tissue sections. Microvilli are present on the internal lumen side of our organoids and lysosomes are abundant. The intercellular space is open, and signs of autophagy and apoptosis appear in organoids co-cultured with HSCs (Figure 6.10), but this is not the case in TNF treatments, where the cell nuclei and mitochondria become rounder, and tighter bonds between cells are formed (Figure 6.11). Hypoxia caused a drastically unorganised cytoplasm with clear signs of autophagy as well as the abundant release of LAMP2 positive lysosomes (Figures 6.12 and 6.13).

By using HRSEM we found that we could image larger areas making it easier to find ROIs and make more discoveries in our organoids, such as cell morphology not being as uniformly hexagonal as hepatocytes are *in vivo*, we also observed multiple features of liver organoid cell ultrastructure including signs of cell stress, such as abundant lysosomes, autophagy, and apoptosis. However, there is a minor limitation of surface conductance that requires a thin layer of carbon or heavy metal coating, usually gold.

In organoid biology, ultrastructure analysis has been mostly overlooked (Dekkers *et al* 2019), we hope that these accessible methods will give researchers the tools they need to better understand their organoid models and to use them to comprehensively characterise disease pathogenesis and drug development.

CHAPTER 7

SUMMARY, DISCUSSION AND CONCLUDING REMARKS

KEY FINDINGS

1. We established and described a 3D organoid cell culture model from mouse liver tissue.

2. Characterised the capacity of these organoids to shift from modelling a stem-like phenotype to a hepatic phenotype and observed variation in cell type.

3. Designed an *in vitro* liver injury model that accurately represented certain aspects of liver injury, such as trans-differentiation of HSCs from a quiescent to an activated phenotype.

4. Halofuginone treatment induces genes suppression and causes a reduction in HSC proliferation. This did not lead to an increase in hepatocyte survival.

5. TNF treatment induced the genetic characteristics of the liver injury initiation phase, with gene sets related to the interferon gamma response inflammation, hypoxia, and apoptosis positively enriched in the model, and the cell nuclei and mitochondria become rounder with tighter bonds between each cell.

6. Crosstalk between the liver injury phenotype organoid tissues and the HSCs did not induce a fibrous phenotype.

7. We demonstrated a novel method for characterising the topology and ultrastructure of organoids using chemical tissue processing and HRSEM, that can also be combined with CLEM.

8. The cell ultrastructure of organoids was not as uniform or typically hexagonally shaped as hepatocytes are *in vivo*.

9. We observed multiple features of liver organoid cell ultrastructure including signs of cell stress, such as abundant lysosomes, autophagy, and apoptosis.

CHAPTER 7 SUMMARY, DISCUSSION AND CONCLUDING REMARKS

This thesis aimed to establish and describe a 3D organoid cell culture model from mouse liver tissue, characterise the capacity of these organoids to model liver characteristics *in vitro*, and use this model for preclinical drug discovery of an anti-fibrosis drug. The model was designed to represent the hepatic phenotype observed during liver injury, the intercellular interactions between liver inflammatory cells (represented by the introduction of TNF and TGF-β into the model), hepatocytes, and HSCs, as well as HSC activation, and the TNF and TGF-β related signalling pathways.

Ductal structures and single cells were expanded into organoids that displayed self-folding, budding and expansion in cell culture over the expected timeframe and was comparable with that described by Broutier *et al* 2016. A shift in gene and protein expression characteristic of a change from a liver stem-like phenotype to a differentiated hepatocyte phenotype was induced and a variation in cell types within the organoids was observed. That the organoids produced accurately modelled the morphological, genetic and protein characteristics of mouse liver tissue *in vitro*.

An *in vitro* model of liver injury was also designed by combining mouse liver organoids with HSCs in a transwell system. This model did accurately represent specific aspects of liver injury *in vitro*, such as trans-differentiation of HSCs from a quiescent to a SMA positive activated phenotype was dependent on exposure to hepatocyte, TNF or TGF-β, but did not replicate the expected gene expression for liver injury such as the HSC gene expression of *Col1a1* and *Col4a1* which encode for collagens I and IV and are typical of a fibrotic ECM phenotype *in vivo* (Robinson *et al* 2016), neither did we observe or have differential collagen I protein expression. The preclinical anti-fibrosis drug Halofuginone caused a selective reduction in HSC proliferation, and supressed *Col1a1*, *Mmp14* and *Timp2* under select liver injury conditions although this did not result in an increase in hepatocyte survival, hence it was not modelling a recovery phenotype. Interestingly the liver injury cytokine TNF induced unique

phenotypes in the liver organoids and HSCs of our model with genetic characteristics of the liver injury initiation phase being upregulated as seen in previous studies (Yang and Seki 2015; Tu et al 2015; Tsuchida and Friedman 2017). The TNF dependent HSC phenotype upregulated TNF/NFκB related pathways while the *Col1a1* gene and the genes of proteins that interact with Collagen I were downregulated which has been observed *in vitro* previously (Saile *et al* 1999; Yang and Seki 2015). The inclusion of organoids in the co-culture did not lead to a more fibrous phenotype as would be necessary in a liver injury model (Tu *et al* 2015; Yang and Seki 2015).

Gene expression in networks/sets related to the interferon gamma response inflammation, hypoxia, and apoptosis were positively enriched in each cell population treated with TNF. Yet collagen I was downregulated in HSCs with the upregulated TNF response. Hence crosstalk between the liver injury phenotype organoid tissues and the HSCs did not induce a fibrous phenotype.

To better understand the cellular substructure of the organoids we applied a novel HRSEM approach (Cohen Hyams *et al* 2020). This allowed the improved ability to characterise the topology and ultrastructure of organoids. This technique permitted for wide area (500 x 500 μm^2) imaging of samples to ensure the discovery of ROIs at similar resolution to TEM. It is low-cost and not limited by sample thickness (~ 120-250 nm thickness) or by electron beam damage to delicate structures and can be combined easily with correlate light electron microscopy. We found that liver organoid differentiation caused little change to organoid topological morphology and that the cell ultrastructure of our organoid was not as uniform or typically hexagonally shaped as hepatocytes *in vivo*, probably due to being defined by vascular and biliary structures which are lacking in organoids (Sherlock & Dooley 2002; Bioulac-Sage *et al* 2007). Nonetheless, we demonstrated multiple features of liver organoid cell ultrastructure including signs of cell stress with abundant lysosomes, autophagy, and apoptosis.

CHAPTER 7 SUMMARY, DISCUSSION AND CONCLUDING REMARKS

From these results it can be concluded that while there is considerable potential capacity of liver organoids to recapitulate an *in vivo* liver injury cellular phenotype there are still many limitations. There is a lack of an upregulated collagen I gene and protein expression in HSCs, despite a clear TNF responses in both cell populations. Also, the ultrastructure morphology of our organoids was not uniform or a typically hexagonal, with a greater cytoplasm to nucleus ratio than what is observed in hepatocytes *in vivo*, indicating that organoids still fall short of the differentiated tissues we are trying to replicate. These limitations could be overcome by designing a culture where the two cell populations can directly bind to each other, such as growing the organoids and the HSC cell line on each side of a permeable membrane without any space in between the organoids and cells as opposed to the transwell system we used, that had a space in between the cell cultures. This could take inspiration from organ-on-a-chip devices that have been used to model the intestine (Workman *et al* 2017; Kasendra *et al* 2018). The cell populations could also be cultured together in an ECM and separated for analysis by cell sorting, although getting enough biological material to do meaningful experiments will be a challenge, and immunolabelling through a protein ECM scaffold could interfere with labelling accuracy and lead to false positives. Using a cell line like JS1 to represent the HSC cell population should be a reasonable substitute for primary mouse hepatic stallate cells, as the line was derived from the liver of a male C57Bl/6 mouse. Although as stated in the introduction; cell lines lack some differentiation potential compared to primary cells. Maybe the results would be more representative of liver injury in vitro if we used primary mouse HSCs instead.

Due to the limitations observed with the organoids generated as part of this study and what has also been revealed by others (Huch *et al* 2013; Huch *et al* 2015; Broutier *et al* 2016) it can be concluded that organoids are best suited for investigating individual mechanisms of disease as opposed to the multidimensional multicellular processes as observed in liver injury. For

example, investigating diseases that are caused by single gene mutations, as demonstrated in cystic fibrosis research (Schwank *et al* 2013), or α1-antitrypsin deficiency research (Huch *et al* 2015). Organoids would also be best suited for replicating undifferentiated embryonic-like tissues or dedifferentiated tumour tissues (Clevers 2016; Broutier *et al* 2017; Lui *et al* 2020; Driehuis *et al* 2020).

Our capacity to extensively characterise organoids has significant implications for diagnosis of dedifferentiated tumour tissues, especially now with the widespread adoption of single-cell sequencing (Nawy 2013; Hwang *et al* 2018). As demonstrated by Broutier and colleagues in 2017 tumour organoids from HCC, CC and combined CHC retained features from their tissue of origin. Cancer-related genetic variants, gene expression profiles and tissue histology, can be used to develop drug assays to identify patient-specific drug sensitivity (Broutier *et al* 2017). That said the adoption of organoids as diagnostic tool in medicine will require automation, due to the technical challenges of generating large scale cultures for organoid assays, for drug development or clinical pathology. There is very little to date published on the automation of organoid culturing using liquid handling technology, but the small scale that is 1-6 cell culture plates at a time (either in a 24, 96 or 384 well configuration) a Formulatrix® Mantis® microfluidic liquid handler (Formulatrix Inc., Bedford MA, USA) would be able to produce high throughput and consistent organoid cultures, as demonstrated at the Massachusetts Institute of Technology (Mean 2019). For scales greater than 6 cell culture plates at a time, extensive liquid handling set ups, such as an array of Hamilton® Verso® and Microlab Vantage® liquid handling systems (HamiltonRobotics®, Reno NV, USA) could be adapted to organoid culture (Miyao 2018).

Currently, 3D organoid cell culture models for the study of liver injury is still in the early stages of development, but this thesis has provided some very encouraging results. Organoids model the morphological, genetic and protein characteristics of liver tissue *in vitro*, aspects of liver

injury were replicated, anti-fibrosis drugs can be shown to selectively reduce HSC proliferation *in vitro*, and the development of a novel method of organoid ultrastructure analysis that is assessable to more scientist for the future.

REFERENCES

REFERENCES

Alberts, B, Johnson, A, Lewis, J, Raff, M, Roberts, K & Walter, P 2008, *Molecular Biology of the Cell*, 5th Edition, Garland Science, Taylor & Francis Group, LLC, pp. 582–613.

Allen, JW & Bhatia, SN 2003, 'Formation of steady-state oxygen gradients in vitro: Application to liver zonation', *Biotechnology and Bioengineering*, vol. 82, no. 3, pp. 253–262.

Allen, JW, Khetani, SR & Bhatia, SN 2005, 'In vitro zonation and toxicity in a hepatocyte bioreactor', *Toxicological Sciences: An Official Journal of the Society of Toxicology*, vol. 84, no. 1, pp. 110–119 <https://pubmed.ncbi.nlm.nih.gov/15590888/>.

Amara, S, Lopez, K, Banan, B, Brown, S-K, Whalen, M, Myles, E, Ivy, MT, Johnson, T, Schey, KL & Tiriveedhi, V 2015, 'Synergistic effect of pro-inflammatory TNFα and IL-17 in periostin mediated collagen deposition: potential role in liver fibrosis', *Molecular Immunology*, vol. 64, no. 1, pp. 26–35, <https://pubmed.ncbi.nlm.nih.gov/25467797/>.

Anthony, PP, Ishak, KG, Nayak, NC, Poulsen, HE, Scheuer, PJ & Sobin, LH 1977, 'The morphology of cirrhosis: definition, nomenclature, and classification', *Bulletin of the World Health Organization*, vol. 55, no. 4, pp. 521–540, <https://www.ncbi.nlm.nih.gov/pmc/articles/PMC2366674/>.

Apte, U, Thompson, MD, Cui, S, Liu, B, Cieply, B & Monga, SPS 2007, 'Wnt/β-catenin signaling mediates oval cell response in rodents', *Hepatology*, vol. 47, no. 1, pp. 288–295, <https://aasldpubs.onlinelibrary.wiley.com/doi/full/10.1002/hep.21973>.

REFERENCES

Arthur, MJ 2000, 'Fibrogenesis II. Metalloproteinases and their inhibitors in liver fibrosis', *American Journal of Physiology. Gastrointestinal and Liver Physiology*, vol. 279, no. 2, pp. G245-249, <https://pubmed.ncbi.nlm.nih.gov/10915630/>.

Ashley, EA 2016, 'Towards precision medicine', *Nature Reviews Genetics*, vol. 17, no. 9, pp. 507–522.

Astashkina, A, Mann, B & Grainger, DW 2012, 'A critical evaluation of in vitro cell culture models for high-throughput drug screening and toxicity', *Pharmacology & Therapeutics*, vol. 134, no. 1, pp. 82–106.

Avorn, J 2015, 'The $2.6 Billion Pill — Methodologic and Policy Considerations', *New England Journal of Medicine*, vol. 372, no. 20, pp. 1877–1879.

Bale, SS, Golberg, I, Jindal, R, McCarty, WJ, Luitje, M, Hegde, M, Bhushan, A, Usta, OB & Yarmush, ML 2015, 'Long-Term Coculture Strategies for Primary Hepatocytes and Liver Sinusoidal Endothelial Cells', *Tissue Engineering Part C: Methods*, vol. 21, no. 4, pp. 413–422.

Bartolomeo, N, Trerotoli, P & Serio, G 2011, 'Progression of liver cirrhosis to HCC: an application of hidden Markov model', *BMC Medical Research Methodology*, vol. 11, no. 1.

Sharma B, John S. Hepatic Cirrhosis. StatPearls Publishing; 2019 <https://www.ncbi.nlm.nih.gov/books/NBK482419/>

Bataller, R & Brenner, DA 2005, 'Liver fibrosis', *Journal of Clinical Investigation*, vol. 115, no. 2, pp. 209–218.

Baudoin, R, Prot, JM, Nicolas, G, Brocheton, J, Brochot, C, Legallais, C, Benech, H & Leclerc, E 2013, 'Evaluation of seven drug metabolisms and clearances by cryopreserved human

REFERENCES

primary hepatocytes cultivated in microfluidic biochips', *Xenobiotica; the Fate of Foreign Compounds in Biological Systems*, vol. 43, no. 2, pp. 140–152, <https://pubmed.ncbi.nlm.nih.gov/22830982/>.

Ben-Ze'ev, A, Robinson, GS, Bucher, NL & Farmer, SR 1988, 'Cell-cell and cell-matrix interactions differentially regulate the expression of hepatic and cytoskeletal genes in primary cultures of rat hepatocytes', *Proceedings of the National Academy of Sciences of the United States of America*, vol. 85, no. 7, pp. 2161–2165, <https://pubmed.ncbi.nlm.nih.gov/3353374/>.

Bhise, NS, Manoharan, V, Massa, S, Tamayol, A, Ghaderi, M, Miscuglio, M, Lang, Q, Shrike Zhang, Y, Shin, SR, Calzone, G, Annabi, N, Shupe, TD, Bishop, CE, Atala, A, Dokmeci, MR & Khademhosseini, A 2016, 'A liver-on-a-chip platform with bioprinted hepatic spheroids', *Biofabrication*, vol. 8, no. 1, p. 014101, <http://adsabs.harvard.edu/abs/2016BioFa...8a4101B>.

Bioulac-Sage, P, Le Bail, B & Balabaud, C 2007, *Textbook of Hepatology: From Basic Science to Clinical Practice, 3rd Edition | Wiley*, Wiley.com, Blackwell Publishing Ltd, <https://www.wiley.com/en-us/Textbook+of+Hepatology%3A+From+Basic+Science+to+Clinical+Practice%2C+3rd+Edition-p-9781405181518>.

Bollong, MJ, Lee, G, Coukos, JS, Yun, H, Zambaldo, C, Chang, JW, Chin, EN, Ahmad, I, Chatterjee, AK, Lairson, LL, Schultz, PG & Moellering, RE 2018, 'A metabolite-derived protein modification integrates glycolysis with KEAP1-NRF2 signalling', *Nature*, vol. 562, no. 7728, pp. 600–604, <https://pubmed.ncbi.nlm.nih.gov/30323285/>.

REFERENCES

Boulter, L, Govaere, O, Bird, TG, Radulescu, S, Ramachandran, P, Pellicoro, A, Ridgway, RA, Seo, SS, Spee, B, Van Rooijen, N, Sansom, OJ, Iredale, JP, Lowell, S, Roskams, T & Forbes, SJ 2012, 'Macrophage-derived Wnt opposes Notch signaling to specify hepatic progenitor cell fate in chronic liver disease', *Nature Medicine*, vol. 18, no. 4, pp. 572–579, <https://pubmed.ncbi.nlm.nih.gov/22388089/>.

Boyer, JL 2013, 'Bile Formation and Secretion', *Comprehensive Physiology*, vol. 3, no. 3. doi:10.1002/cphy.c120027

Bray, F, Ferlay, J, Soerjomataram, I, Siegel, RL, Torre, LA & Jemal, A 2018, 'Global cancer statistics 2018: GLOBOCAN estimates of incidence and mortality worldwide for 36 cancers in 185 countries', *CA: A Cancer Journal for Clinicians*, vol. 68, no. 6, pp. 394–424.

Broutier, L, Andersson-Rolf, A, Hindley, CJ, Boj, SF, Clevers, H, Koo, B-K & Huch, M 2016, 'Culture and establishment of self-renewing human and mouse adult liver and pancreas 3D organoids and their genetic manipulation', *Nature Protocols*, vol. 11, no. 9, pp. 1724–1743.

Broutier, L, Mastrogiovanni, G, Verstegen, MM, Francies, HE, Gavarró, LM, Bradshaw, CR, Allen, GE, Arnes-Benito, R, Sidorova, O, Gaspersz, MP, Georgakopoulos, N, Koo, B-K, Dietmann, S, Davies, SE, Praseedom, RK, Lieshout, R, IJzermans, JNM, Wigmore, SJ, Saeb-Parsy, K & Garnett, MJ 2017, 'Human primary liver cancer–derived organoid cultures for disease modeling and drug screening', *Nature Medicine*, vol. 23, no. 12, pp. 1424–1435, <https://www.nature.com/articles/nm.4438>.

Brown, JJ, Parashar, B, Moshage, H, Tanaka, KE, Engelhardt, D, Rabbani, E, Roy-Chowdhury, N & Roy-Chowdhury, J 2000, 'A long-term hepatitis B viremia model generated by transplanting nontumorigenic immortalized human hepatocytes in Rag-2-deficient mice',

REFERENCES

Hepatology (Baltimore, Md.), vol. 31, no. 1, pp. 173–181, <https://pubmed.ncbi.nlm.nih.gov/10613743/>.

Bruck, R 2001, 'Halofuginone to prevent and treat thioacetamide-induced liver fibrosis in rats', *Hepatology*, vol. 33, no. 2, pp. 379–386.

Burt, A & Day, C 2002, *Pathology of the Liver*, 4th Edition, Churchill Livingstone, pp. 67–105.

Caron, JM 1990, 'Induction of albumin gene transcription in hepatocytes by extracellular matrix proteins', *Molecular and Cellular Biology*, vol. 10, no. 3, pp. 1239–1243, <https://pubmed.ncbi.nlm.nih.gov/2406565/>.

Carpentier, R, Suñer, RE, van Hul, N, Kopp, JL, Beaudry, J, Cordi, S, Antoniou, A, Raynaud, P, Lepreux, S, Jacquemin, P, Leclercq, IA, Sander, M & Lemaigre, FP 2011, 'Embryonic Ductal Plate Cells Give Rise to Cholangiocytes, Periportal Hepatocytes, and Adult Liver Progenitor Cells', *Gastroenterology*, vol. 141, no. 4, pp. 1432-1438.e4.

Chakradhar, S 2017, 'Put to the test: Organoid-based testing becomes a clinical tool', *Nature Medicine*, vol. 23, no. 7, pp. 796–799, <https://pubmed.ncbi.nlm.nih.gov/28697178/>.

Chamberlain, LM, Godek, ML, Gonzalez-Juarrero, M & Grainger, DW 2009, 'Phenotypic non-equivalence of murine (monocyte-) macrophage cells in biomaterial and inflammatory models', *Journal of Biomedical Materials Research. Part A*, vol. 88, no. 4, pp. 858–871, <https://pubmed.ncbi.nlm.nih.gov/18357567/>.

Chen, C-J, Yang, H-I, Su, J, Jen, C-L, You, S-L, Lu, S-N, Huang, G-T, Iloeje, UH & REVEAL-HBV Study Group 2006, 'Risk of hepatocellular carcinoma across a biological gradient of

REFERENCES

serum hepatitis B virus DNA level', *JAMA*, vol. 295, United States, no. 1, pp. 65–73, <https://www.ncbi.nlm.nih.gov/pubmed/16391218>.

Chen, CJ, Yu, MW & Liaw, YF 1997, 'Epidemiological characteristics and risk factors of hepatocellular carcinoma', *Journal of Gastroenterology and Hepatology*, vol. 12, no. 9-10, pp. S294-308, <https://pubmed.ncbi.nlm.nih.gov/9407350/>.

Choucha Snouber, L, Bunescu, A, Naudot, M, Legallais, C, Brochot, C, Dumas, ME, Elena-Herrmann, B & Leclerc, E 2013, 'Metabolomics-on-a-chip of hepatotoxicity induced by anticancer drug flutamide and Its active metabolite hydroxyflutamide using HepG2/C3a microfluidic biochips', *Toxicological Sciences: An Official Journal of the Society of Toxicology*, vol. 132, no. 1, pp. 8–20, <https://pubmed.ncbi.nlm.nih.gov/22843567/>.

Clevers, H 2016, 'Modeling Development and Disease with Organoids', *Cell*, vol. 165, no. 7, pp. 1586–1597.

Cohen Hyams, T, Mam, K & Killingsworth, MC 2020, 'Scanning electron microscopy as a new tool for diagnostic pathology and cell biology', *Micron*, vol. 130, p. 102797, <https://www.sciencedirect.com/science/article/abs/pii/S0968432819303154>.

Collins, FS & MacKusick, V 2001, 'Implications of the Human Genome Project for Medical Science', *JAMA*, vol. 285, no. 5, p. 540, <https://jamanetwork.com/journals/jama/fullarticle/193524>.

Copple, BL 2010, 'Hypoxia stimulates hepatocyte epithelial to mesenchymal transition by hypoxia-inducible factor and transforming growth factor-β-dependent mechanisms', *Liver International*, vol. 30, no. 5, pp. 669–682.

REFERENCES

Copple, BL, Bai, S, Burgoon, LD & Moon, J-O 2010, 'Hypoxia-inducible factor-1α regulates the expression of genes in hypoxic hepatic stellate cells important for collagen deposition and angiogenesis', *Liver International*, vol. 31, no. 2, pp. 230–244.

Copple, BL, Kaska, S & Wentling, C 2012, 'Hypoxia-Inducible Factor Activation in Myeloid Cells Contributes to the Development of Liver Fibrosis in Cholestatic Mice', *The Journal of Pharmacology and Experimental Therapeutics*, vol. 341, no. 2, pp. 307–316, <https://www.ncbi.nlm.nih.gov/pmc/articles/PMC3336817/>.

Crawford, J 2002, 'Liver cirrhosis', in *Pathology of the liver*, CHURCHILL LIVINGSTONE, pp. 575–619.

Crosnier, C, Stamataki, D & Lewis, J 2006, 'Organizing cell renewal in the intestine: stem cells, signals and combinatorial control', *Nature Reviews. Genetics*, vol. 7, no. 5, pp. 349–359, <https://pubmed.ncbi.nlm.nih.gov/16619050/>.

Cummings, BS, Lasker, JM & Lash, LH 2000, 'Expression of Glutathione-Dependent Enzymes and Cytochrome P450s in Freshly Isolated and Primary Cultures of Proximal Tubular Cells from Human Kidney', *Journal of Pharmacology and Experimental Therapeutics*, vol. 293, no. 2, pp. 677–685, <https://jpet.aspetjournals.org/content/293/2/677>.

de Boer, P, Hoogenboom, JP & Giepmans, BNG 2015, 'Correlated light and electron microscopy: ultrastructure lights up!', *Nature Methods*, vol. 12, no. 6, pp. 503–513.

de Gottardi, A, Vinciguerra, M, Sgroi, A, Moukil, M, Ravier-Dall'Antonia, F, Pazienza, V, Pugnale, P, Foti, M & Hadengue, A 2007, 'Microarray analyses and molecular profiling of steatosis induction in immortalized human hepatocytes', *Laboratory Investigation; a Journal of Technical Methods and Pathology*, vol. 87, no. 8, pp. 792–806, <https://pubmed.ncbi.nlm.nih.gov/17558421/>.

REFERENCES

de Graaf, IAM, Olinga, P, de Jager, MH, Merema, MT, de Kanter, R, van de Kerkhof, EG & Groothuis, GMM 2010, 'Preparation and incubation of precision-cut liver and intestinal slices for application in drug metabolism and toxicity studies', *Nature Protocols*, vol. 5, no. 9, pp. 1540–1551, <http://www.nature.com/articles/nprot.2010.111>.

Dekkers, JF, Alieva, M, Wellens, LM, Ariese, HCR, Jamieson, PR, Vonk, AM, Amatngalim, GD, Hu, H, Oost, KC, Snippert, HJG, Beekman, JM, Wehrens, EJ, Visvader, JE, Clevers, H & Rios, AC 2019, 'High-resolution 3D imaging of fixed and cleared organoids', *Nature Protocols*, vol. 14, no. 6, pp. 1756–1771, <https://www.nature.com/articles/s41596-019-0160-8>.

Dekkers, JF, Wiegerinck, CL, de Jonge, HR, Bronsveld, I, Janssens, HM, de Winter-de Groot, KM, Brandsma, AM, de Jong, NWM, Bijvelds, MJC, Scholte, BJ, Nieuwenhuis, EES, van den Brink, S, Clevers, H, van der Ent, CK, Middendorp, S & Beekman, JM 2013, 'A functional CFTR assay using primary cystic fibrosis intestinal organoids', *Nature Medicine*, vol. 19, no. 7, pp. 939–945.

DiMasi, JA, Reichert, JM, Feldman, L & Malins, A 2013, 'Clinical Approval Success Rates for Investigational Cancer Drugs', *Clinical Pharmacology & Therapeutics*, vol. 94, no. 3, pp. 329–335.

Dorrell, C, Erker, L, Lanxon-Cookson, KM, Abraham, SL, Victoroff, T, Ro, S, Canaday, PS, Streeter, PR & Grompe, M 2008, 'Surface markers for the murine oval cell response', *Hepatology (Baltimore, Md.)*, vol. 48, no. 4, pp. 1282–1291, <https://pubmed.ncbi.nlm.nih.gov/18726953/>.

Dorrell, C, Erker, L, Schug, J, Kopp, JL, Canaday, PS, Fox, AJ, Smirnova, O, Duncan, AW, Finegold, MJ, Sander, M, Kaestner, KH & Grompe, M 2011, 'Prospective isolation of a

REFERENCES

bipotential clonogenic liver progenitor cell in adult mice', *Genes & Development*, vol. 25, no. 11, pp. 1193–1203, <https://pubmed.ncbi.nlm.nih.gov/21632826/>.

Driehuis, E, Kretzschmar, K & Clevers, H 2020, 'Establishment of patient-derived cancer organoids for drug-screening applications', Nature Protocols, vol. 15, no. 10, pp. 3380–3409.

Dunn, JC, Tompkins, RG & Yarmush, ML 1992, 'Hepatocytes in collagen sandwich: evidence for transcriptional and translational regulation.', *The Journal of Cell Biology*, vol. 116, no. 4, pp. 1043–1053.

Dunn, JCY, Tompkins, RG & Yarmush, ML 1991, 'Long-term in vitro function of adult hepatocytes in a collagen sandwich configuration', *Biotechnology Progress*, vol. 7, no. 3, pp. 237–245.

El-Serag, HB 2012, 'Epidemiology of Viral Hepatitis and Hepatocellular Carcinoma', *Gastroenterology*, vol. 142, no. 6, pp. 1264-1273.e1.

El-Serag, HB & Rudolph, KL 2007, 'Hepatocellular carcinoma: epidemiology and molecular carcinogenesis', *Gastroenterology*, vol. 132, no. 7, pp. 2557–2576, <https://www.ncbi.nlm.nih.gov/pubmed/17570226>.

Elkin, M, Ariel, I, Miao, HQ, Nagler, A, Pines, M, de-Groot, N, Hochberg, A & Vlodavsky, I 1999a, 'Inhibition of bladder carcinoma angiogenesis, stromal support, and tumor growth by halofuginone', *Cancer Research*, vol. 59, no. 16, pp. 4111–4118, <https://pubmed.ncbi.nlm.nih.gov/10463616/>.

Elkin, M, Miao, HQ, Nagler, A, Aingorn, E, Reich, R, Hemo, I, Dou, HL, Pines, M & Vlodavsky, I 2000, 'Halofuginone: a potent inhibitor of critical steps in angiogenesis progression', *FASEB journal: official publication of the Federation of American Societies for*

REFERENCES

Experimental Biology, vol. 14, no. 15, pp. 2477–2485, <https://pubmed.ncbi.nlm.nih.gov/11099465/>.

Elkin, M, Reich, R, Nagler, A, Aingorn, E, Pines, M, de-Groot, N, Hochberg, A & Vlodavsky, I 1999b, 'Inhibition of matrix metalloproteinase-2 expression and bladder carcinoma metastasis by halofuginone', *Clinical Cancer Research: An Official Journal of the American Association for Cancer Research*, vol. 5, no. 8, pp. 1982–1988, <https://pubmed.ncbi.nlm.nih.gov/10473075/>.

Eng, FJ & Friedman, SL 2000, 'Fibrogenesis I. New insights into hepatic stellate cell activation: the simple becomes complex', *American Journal of Physiology. Gastrointestinal and Liver Physiology*, vol. 279, no. 1, pp. G7–G11, <https://pubmed.ncbi.nlm.nih.gov/10898741/>.

Esch, EW, Bahinski, A & Huh, D 2015, 'Organs-on-chips at the frontiers of drug discovery', *Nature Reviews Drug Discovery*, vol. 14, no. 4, pp. 248–260.

Fabregat, I, Moreno-Càceres, J, Sánchez, A, Dooley, S, Dewidar, B, Giannelli, G & ten Dijke, P 2016, 'TGF-β signalling and liver disease', *The FEBS Journal*, vol. 283, no. 12, pp. 2219–2232.

Fan, D & Kassiri, Z 2020, 'Biology of Tissue Inhibitor of Metalloproteinase 3 (TIMP3), and Its Therapeutic Implications in Cardiovascular Pathology', *Frontiers in Physiology*, vol. 11, no. 661, <https://pubmed.ncbi.nlm.nih.gov/32612540/>.

Fasel, JHD 2008, 'Portal Venous Territories Within the Human Liver: An Anatomical Reappraisal', *The Anatomical Record: Advances in Integrative Anatomy and Evolutionary Biology*, vol. 291, no. 6, pp. 636–642.

REFERENCES

Fasel, JHD, Majno, PE & Peitgen, H-O 2010, 'Liver segments: an anatomical rationale for explaining inconsistencies with Couinaud's eight-segment concept', *Surgical and radiologic anatomy: SRA*, vol. 32, no. 8, pp. 761–765, <https://pubmed.ncbi.nlm.nih.gov/20111966/>.

Fatehullah, A, Tan, SH & Barker, N 2016, 'Organoids as an in vitro model of human development and disease', *Nature Cell Biology*, vol. 18, no. 3, pp. 246–254, <https://www.nature.com/articles/ncb3312?platform=hootsuitehttps%3A%2F%2Fwww.nature.com%2Farticles%2Fs41586-019-0889-9%3Fplatform%3Dhootsuite>.

Fattovich, G, Stroffolini, T, Zagni, I & Donato, F 2004, 'Hepatocellular carcinoma in cirrhosis: Incidence and risk factors', *Gastroenterology*, vol. 127, no. 5, pp. S35–S50.

Ferlay, J, Soerjomataram, I, Dikshit, R, Eser, S, Mathers, C, Rebelo, M & Parkin, D 2015, 'Cancer Incidence and Mortality Worldwide: Sources, Methods and Major Patterns in GLOBOCAN 2012', *International journal of cancer*, vol. 236, no. 5, pp. E359-386.

Fiorotto, R, Raizner, A, Morell, CM, Torsello, B, Scirpo, R, Fabris, L, Spirli, C & Strazzabosco, M 2013, 'Notch signaling regulates tubular morphogenesis during repair from biliary damage in mice', *Journal of Hepatology*, vol. 59, no. 1, pp. 124–130, <https://pubmed.ncbi.nlm.nih.gov/23500150/>.

Fogel, AL & Kvedar, JC 2018, 'Artificial intelligence powers digital medicine', *npj Digital Medicine*, vol. 1, no. 1.

Forner, A, Reig, M & Bruix, J 2018, 'Hepatocellular carcinoma', *The Lancet*, vol. 391, no. 10127, pp. 1301–1314.

REFERENCES

Freeman, AE & Hoffman, RM 1986, 'In vivo-like growth of human tumors in vitro.', *Proceedings of the National Academy of Sciences of the United States of America*, vol. 83, no. 8, pp. 2694–2698, <https://www.ncbi.nlm.nih.gov/pmc/articles/PMC323366/>.

Friedman, SL 1993, 'The Cellular Basis of Hepatic Fibrosis -- Mechanisms and Treatment Strategies', *New England Journal of Medicine*, vol. 328, no. 25, pp. 1828–1835.

Friedrich, J, Seidel, C, Ebner, R & Kunz-Schughart, LA 2009, 'Spheroid-based drug screen: considerations and practical approach', *Nature Protocols*, vol. 4, no. 3, pp. 309–324.

Gaudio, E, Carpino, G, Cardinale, V, Franchitto, A, Onori, P & Alvaro, D 2009, 'New insights into liver stem cells', *Digestive and Liver Disease*, vol. 41, no. 7, pp. 455–462.

Geerts, A, Geuze, HJ, Slot, JW, Voss, B, Schuppan, D, Schellinck, P & Wisse, E 1986, 'Immunogold localization of procollagen III, fibronectin and heparan sulfate proteoglycan on ultrathin frozen sections of the normal rat liver', *Histochemistry*, vol. 84, no. 4-6, pp. 355–362, <https://pubmed.ncbi.nlm.nih.gov/2941396/>.

Ginsburg, GS & Phillips, KA 2018, 'Precision Medicine: From Science To Value', *Health Affairs*, vol. 37, no. 5, pp. 694–701.

Gnainsky, Y, Spira, G, Paizi, M, Bruck, R, Nagler, A, Abu-Amara, SN, Geiger, B, Genina, O, Monsonego-Ornan, E & Pines, M 2004, 'Halofuginone, an inhibitor of collagen synthesis by rat stellate cells, stimulates insulin-like growth factor binding protein-1 synthesis by hepatocytes', *Journal of Hepatology*, vol. 40, no. 2, pp. 269–277, <https://pubmed.ncbi.nlm.nih.gov/14739098/>.

Godoy, P, Hewitt, NJ, Albrecht, U, Andersen, ME, Ansari, N, Bhattacharya, S, Bode, JG, Bolleyn, J, Borner, C, Böttger, J, Braeuning, A, Budinsky, RA, Burkhardt, B, Cameron, NR,

REFERENCES

Camussi, G, Cho, C-S, Choi, Y-J, Craig Rowlands, J, Dahmen, U & Damm, G 2013, 'Recent advances in 2D and 3D in vitro systems using primary hepatocytes, alternative hepatocyte sources and non-parenchymal liver cells and their use in investigating mechanisms of hepatotoxicity, cell signaling and ADME', *Archives of Toxicology*, vol. 87, no. 8, pp. 1315–1530.

Gomez-Lechon, M, Donato, M, Castell, J & Jover, R 2003, 'Human Hepatocytes as a Tool for Studying Toxicity and Drug Metabolism', *Current Drug Metabolism*, vol. 4, no. 4, pp. 292–312.

Gomez-Lechon, M, Donato, M, Lahoz, A & Castell, J 2008, 'Cell Lines: A Tool for In Vitro Drug Metabolism Studies', *Current Drug Metabolism*, vol. 9, no. 1, pp. 1–11.

Gómez-Lechón, MJ, Castell, JV & Donato, MT 2007, 'Hepatocytes--the choice to investigate drug metabolism and toxicity in man: in vitro variability as a reflection of in vivo', *Chemico-Biological Interactions*, vol. 168, no. 1, pp. 30–50, <https://pubmed.ncbi.nlm.nih.gov/17134688/>.

Granot, I, Bartov, I, Plavnik, I, Wax, E, Hurwitz, S & Pines, M 1991, 'Increased Skin Tearing in Broilers and Reduced Collagen Synthesis in Skin In Vivo and In Vitro in Response to the Coccidiostat Halofuginone1', *Poultry Science*, vol. 70, no. 7, pp. 1559–1563, <https://www.sciencedirect.com/science/article/pii/S0032579119332663#>.

Granot, I, Halevy, O, Hurwitz, S & Pines, M 1993, 'Halofuginone: an inhibitor of collagen type I synthesis', *Biochimica Et Biophysica Acta*, vol. 1156, no. 2, pp. 107–112, <https://pubmed.ncbi.nlm.nih.gov/8427869/>.

REFERENCES

Gressner, AM 1992, 'Hepatic fibrogenesis: the puzzle of interacting cells, fibrogenic cytokines, regulatory loops, and extracellular matrix molecules', *Zeitschrift Fur Gastroenterologie*, vol. 30 Suppl 1, pp. 5–16, <https://pubmed.ncbi.nlm.nih.gov/1449018/>.

Gripon, P, Rumin, S, Urban, S, Le Seyec, J, Glaise, D, Cannie, I, Guyomard, C, Lucas, J, Trepo, C & Guguen-Guillouzo, C 2002, 'Infection of a human hepatoma cell line by hepatitis B virus', *Proceedings of the National Academy of Sciences of the United States of America*, vol. 99, no. 24, pp. 15655–15660, <https://pubmed.ncbi.nlm.nih.gov/12432097/>.

Grix, T, Ruppelt, A, Thomas, A, Amler, A-K, Noichl, B, Lauster, R & Kloke, L 2018, 'Bioprinting Perfusion-Enabled Liver Equivalents for Advanced Organ-on-a-Chip Applications', *Genes*, vol. 9, no. 4, p. 176.

Groothuis, GM, Hulstaert, CE, Kalicharan, D & Hardonk, MJ 1981, 'Plasma membrane specialization and intracellular polarity of freshly isolated rat hepatocytes', *European Journal of Cell Biology*, vol. 26, no. 1, pp. 43–51, <https://pubmed.ncbi.nlm.nih.gov/6276181/>.

Guo J, Loke J, Zheng F, Hong F, Yea S, Fukata M, Tarocchi M, Abar OT, Huang H, Sninsky JJ, Friedman SL 2009. Functional linkage of cirrhosis-predictive single nucleotide polymorphisms of Toll-like receptor 4 to hepatic stellate cell responses, *Hepatology*; 49(3): 960-8.

Halevy, O, Nagler, A, Levi-Schaffer, F, Genina, O & Pines, M 1996, 'Inhibition of collagen type I synthesis by skin fibroblasts of graft versus host disease and scleroderma patients: effect of halofuginone', *Biochemical Pharmacology*, vol. 52, no. 7, pp. 1057–1063, <https://pubmed.ncbi.nlm.nih.gov/8831725/>.

Hartung, T & Daston, G 2009, 'Are In Vitro Tests Suitable for Regulatory Use?', *Toxicological Sciences*, vol. 111, no. 2, pp. 233–237.

REFERENCES

Heim, D, Cornils, K, Schulze, K, Fehse, B, Lohse, AW, Brümmendorf, TH & Wege, H 2015, 'Retroviral insertional mutagenesis in telomerase-immortalized hepatocytes identifies RIPK4 as novel tumor suppressor in human hepatocarcinogenesis', *Oncogene*, vol. 34, no. 3, pp. 364–372, <https://pubmed.ncbi.nlm.nih.gov/24413083/>.

Holt, DJ, Chamberlain, LM & Grainger, DW 2010, 'Cell-cell signaling in co-cultures of macrophages and fibroblasts', *Biomaterials*, vol. 31, no. 36, pp. 9382–9394, <https://pubmed.ncbi.nlm.nih.gov/20932568/>.

Homan, KA, Gupta, N, Kroll, KT, Kolesky, DB, Skylar-Scott, M, Miyoshi, T, Mau, D, Valerius, MT, Ferrante, T, Bonventre, JV, Lewis, JA & Morizane, R 2019, 'Flow-enhanced vascularization and maturation of kidney organoids in vitro', *Nature Methods*, vol. 16, no. 3, pp. 255–262, <https://www.nature.com/articles/s41592-019-0325-y>.

Hu, M, Kurobe, M, Jeong, YJ, Fuerer, C, Ghole, S, Nusse, R & Sylvester, KG 2007, 'Wnt/beta-catenin signaling in murine hepatic transit amplifying progenitor cells', *Gastroenterology*, vol. 133, no. 5, pp. 1579–1591, <https://pubmed.ncbi.nlm.nih.gov/17983805/>.

Huang, LE, Gu, J, Schau, M & Bunn, HF 1998, 'Regulation of hypoxia-inducible factor 1 is mediated by an O2-dependent degradation domain via the ubiquitin-proteasome pathway', *Proceedings of the National Academy of Sciences*, vol. 95, no. 14, pp. 7987–7992.

Huch, M, Dorrell, C, Boj, SF, van Es, JH, Li, VSW, van de Wetering, M, Sato, T, Hamer, K, Sasaki, N, Finegold, MJ, Haft, A, Vries, RG, Grompe, M & Clevers, H 2013, 'In vitro expansion of single Lgr5+ liver stem cells induced by Wnt-driven regeneration', *Nature*, vol. 494, no. 7436, pp. 247–250.

Huch, M, Gehart, H, van Boxtel, R, Hamer, K, Blokzijl, F, Verstegen, Monique MA, Ellis, E, van Wenum, M, Fuchs, Sabine A, de Ligt, J, van de Wetering, M, Sasaki, N, Boers, Susanne J,

REFERENCES

Kemperman, H, de Jonge, J, Ijzermans, Jan NM, Nieuwenhuis, Edward ES, Hoekstra, R, Strom, S & Vries, Robert RG 2015, 'Long-Term Culture of Genome-Stable Bipotent Stem Cells from Adult Human Liver', *Cell*, vol. 160, no. 1-2, pp. 299–312.

Huch, M, Knoblich, JA, Lutolf, MP & Martinez-Arias, A 2017, 'The hope and the hype of organoid research', *Development*, vol. 144, no. 6, pp. 938–941.

Huo S, Yu H, Li C, Zhang J, Liu T. Effect of halofuginone on the inhibition of proliferation and invasion of hepatocellular carcinoma HepG2 cell line. Int J Clin Exp Pathol. 2015;8(12):15863-15870. Published 2015 Dec 1.

Hwang, B, Lee, JH & Bang, D 2018, 'Single-cell RNA sequencing technologies and bioinformatics pipelines', Experimental & Molecular Medicine, vol. 50, no. 8.

Ikeda, M, Kato, N, Mizutani, T, Sugiyama, K, Tanaka, K & Shimotohno, K 1997, 'Analysis of the cell tropism of HCV by using in vitro HCV-infected human lymphocytes and hepatocytes', *Journal of Hepatology*, vol. 27, no. 3, pp. 445–454, <https://pubmed.ncbi.nlm.nih.gov/9314120/>.

Iredale, J & Guha, I 2007, *Textbook of Hepatology: from Basic Science to Clinical Practice*, 3rd Edition, Blackwell Publishing Ltd, pp. 583–603.

Ishikawa, T, Factor, VM, Marquardt, JU, Raggi, C, Seo, D, Kitade, M, Conner, EA & Thorgeirsson, SS 2012, 'Hepatocyte growth factor/c-metsignaling is required for stem-cell-mediated liver regeneration in mice', *Hepatology*, vol. 55, no. 4, pp. 1215–1226, <http://onlinelibrary.wiley.com/doi/10.1002/hep.24796/abstract>.

REFERENCES

Itoh, T, Kamiya, Y, Okabe, M, Tanaka, M & Miyajima, A 2009, 'Inducible expression of Wnt genes during adult hepatic stem/progenitor cell response', *FEBS letters*, vol. 583, no. 4, pp. 777–781, <https://pubmed.ncbi.nlm.nih.gov/19174158/>.

Jung, G, Kim, E-J, Cicvaric, A, Sase, S, Gröger, M, Höger, H, Sialana, FJ, Berger, J, Monje, FJ & Lubec, G 2015, 'Drebrin depletion alters neurotransmitter receptor levels in protein complexes, dendritic spine morphogenesis and memory-related synaptic plasticity in the mouse hippocampus', *Journal of Neurochemistry*, vol. 134, no. 2, pp. 327–339, <https://pubmed.ncbi.nlm.nih.gov/25865831/>.

Jung, H-R, Kang, HM, Ryu, J-W, Kim, D-S, Noh, KH, Kim, E-S, Lee, H-J, Chung, K-S, Cho, H-S, Kim, N-S, Im, D-S, Lim, JH & Jung, C-R 2017, 'Cell Spheroids with Enhanced Aggressiveness to Mimic Human Liver Cancer In Vitro and In Vivo', *Scientific Reports*, vol. 7, <https://www.ncbi.nlm.nih.gov/pmc/articles/PMC5585316/>.

Jungermann, K & Kietzmann, T 2000, 'Oxygen: Modulator of metabolic zonation and disease of the liver', *Hepatology*, vol. 31, no. 2, pp. 255–260.

Kamiya, A, Kakinuma, S, Yamazaki, Y & Nakauchi, H 2009, 'Enrichment and clonal culture of progenitor cells during mouse postnatal liver development in mice', *Gastroenterology*, vol. 137, no. 3, pp. 1114–1126, 1126.e1-14, <https://pubmed.ncbi.nlm.nih.gov/19524574/>.

Karakoyun, B 2017, 'The Promising Role of Anti-Fibrotic Agent Halofuginone in Liver Fibrosis/Cirrhosis', *Liver Cirrhosis - Update and Current Challenges*, <https://www.intechopen.com/books/liver-cirrhosis-update-and-current-challenges/the-promising-role-of-anti-fibrotic-agent-halofuginone-in-liver-fibrosis-cirrhosis>.

Kasendra, M, Tovaglieri, A, Sontheimer-Phelps, A, Jalili-Firoozinezhad, S, Bein, A, Chalkiadaki, A, Scholl, W, Zhang, C, Rickner, H, Richmond, CA, Li, H, Breault, DT & Ingber,

REFERENCES

DE 2018, 'Development of a primary human Small Intestine-on-a-Chip using biopsy-derived organoids', *Scientific Reports*, vol. 8, no. 1.

Kato, N, Ikeda, M, Mizutani, T, Sugiyama, K, Noguchi, M, Hirohashi, S & Shimotohno, K 1996, 'Replication of hepatitis C virus in cultured non-neoplastic human hepatocytes', *Japanese Journal of Cancer Research: Gann*, vol. 87, no. 8, pp. 787–792, <https://pubmed.ncbi.nlm.nih.gov/8797883/>.

Kegel, V, Deharde, D, Pfeiffer, E, Zeilinger, K, Seehofer, D & Damm, G 2016, 'Protocol for Isolation of Primary Human Hepatocytes and Corresponding Major Populations of Non-parenchymal Liver Cells', *Journal of visualized experiments : JoVE*, vol. 109, MyJove Corporation, no. e53069, <https://www.ncbi.nlm.nih.gov/pubmed/27077489>.

Keller, TL, Zocco, D, Sundrud, MS, Hendrick, M, Edenius, M, Yum, J, Kim, Y-J, Lee, H-K, Cortese, JF, Wirth, DF, Dignam, JD, Rao, A, Yeo, C-Y, Mazitschek, R & Whitman, M 2012, 'Halofuginone and other febrifugine derivatives inhibit prolyl-tRNA synthetase', *Nature Chemical Biology*, vol. 8, no. 3, pp. 311–317, <https://pubmed.ncbi.nlm.nih.gov/22327401/>.

Kern, A, Bader, A, Pichlmayr, R & Sewing, KF 1997, 'Drug metabolism in hepatocyte sandwich cultures of rats and humans', *Biochemical Pharmacology*, vol. 54, no. 7, pp. 761–772, <https://pubmed.ncbi.nlm.nih.gov/9353130/>.

Kidambi, S, Yarmush, RS, Novik, E, Chao, P, Yarmush, ML & Nahmias, Y 2009, 'Oxygen-mediated enhancement of primary hepatocyte metabolism, functional polarization, gene expression, and drug clearance', *Proceedings of the National Academy of Sciences of the United States of America*, vol. 106, no. 37, pp. 15714–15719, <https://www.ncbi.nlm.nih.gov/pmc/articles/PMC2747185/>.

REFERENCES

Kietzmann, T 2017, 'Metabolic zonation of the liver: The oxygen gradient revisited', *Redox Biology*, vol. 11, pp. 622–630.

Killingsworth, MC & Bobryshev, YV 2016, 'Correlative Light- and Electron Microscopy Using Quantum Dot Nanoparticles', *Journal of Visualized Experiments*, no. 114.

Killingsworth, MC, Lai, K, Wu, X, Yong, JLC & Lee, CS 2012, 'Quantum Dot Immunocytochemical Localization of Somatostatin in Somatostatinoma by Widefield Epifluorescence, Super-resolution Light, and Immunoelectron Microscopy', *Journal of Histochemistry & Cytochemistry*, vol. 60, no. 11, pp. 832–843.

Kim, J, Koo, B-K & Knoblich, JA 2020, 'Human organoids: model systems for human biology and medicine', *Nature Reviews Molecular Cell Biology*, vol. 21, no. 10, pp. 571–584.

Kitade, M, Factor, VM, Andersen, JB, Tomokuni, A, Kaji, K, Akita, H, Holczbauer, A, Seo, D, Marquardt, JU, Conner, EA, Lee, S-B, Lee, Y-H & Thorgeirsson, SS 2013, 'Specific fate decisions in adult hepatic progenitor cells driven by MET and EGFR signaling', *Genes & Development*, vol. 27, no. 15, pp. 1706–1717, <https://pubmed.ncbi.nlm.nih.gov/23913923/>.

Kordes, C & Häussinger, D 2013, 'Hepatic stem cell niches', *The Journal of Clinical Investigation*, vol. 123, no. 5, pp. 1874–1880, <https://pubmed.ncbi.nlm.nih.gov/23635785/>.

Kramer, N, Pratscher, B, Meneses, AMC, Tschulenk, W, Walter, I, Swoboda, A, Kruitwagen, HS, Schneeberger, K, Penning, LC, Spee, B, Kieslinger, M, Brandt, S & Burgener, IA 2020, 'Generation of Differentiating and Long-Living Intestinal Organoids Reflecting the Cellular Diversity of Canine Intestine', *Cells*, vol. 9, no. 4, <https://www.ncbi.nlm.nih.gov/pmc/articles/PMC7226743/>.

REFERENCES

Kuwajima, M, Mendenhall, JM, Lindsey, LF & Harris, KM 2013, 'Automated Transmission-Mode Scanning Electron Microscopy (tSEM) for Large Volume Analysis at Nanoscale Resolution', in MA Fox (ed.), *PLoS ONE*, vol. 8, no. 3, p. e59573.

Lamers, MM, Beumer, J, Vaart, J van der, Knoops, K, Puschhof, J, Breugem, TI, Ravelli, RBG, Schayck, JP van, Mykytyn, AZ, Duimel, HQ, Donselaar, E van, Riesebosch, S, Kuijpers, HJH, Schippers, D, Wetering, WJ van de, Graaf, M de, Koopmans, M, Cuppen, E, Peters, PJ & Haagmans, BL 2020, 'SARS-CoV-2 productively infects human gut enterocytes', *Science*, vol. 369, no. 6499, pp. 50–54, <https://science.sciencemag.org/content/early/2020/04/30/science.abc1669>.

Lan, T, Kisseleva, T & Brenner, DA 2015, 'Deficiency of NOX1 or NOX4 Prevents Liver Inflammation and Fibrosis in Mice through Inhibition of Hepatic Stellate Cell Activation', in MA Avila (ed.), *PLOS ONE*, vol. 10, no. 7, p. e0129743.

Lancaster, MA & Knoblich, JA 2014, 'Organogenesis in a dish: Modeling development and disease using organoid technologies', *Science*, vol. 345, no. 6194, pp. 1247125–1247125.

LeCluyse, EL, Audus, KL & Hochman, JH 1994, 'Formation of extensive canalicular networks by rat hepatocytes cultured in collagen-sandwich configuration', *The American Journal of Physiology*, vol. 266, no. 6 Pt 1, pp. C1764-1774, <https://pubmed.ncbi.nlm.nih.gov/8023906/>.

Leduc, EH & Wilson, JW 1958, 'Injury to liver cells in carbon tetrachloride poisoning; histochemical changes induced by carbon tetrachloride in mouse liver protected by sulfaguanidine', *A.M.A. Archives of Pathology*, vol. 65, no. 2, pp. 147–157, <https://pubmed.ncbi.nlm.nih.gov/13497406/>.

REFERENCES

Lee, JS, Shin, J, Park, H-M, Kim, Y-G, Kim, B-G, Oh, J-W & Cho, S-W 2013, 'Liver Extracellular Matrix Providing Dual Functions of Two-Dimensional Substrate Coating and Three-Dimensional Injectable Hydrogel Platform for Liver Tissue Engineering', *Biomacromolecules*, vol. 15, no. 1, pp. 206–218.

Lee, WM 2003, 'Drug-Induced Hepatotoxicity', *New England Journal of Medicine*, vol. 349, no. 5, pp. 474–485.

Lee, YJ & Streuli, CH 1999, 'Extracellular matrix selectively modulates the response of mammary epithelial cells to different soluble signaling ligands', *The Journal of Biological Chemistry*, vol. 274, no. 32, pp. 22401–22408, <https://pubmed.ncbi.nlm.nih.gov/10428812/>.

Leiba, M, Jakubikova, J, Klippel, S, Mitsiades, CS, Hideshima, T, Tai, Y-T, Leiba, A, Pines, M, Richardson, PG, Nagler, A & Anderson, KC 2012, 'Halofuginone inhibits multiple myeloma growth in vitro and in vivo and enhances cytotoxicity of conventional and novel agents', *British Journal of Haematology*, vol. 157, no. 6, pp. 718–731, <https://pubmed.ncbi.nlm.nih.gov/22533681/>.

Lempp, FA, Schlund, F, Rieble, L, Nussbaum, L, Link, C, Zhang, Z, Ni, Y & Urban, S 2019, 'Recapitulation of HDV infection in a fully permissive hepatoma cell line allows efficient drug evaluation', *Nature Communications*, vol. 10, no. 1, p. 2265, <https://pubmed.ncbi.nlm.nih.gov/31118422/>.

Lindquist, JN, Marzluff, WF & Stefanovic, B 2000, 'Fibrogenesis. III. Posttranscriptional regulation of type I collagen', *American Journal of Physiology. Gastrointestinal and Liver Physiology*, vol. 279, no. 3, pp. G471-476, <https://pubmed.ncbi.nlm.nih.gov/10960344/>.

REFERENCES

Liu, C, Qin, T, Huang, Y, Li, Y, Chen, G & Sun, C 2020, 'Drug screening model meets cancer organoid technology', *Translational Oncology*, vol. 13, no. 11, <https://www.ncbi.nlm.nih.gov/pmc/articles/PMC7451679/>.

Liu, X, Brouwer, KLR, Gan, LL, Brouwer, KR, Stieger, B, Meier, PJ, Audus, KL & LeCluyse, EL 1998, 'Partial maintenance of taurocholate uptake by adult rat hepatocytes cultured in a collagen sandwich configuration', *Pharmaceutical Research*, vol. 15, no. 10, pp. 1533–1539.

Llovet, JM, Zucman-Rossi, J, Pikarsky, E, Sangro, B, Schwartz, M, Sherman, M & Gores, G 2016, 'Hepatocellular carcinoma', *Nature Reviews Disease Primers*, vol. 2, no. 1.

Lu, F 1996, *Biotransformation of toxicants, in: Basic Toxicology: Fundamentals, Target Organs and Risk Assessment*, 3rd Edition, Taylor and Francis, Washington, DC, pp. 27–39.

Luedde, T, Kaplowitz, N & Schwabe, RF 2014, 'Cell Death and Cell Death Responses in Liver Disease: Mechanisms and Clinical Relevance', *Gastroenterology*, vol. 147, no. 4, pp. 765-783.e4, <https://www.ncbi.nlm.nih.gov/pmc/articles/PMC4531834/>.

Macsween, RNM, Burt, AD, Portmann, B & Ferrell, LD 2012, *MacSween's pathology of the liver*, Churchill Livingstone/Elsevier, Edinburgh ; New York.

Malhi, H & Gores, GJ 2008, 'Cellular and Molecular Mechanisms of Liver Injury', *Gastroenterology*, vol. 134, no. 6, pp. 1641–1654.

Marquardt, JU, Andersen, JB & Thorgeirsson, SS 2015, 'Functional and genetic deconstruction of the cellular origin in liver cancer', *Nature Reviews. Cancer*, vol. 15, no. 11, pp. 653–667, <https://pubmed.ncbi.nlm.nih.gov/26493646/>.

REFERENCES

Marrero, JA, Fontana, RJ, Fu, S, Conjeevaram, HS, Su, GL & Lok, AS 2005, 'Alcohol, tobacco and obesity are synergistic risk factors for hepatocellular carcinoma', *Journal of Hepatology*, vol. 42, no. 2, pp. 218–224, <https://pubmed.ncbi.nlm.nih.gov/15664247/>.

Matsuo, A, Yoshida, T, Yasukawa, T, Miki, R, Kume, K & Kume, S 2011, 'Epiplakin1 is expressed in the cholangiocyte lineage cells in normal liver and adult progenitor cells in injured liver', *Gene Expr. Patterns*, vol. 11, pp. 255–262, <https://europepmc.org/article/med/21216305>.

Mean, B 2019, 'A Technique for Scalable Organoid Culture'. <https://www.youtube.com/watch?v=dOzx8GfDkk8&t=894s&ab_channel=formulatrix>

Michalopoulos, G, Cianciulli, HD, Novotny, AR, Kligerman, AD, Strom, SC & Jirtle, RL 1982, 'Liver regeneration studies with rat hepatocytes in primary culture', *Cancer Research*, vol. 42, no. 11, pp. 4673–4682, <https://pubmed.ncbi.nlm.nih.gov/6215120/>.

Milani, S, Herbst, H, Schuppan, D, Hahn, EG & Stein, H 1989, 'In situ hybridization for procollagen types I, III and IV mRNA in normal and fibrotic rat liver: Evidence for predominant expression in nonparenchymal liver cells', *Hepatology*, vol. 10, no. 1, pp. 84–92.

Milyavsky, M, Shats, I, Erez, N, Tang, X, Senderovich, S, Meerson, A, Tabach, Y, Goldfinger, N, Ginsberg, D, Harris, CC & Rotter, V 2003, 'Prolonged culture of telomerase-immortalized human fibroblasts leads to a premalignant phenotype', *Cancer Research*, vol. 63, no. 21, pp. 7147–7157, <https://pubmed.ncbi.nlm.nih.gov/14612508/>.

Mitra, A, Mishra, L & Li, S 2013, 'Technologies for deriving primary tumor cells for use in personalized cancer therapy', *Trends in biotechnology*, vol. 31, no. 6, pp. 347–354, <https://www.ncbi.nlm.nih.gov/pmc/articles/PMC3665643/>.

REFERENCES

Miyajima, A, Tanaka, M & Itoh, T 2014, 'Stem/Progenitor Cells in Liver Development, Homeostasis, Regeneration, and Reprogramming', *Cell Stem Cell*, vol. 14, no. 5, pp. 561–574.

Miyao, D 2018, 'Automated Chemical Storage and High-throughput Compound Synthesis using the Hamilton Verso and MICROLAB VANTAGE Liquid Handling System'. < https://www.youtube.com/watch?v=MUv60VUY6i8&t=7s&ab_channel=HamiltonRobotics>

Moffat, JG, Vincent, F, Lee, JA, Eder, J & Prunotto, M 2017, 'Opportunities and challenges in phenotypic drug discovery: an industry perspective', *Nature Reviews Drug Discovery*, vol. 16, no. 8, pp. 531–543.

Monteil, V, Kwon, H & Prado, P 2020, 'Inhibition of SARS-CoV-2 Infections in Engineered Human Tissues Using Clinical-Grade Soluble Human ACE2.', *Cell*, vol. 181, no. 4, pp. 905–913.

Moon, J-O, Welch, TP, Gonzalez, FJ & Copple, BL 2009, 'Reduced liver fibrosis in hypoxia-inducible factor-1alpha-deficient mice', *American Journal of Physiology. Gastrointestinal and Liver Physiology*, vol. 296, no. 3, pp. G582-592, <https://pubmed.ncbi.nlm.nih.gov/19136383/>.

Morgan, RL, Baack, B, Smith, BD, Yartel, A, Pitasi, M & Falck-Ytter, Y 2013, 'Eradication of hepatitis C virus infection and the development of hepatocellular carcinoma: a meta-analysis of observational studies', *Annals of Internal Medicine*, vol. 158, no. 5 Pt 1, pp. 329–337, <https://pubmed.ncbi.nlm.nih.gov/23460056/>.

Morgan, TR, Mandayam, S & Jamal, MM 2004, 'Alcohol and hepatocellular carcinoma', *Gastroenterology*, vol. 127, no. 5, pp. S87–S96.

REFERENCES

Nagler, A, Miao, HQ, Aingorn, H, Pines, M, Genina, O & Vlodavsky, I 1997, 'Inhibition of collagen synthesis, smooth muscle cell proliferation, and injury-induced intimal hyperplasia by halofuginone', *Arteriosclerosis, Thrombosis, and Vascular Biology*, vol. 17, no. 1, pp. 194–202, <https://pubmed.ncbi.nlm.nih.gov/9012656/>.

Nakatsukasa, H, Nagy, P, Evarts, RP, Hsia, CC, Marsden, E & Thorgeirsson, SS 1990, 'Cellular distribution of transforming growth factor-beta 1 and procollagen types I, III, and IV transcripts in carbon tetrachloride-induced rat liver fibrosis', *The Journal of Clinical Investigation*, vol. 85, no. 6, pp. 1833–1843, <https://pubmed.ncbi.nlm.nih.gov/1693377/>.

Nantasanti, S, de Bruin, A, Rothuizen, J, Penning, LC & Schotanus, BA 2016, 'Concise Review: Organoids Are a Powerful Tool for the Study of Liver Disease and Personalized Treatment Design in Humans and Animals', *STEM CELLS Translational Medicine*, vol. 5, no. 3, pp. 325–330.

Nath, S & Devi, GR 2016, 'Three-dimensional culture systems in cancer research: Focus on tumor spheroid model', *Pharmacology & Therapeutics*, vol. 163, pp. 94–108.

Nawy, T 2013, 'Single-cell sequencing', *Nature Methods*, vol. 11, no. 1, pp. 18–18.

Nelson, EF, Huang, CW, Ewel, JM, Chang, AA & Yuan, C 2012, 'Halofuginone down-regulates Smad3 expression and inhibits the TGFbeta-induced expression of fibrotic markers in human corneal fibroblasts', *Molecular Vision*, vol. 18, pp. 479–487, <https://pubmed.ncbi.nlm.nih.gov/22393274/>.

Novo, E & Parola, M 2008, 'Redox mechanisms in hepatic chronic wound healing and fibrogenesis', *Fibrogenesis & Tissue Repair*, vol. 1, no. 1, p. 5.

REFERENCES

Nuciforo, S, Fofana, I, Matter, MS, Blumer, T, Calabrese, D, Boldanova, T, Piscuoglio, S, Wieland, S, Ringnalda, F, Schwank, G, Terracciano, LM, Ng, CKY & Heim, MH 2018, 'Organoid Models of Human Liver Cancers Derived from Tumor Needle Biopsies', *Cell Reports*, vol. 24, no. 5, pp. 1363–1376, <https://pubmed.ncbi.nlm.nih.gov/30067989/>.

Ohara, N, Schaffner, T & Reichen, J 1993, 'Structure-function relationship in secondary biliary cirrhosis in the rat. Stereologic and hemodynamic characterization of a model', *Journal of Hepatology*, vol. 17, no. 2, pp. 155–162, <https://pubmed.ncbi.nlm.nih.gov/8445230/>.

Okabe, M, Tsukahara, Y, Tanaka, M, Suzuki, K, Saito, S, Kamiya, Y, Tsujimura, T, Nakamura, K & Miyajima, A 2009, 'Potential hepatic stem cells reside in EpCAM+ cells of normal and injured mouse liver', *Development (Cambridge, England)*, vol. 136, no. 11, pp. 1951–1960, <https://pubmed.ncbi.nlm.nih.gov/19429791/>.

Ooft, SN, Weeber, F, Dijkstra, KK, McLean, CM, Kaing, S, van Werkhoven, E, Schipper, L, Hoes, L, Vis, DJ, van de Haar, J, Prevoo, W, Snaebjornsson, P, van der Velden, D, Klein, M, Chalabi, M, Boot, H, van Leerdam, M, Bloemendal, HJ, Beerepoot, LV & Wessels, L 2019, 'Patient-derived organoids can predict response to chemotherapy in metastatic colorectal cancer patients', *Science Translational Medicine*, vol. 11, no. 513, p. eaay2574, <https://stm.sciencemag.org/content/11/513/eaay2574.full>.

Orloff, J 2009, *Handbook of Charged Particle Optics*, 2nd Edition, CRC Press, pp. 87–128.

Page, JL, Johnson, MC, Olsavsky, KM, Strom, SC, Zarbl, H & Omiecinski, CJ 2007, 'Gene Expression Profiling of Extracellular Matrix as an Effector of Human Hepatocyte Phenotype in Primary Cell Culture', *Toxicological Sciences*, vol. 97, no. 2, pp. 384–397.

REFERENCES

Pan, C, Kumar, C, Bohl, S, Klingmueller, U & Mann, M 2008, 'Comparative Proteomic Phenotyping of Cell Lines and Primary Cells to Assess Preservation of Cell Type-specific Functions', *Molecular & Cellular Proteomics*, vol. 8, no. 3, pp. 443–450.

Papatheodoridis, GV, Chan, HL-Y, Hansen, BE, Janssen, HLA & Lampertico, P 2015, 'Risk of hepatocellular carcinoma in chronic hepatitis B: assessment and modification with current antiviral therapy', *Journal of Hepatology*, vol. 62, no. 4, pp. 956–967, <https://pubmed.ncbi.nlm.nih.gov/25595883/>.

Pauli, C, Hopkins, BD, Prandi, D, Shaw, R, Fedrizzi, T, Sboner, A, Sailer, V, Augello, M, Puca, L, Rosati, R, McNary, TJ, Churakova, Y, Cheung, C, Triscott, J, Pisapia, D, Rao, R, Mosquera, JM, Robinson, B, Faltas, BM & Emerling, BE 2017, 'Personalized In Vitro and In Vivo Cancer Models to Guide Precision Medicine', *Cancer Discovery*, vol. 7, no. 5, pp. 462–477.

Pines, M 2014, 'Halofuginone for fibrosis, regeneration and cancer in the gastrointestinal tract', *World Journal of Gastroenterology*, vol. 20, no. 40, pp. 14778–14786, <https://pubmed.ncbi.nlm.nih.gov/25356039/>.

Pines, M & Spector, I 2015, 'Halofuginone — The Multifaceted Molecule', *Molecules*, vol. 20, no. 1, pp. 573–594, <https://www.ncbi.nlm.nih.gov/pmc/articles/PMC6272571/#:~:text=The%20mechanism%20by%20which%20halofuginone>.

Pinyol, R, Montal, R, Bassaganyas, L, Sia, D, Takayama, T, Chau, G-Y, Mazzaferro, V, Roayaie, S, Lee, HC, Kokudo, N, Zhang, Z, Torrecilla, S, Moeini, A, Rodriguez-Carunchio, L, Gane, E, Verslype, C, Croitoru, AE, Cillo, U, de la Mata, M & Lupo, L 2019, 'Molecular predictors of prevention of recurrence in HCC with sorafenib as adjuvant treatment and

REFERENCES

prognostic factors in the phase 3 STORM trial', *Gut*, vol. 68, no. 6, pp. 1065–1075, <https://pubmed.ncbi.nlm.nih.gov/30108162/>.

Poisson, J, Lemoinne, S, Boulanger, C, Durand, F, Moreau, R, Valla, D & Rautou, P 2017, 'Liver sinusoidal endothelial cells: Physiology and role in liver diseases', *Journal of Hepatology*, vol. 66, no. 1, pp. 212–227, <https://www.sciencedirect.com/science/article/pii/S0168827816303336>.

Ponsoda, X, Pareja, E, Gómez-Lechón, MJ, Fabra, R, Carrasco, E, Trullenque, R & Castell, JV 2001, 'Drug biotransformation by human hepatocytes. In vitro/in vivo metabolism by cells from the same donor', *Journal of Hepatology*, vol. 34, no. 1, pp. 19–25, <https://pubmed.ncbi.nlm.nih.gov/11211902/>.

Popov, Y, Patsenker, E, Bauer, M, Niedobitek, E, Schulze-Krebs, A & Schuppan, D 2006, 'Halofuginone induces matrix metalloproteinases in rat hepatic stellate cells via activation of p38 and NFkappaB', *The Journal of Biological Chemistry*, vol. 281, no. 22, pp. 15090–15098, <https://pubmed.ncbi.nlm.nih.gov/16489207/>.

Prozialeck, WC, Edwards, JR, Lamar, PC & Smith, CS 2006, 'Epithelial barrier characteristics and expression of cell adhesion molecules in proximal tubule-derived cell lines commonly used for in vitro toxicity studies', *Toxicology in vitro: an international journal published in association with BIBRA*, vol. 20, no. 6, pp. 942–953, <https://pubmed.ncbi.nlm.nih.gov/16387471/>.

Puche, JE, Lee, YA, Jiao, J, Aloman, C, Fiel, MI, Muñoz, U, Kraus, T, Lee, T, Yee, HF & Friedman, SL 2013, 'A novel murine model to deplete hepatic stellate cells uncovers their role in amplifying liver damage in mice', *Hepatology (Baltimore, Md.)*, vol. 57, no. 1, pp. 339–350, <https://pubmed.ncbi.nlm.nih.gov/22961591/>.

REFERENCES

Ramboer, E, Vanhaecke, T, Rogiers, V & Vinken, M 2015, 'Immortalized human hepatic cell lines for in vitro testing and research purposes', *Methods in molecular biology (Clifton, N.J.)*, vol. 1250, pp. 53–76, <https://www.ncbi.nlm.nih.gov/pmc/articles/PMC4579543/>.

Ranga, A, Gjorevski, N & Lutolf, MP 2014, 'Drug discovery through stem cell-based organoid models', *Advanced Drug Delivery Reviews*, vol. 69-70, pp. 19–28.

Reich, M, Liefeld, T, Gould, J, Lerner, J, Tamayo, P & Mesirov, JP 2006, 'GenePattern 2.0', *Nature Genetics*, vol. 38, no. 5, pp. 500–501, <https://pubmed.ncbi.nlm.nih.gov/16642009/>.

Remon, J & Dienstmann, R 2018, 'Precision oncology: separating the wheat from the chaff', *ESMO Open*, vol. 3, no. 6, p. e000446.

Rios, AC & Clevers, H 2018, 'Imaging organoids: a bright future ahead', *Nature Methods*, vol. 15, no. 1, pp. 24–26.

Robinson, MW, Harmon, C & O'Farrelly, C 2016, 'Liver immunology and its role in inflammation and homeostasis', *Cellular & Molecular Immunology*, vol. 13, no. 3, pp. 267–276.

Rodriguez-Almazan, C 2008, 'Structural Basis of Human Triosephosphate Isomerase Deficiency: MUTATION E104D IS RELATED TO ALTERATIONS OF A CONSERVED WATER NETWORK AT THE DIMER INTERFACE', *Journal of Biological Chemistry*, vol. 283, no. 34, pp. 23254–23263, <https://www.sciencedirect.com/science/article/pii/S0021925819493824>.

Rodríguez-Antona, C, Donato, MT, Boobis, A, Edwards, RJ, Watts, PS, Castell, JV & Gómez-Lechón, M-J . 2002, 'Cytochrome P450 expression in human hepatocytes and hepatoma cell lines: molecular mechanisms that determine lower expression in cultured cells', *Xenobiotica;*

REFERENCES

the Fate of Foreign Compounds in Biological Systems, vol. 32, no. 6, pp. 505–520, <https://pubmed.ncbi.nlm.nih.gov/12160483/>.

Roth, GA, Abate, D, Abate, KH, Abay, SM, Abbafati, C, Abbasi, N, Abbastabar, H, Abd-Allah, F, Abdela, J, Abdelalim, A, Abdollahpour, I, Abdulkader, RS, Abebe, HT, Abebe, M, Abebe, Z, Abejie, AN, Abera, SF, Abil, OZ, Abraha, HN & Abrham, AR 2018, 'Global, regional, and national age-sex-specific mortality for 282 causes of death in 195 countries and territories, 1980–2017: a systematic analysis for the Global Burden of Disease Study 2017', *The Lancet*, vol. 392, no. 10159, pp. 1736–1788.

Roth, KJ & Copple, BL 2015, 'Role of Hypoxia-Inducible Factors in the Development of Liver Fibrosis', *Cellular and Molecular Gastroenterology and Hepatology*, vol. 1, no. 6, pp. 589–597, <https://pubmed.ncbi.nlm.nih.gov/28210703/>.

Rountree, CB, Barsky, L, Ge, S, Zhu, J, Senadheera, S & Crooks, GM 2007, 'A CD133-expressing murine liver oval cell population with bilineage potential', *Stem Cells (Dayton, Ohio)*, vol. 25, no. 10, pp. 2419–2429, <https://pubmed.ncbi.nlm.nih.gov/17585168/>.

Rui, L 2014, 'Energy Metabolism in the Liver', *Comprehensive Physiology*, vol. 4, no. 1, pp. 177–197.

Sachs, N, Papaspyropoulos, A, Zomer-van Ommen, DD, Heo, I, Böttinger, L, Klay, D, Weeber, F, Huelsz-Prince, G, Iakobachvili, N, Amatngalim, GD, de Ligt, J, van Hoeck, A, Proost, N, Viveen, MC, Lyubimova, A, Teeven, L, Derakhshan, S, Korving, J, Begthel, H & Dekkers, JF 2019, 'Long-term expanding human airway organoids for disease modeling', *The EMBO journal*, vol. 38, no. 4, <https://pubmed.ncbi.nlm.nih.gov/30643021/>.

REFERENCES

Saile, B, Matthes, N, Knittel, T & Ramadori, G 1999, 'Transforming growth factor ? and tumor necrosis factor ? inhibit both apoptosis and proliferation of activated rat hepatic stellate cells', *Hepatology*, vol. 30, no. 1, pp. 196–202.

Schlessinger, J 1997, 'Direct Binding and Activation of Receptor Tyrosine Kinases by Collagen', *Cell*, vol. 91, no. 7, pp. 869–872.

Schulze, K, Nault, J-C & Villanueva, A 2016, 'Genetic profiling of hepatocellular carcinoma using next-generation sequencing', *Journal of Hepatology*, vol. 65, no. 5, pp. 1031–1042, <https://pubmed.ncbi.nlm.nih.gov/27262756/>.

Schwank, G, Koo, B-K, Sasselli, V, Dekkers, Johanna F, Heo, I, Demircan, T, Sasaki, N, Boymans, S, Cuppen, E, van der Ent, Cornelis K, Nieuwenhuis, Edward ES, Beekman, Jeffrey M & Clevers, H 2013, 'Functional Repair of CFTR by CRISPR/Cas9 in Intestinal Stem Cell Organoids of Cystic Fibrosis Patients', *Cell Stem Cell*, vol. 13, no. 6, pp. 653–658.

Seki, E & Schwabe, RF 2015, 'Hepatic inflammation and fibrosis: Functional links and key pathways', *Hepatology*, vol. 61, no. 3, pp. 1066–1079, <https://www.ncbi.nlm.nih.gov/pmc/articles/PMC4306641/>.

Seo, HR 2015, 'Roles of Tumor Microenvironment in Hepatocelluar Carcinoma', *Current Medicinal Chemistry*, vol. 11, no. 2, pp. 82–93, <https://www.ncbi.nlm.nih.gov/pmc/articles/PMC4997931/>.

Sepanlou, SG, Safiri, S, Bisignano, C, Ikuta, KS, Merat, S, Saberifiroozi, M, Poustchi, H, Tsoi, D, Colombara, DV, Abdoli, A, Adedoyin, RA, Afarideh, M, Agrawal, S, Ahmad, S, Ahmadian, E, Ahmadpour, E, Akinyemiju, T, Akunna, CJ, Alipour, V & Almasi-Hashiani, A 2020, 'The global, regional, and national burden of cirrhosis by cause in 195 countries and territories,

REFERENCES

1990–2017: a systematic analysis for the Global Burden of Disease Study 2017', *The Lancet Gastroenterology & Hepatology*, vol. 5, no. 3, pp. 245–266.

Sherlock, S & Dooley, J 2002, *Diseases of the Liver and Biliary System*, 11th Edition, Blackwell Science Ltd.

Shin, S, Walton, G, Aoki, R, Brondell, K, Schug, J, Fox, A, Smirnova, O, Dorrell, C, Erker, L, Chu, AS, Wells, RG, Grompe, M, Greenbaum, LE & Kaestner, KH 2011, 'Foxl1-Cre-marked adult hepatic progenitors have clonogenic and bilineage differentiation potential', *Genes & Development*, vol. 25, no. 11, pp. 1185–1192, <https://www.ncbi.nlm.nih.gov/pmc/articles/PMC3110956/>.

Shipley, LC, Axley, D & Singal, A 2019, *Liver Fibrosis : A Clinical Update*, www.semanticscholar.org, <https://www.semanticscholar.org/paper/Liver-Fibrosis-%3A-A-Clinical-Update-Shipley-Axley/22c455f5d321768ac79b6bb24a2c59ca8b31ef72>.

Singal, AK, Singh, A, Jaganmohan, S, Guturu, P, Mummadi, R, Kuo, Y & Sood, GK 2010, 'Antiviral Therapy Reduces Risk of Hepatocellular Carcinoma in Patients With Hepatitis C Virus–Related Cirrhosis', *Clinical Gastroenterology and Hepatology*, vol. 8, no. 2, pp. 192–199, <https://www.sciencedirect.com/science/article/pii/S1542356509010854>.

Smith, A 2006, 'A glossary for stem-cell biology', *Nature*, vol. 441, no. 7097, pp. 1060–1060.

Song, HY, Rothe, M & Goeddel, DV 1996, 'The tumor necrosis factor-inducible zinc finger protein A20 interacts with TRAF1/TRAF2 and inhibits NF-kappaB activation.', *Proceedings of the National Academy of Sciences of the United States of America*, vol. 93, no. 13, pp. 6721–6725, <https://www.ncbi.nlm.nih.gov/pmc/articles/PMC39093/>.

REFERENCES

Song, Y, Kim, S, Kim, KM, Choi, EK, Kim, J & Seo, HR 2016, 'Activated hepatic stellate cells play pivotal roles in hepatocellular carcinoma cell chemoresistance and migration in multicellular tumor spheroids', *Scientific Reports*, vol. 6, <https://www.ncbi.nlm.nih.gov/pmc/articles/PMC5113076/>.

Soto-Gutierrez, A, Gough, A, Vernetti, LA, Taylor, D & Monga, SP 2017, 'Pre-clinical and clinical investigations of metabolic zonation in liver diseases: The potential of microphysiology systems', *Experimental Biology and Medicine*, vol. 242, no. 16, pp. 1605–1616, <https://www.ncbi.nlm.nih.gov/pmc/articles/PMC5661767/>.

Starokozhko, V & Groothuis, GMM 2016, 'Judging the value of "liver-on-a-chip" devices for prediction of toxicity', *Expert Opinion on Drug Metabolism & Toxicology*, vol. 13, no. 2, pp. 125–128.

Subramanian, A, Tamayo, P, Mootha, VK, Mukherjee, S, Ebert, BL, Gillette, MA, Paulovich, A, Pomeroy, SL, Golub, TR, Lander, ES & Mesirov, JP 2005, 'Gene set enrichment analysis: A knowledge-based approach for interpreting genome-wide expression profiles', *Proceedings of the National Academy of Sciences*, vol. 102, no. 43, pp. 15545–15550.

Sudo, K, Yamada, Y, Moriwaki, H, Saito, K & Seishima, M 2005, 'Lack of tumor necrosis factor receptor type 1 inhibits liver fibrosis induced by carbon tetrachloride in mice', *Cytokine*, vol. 29, no. 5, pp. 236–244, <https://pubmed.ncbi.nlm.nih.gov/15760680/>.

Suzuki, A, Sekiya, S, Onishi, M, Oshima, N, Kiyonari, H, Nakauchi, H & Taniguchi, H 2008, 'Flow cytometric isolation and clonal identification of self-renewing bipotent hepatic progenitor cells in adult mouse liver', *Hepatology (Baltimore, Md.)*, vol. 48, no. 6, pp. 1964–1978, <https://pubmed.ncbi.nlm.nih.gov/18837044/>.

REFERENCES

Tabibian, JH, Masyuk, AI, Masyuk, TV, O'Hara, SP & LaRusso, NF 2013, 'Physiology of Cholangiocytes', *Comprehensive Physiology*, vol. 3, no. 1, pp. 541–565.

Tacke, F & Weiskirchen, R 2018, 'An update on the recent advances in antifibrotic therapy', *Expert Review of Gastroenterology & Hepatology*, vol. 12, no. 11, pp. 1143–1152, <https://pubmed.ncbi.nlm.nih.gov/30261763/>.

Takase, HM, Itoh, T, Ino, S, Wang, T, Koji, T, Akira, S, Takikawa, Y & Miyajima, A 2013, 'FGF7 is a functional niche signal required for stimulation of adult liver progenitor cells that support liver regeneration', *Genes & Development*, vol. 27, no. 2, pp. 169–181, <https://pubmed.ncbi.nlm.nih.gov/23322300/>.

Tanimizu, N & Mitaka, T 2014, 'Re-evaluation of liver stem/progenitor cells', *Organogenesis*, vol. 10, no. 2, pp. 208–215.

Tiriac, H, Belleau, P, Engle, DD, Plenker, D, Deschênes, A, Somerville, TDD, Froeling, FEM, Burkhart, RA, Denroche, RE, Jang, G-H, Miyabayashi, K, Young, CM, Patel, H, Ma, M, LaComb, JF, Palmaira, RLD, Javed, AA, Huynh, JC, Johnson, M & Arora, K 2018, 'Organoid Profiling Identifies Common Responders to Chemotherapy in Pancreatic Cancer', *Cancer Discovery*, vol. 8, no. 9, pp. 1112–1129.

Torricelli, P, Antonelli, F, Ferorelli, P, De Martino, A, Shevchenko, A, Siciliano, A & Beninati, S 2016, 'Organ Culture Model of Liver for the Study of Cancer Treatment for Hepatocellular Carcinoma', *Cancer Research Journal*, vol. 4, no. 2, p. 37.

Trefts, E, Gannon, M & Wasserman, DH 2017, 'The liver', *Current Biology*, vol. 27, no. 21, pp. R1147–R1151.

REFERENCES

Treyer, A & Müsch, A 2013, 'Hepatocyte Polarity', *Comprehensive Physiology*, vol. 3, no. 1, pp. 243–287, <https://www.ncbi.nlm.nih.gov/pmc/articles/PMC3697931/>.

Tsochatzis, EA, Bosch, J & Burroughs, AK 2014, 'Liver cirrhosis', *The Lancet*, vol. 383, no. 9930, pp. 1749–1761, <https://www.thelancet.com/journals/lancet/article/PIIS0140-6736(14)60121-5/fulltext>.

Tsuchida, T & Friedman, SL 2017, 'Mechanisms of hepatic stellate cell activation', *Nature Reviews Gastroenterology & Hepatology*, vol. 14, no. 7, pp. 397–411.

Tu, T, Calabro, SR, Lee, A, Maczurek, AE, Budzinska, MA, Warner, FJ, McLennan, SV & Shackel, NA 2015, 'Hepatocytes in liver injury: Victim, bystander, or accomplice in progressive fibrosis?', *Journal of Gastroenterology and Hepatology*, vol. 30, no. 12, pp. 1696–1704.

Usta, OB, McCarty, WJ, Bale, S, Hegde, M, Jindal, R, Bhushan, A, Golberg, I & Yarmush, ML 2015, 'Microengineered cell and tissue systems for drug screening and toxicology applications: Evolution ofin-vitroliver technologies', *TECHNOLOGY*, vol. 03, no. 01, pp. 1–26.

Vaira, V, Fedele, G, Pyne, S, Fasoli, E, Zadra, G, Bailey, D, Snyder, E, Faversani, A, Coggi, G, Flavin, R, Bosari, S & Loda, M 2010, 'Preclinical model of organotypic culture for pharmacodynamic profiling of human tumors', *Proceedings of the National Academy of Sciences of the United States of America*, vol. 107, no. 18, pp. 8352–8356, <https://www.ncbi.nlm.nih.gov/pmc/articles/PMC2889536/>.

van den Berg, CW, Ritsma, L, Avramut, MC, Wiersma, LE, van den Berg, BM, Leuning, DG, Lievers, E, Koning, M, Vanslambrouck, JM, Koster, AJ, Howden, SE, Takasato, M, Little, MH & Rabelink, TJ 2018, 'Renal Subcapsular Transplantation of PSC-Derived Kidney Organoids

REFERENCES

Induces Neo-vasculogenesis and Significant Glomerular and Tubular Maturation In Vivo', *Stem Cell Reports*, vol. 10, no. 3, pp. 751–765, <https://www.sciencedirect.com/science/article/pii/S2213671118300675#bib19>.

Verrier, ER, Colpitts, C, Schuster, C, Zeisel, M & Baumert, T 2016a, 'Cell Culture Models for the Investigation of Hepatitis B and D Virus Infection', *Viruses*, vol. 8, no. 9, p. 261.

Verrier, ER, Colpitts, CC, Bach, C, Heydmann, L, Weiss, A, Renaud, M, Durand, SC, Habersetzer, F, Durantel, D, Abou-Jaoudé, G, López Ledesma, MM, Felmlee, DJ, Soumillon, M, Croonenborghs, T, Pochet, N, Nassal, M, Schuster, C, Brino, L, Sureau, C & Zeisel, MB 2016b, 'A targeted functional RNA interference screen uncovers glypican 5 as an entry factor for hepatitis B and D viruses', *Hepatology (Baltimore, Md.)*, vol. 63, no. 1, pp. 35–48, <https://pubmed.ncbi.nlm.nih.gov/26224662/>.

Vogel, W, Gish, GD, Alves, F & Pawson, T 1997, 'The Discoidin Domain Receptor Tyrosine Kinases Are Activated by Collagen', *Molecular Cell*, vol. 1, no. 1, pp. 13–23, <https://www.sciencedirect.com/science/article/pii/S1097276500800039>.

Waki, K, Anno, K, Ono, T, Ide, T, Chayama, K & Tahara, H 2010, 'Establishment of functional telomerase immortalized human hepatocytes and a hepatic stellate cell line for telomere-targeting anticancer drug development', *Cancer Science*, vol. 101, no. 7, pp. 1678–1685, <https://www.ncbi.nlm.nih.gov/pubmed/20456367>.

Wang, H, Naghavi, M, Allen, C, Barber, RM, Bhutta, ZA, Carter, A, Casey, DC, Charlson, FJ, Chen, AZ, Coates, MM, Coggeshall, M, Dandona, L, Dicker, DJ, Erskine, HE, Ferrari, AJ, Fitzmaurice, C, Foreman, K, Forouzanfar, MH, Fraser, MS & Fullman, N 2016, 'Global, regional, and national life expectancy, all-cause mortality, and cause-specific mortality for 249

REFERENCES

causes of death, 1980–2015: a systematic analysis for the Global Burden of Disease Study 2015', *The Lancet*, vol. 388, no. 10053, pp. 1459–1544.

Wang, Y, Wang, H, Deng, P, Chen, W, Guo, Y, Tao, T & Qin, J 2018, 'In situ differentiation and generation of functional liver organoids from human iPSCs in a 3D perfusable chip system', *Lab on a Chip*, vol. 18, no. 23, pp. 3606–3616.

Ware, BR, Durham, MJ, Monckton, CP & Khetani, SR 2017, 'A Cell Culture Platform to Maintain Long-term Phenotype of Primary Human Hepatocytes and Endothelial Cells', *Cellular and Molecular Gastroenterology and Hepatology*, vol. 5, no. 3, pp. 187–207, <https://www.ncbi.nlm.nih.gov/pmc/articles/PMC5782488/>.

Wasser, S & Tan, CE 1999, 'Experimental models of hepatic fibrosis in the rat', *Annals of the Academy of Medicine, Singapore*, vol. 28, no. 1, pp. 109–111, <https://pubmed.ncbi.nlm.nih.gov/10374036/>.

Weiskirchen, R & Tacke, F 2014, 'Cellular and molecular functions of hepatic stellate cells in inflammatory responses and liver immunology', *Hepatobiliary Surgery and Nutrition*, vol. 3, no. 6, pp. 344–363, <https://pubmed.ncbi.nlm.nih.gov/25568859/>.

Weiswald, L-B, Bellet, D & Dangles-Marie, V 2015, 'Spherical Cancer Models in Tumor Biology', *Neoplasia*, vol. 17, no. 1, pp. 1–15.

Wisse, E, Luo, D, Vermijlen, D, Kanellopoulou, C, De Zanger, R & Braet, F 1997, 'On the function of pit cells, the liver-specific natural killer cells', *Seminars in Liver Disease*, vol. 17, no. 4, pp. 265–286, <https://pubmed.ncbi.nlm.nih.gov/9408963/>.

Workman, MJ, Gleeson, JP, Troisi, EJ, Estrada, HQ, Kerns, SJ, Hinojosa, CD, Hamilton, GA, Targan, SR, Svendsen, CN & Barrett, RJ 2018, 'Enhanced Utilization of Induced Pluripotent

REFERENCES

Stem Cell–Derived Human Intestinal Organoids Using Microengineered Chips', *Cellular and Molecular Gastroenterology and Hepatology*, vol. 5, no. 4, pp. 669-677.e2, <https://www.sciencedirect.com/science/article/pii/S2352345X1730187X>.

Workman, MJ, Mahe, MM, Trisno, S, Poling, HM, Watson, CL, Sundaram, N, Chang, C-F, Schiesser, J, Aubert, P, Stanley, EG, Elefanty, AG, Miyaoka, Y, Mandegar, MA, Conklin, BR, Neunlist, M, Brugmann, SA, Helmrath, MA & Wells, JM 2017, 'Engineered human pluripotent-stem-cell-derived intestinal tissues with a functional enteric nervous system', *Nature Medicine*, vol. 23, no. 1, pp. 49–59, <https://www.nature.com/articles/nm.4233>.

Wright, MC & Paine, AJ 1992, 'Evidence that the loss of rat liver cytochrome P450 in vitro is not solely associated with the use of collagenase, the loss of cell-cell contacts and/or the absence of an extracellular matrix', *Biochemical Pharmacology*, vol. 43, no. 2, pp. 237–243, <https://pubmed.ncbi.nlm.nih.gov/1310850/>.

Xinaris, C, Benedetti, V, Novelli, R, Abbate, M, Rizzo, P, Conti, S, Tomasoni, S, Corna, D, Pozzobon, M, Cavallotti, D, Yokoo, T, Morigi, M, Benigni, A & Remuzzi, G 2016, 'Functional Human Podocytes Generated in Organoids from Amniotic Fluid Stem Cells', *Journal of the American Society of Nephrology*, vol. 27, no. 5, pp. 1400–1411, <https://jasn.asnjournals.org/content/27/5/1400>.

Xu, JJ, Diaz, D & O'Brien, PJ 2004, 'Applications of cytotoxicity assays and pre-lethal mechanistic assays for assessment of human hepatotoxicity potential', *Chemico-Biological Interactions*, vol. 150, no. 1, pp. 115–128.

Yamasaki, K, Kawasaki, S, Young, RD, Fukuoka, H, Tanioka, H, Nakatsukasa, M, Quantock, AJ & Kinoshita, S 2009, 'Genomic Aberrations and Cellular Heterogeneity in SV40-Immortalized Human Corneal Epithelial Cells', *Investigative Ophthalmology & Visual*

REFERENCES

Science, vol. 50, no. 2, pp. 604–613, <https://iovs.arvojournals.org/article.aspx?articleid=2184985>.

Yang, K, Guo, C, Woodhead, JL, St Claire, RL, Watkins, PB, Siler, SQ, Howell, BA & Brouwer, KLR 2016, 'Sandwich-Cultured Hepatocytes as a Tool to Study Drug Disposition and Drug-Induced Liver Injury', *Journal of Pharmaceutical Sciences*, vol. 105, no. 2, pp. 443–459, <https://pubmed.ncbi.nlm.nih.gov/26869411/>.

Yang, W, Yan, H-X, Chen, L, Liu, Q, He, Y-Q, Yu, L-X, Zhang, S-H, Huang, D-D, Tang, L, Kong, X-N, Chen, C, Liu, S-Q, Wu, M-C & Wang, H-Y 2008, 'Wnt/β-Catenin Signaling Contributes to Activation of Normal and Tumorigenic Liver Progenitor Cells', *Cancer Research*, vol. 68, no. 11, pp. 4287–4295, <https://cancerres.aacrjournals.org/content/68/11/4287>.

Yang, YM & Seki, E 2015, 'TNFα in liver fibrosis', *Current pathobiology reports*, vol. 3, no. 4, pp. 253–261, <https://www.ncbi.nlm.nih.gov/pmc/articles/PMC4693602/>.

Yanni, SB, Augustijns, PF, Benjamin, DK, Brouwer, KLR, Thakker, DR & Annaert, PP 2010, 'In Vitro Investigation of the Hepatobiliary Disposition Mechanisms of the Antifungal Agent Micafungin in Humans and Rats', *Drug Metabolism and Disposition*, vol. 38, no. 10, pp. 1848–1856.

Yoshida, K & Matsuzaki, K 2012, 'Differential Regulation of TGF-β/Smad Signaling in Hepatic Stellate Cells between Acute and Chronic Liver Injuries', *Frontiers in Physiology*, vol. 3, no. 53, <https://www.ncbi.nlm.nih.gov/pmc/articles/PMC3307138/>.

Yovchev, MI, Grozdanov, PN, Joseph, B, Gupta, S & Dabeva, MD 2007, 'Novel hepatic progenitor cell surface markers in the adult rat liver', *Hepatology (Baltimore, Md.)*, vol. 45, no. 1, pp. 139–149, <https://pubmed.ncbi.nlm.nih.gov/17187413/>.

REFERENCES

Yu, L-X, Ling, Y & Wang, H-Y 2018, 'Role of nonresolving inflammation in hepatocellular carcinoma development and progression', *npj Precision Oncology*, vol. 2, no. 1.

Yu, S, Chen, J, Wu, M, Chen, H, Kato, N & Yuan, Z 2010, 'Hepatitis B virus polymerase inhibits RIG-I- and Toll-like receptor 3-mediated beta interferon induction in human hepatocytes through interference with interferon regulatory factor 3 activation and dampening of the interaction between TBK1/IKK and DDX3', *Journal of General Virology*, vol. 91, no. 8, pp. 2080–2090.

Yu, Y, Liu, H, Ikeda, Y, Amiot, BP, Rinaldo, P, Duncan, SA & Nyberg, SL 2012, 'Hepatocyte-like cells differentiated from human induced pluripotent stem cells: Relevance to cellular therapies', *Stem cell research*, vol. 9, no. 3, pp. 196–207, <https://www.ncbi.nlm.nih.gov/pmc/articles/PMC3619384/>.

Zcharia, E, Atzmon, R, Nagler, A, Shimoni, A, Peretz, T, Vlodavsky, I & Nagler, A 2012, 'Inhibition of matrix metalloproteinase-2 by halofuginone is mediated by the Egr1 transcription factor', *Anti-Cancer Drugs*, vol. 23, no. 10, pp. 1022–1031.

Zeilinger, K, Freyer, N, Damm, G, Seehofer, D & Knöspel, F 2016, 'Cell sources forin vitrohuman liver cell culture models', *Experimental Biology and Medicine*, vol. 241, no. 15, pp. 1684–1698.

Zhang, D, Luo, G, Ding, X & Lu, C 2012, 'Preclinical experimental models of drug metabolism and disposition in drug discovery and development', *Acta Pharmaceutica Sinica B*, vol. 2, no. 6, pp. 549–561.